Distribution Agreement

In presenting this thesis or dissertation as a partial fulfillment of the requirements for an advanced degree from Emory University, I hereby grant to Emory University and its agents the non-exclusive license to archive, make accessible, and display my thesis or dissertation in whole or in part in all forms of media, now or hereafter known, including display on the world wide web. I understand that I may select some access restrictions as part of the online submission of this thesis or dissertation. I retain all ownership rights to the copy right of the thesis or dissertation. I also retain the right to use in future works (such as articles or books) all or part of this thesis or dissertation.

Signature:

_____ _____

Samuel A. Druzak Date

Differential regulation of Peroxisome Proliferator Activating Receptors (PPARs) via host and microbial derived processes

By

Samuel A. Druzak
Doctor of Philosophy

Graduate Division of Biological and Biomedical Science
Molecular and Systems Pharmacology

Eric Ortlund, Ph.D.
Advisor

Christine Dunham, Ph.D.
Committee Member

Edward Morgan, Ph.D.
Committee Member

John Calvert, Ph.D.
Committee Member

Accepted:

Kimberly Jacob Arriola, Ph.D.
Dean of the James T. Laney School of Graduate Studies

Date

Differential regulation of Peroxisome Proliferator Activating Receptors (PPARs) via host and microbial derived processes

By

Samuel A. Druzak
B.S., Emory University

Advisor: Eric Ortlund, Ph.D.

An Abstract of
a dissertation submitted to the Faculty of the
James T. Laney School of Graduate Studies of Emory University
in partial fulfillment of the requirements for the degree of
Doctor of Philosophy
In
Graduate Division of Biological
Molecular and Systems Pharmacology
2022

Abstract:

Nuclear receptors (NRs) are a highly conserved group of ligand regulated transcription factors. In humans there are 48 members with each member playing unique complementary roles that allow for generation and maintenance of multicellular life. The peroxisome proliferator-activated (PPARs) subfamily of NRs regulate metabolism, inflammation, and proliferation, making them attractive targets to modulate metabolic syndrome, inflammatory disease, and cancer. Many drugs have been successfully developed to target these receptors specifically to treat metabolic disease (i.e. fibrates and glitazones). While much of the therapeutic potential of PPARs has been realized, undesired tissue specific effects as well as an inability to treat the underlying cause of metabolic disease limit the utility of these treatments and have stifled development of new PPAR modulators. To address these problems, this present work seeks to elucidate novel mechanisms by which host proteins and microbes regulate PPARs. We began our characterization by investigating the mechanism by which PPARs acquire ligand. Previously, our lab has demonstrated that FABP5 enhances PPARδ transactivation in a polyunsaturated fatty acid dependent manner. Here we have uncovered a member of the STARD family capable of regulating PPAR activity. Our characterization of the STARD2-PPARδ interaction uncovered a previously unknown role of lipid transport proteins in directly engaging with and repressing PPARδ activity in a ligand dependent manner. In parallel, we have also characterized the role that gut flora play in regulating PPAR activity. We identified a gut derived obesogen delta-valerobetaine (VB). Treatment of mice with VB results in diet induced weight gain and hepatic steatosis. This phenotype was posited to occur by inhibiting lipid metabolism and influencing the activity of hepatic PPARs. Here we describe the molecular mechanism the underpins the observed phenotype and show that VB is capable of altering carnitine biosynthesis and carnitine shuttling, effectively decreasing lipid metabolism. Taken together we have identified two novel mechanisms by which host and microbial processes are able to affect PPAR activity and have uncovered several new targets capable of tuning PPAR transactivation upstream of directly modulating these receptors.

Differential regulation of Peroxisome Proliferator Activating Receptors (PPARs) via host and microbial derived processes

By

Samuel A. Druzak
B.S., Emory University

Advisor: Eric Ortlund, Ph.D.

A dissertation submitted to the Faculty of the
James T. Laney School of Graduate Studies of Emory University
in partial fulfillment of the requirements for the degree of
Doctor of Philosophy
In
Graduate Division of Biological
Molecular and Systems Pharmacology
2022

Table of Contents

List of Figures

Chapter 1:

Chapter 2:

Chapter 3:

Chapter 4:

Appendix I:

List of Tables

Chapter 1:

Chapter 2:

Chapter 3:

Appendix I:

List of Abbreviations

a-Syn	Alpha-synuclein
AAV	Adeno-associated virus
ACBP	Acyl-CoA binding protein
ACCA2	acetyl-CoA acyltransferase 2
Acots	Acyl-CoA Thioesterase
ACSL	Acyl-CoA Synthetase Long Chain
ADRP	Adipose differentiation-related protein
AF-1	Activation function surface 1
AF-2	Activation function surface 2
ANGPLT4	Angiopoietin-like 4
APS	Advanced Photon Source
AR	Androgen receptor
BBOX	Butyrobetaine dioxygenase
BRET	Bioluminescence Resonance Energy Transfer
BSA	Bovine serum albumin
CACT	Carnitine-acylcarnitine translocase
CAR	Constitutive androstane receptor
CHEA	ChIP Enrichment Analysis
CLA	Conjugated linoleic acid
CMV	Cytomegalovirus
COUP-TFα	Chicken ovalbumin upstream promoter-transcription factor a

COUP-TFβ	Chicken ovalbumin upstream promoter-transcription factor b
COUP-TFγ	Chicken ovalbumin upstream promoter-transcription factor g
CPT2	Carnitine palmitoyltransferase II
CRABPII	Cellular retinoic acid-binding protein
CRAL	Cellular retinaldehyde-binding protein
CRAT	Carnitine O-acetyltransferase
CTRL	Control
CYP	Cytochrome P450
DAX1	Dosage-sensitive sex reversal-adrenal hypoplasia congenital critical region on the X chromosome, Gene 1
DBD	DNA binding domain
DEGs	Differentially expressed genes
DTT	Dithiothreitol
ECH1	Enoyl-CoA Hydratase 1
EDTA	Ethylenediaminetetraacetic acid
ER	Endoplasmic reticulum
ERRα	Estrogen-related receptor-a
ERRβ	Estrogen-related receptor-b
ERRγ	Estrogen-related receptor-g
ERα	Estrogen receptor-a
ERβ	Estrogen receptor-b

ETFDH	Electron Transfer Flavoprotein Dehydrogenase
FABP	Fatty acid binding protein
FBS	Fetal bovine serum
FEM	Feature enhanced map
FFA	Free fatty acids
FL	Full length
FXR	Farnesoid X receptor
FXRβ	Farnesoid X receptor-b
GCNF	Germ cell nuclear factor
GF	Germ free
GLTP	Glycolipid transfer protein
GR	Glucocorticoid receptor
GTT	Glucose tolerance test
HBS	HEPES buffered saline
HC	Homocarnitine
HEK293	Human embryoinic kidney ceks 239
HEPES	4-(2-hydroxyethyl)-1-piperazineethanesulfonic acid
HFD	High Fat Diet
HIF1a	Hypoxia-inducible factor 1-alpha
HMGCS2	3-Hydroxy-3-Methylglutaryl-CoA Synthase 2
HNF4α	Hepatocyte nuclear factor-4-a
HNF4γ	Hepatocyte nuclear factor-4-g

i.v.	Intravenus
ILK	Integrin Linked Kinase
IMAC	Immobilized metal affinity chromatography
IPTG	Isopropyl-1-thio-D-galactopyranoside
ITT	Insulin tolerance test
KD	Knock down
KEGG	Kyoto Encyclopedia of Genes and Genomes
KLF10	Kruppel Like Factor 10
KO	Knock out
L-Pctp-/-	Liver specific pctp knockout
LBD	Ligand binding domain
LRH-1	Liver receptor homolog-1
LTML	13C-labeled Trimethyllysine
LTP	Lipid transport proteins
LXR	Liver X receptor
LXRα	Liver X receptor-a
LXRβ	Liver X receptor-b
MCAD	Medium-chain acyl-CoA dehydrogenase
MCD	Methionine and choline depleted
MetS	Metabolic syndrome
ML	MD-2-related lipid-recognition
MLYCD	Malonyl-CoA Decarboxylase

MR	Mineralocorticoid receptor
MS	Mass spectrometry
N-Luc	Nano-luciferase
NAFLD	Non-alcoholic fatty liver disease
Nano-PCA	Nano-luciferase protein complementation assay
ND	Normal diet
NEFA	Non-esterified fatty acids
NGF1-B	Nerve growth factor 1B
NHS	N-Hydroxysuccinimide
NLS	Nuclear localization signals
NMR	Nuclear magnetic resonance
NOR-1	Neuron-derived orphan receptor 1
NPC1	Niemann–Pick C1
NR	Nuclear receptor
NURR1	Nurr-related factor 1
OSBP	Oxysterol-binding protein
PAX3	Paired Box 3
PBS	Phosphate buffered saline
PC	Phosphatidylcholine
PC-TP	Phosphatidylcholine transfer protein
PCR	Polymerase chain reaction
PDPK1	3-Phosphoinositide Dependent Protein Kinase 1
PE	Phosphatidylethanolamine

PEG	Polyethylene glycol
PITP	Phosphatidylinositol transfer protein
PL	Phospholipid
PMSF	Phenylmethylsulfonyl fluorid
PNR	Photoreceptor-cell-specific nuclear receptor
PPAR	Peroxisome proliferator-activated receptors
PPARGC1a	PPARG Coactivator 1 Alpha
PPARα	Peroxisome proliferator-activated receptor-a
PPARγ	Peroxisome proliferator-activated receptor-g
PPARδ	Peroxisome proliferator-activated receptor-d
PR	Progesterone receptor
PTEN	Phosphatase And Tensin Homolog
PTM	Post translational modification
PTT	Pyruvate tolerance test
PUFA	Polyunsaturated fatty acid
PXR	Pregname X receptor
RA	Retinoic acid
RARα	Retinoic acid receptor-a
RARβ	Retinoic acid receptor-b
RARγ	Retinoic acid receptor-g

RER	Respiratory exchange ratio
REV-ERBα	Reverse-Erb-a
REV-ERBβ	Reverse-Erb-b
RORα	Retinoic acid-related orphan-a
RORβ	Retinoic acid-related orphan-b
RORγ	Retinoic acid-related orphan-g
RXRα	Retinoid X receptor-a
RXRβ	Retinoid X receptor-b
RXRγ	Retinoid X receptor-g
SCP2	sterol carrier protein 2
SEA	Similarity ensemble approach
SER-CAT	Southeast Regional Collaborative Access Team
SF-1	Steroidogenic factor 1
SHP	Short heterodimeric partner
siRNA	Short inhibitory RNA
SLC	Solute carrier
StAR	Steroidogenic acute regulatory
STARDs	Steroidogenic acute regulatory related transfer domains
TBG	Thyroxine-binding globulin
TBS	Tris buffered saline
TCA	Tricarboxylic acid
TCEP	Tris(2-carboxyethyl)phosphine
TEV	Tobacco Etch Virus

TG	Triglycerides
Them1/2	Thioesterase superfamily member 1/2
TML	Trimethyllysine
TR2	Testicular receptor 2
TR4	Testicular receptor 4
TRIC	Temperature-Related Intensity Change
TRIS	Tris(hydroxymethyl)aminomethane hydrochloride
TRα	Thyroid hormone receptor-a
TRβ	Thyroid hormone receptor-b
TXR	Tailless homolog orphan receptor
VB	Delta-valerobetaine
VDR	Vitamin D receptor
WT	Wild type
γBB	Gamma butyrobetaine

Chapter 1: Differential regulations of peroxisome proliferator activating receptors via host and microbial derived processes

1.1 Introduction to Nuclear Receptors

Nuclear receptors (NRs) are ligand activated transcription factors that play an important role in many biological processes such as development, metabolism, inflammation, reproduction, and circadian rhythm. (Kininis and Kraus 2008; Gustafsson 2016) They are confined to metazoans, with 48 members present in humans. (Mazaira et al. 2018) NR activity is controlled by small lipophilic compounds that bind to a C-terminal ligand binding domain (LBD), inducing a conformational change that stimulates nuclear localization and/or repositions the activation function surface 2 (AF-2) within the LBD to enable binding of transcriptional co-regulator proteins that in turn activate or repress gene transcription. (Nagy and Schwabe 2004; Li, Lambert, and Xu 2003) NRs also contain a DNA binding domain (DBD) that recognizes specific DNA sequences, targeting the receptor to the promoter region of particular genes. (Gronemeyer and Moras, 1995) In addition to these structured domains, NRs have a disordered N-terminal region that contains the activation function surface 1 (AF-1) that also interacts with co-regulator proteins (Kumar and Thompson 2003) , and an unstructured hinge region connecting the DBD and LBD (Figure1.1). (Pawlak et al., 2012) NRs have been realized as a target for pharmaceutical development due to their essential role in controlling gene transcription, their ability to be controlled by small molecules, and their role in many pathophysiological processes. (Mukherjee and Mani 2010; Sladek 2003) (Gross and Staels 2007; Schulman 2010)

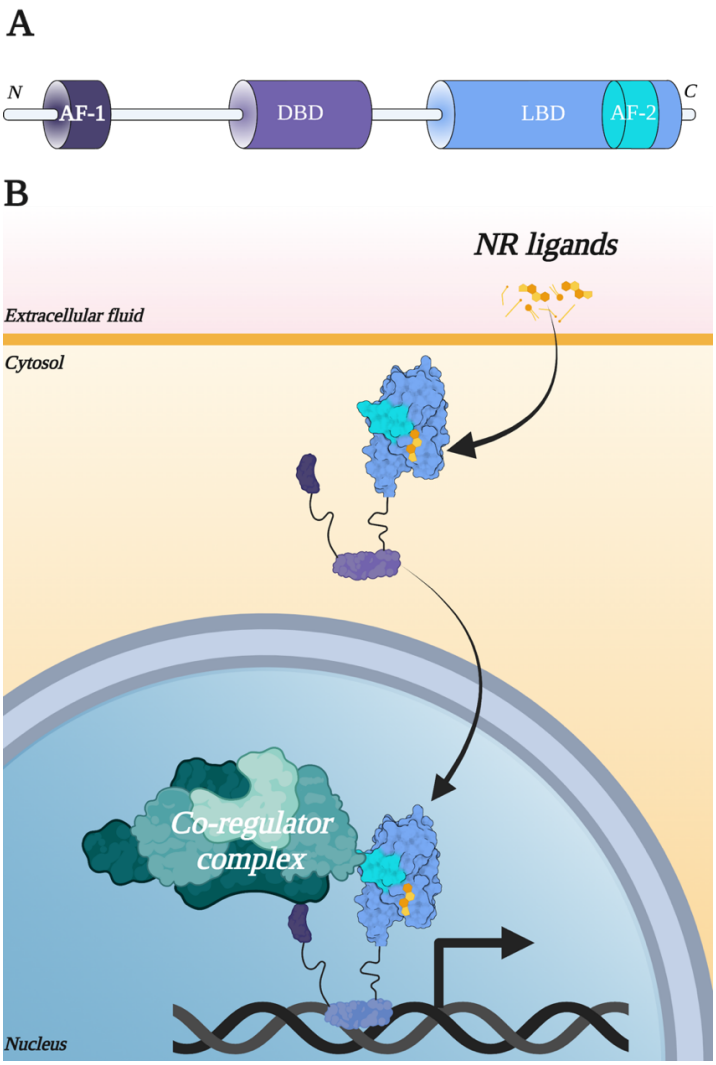

Figure 1 - 1: Domain structure of nuclear receptors.

A.) Nuclear receptors contain a disordered N-terminal domain (NTD) wherein lies activation function surface 1 (AF-1), a DNA binding domain (DBD), a disorder hinge region, and a ligand binding domain (LBD). The activation function surface 2 (AF-2) is within the ligand binding domain and interacts with transcriptional coregulators. **B.)** NR ligands bind to the LBD, which activates nuclear localization and/or recruitment of coregulator complexes to activate or repress transcription.

1.2 Various Lipids Control NR Function

The first subset of discovered NRs are known as steroid receptors. These steroid receptors were discovered by a process known as “classical endocrinology”, whereby the ligands were known and used to capture their cognate receptor. The estrogen receptors was first identified in the 1950s when Dr. Elwood Jensen discovered that estrogen mediated its effect in a tissue through binding to a protein rather than being metabolized, which was the previously accepted mode of action. (Jensen 1958; Jensen and DeSombre 1972; Jensen et al. 2010; Mazaira et al. 2018) This led to the discovery of several other NRs that bound to known hormones, such as the progesterone receptor (O'Malley, Sherman, and Toft 1970) , androgen receptor (Aakvaag et al. 1972) , thyroid receptor (MacLeod and Baxter, 1975), glucocorticoid receptor (Ringold et al. 1975; Hollenberg et al. 1985) , and mineralocorticoid receptor.

Following sequencing of the human genome, new NRs were identified; however, the ligands for these receptors were unknown leading to their designation as *orphan* NRs. (Giguère, 1999; Giguère et al., 1988) Over the last 30 years, the ligands for many *orphan* NRs have been identified through a process termed “reverse endocrinology”, whereby the nuclear receptor is known and is used to identify the cognate ligand. NRs characterized using reverse endocrinology are designated as *adopted-orphans*. The adopted NRs bind to a variety of lipid molecules including fatty acids, retinoids, sterols, oxy-sterols, and phospholipids (Table 1.1). This positions NRs to serve as nutritional probes, sensing the lipid landscape of the cell through their LBD, and in response, regulate transcription of genes involved in lipid metabolism, transport, and processing. (Liu et al., 2015)

Table 1-1 Human nuclear receptor superfamily with ligand preference

Family	Common name	Abbreviation	Gene name	Ligand
0B	Dosage-sensitive sex reversal-adrenal hypoplasia congenital critical region on the X chromosome, Gene 1	DAX1	*NR0B1*	Orphan
	Short heterodimeric partner	SHP	*NR0B2*	Orphan? Retinoid like compounds (Dawson et al., 2007; Farhana et al., 2007)
1A	Thyroid hormone receptor-a	TRα	*THRA*	Thyroid hormones
	Thyroid hormone receptor-b	TRβ	*TRB*	Thyroid hormones
1B	Retinoic acid receptor-a	RARα	*RARA*	Retinoic acids
	Retinoic acid receptor-b	RARβ	*RARB*	Retinoic acids
	Retinoic acid receptor-g	RARγ	*RARG*	Retinoic acids
1C	Peroxisome proliferator-activated receptor-a	PPARα	*PPARA*	Unsaturated fatty acids, eicosanoids (Grygiel-Górniak, 2014), branched chain fatty acids (Zomer et al., 2000), oleoylethanolamide (Fu et al., 2003), (16:0/18:1) Phosphatidylcholine (Chakravarthy et al., 2009a)
	Peroxisome proliferator-activated receptor-d	PPARδ	*PPARD*	Unsaturated fatty acids, eicosanoids (Grygiel-Górniak, 2014)

	Peroxisome proliferator-activated receptor-g	PPARγ	*PPARG*	Unsaturated fatty acids, eicosanoids (Grygiel-Górniak, 2014), cyclic phosphatidic acid (Tsukahara et al., 2010)
1D	Reverse-Erb-a	REV-ERBα	*NR1D1*	Heme (Raghuram et al., 2007)
	Reverse-Erb-b	REV-ERBβ	*NR1D2*	Heme (Raghuram et al., 2007)
1F	Retinoic acid-related orphan-a	RORα	*RORA*	Sterols (Bitsch et al., 2003; Wang et al., 2010)
	Retinoic acid-related orphan-b	RORβ	*RORB*	Retinoids (Stehlin-Gaon et al., 2003)
	Retinoic acid-related orphan-g	RORγ	*RORC*	Sterols (Wang et al., 2010)
1H	Farnesoid X receptor	FXR	*NR1H4*	Bile acids (Makishima et al., 1999; Wang et al., 1999)
	Farnesoid X receptor-b	FXRβ	*NR1H5P*	Orphan
	Liver X receptor-a	LXRα	*NR1H3*	Oxysterols
	Liver X receptor-b	LXRβ	*NR1H2*	Oxysterols
1I	Vitamin D receptor	VDR	*VDR*	1α,25-dihydroxyvitamin D3
	Pregname X receptor	PXR	*NR1I2*	Endobiotics and xenobiotics
	Constitutive androstane receptor	CAR	*NR1I3*	Xenobiotics
2A	Hepatocyte nuclear factor-4-a	HNF4α	*HNF4A*	Fatty acids
	Hepatocyte nuclear factor-4-g	HNF4γ	*HNF4G*	Fatty acids
2B	Retinoid X receptor-a	RXRα	*RXRA*	9-Cis retinoic acid (Levin et al., 1992), Unsaturated fatty acids (Dawson and Xia, 2012),

				1-Cis-13,14-dihydroretinoic acid (de Lera Á et al., 2016)
	Retinoid X receptor-b	RXRβ	*RXRB*	9-Cis retinoic acid (Levin et al., 1992), Unsaturated fatty acids (Dawson and Xia, 2012), 1-Cis-13,14-dihydroretinoic acid (de Lera Á et al., 2016)
	Retinoid X receptor-g	RXRγ	*RXRG*	9-Cis retinoic acid (Levin et al., 1992), Unsaturated fatty acids (Dawson and Xia, 2012), 1-Cis-13,14-dihydroretinoic acid (de Lera Á et al., 2016)
2C	Testicular receptor 2	TR2	*NR2C1*	Orphan
	Testicular receptor 4	TR4	*NR2C2*	Orphan
2E	Tailless homolog orphan receptor	TXR	*NR2E1*	Orphan
	Photoreceptor-cell-specific nuclear receptor	PNR	*NR1E3*	Orphan
2F	Chicken ovalbumin upstream promoter-transcription factor a	COUP-TFα	*NR2F1*	Orphan
	Chicken ovalbumin upstream promoter-transcription factor b	COUP-TFβ	*NR2F2*	Orphan
	Chicken ovalbumin upstream promoter-transcription factor g	COUP-TFγ	*NR2F3*	Orphan
3A	Estrogen receptor-a	ERα	*ESR1*	Estrogens

	Estrogen receptor-b	ERβ	*ESR2*	Estrogens
3B	Estrogen-related receptor-a	ERRα	*ESRRA*	Orphan
	Estrogen-related receptor-b	ERRβ	*ESRRB*	Orphan
	Estrogen-related receptor-g	ERRγ	*ESRRG*	Orphan
3C	Androgen receptor	AR	*AR*	Androgens
	Glucocorticoid receptor	GR	*NR3C1*	Glucocorticoids
	Mineralocorticoid receptor	MR	*NR3C2*	Mineralocorticoids and glucocorticoids
	Progesterone receptor	PR	*PGR*	Progesterone
4A	Nerve growth factor 1B	NGF1-B	*NR4A1*	Orphan
	Nurr-related factor 1	NURR1	*NR4A2*	Unsaturated fatty acids
	Neuron-derived orphan receptor 1	NOR-1	*NR4A3*	Orphan
5A	Steroidogenic factor 1	SF-1	*NR5A1*	Phospholipids
	Liver receptor homolog-1	LRH-1	*NR5A2*	Phospholipids
6A	Germ cell nuclear factor	GCNF	*NR6A1*	Orphan

1.3 PPAR family of nuclear receptors:

The peroxisome proliferator-activated receptors (PPARs) belong to the NR1C subfamily of nuclear receptors of which there are three members, NR1C1 (PPARα), NR1C2 (PPARδ) and NR1C3 (PPARγ). PPARs are nutrient sensors that bind lipophilic ligands and regulate metabolism, inflammation, and proliferation. Tissue expression of PPARs is varied depending on isoform with each member playing separate but complementary roles. PPARα is primarily expressed in the liver where it regulates lipid metabolism in the fasted state. (Kersten et al., 1999) PPARγ is highly expressed in the adipose tissue where it regulates adipocyte differentiation, adipokine signaling and lipid metabolism. (Spiegelman, 1998) PPARδ is ubiquitously expressed, with highest expression in the skeletal muscle, where it regulates lipid metabolism. (Neels and Grimaldi, 2014) Despite low hepatic expression, PPARδ has also been shown to play an important role in regulating liver metabolism during the fed state. (Sommars et al., 2019) In addition to their tissue-specific roles in controlling metabolism, all members of the NR1C family have also been shown to have anti-inflammatory actions. Given their vital roles in controlling metabolism and inflammation, PPARs are promising targets to treat many disease states. There is a growing body of evidence that these same pathogenic processes alter PPAR ligand abundance and activity. In the subsequent chapters, I will describe how dysregulation of PPAR activity has been shown to play a role in the pathogenesis of metabolic syndrome and the effects of gut dysbiosis.

The NR1C subfamily of nuclear receptors binds to the largest variety of lipid ligands (e.g. unsaturated fatty acids, eicosanoids, phospholipids, and even steroids), which is consistent with their exceptionally large ligand binding pocket. (Weikum et al., 2018) The ligands that PPAR bind are also known to be changed by heightened inflammatory states, altered gut microbiome composition, and changes in nutrient status. Many of the metabolites that PPARs bind are

generated in the cytosol or distal tissues, while PPAR expression is restricted to the nucleus, leading to the question, how do these receptors gain access to these ligands?

1.4 How do PPARs Acquire Lipids?

Although lipids are key regulators of PPAR function, we do not know how PPARs acquire lipophilic ligands. PPARs are soluble proteins that exist in the nucleus while lipids are hydrophobic in nature, primarily generated in the cytosol, and not readily solubilized in the aqueous environment of the cell; therefore, they are generally sequestered within membranes. This creates a biophysical hurdle for lipids to overcome in order to signal through PPARs (Sever and Glass, 2013). There are three potential mechanisms by which PPARs acquire their preferred lipids. One, PPARs could directly interact with membranes and extract lipids through an entropy driven mechanism. Secondly, PPARs could acquire lipids co-translationally at membrane bound ribosomes on the endoplasmic reticulum (Blind, 2014). Thirdly, lipid transfer proteins (LTPs) could carry lipids from membranes to PPARs (Chiapparino et al., 2016). Evidence does exist to support the role of proteins solubilizing hydrophobic molecules, to transport them throughout the body and/or cell. For instance, steroid hormones, which are generated in one tissue, must travel throughout the blood to activate specific receptors in other distal tissues. Transport of these hormones is assisted via binding to proteins such as albumin or other more specialized proteins, such as the sex hormone binding protein. Similar to transport of steroid hormones throughout the body, LTPs may solubilize and transport lipids throughout the cell to NRs located in the nucleus. The rest this of this chapter will highlight this evidence.

1.5 Lipid Transfer Proteins

LTPs were first identified in the 1960s to be the mediators of nonvesicular lipid transport between membranes. (Helmkamp et al., 1974; Wirtz and Zilversmit, 1968) Since these early days,

the number of identified LTPs and their understood functional roles have vastly expanded. (Wong et al., 2017) There are approximately 125 distinct human genes that encode for LTPs that are grouped into ten families: calycin, StAR related transfer (START) domains (STARDs), MD-2-related lipid-recognition (ML), BPI/LBP/CETP N-terminal domain, oxysterol-binding protein (OSBP), phosphatidylinositol transfer protein (PITP), sterol carrier protein 2 (SCP2), Niemann–Pick C1 (NPC1), CRAL-TRIO domain, and glycolipid transfer protein (GLTP). (Chiapparino et al., 2016)

These distinct groups of LTPs adopt a range of folds, with some containing β-barrels with few α-helices like the calycin family, while others contain only α-helices like the CRAL-TRIO and GLTP families. (Chiapparino et al., 2016) However, all LTPs contain a hydrophobic pocket that accommodates a lipid and shields it from the aqueous cellular environment. Most LTPs bind to a singular lipid, though some LTPs, like FABP1 (calycin family), contain large interior cavities that are able to bind to multiple lipids simultaneously, while others can oligomerize and form tunnels to bind and shuttle several lipids such as CETP. (Qiu et al., 2007; Sharma and Sharma, 2011) Though LTPs are capable of binding to a wide range of lipids, they contain structural features that enable specificity. The shape and size of the interior pocket of LTPs specify which lipids bind. For instance, certain members of the STARD family, such as STARD1 and STARD3, contain an interior pocket size of 1014–1122 $Å^3$, which is close to the size of their natural ligand cholesterol, while other members, like STARD2, contain much larger pockets that can accommodate phospholipids. (Thorsell et al., 2011) LTPs also select for lipids through polar residues within the pocket that can engage electrostatically with polar moieties on the lipid, similar to the NR- LBD.

The physiological roles of LTPs remain largely unexplored. Many LTPs are multidomain proteins, with each unit exhibiting a different function, making it difficult to assign a physiological role to LTPs. This is due, in part, to difficulties in deciphering the role of the lipid transport domain, as compared to the other appended domains. In general, LTPs are involved in metabolism, inflammation, and aging. (Hotamisligil and Bernlohr, 2015a) Disruption of LTPs can lead to diseases like Niemann–Pick disease type C, and lipoid congenital adrenal hyperplasia. (Bose et al., 1996; Vanier, 2015) Specific LTPs in *C. elegans* expanded lifespan when overexpressed. (Duffy J, 2017; Folick et al., 2015; Tillman et al., 2019) Deletion of certain LTPs like FABP4 and FABP5 increases insulin sensitivity and protects against atherosclerosis in mice. (Hotamisligil and Bernlohr, 2015a) An overview of all LTP families have been previously reviewed. (Chiapparino et al., 2016; Hanada, 2018; Wong et al., 2017)

Though the functional roles of LTPs are diverse, they can be grouped into three main modes of action: lipid transporters that shuttle lipids between membranes, lipid chaperones that carry lipids to other proteins, and lipid sensors that regulate signaling and protein activity. (Chiapparino et al., 2016)

1.5.1 FABPs

Of all LTPs, there is the most support for FABPs to interact with PPARs. There are 9 members of the calycin family, all of which bind and transport fatty acids throughout the cell. Each member of this family has unique expression profiles and subcellular locations. In tissues where fatty acids are used as an energy source, these proteins can compose up to 5% of all soluble proteins. Additionally, FABP levels can be influenced by external factors such as diet and exercise, suggesting that this family of proteins responds to nutrient status to regulate lipid homeostasis. (Furuhashi and Hotamisligil, 2008; Hotamisligil and Bernlohr, 2015b)

There are several lines of evidence that support FABPs interaction with PPARs to regulate transcription. For one, FABPs bind to the same endogenous lipids and drugs that activate nuclear receptors. (Tan et al., 2002; Velkov, 2013) Second, multiple FABPs contain nuclear localization signals (NLS) and are readily visualized within the nucleus. (Armstrong et al., 2014a; Gillilan et al., 2007; Sessler and Noy, 2005) Finally, there are several examples of FABPs interacting with PPARs, detailed below (Figure 1.2). (Budhu et al., 2001; Hostetler et al., 2009; Hughes et al., 2015; Velkov, 2013) (Kaczocha et al., 2012; Tan et al., 2002)

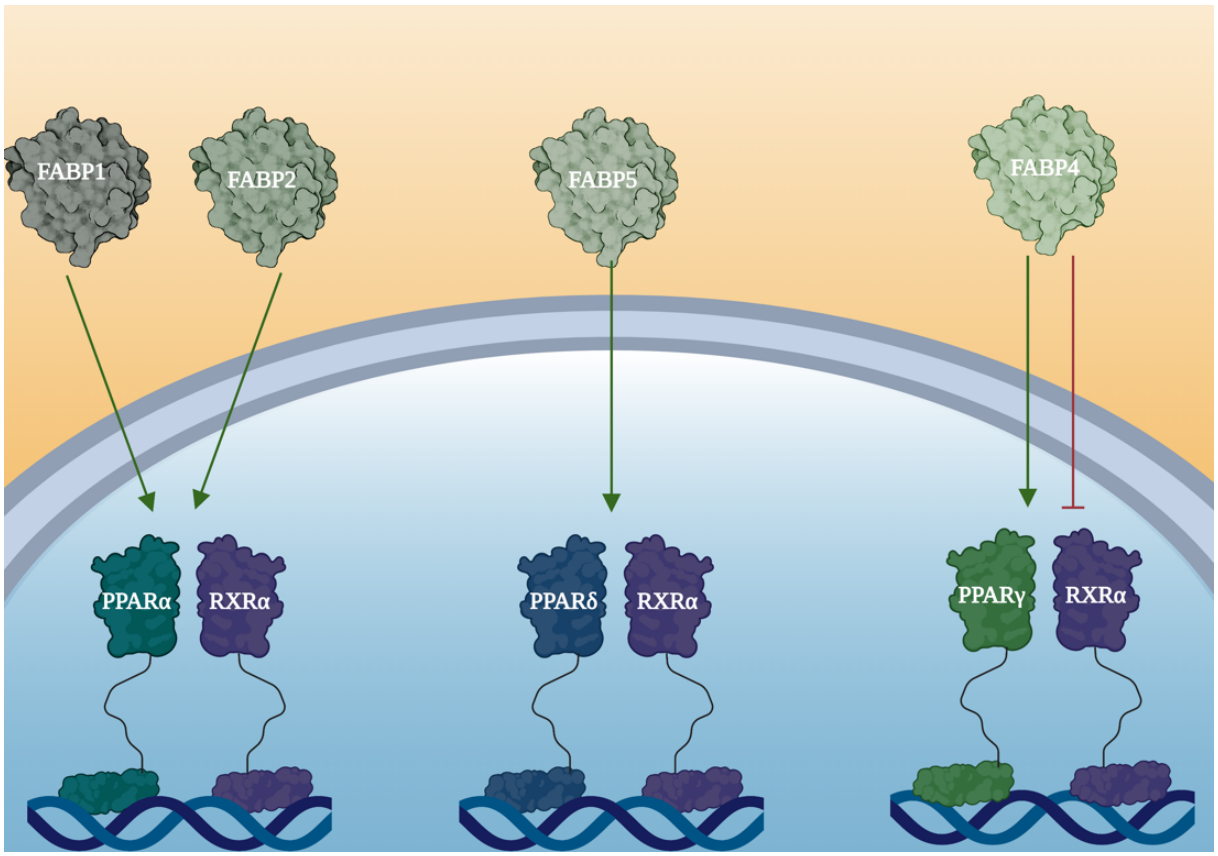

Figure 1 - 2: Schematic of experimentally established FABPs-PPAR interactions.

FABPs (colored in green) interact with and regulate the activity of specific PPARs (colored in hues of blue). Green arrows represent LTP enhancement of NR transcriptional activity, while red lines depict suppression of transcriptional activity. FABP4 has been reported to enhance and suppress the activity of PPARγ.

1.6 Case Studies: FABP—PPAR Interaction

1.6.1 FABP5—PPARδ

The first report of an LTP regulating transcription is that of cellular retinoic acid binding proteins (CRABPs) mediating the transfer of retinoic acid (RA) to the nucleus in 1986. (Takase et al., 1986) It was later shown by two groups in 1999 that CRABPII, but not CRABPI, directly interacted with retinoic acid receptor a (RARa) and enhanced its transcriptional activity through the transfer of RARa activating ligands (Budhu and Noy, 2002; Delva et al., 1999; Dong et al., 1999). Soon after identifying CRABPII-RARα interaction, FABP5 was shown to interact with PPARδ. (Tan et al., 2002) Similar to CRABPII, FABP5 enhances PPARδ activity, but only when ligand is limiting. (Tan et al., 2002; Yu et al., 2014) FABP5 also contains a cryptic tertiary NLS that is activated only when specific lipids bind. (Armstrong et al., 2014a) In addition to binding long-chain fatty acids (Armstrong et al., 2014a), FABP5 also binds RA, which induces nuclear translocation and transactivation of PPARδ. (Schug et al., 2007a; Schug et al., 2008) CRABPII and FABP5 compete for RA, and the ratio of CRABPII/FABP5 within a cell determines which NR is activated. (Schug et al., 2007a; Schug et al., 2008) RA signaling through RARα is proapoptotic and anticarcinogenic (Soprano et al., 2004), while RA activating PPARδ promotes cell survival. (Wang et al., 2006) Elevated levels of FABP5 diverts RA from signaling through RARα towards PPARδ, progressing cancer. (Schug et al., 2007a; Schug et al., 2008) In line with this, elevated FABP5 levels and PPARδ activity are linked with many cancers, and deletion/ inhibition of FABP5 is protective against tumor growth. (Carbonetti et al., 2019; Levi et al., 2013; Levi et al., 2015; Morgan et al., 2010)

1.6.2 FABP4—PPARγ

Like CRABPII and FABP5, FABP4 contains a tertiary NLS that is unveiled by bindning specific lipid ligands. (Ayers et al., 2007; Gillilan et al., 2007) Using molecular dynamics, α-Karyopherin, which drives nuclear import of binding partners, is predicted to interact with the FABP4 NLS. (Amber-Vitos et al., 2015) Additionally, FABP4 contains a nuclear export signal consisting of a patch of hydrophobic residues that are necessary for regulation of PPARγ activity. (Ayers et al., 2007; Gillilan et al., 2007) In an elegant stop flow kinetics experiment by Tan et. al. (Tan et al., 2002), FABP4 pre-loaded with troglitazone channeled the ligand to the PPARγ LBD, suggesting the mechanism of regulation occurs through ligand transfer. There is debate over whether FABP4 activates or represses PPARγ activity, as early studies show FABP4 enhances PPARγ transcriptional activity (Ayers et al., 2007; Lamas Bervejillo et al., 2020; Tan et al., 2002), while several other studies show FABP4 represses. (Garin-Shkolnik et al., 2014; Helledie et al., 2000; Makowski et al., 2005) Interestingly, mice lacking FABP4 are protected from diet-induced and genetically-driven diabetes (Hotamisligil and Bernlohr, 2015a; Hotamisligil et al., 1996; Uysal et al., 2000), and display elevated levels of lipogenesis and decreased lipolysis (Hertzel et al., 2006), characteristic of elevated PPARγ activity. (He et al., 2003; Tamori et al., 2002) Indeed, deletion of FABP4 in macrophages derived from mice led to increased PPARγ transactivation. (Makowski et al., 2005) Furthermore, FABP4 decreases PPARγ abundance and activity through promoting proteasomal degradation. (Garin-Shkolnik et al., 2014) The discrepancies between these data merit further investigation.

1.6.3 FABP1— PPARα

FABP1 was first postulated to signal through PPARs when it was identified to localize to the nucleus and bind to PPAR ligands. (Lawrence et al., 2000; Wolfrum et al., 1999) FABP1 was later confirmed to directly interact with PPARα through several experiments, such as pull-down

assays, two-hybrid assays, fluorescence resonance energy transfer (FRET) assays, and nuclear magnetic resonance. (Hostetler et al., 2009; McIntosh et al., 2009; Patil et al., 2019; Velkov, 2013; Wolfrum et al., 2001a) Furthermore, FABP1 enhances PPARα transactivation by increasing PPARα association with coactivators. (Hughes et al., 2015; McIntosh et al., 2009; Wolfrum et al., 2001a) Unlike CRABPII, FABP4, and FABP5, FABP1 does not contain an NLS, though nuclear localization still occurs in a ligand-dependent manner. (Hughes et al., 2015) Rather, FABP1 passively diffuses into the nucleus, and ligand binding promotes a conformation compatible with PPARα binding, slowing nuclear egress of FABP1. (Hughes et al., 2015; Patil et al., 2019) Interestingly, glucose also binds to FABP1, inducing a conformational change that enhances its ability to bind to lipid and signal through PPARα. (Hostetler et al., 2010; Petrescu et al., 2013a; Petrescu et al., 2013b) FABP1's unique ability to bind both glucose and lipids enables it to coordinate multiple metabolic signals to control PPARα.

1.7 Structural Insights into Ligand Driven Nuclear Import of FABPs

The general conserved structure of FABPs is a β-barrel composed of ten anti-parallel β-sheets that encapsulate a hydrophobic molecule and a α-helical lid containing a helix-loop-helix motif that serves as a gate for ligand binding. The α-helical lid and loops between βC-βD, βE-βF, βG-βH, and βI-βJ make up the portal region where ligand enters and exits. The NLS present in CRABPII, FABP5, and FABP4 consists of a basic patch of residues (K … RK) on the α-helical lid (Fig. 3A). Nuclear localization of these FABPs occurs only when activating ligands bind. These FABPs sense ligands through a hydrophobic switch. When activating ligands bind it stabilizes the α-helical lid and NLS, while inactivating ligands break this clamp, destabilizing the α-helical lid and NLS (Fig. 3B). (Armstrong et al., 2014a; Gillilan et al., 2007) This switch consists of two hydrophobic residues in the loop between βC and βD strands (CRABPII: V58, FABP4: F57, and

FABP5: L60) and the α-helical lid (CRABPII: I31, FABP4: V32, and FABP5: M35) (Fig. 3A). (Armstrong et al., 2014a; Gillilan et al., 2007) Structures of FABPs bound to inactivating ligands show the ligand protruding into this switch region, preventing the hydrophobic interaction (Fig. 3B). In contrast, activating ligands do not interfere with this region, allowing the switch residues to hydrophobically interact, stabilizing the NLS (Fig. 3B). For example, linoleic acid and arachidonic acid, both polyunsaturated acids (PUFAs), induce FABP5 nuclear localization, while saturated and monosaturated fatty acids do not have this effect. (Armstrong et al., 2014a) This is do to the fact that PUFAs adopt a "U" conformation within the pocket and do not disrupt the interaction between the switch residues, while inactivating ligands adopt an "L" shape, which disrupts this interaction. (Armstrong et al., 2014a)

Ligand driven interaction between FABP1 and PPARα occurs through a different mechanism as FABP1 does not contain an NLS, but still interacts with and regulates PPARα in a ligand dependent manner. (Hughes et al., 2015) Activating ligand GW7647 binding to FABP1 induces a conformational change in charged residues on the exterior of FABP1, altering the electrostatic surface potential, which promotes interaction with PPARα. Charged residues within loops in the portal region of FABP1 (K57, E77, and K96) are essential for this interaction, as mutagenesis of these residues disrupts interaction with and regulation of PPARα activity. (Patil et al., 2019) Similarly, mutation of residues in the loops within the portal region of CRABPII (Q75, P81, and K102) also disrupts CRABPII association with RARα. (Budhu et al., 2001)

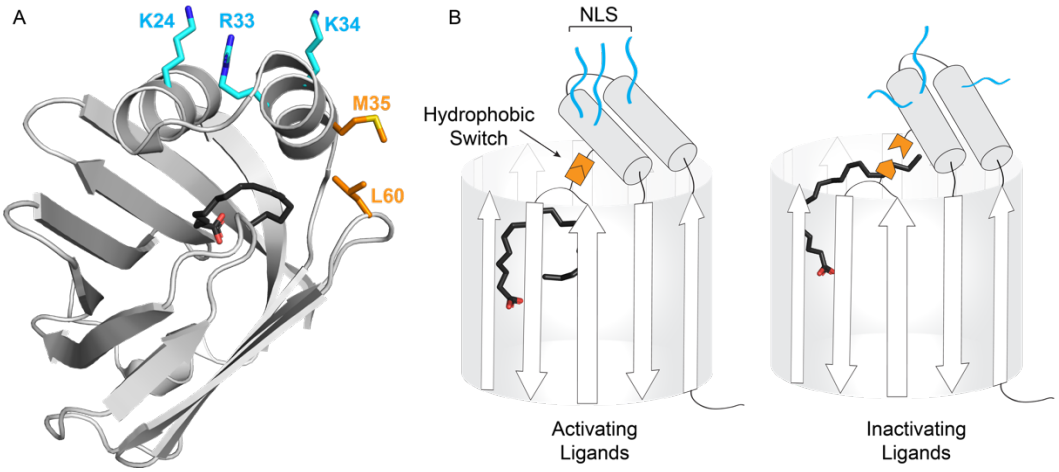

Figure 1 - 3: Ligand driven nuclear localization of FABPs.

A.) Structure of FABP5 bound to linoleic acid (PDB code: 4LKT) (Armstrong et al., 2014a). Linoleic acid (black) adopts a "U" shaped conformation in the interior pocket. Hydrophobic switch residues (M35 and L60) are colored orange. NLS residues (K24, R33, and K34) are colored cyan. **B**.) Schematic of ligand driven nuclear localization. Activating ligands promote the α-helical lid to pack onto the mouth of the cavity, which is driven by a hydrophobic interaction between residues in the α-helical lid and the loop between bC and bD (hydrophobic switch, orange). This conformation stabilizes the NLS and promotes nuclear localization. Inactivating ligands sterically disrupt this hydrophobic interaction, which destabilizes the NLS.

1.8 Gut microbiome regulation of PPARs:

In the last 20 years the scientific community has begun to appreciate the impact bacteria in our gut have on human health and disease. The effect of the gut microbiome has on host metabolism is underscored by the phenotype of germ free (GF) mice. GF mice are kept in sterile environments and are unable to develop a gut microbiome. Introducing a gut microbiome to germ free mice leads to the generation of a conventionalized mouse. Amongst many phenotypic differences, GF mice fed high fat diet gain less weight, have lower levels of circulating triglycerides, and have improved glycemic control when compared to conventionalized controls. (Bäckhed et al., 2007) Furthermore, certain species of bacteria are sufficient to drive diet induced obesity and the development diabetic phenotype when implanted into germ free mice. (Fei and Zhao, 2013) Taken together this data highlights a vital role for the gut microbiome composition in driving diet induced metabolic diseases.

PPARs have been shown to play an integral role in regulating many processes that underpin the beneficial metabolic effects associated with the GF mouse, leading to the hypothesis that these two systems communicate. Evidence in chickens selectively bred for either high fat or low fat body composition, housed in the same environment, have suggest an interplay between host genotype, microbiota composition, and the resulting phenotype.(Zhao et al., 2013) Transcriptomic analysis comparing these two groups reveal aberrant regulation of many metabolic processes, including PPAR controlled metabolism. (Ding et al., 2016)

There are two mechanisms by which the gut is capable of driving deleterious health outcomes. First, gut dysbiosis can drive a heightened inflammatory state. This occurs through an increase in gut composition of ‘bad’ bacteria that release proinflammatory molecules such as lipopolysaccharide. The increase in the inflammatory mediators is thought to play a role in the

etiology of diseases such as inflammatory bowel disease (IBD) and non-alcoholic fatty liver disease. (Bibbò et al., 2018; Candelli et al., 2021; Gagnière et al., 2016)

Each of the aforementioned indications were associated with aberrant PPAR signaling. Inflammatory bowel disease severity was shown to be attenuated when mice were fed a diet rich in conjugated linoleic acid (CLA). CLA rich diet induced the expression of PPARγ while reducing the expression of PPARδ. This increase in PPARγ expression was complemented by increases in PPARγ controlled transcripts, as well as a reduction in levels of NFKb p65. Importantly the effect of CLA diet was lost when PPARγ was knocked down in the colon. (Bassaganya-Riera et al., 2004) Another study has shown that activation of PPARγ is able to correct diet induced gut dysbiosis that could play a role in IBD. (Tomas et al., 2016) These data suggest the role of PPARγ in regulating gut dysbiosis driven inflammation is two fold; one, decreasing host inflammatory processes and two, favorably altering gut microbe composition. Second, gut dysbiosis can affect levels of metabolites and signaling molecules. Changes in these metabolites is thought to either drive or exacerbate complications related to a myriad of disease states. At any given moment up to 10% of the circulating metabolome in humans can be traced back to the gut. (Wikoff et al., 2009) Many of these metabolites have unknown chemical composition and function, begging the question: what is the role of these metabolites in driving pathological processes associated with gut dysbiosis? Recent reports have identified a novel gut microbiome derived metabolite, delta-Valerobetaine (VB). VB was identified as one of the most enriched metabolites in the livers from conventionalized mice. VB has been recently implicated in dysregulation of metabolic processes as well as neuronal deficits associated with ageing (Go et al., 2020; Mossad et al., 2021) and is known to be produced by a suite of 'bad' bacteria species: *Lactobacilli, Escherichia coli, Salmonella typhimurium*, *Bifidobacterium longum*. Studies from our lab, have demonstrated that

VB is capable of driving metabolic dysregulation. Under high fat diet, both conventionalized and GF mice treated with VB not only gain more weight than untreated controls but accumulate liver triglycerides resulting in a phenotype similar to non-alcoholic fatty liver disease. RNAseq experiments show severe dysregulation of PPAR mediated transactivation. We confirmed this observation using a luciferase reporter assay investigating PPARα activity. Furthermore, epidemiological evidence supports a role of VB in driving central adiposity within the human population. (Liu et al., 2021) While evidence suggests this perturbation in metabolic homeostasis is driven by VB, and implicates aberrant PPAR transcription and carnitine homeostasis, the detailed molecular mechanism remain elusive.

1.9 PPARs and COVID-19:

Viruses are a diverse form of parasitic life whose reproduction requires a host. To accomplish this, viruses must hijack host processes from interactions with extracellular receptors, leading to viral entry, to transcription and translation, resulting in the production of viral genomes and proteins. For many viruses, including SARS-CoV-2, they must also alter the host metabolic state to prime cells to produce new viral particles. The importance of viral manipulation of host metabolism is underscored by prophylactic strategies used to attenuate COVID-19 severity by modulating diet and exercise. (Heffernan et al., 2020; Soliman et al., 2020) Due to the outbreak of SARS-CoV-2 many researchers have renewed interest in targeting host metabolism to attenuate viral disease severity. PPARs are an attractive therapeutic target to modulate this due to their known roles in modulating host metabolism and inflammation.

Viral entry of SARs-CoV-2 is mediated by interactions between the viral spike protein and the host angiotensin converting enzyme-2 (ACE-2) receptor. In normal physiology ACE-2 is an important receptor involved in controlling vascular tone. Following viral infection ACE-2 is down-

regulated (Lei et al., 2021) resulting in dysregulation of the host cardiovascular system. This is particularly important for older individuals with hardened vasculature or obese individuals who are hypertensive. (Dalan et al., 2020) Coincidentally, age and obesity are both risk factors known to be associated with more severe COVID infections. (Garg et al., 2020) Pioglitazone, a PPARγ agonist, also increases the expression of ACE-2, making PPARγ agonist an attractive therapeutic for individuals with stressed cardiovascular systems infected with SARs-CoV-2. (Carboni et al., 2020)

One of the hallmarks of severe COVID infection is an exacerbated inflammatory response mirroring cytokine storm. Current treatment modalities have since incorporated anti-inflammatory steroids, specifically dexamethasone, to mitigate this. (Group, 2021) Similar to targeting glucocorticoid receptor, PPARα has been shown to play an anti-inflammatory role in the lung and liver. (Abdelmegeed et al., 2011; Yoo et al., 2013) Furthermore, pulmonary PPARα expression levels are decreased in the presence of inflammatory mediators known to be increased during SARs-CoV-2 infection. (Heffernan et al., 2020) Treatment with fenofibrate, a PPARα agonist, is able to mitigate the aberrant metabolism associated with infection of SARs-CoV-2 and inhibit viral replication in the lung. (Ehrlich et al., 2020) Other PPAR agonists have shown promise as a treatment for the heightened inflammatory state associated with COVID infection by decreasing the expression of pro-inflammatory mediators such as TNFα and various interleukins. (Ciavarella et al., 2020)

While evidence of PPARδ regulating disease progression of SARS-CoV-2 is lacking, a role for exercise in mitigating disease progression is well documented. (Heffernan et al., 2020) This lack of pharmacological evidence is likely due to the absence of FDA approved PPARδ specific agonists. Previous reports of PPARδ agonists have shown that directly agonizing this

receptor mirror the effect of exercise, as treated mice run longer and farther than untreated controls. (Fan et al., 2017) Furthermore, PPARδ is capable of slowing the progression of atherosclerosis as activating this receptor with the agonist GW501516 resulted in a decrease in plasma triglycerides due to an increase in hepatic clearance of VLDL. PPARδ has also shown an important role in regulating whole body metabolism by controlling hepatic lipogenesis resulting in activation beta-oxidation in the muscle. (Liu et al., 2013) Similar to PPARα and PPARγ, PPARδ has also been shown to regulate inflammation in a number of disease states. Not only does PPARδ regulate transcription of genes such as RGS 4 & 5, but activating PPARδ also suppresses the expression of adhesion proteins such as CXCL7, CCL21 and MCP-1. (Barish et al., 2008) This suppression of adhesion molecules via PPARδ activation is thought to be a result of its unique regulation BCL-6 activity. (Fan et al., 2008) While promising these results are confounded by the known role of obesity and associated co-morbidities in exacerbating the severity of COVID infections and merit further investigation.

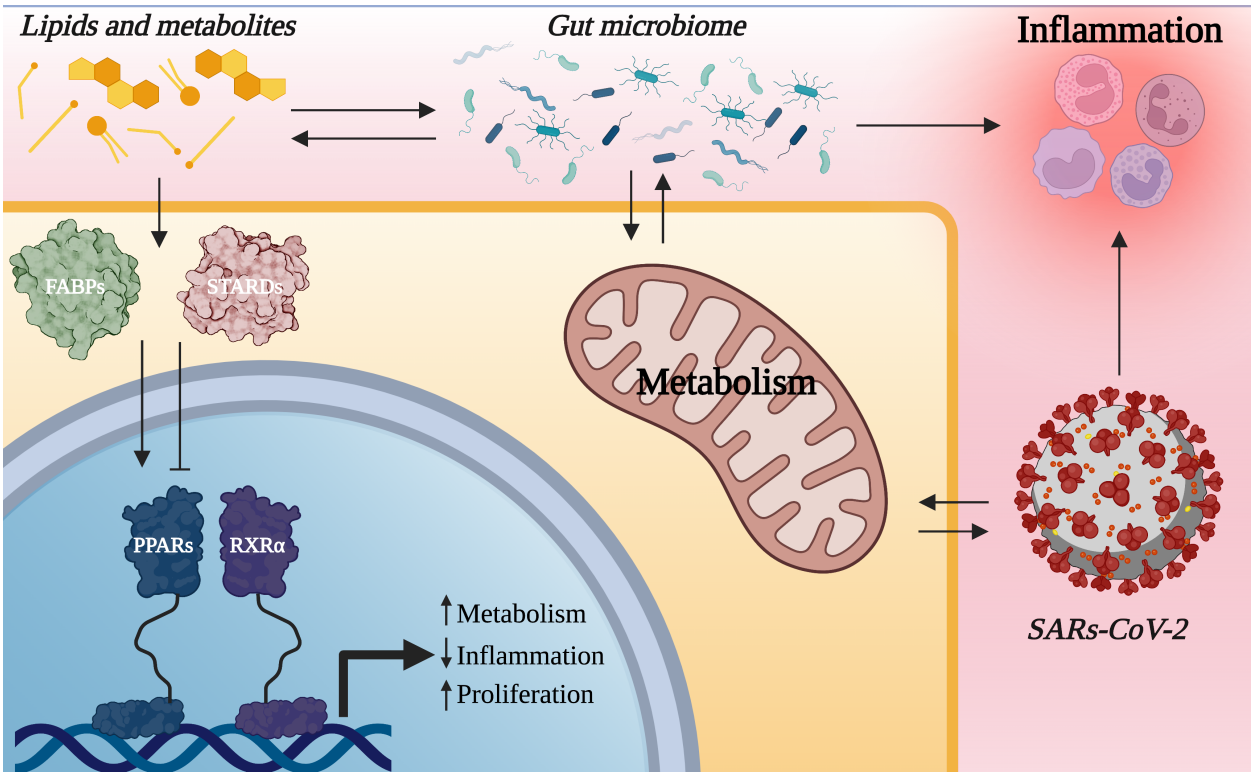

Figure 1 - 4: Summary of PPAR regulation of host metabolic and pathogenic process.

As described in the previous chapter PPARs can regulate many different metabolic, and inflammatory processes. Through these actions PPARs can regulate the severity of many pathogenic processes including gut dysbiosis and SARs-CoV-2. This regulation is not unidirectional as both viruses and microbes are known to effect metabolism and inflammation. Due to PPARs restricted expression in the nucleus, altered ligand abundance driven by viral infections or gut dysbiosis is conferred to PPARs via various lipid binding proteins, namely the FABPs and the STARD proteins.

2.10 References

Aakvaag, A., K. J. Tveter, O. Unhjem, and A. Attramadal. 1972. 'Receptors and binding of androgens in the prostate', *J Steroid Biochem*, 3: 375-84.

Abdelmegeed, Mohamed A, Seong-Ho Yoo, Lauren E Henderson, Frank J Gonzalez, Kimberley J Woodcroft, and Byoung-Joon Song. 2011. 'PPARα expression protects male mice from high fat–induced nonalcoholic fatty liver', *The Journal of nutrition*, 141: 603-10.

Amber-Vitos, O., N. Kucherenko, E. Nachliel, M. Gutman, and Y. Tsfadia. 2015. 'The Interaction of FABP with Kapalpha', *PLoS One*, 10: e0132138.

Armstrong, E. H., D. Goswami, P. R. Griffin, N. Noy, and E. A. Ortlund. 2014. 'Structural basis for ligand regulation of the fatty acid-binding protein 5, peroxisome proliferator-activated receptor beta/delta (FABP5-PPARbeta/delta) signaling pathway', *J Biol Chem*, 289: 14941-54.

Arriza, J. L., C. Weinberger, G. Cerelli, T. M. Glaser, B. L. Handelin, D. E. Housman, and R. M. Evans. 1987. 'Cloning of human mineralocorticoid receptor complementary DNA: structural and functional kinship with the glucocorticoid receptor', *Science*, 237: 268-75.

Ayers, S. D., K. L. Nedrow, R. E. Gillilan, and N. Noy. 2007. 'Continuous nucleocytoplasmic shuttling underlies transcriptional activation of PPARgamma by FABP4', *Biochemistry*, 46: 6744-52.

Bäckhed, F., J. K. Manchester, C. F. Semenkovich, and J. I. Gordon. 2007. 'Mechanisms underlying the resistance to diet-induced obesity in germ-free mice', *Proc Natl Acad Sci U S A*, 104: 979-84.

Barish, Grant D, Annette R Atkins, Michael Downes, Peter Olson, Ling-Wa Chong, Mike Nelson, Yuhua Zou, Hoosang Hwang, Heonjoong Kang, and Linda Curtiss. 2008. 'PPARδ regulates multiple proinflammatory pathways to suppress atherosclerosis', *Proceedings of the National Academy of Sciences*, 105: 4271-76.

Bassaganya-Riera, Josep, Kathryn Reynolds, Susan Martino-Catt, Yongzhi Cui, Lothar Hennighausen, Frank Gonzalez, Jurg Rohrer, Alejandro Uribe Benninghoff, and Raquel Hontecillas. 2004. 'Activation of PPAR γ and δ by conjugated linoleic acid mediates protection from experimental inflammatory bowel disease', *Gastroenterology*, 127: 777-91.

Bibbò, Stefano, Gianluca Ianiro, Maria Pina Dore, Claudia Simonelli, Estelle E Newton, and Giovanni Cammarota. 2018. 'Gut microbiota as a driver of inflammation in nonalcoholic fatty liver disease', *Mediators of inflammation*, 2018.

Bitsch, F., R. Aichholz, J. Kallen, S. Geisse, B. Fournier, and J. M. Schlaeppi. 2003. 'Identification of natural ligands of retinoic acid receptor-related orphan receptor alpha ligand-binding domain expressed in Sf9 cells--a mass spectrometry approach', *Anal Biochem*, 323: 139-49.

Blind, R. D. 2014. 'Disentangling biological signaling networks by dynamic coupling of signaling lipids to modifying enzymes', *Adv Biol Regul*, 54: 25-38.

Blind, R. D., M. Suzawa, and H. A. Ingraham. 2012. 'Direct modification and activation of a nuclear receptor-PIP_2 complex by the inositol lipid kinase IPMK', *Sci Signal*, 5: ra44.

Bose, H. S., T. Sugawara, J. F. Strauss, 3rd, and W. L. Miller. 1996. 'The pathophysiology and genetics of congenital lipoid adrenal hyperplasia', *N Engl J Med*, 335: 1870-8.

Budhu, A., R. Gillilan, and N. Noy. 2001. 'Localization of the RAR interaction domain of cellular retinoic acid binding protein-II', *J Mol Biol*, 305: 939-49.

Budhu, A. S., and N. Noy. 2002. 'Direct channeling of retinoic acid between cellular retinoic acid-binding protein II and retinoic acid receptor sensitizes mammary carcinoma cells to retinoic acid-induced growth arrest', *Mol Cell Biol*, 22: 2632-41.

Candelli, Marcello, Laura Franza, Giulia Pignataro, Veronica Ojetti, Marcello Covino, Andrea Piccioni, Antonio Gasbarrini, and Francesco Franceschi. 2021. 'Interaction between lipopolysaccharide and gut microbiota in inflammatory bowel diseases', *International journal of molecular sciences*, 22: 6242.

Carbonetti, G., T. Wilpshaar, J. Kroonen, K. Studholme, C. Converso, S. d'Oelsnitz, and M. Kaczocha. 2019. 'FABP5 coordinates lipid signaling that promotes prostate cancer metastasis', *Sci Rep*, 9: 18944.

Carboni, Elena, Anna R Carta, and Ezio Carboni. 2020. 'Can pioglitazone be potentially useful therapeutically in treating patients with COVID-19?', *Medical hypotheses*, 140: 109776.

Chakravarthy, M. V., I. J. Lodhi, L. Yin, R. R. Malapaka, H. E. Xu, J. Turk, and C. F. Semenkovich. 2009. 'Identification of a physiologically relevant endogenous ligand for PPARalpha in liver', *Cell*, 138: 476-88.

Chiapparino, A., K. Maeda, D. Turei, J. Saez-Rodriguez, and A. C. Gavin. 2016. 'The orchestra of lipid-transfer proteins at the crossroads between metabolism and signaling', *Prog Lipid Res*, 61: 30-9.

Ciavarella, Carmen, Ilenia Motta, Sabrina Valente, and Gianandrea Pasquinelli. 2020. 'Pharmacological (or synthetic) and nutritional agonists of PPAR-γ as candidates for cytokine storm modulation in COVID-19 disease', *Molecules*, 25: 2076.

Cockcroft, S., and N. Carvou. 2007. 'Biochemical and biological functions of class I phosphatidylinositol transfer proteins', *Biochim Biophys Acta*, 1771: 677-91.

Dalan, Rinkoo, Stefan R Bornstein, Ali El-Armouche, Roman N Rodionov, Alexander Markov, Ben Wielockx, Felix Beuschlein, and Bernhard O Boehm. 2020. 'The ACE-2 in COVID-19: foe or friend?', *Hormone and Metabolic Research*, 52: 257-63.

Dawson, M. I., and Z. Xia. 2012. 'The retinoid X receptors and their ligands', *Biochim Biophys Acta*, 1821: 21-56.

Dawson, M. I., Z. Xia, G. Liu, M. Ye, J. A. Fontana, L. Farhana, B. B. Patel, S. Arumugarajah, M. Bhuiyan, X. K. Zhang, Y. H. Han, W. B. Stallcup, J. Fukushi, T. Mustelin, L. Tautz, Y. Su, D. L. Harris, N. Waleh, P. D. Hobbs, L. Jong, W. R. Chao, L. J. Schiff, and B. P. Sani. 2007. 'An adamantyl-substituted retinoid-derived molecule that inhibits cancer cell growth and angiogenesis by inducing apoptosis and binds to small heterodimer partner nuclear receptor: effects of modifying its carboxylate group on apoptosis, proliferation, and protein-tyrosine phosphatase activity', *J Med Chem*, 50: 2622-39.

de Lera Á, R., W. Krezel, and R. Rühl. 2016. 'An Endogenous Mammalian Retinoid X Receptor Ligand, At Last!', *ChemMedChem*, 11: 1027-37.

Delva, L., J. N. Bastie, C. Rochette-Egly, R. Kraïba, N. Balitrand, G. Despouy, P. Chambon, and C. Chomienne. 1999. 'Physical and functional interactions between cellular retinoic acid binding protein II and the retinoic acid-dependent nuclear complex', *Mol Cell Biol*, 19: 7158-67.

Ding, Jinmei, Lele Zhao, Lifeng Wang, Wenjing Zhao, Zhengxiao Zhai, Li Leng, Yuxiang Wang, Chuan He, Yan Zhang, and Heping Zhang. 2016. 'Divergent selection-induced obesity alters the composition and functional pathways of chicken gut microbiota', *Genetics Selection Evolution*, 48: 1-9.

Dong, D., S. E. Ruuska, D. J. Levinthal, and N. Noy. 1999. 'Distinct roles for cellular retinoic acid-binding proteins I and II in regulating signaling by retinoic acid', *J Biol Chem*, 274: 23695-8.

Duffy J, Mutlu AS, Wang M. 2017. 'Lipid Metabolism, Lipid Signalling and Longevity': 307-29.

Ehrlich, Avner, Skyler Uhl, Konstantinos Ioannidis, Matan Hofree, Benjamin R tenOever, and Yaakov Nahmias. 2020. 'The SARS-CoV-2 transcriptional metabolic signature in lung epithelium', *Available at SSRN 3650499*.

Esteves, A., A. Knoll-Gellida, L. Canclini, M. C. Silvarrey, M. André, and P. J. Babin. 2016. 'Fatty acid binding proteins have the potential to channel dietary fatty acids into enterocyte nuclei', *J Lipid Res*, 57: 219-32.

Fan, Weiwei, Wanda Waizenegger, Chun Shi Lin, Vincenzo Sorrentino, Ming-Xiao He, Christopher E Wall, Hao Li, Christopher Liddle, T Yu Ruth, and Annette R Atkins. 2017. 'PPARδ promotes running endurance by preserving glucose', *Cell metabolism*, 25: 1186-93. e4.

Fan, Yanbo, Ying Wang, Zhihui Tang, Hong Zhang, Xiaomei Qin, Yi Zhu, Youfei Guan, Xian Wang, Bart Staels, and Shu Chien. 2008. 'Suppression of pro-inflammatory adhesion molecules by PPAR-δ in human vascular endothelial cells', *Arteriosclerosis, thrombosis, and vascular biology*, 28: 315-21.

Fang, C., F. V. Filipp, and J. W. Smith. 2012. 'Unusual binding of ursodeoxycholic acid to ileal bile acid binding protein: role in activation of FXRα', *J Lipid Res*, 53: 664-73.

Farhana, L., M. I. Dawson, M. Leid, L. Wang, D. D. Moore, G. Liu, Z. Xia, and J. A. Fontana. 2007. 'Adamantyl-substituted retinoid-related molecules bind small heterodimer partner and modulate the Sin3A repressor', *Cancer Res*, 67: 318-25.

Fei, Na, and Liping Zhao. 2013. 'An opportunistic pathogen isolated from the gut of an obese human causes obesity in germfree mice', *The ISME journal*, 7: 880-84.

Folick, A., H. D. Oakley, Y. Yu, E. H. Armstrong, M. Kumari, L. Sanor, D. D. Moore, E. A. Ortlund, R. Zechner, and M. C. Wang. 2015. 'Aging. Lysosomal signaling molecules regulate longevity in Caenorhabditis elegans', *Science*, 347: 83-6.

Fu, J., S. Gaetani, F. Oveisi, J. Lo Verme, A. Serrano, F. Rodríguez De Fonseca, A. Rosengarth, H. Luecke, B. Di Giacomo, G. Tarzia, and D. Piomelli. 2003. 'Oleylethanolamide regulates feeding and body weight through activation of the nuclear receptor PPAR-alpha', *Nature*, 425: 90-3.

Furuhashi, Masato, and Gökhan S Hotamisligil. 2008. 'Fatty acid-binding proteins: role in metabolic diseases and potential as drug targets', *Nature reviews Drug discovery*, 7: 489-503.

Gagnière, Johan, Jennifer Raisch, Julie Veziant, Nicolas Barnich, Richard Bonnet, Emmanuel Buc, Marie-Agnès Bringer, Denis Pezet, and Mathilde Bonnet. 2016. 'Gut microbiota imbalance and colorectal cancer', *World journal of gastroenterology*, 22: 501.

Garg, Shikha, Lindsay Kim, Michael Whitaker, Alissa O'Halloran, Charisse Cummings, Rachel Holstein, Mila Prill, Shua J Chai, Pam D Kirley, and Nisha B Alden. 2020. 'Hospitalization rates and characteristics of patients hospitalized with laboratory-confirmed coronavirus disease 2019—COVID-NET, 14 States, March 1–30, 2020', *Morbidity and mortality weekly report*, 69: 458.

Garin-Shkolnik, T., A. Rudich, G. S. Hotamisligil, and M. Rubinstein. 2014. 'FABP4 attenuates PPARγ and adipogenesis and is inversely correlated with PPARγ in adipose tissues', *Diabetes*, 63: 900-11.

Giguère, V. 1999. 'Orphan nuclear receptors: from gene to function', *Endocr Rev*, 20: 689-725.
Giguère, V., N. Yang, P. Segui, and R. M. Evans. 1988. 'Identification of a new class of steroid hormone receptors', *Nature*, 331: 91-4.
Gillilan, R. E., S. D. Ayers, and N. Noy. 2007. 'Structural basis for activation of fatty acid-binding protein 4', *J Mol Biol*, 372: 1246-60.
Go, Young-Mi, Ken Liu, Zachery Jarrell, Moriah Bellissimo, and Dean Jones. 2020. 'Association of Microbiome Metabolite Valerobetaine with Aging', *Current Developments in Nutrition*, 4: 26-26.
Grober, J., I. Zaghini, H. Fujii, S. A. Jones, S. A. Kliewer, T. M. Willson, T. Ono, and P. Besnard. 1999. 'Identification of a bile acid-responsive element in the human ileal bile acid-binding protein gene. Involvement of the farnesoid X receptor/9-cis-retinoic acid receptor heterodimer', *J Biol Chem*, 274: 29749-54.
Gronemeyer, H., and D. Moras. 1995. 'Nuclear receptors. How to finger DNA', *Nature*, 375: 190-1.
Gross, B., and B. Staels. 2007. 'PPAR agonists: multimodal drugs for the treatment of type-2 diabetes', *Best Pract Res Clin Endocrinol Metab*, 21: 687-710.
Group, RECOVERY Collaborative. 2021. 'Dexamethasone in hospitalized patients with Covid-19', *New England Journal of Medicine*, 384: 693-704.
Grygiel-Górniak, B. 2014. 'Peroxisome proliferator-activated receptors and their ligands: nutritional and clinical implications--a review', *Nutr J*, 13: 17.
Gustafsson, J. A. 2016. 'Historical overview of nuclear receptors', *J Steroid Biochem Mol Biol*, 157: 3-6.
Hammond, Geoffrey L. 1995. 'Potential functions of plasma steroid-binding proteins', *Trends in Endocrinology & Metabolism*, 6: 298-304.
Hanada, K. 2018. 'Lipid transfer proteins rectify inter-organelle flux and accurately deliver lipids at membrane contact sites', *J Lipid Res*, 59: 1341-66.
He, W., Y. Barak, A. Hevener, P. Olson, D. Liao, J. Le, M. Nelson, E. Ong, J. M. Olefsky, and R. M. Evans. 2003. 'Adipose-specific peroxisome proliferator-activated receptor gamma knockout causes insulin resistance in fat and liver but not in muscle', *Proc Natl Acad Sci U S A*, 100: 15712-7.
Heffernan, Kevin S, Sushant M Ranadive, and Sae Young Jae. 2020. 'Exercise as medicine for COVID-19: On PPAR with emerging pharmacotherapy', *Medical hypotheses*, 143: 110197.
Helledie, T., M. Antonius, R. V. Sorensen, A. V. Hertzel, D. A. Bernlohr, S. Kølvraa, K. Kristiansen, and S. Mandrup. 2000. 'Lipid-binding proteins modulate ligand-dependent trans-activation by peroxisome proliferator-activated receptors and localize to the nucleus as well as the cytoplasm', *J Lipid Res*, 41: 1740-51.
Helmkamp, G. M., Jr., M. S. Harvey, K. W. Wirtz, and L. L. Van Deenen. 1974. 'Phospholipid exchange between membranes. Purification of bovine brain proteins that preferentially catalyze the transfer of phosphatidylinositol', *J Biol Chem*, 249: 6382-9.
Hertzel, A. V., L. A. Smith, A. H. Berg, G. W. Cline, G. I. Shulman, P. E. Scherer, and D. A. Bernlohr. 2006. 'Lipid metabolism and adipokine levels in fatty acid-binding protein null and transgenic mice', *Am J Physiol Endocrinol Metab*, 290: E814-23.
Hollenberg, S. M., C. Weinberger, E. S. Ong, G. Cerelli, A. Oro, R. Lebo, E. B. Thompson, M. G. Rosenfeld, and R. M. Evans. 1985. 'Primary structure and expression of a functional human glucocorticoid receptor cDNA', *Nature*, 318: 635-41.

Hostetler, H. A., M. Balanarasimha, H. Huang, M. S. Kelzer, A. Kaliappan, A. B. Kier, and F. Schroeder. 2010. 'Glucose regulates fatty acid binding protein interaction with lipids and peroxisome proliferator-activated receptor α', *J Lipid Res*, 51: 3103-16.

Hostetler, H. A., A. L. McIntosh, B. P. Atshaves, S. M. Storey, H. R. Payne, A. B. Kier, and F. Schroeder. 2009. 'L-FABP directly interacts with PPARalpha in cultured primary hepatocytes', *J Lipid Res*, 50: 1663-75.

Hotamisligil, G. S., and D. A. Bernlohr. 2015a. 'Metabolic functions of FABPs--mechanisms and therapeutic implications', *Nat Rev Endocrinol*, 11: 592-605.

Hotamisligil, G. S., R. S. Johnson, R. J. Distel, R. Ellis, V. E. Papaioannou, and B. M. Spiegelman. 1996. 'Uncoupling of obesity from insulin resistance through a targeted mutation in aP2, the adipocyte fatty acid binding protein', *Science*, 274: 1377-9.

Hotamisligil, Gökhan S, and David A Bernlohr. 2015b. 'Metabolic functions of FABPs—mechanisms and therapeutic implications', *Nature Reviews Endocrinology*, 11: 592-605.

Hughes, M. L., B. Liu, M. L. Halls, K. M. Wagstaff, R. Patil, T. Velkov, D. A. Jans, N. W. Bunnett, M. J. Scanlon, and C. J. Porter. 2015. 'Fatty Acid-binding Proteins 1 and 2 Differentially Modulate the Activation of Peroxisome Proliferator-activated Receptor alpha in a Ligand-selective Manner', *J Biol Chem*, 290: 13895-906.

Janowski, B. A., P. J. Willy, T. R. Devi, J. R. Falck, and D. J. Mangelsdorf. 1996. 'An oxysterol signalling pathway mediated by the nuclear receptor LXR alpha', *Nature*, 383: 728-31.

Jensen, E. V. 1958. 'Studies of growth phenomena using tritium labeled steroids', *Proceedings of the Proc 4th International Congress Biochem*, 15: 119.

Jensen, E. V., and E. R. DeSombre. 1972. 'Mechanism of action of the female sex hormones', *Annu Rev Biochem*, 41: 203-30.

Jensen, E. V., H. I. Jacobson, A. A. Walf, and C. A. Frye. 2010. 'Estrogen action: a historic perspective on the implications of considering alternative approaches', *Physiol Behav*, 99: 151-62.

Jin, L., D. Martynowski, S. Zheng, T. Wada, W. Xie, and Y. Li. 2010. 'Structural basis for hydroxycholesterols as natural ligands of orphan nuclear receptor RORgamma', *Mol Endocrinol*, 24: 923-9.

Kaczocha, M., S. Vivieca, J. Sun, S. T. Glaser, and D. G. Deutsch. 2012. 'Fatty acid-binding proteins transport N-acylethanolamines to nuclear receptors and are targets of endocannabinoid transport inhibitors', *J Biol Chem*, 287: 3415-24.

Kersten, Sander, Josiane Seydoux, Jeffrey M Peters, Frank J Gonzalez, Béatrice Desvergne, and Walter Wahli. 1999. 'Peroxisome proliferator–activated receptor α mediates the adaptive response to fasting', *The Journal of clinical investigation*, 103: 1489-98.

Kininis, M., and W. L. Kraus. 2008. 'A global view of transcriptional regulation by nuclear receptors: gene expression, factor localization, and DNA sequence analysis', *Nucl Recept Signal*, 6: e005.

Krasowski, M. D., A. Ni, L. R. Hagey, and S. Ekins. 2011. 'Evolution of promiscuous nuclear hormone receptors: LXR, FXR, VDR, PXR, and CAR', *Mol Cell Endocrinol*, 334: 39-48.

Kumar, R., and E. B. Thompson. 2003. 'Transactivation functions of the N-terminal domains of nuclear hormone receptors: protein folding and coactivator interactions', *Mol Endocrinol*, 17: 1-10.

Lamas Bervejillo, M., J. Bonanata, G. R. Franchini, A. Richeri, J. M. Marqués, B. A. Freeman, F. J. Schopfer, E. L. Coitiño, B. Córsico, H. Rubbo, and A. M. Ferreira. 2020. 'A FABP4-

PPARγ signaling axis regulates human monocyte responses to electrophilic fatty acid nitroalkenes', *Redox Biol*, 29: 101376.

Lampron, C., C. Rochette-Egly, P. Gorry, P. Dollé, M. Mark, T. Lufkin, M. LeMeur, and P. Chambon. 1995. 'Mice deficient in cellular retinoic acid binding protein II (CRABPII) or in both CRABPI and CRABPII are essentially normal', *Development*, 121: 539-48.

Lawrence, J. W., D. J. Kroll, and P. I. Eacho. 2000. 'Ligand-dependent interaction of hepatic fatty acid-binding protein with the nucleus', *J Lipid Res*, 41: 1390-401.

Lei, Yuyang, Jiao Zhang, Cara R Schiavon, Ming He, Lili Chen, Hui Shen, Yichi Zhang, Qian Yin, Yoshitake Cho, and Leonardo Andrade. 2021. 'SARS-CoV-2 spike protein impairs endothelial function via downregulation of ACE 2', *Circulation research*, 128: 1323-26.

Levi, L., G. Lobo, M. K. Doud, J. von Lintig, D. Seachrist, G. P. Tochtrop, and N. Noy. 2013. 'Genetic ablation of the fatty acid-binding protein FABP5 suppresses HER2-induced mammary tumorigenesis', *Cancer Res*, 73: 4770-80.

Levi, L., Z. Wang, M. K. Doud, S. L. Hazen, and N. Noy. 2015. 'Saturated fatty acids regulate retinoic acid signalling and suppress tumorigenesis by targeting fatty acid-binding protein 5', *Nat Commun*, 6: 8794.

Levin, A. A., L. J. Sturzenbecker, S. Kazmer, T. Bosakowski, C. Huselton, G. Allenby, J. Speck, C. Kratzeisen, M. Rosenberger, A. Lovey, and et al. 1992. '9-cis retinoic acid stereoisomer binds and activates the nuclear receptor RXR alpha', *Nature*, 355: 359-61.

Li, Y., M. H. Lambert, and H. E. Xu. 2003. 'Activation of nuclear receptors: a perspective from structural genomics', *Structure*, 11: 741-6.

Liu, Ken H, Joshua A Owens, Bejan Saeedi, Catherine E Cohen, Moriah P Bellissimo, Crystal Naudin, Trevor Darby, Samuel Druzak, Kristal Maner-Smith, and Michael Orr. 2021. 'Microbial metabolite delta-valerobetaine is a diet-dependent obesogen', *Nature Metabolism*, 3: 1694-705.

Liu, S., M. Downes, and R. M. Evans. 2015. 'Metabolic Regulation by Nuclear Receptors.' in K. Nakao, N. Minato and S. Uemoto (eds.), *Innovative Medicine: Basic Research and Development* (Springer

Copyright 2015, The Author(s). Tokyo).

Liu, Sihao, Jonathan D Brown, Kristopher J Stanya, Edwin Homan, Mathias Leidl, Karen Inouye, Prerna Bhargava, Matthew R Gangl, Lingling Dai, and Ben Hatano. 2013. 'A diurnal serum lipid integrates hepatic lipogenesis and peripheral fatty acid use', *Nature*, 502: 550-54.

MacLeod, K. N., and J. D. Baxter. 1975. 'DNA binding of thyroid hormone receptors', *Biochem Biophys Res Commun*, 62: 577-83.

Majumdar, A., A. D. Petrescu, Y. Xiong, and N. Noy. 2011. 'Nuclear translocation of cellular retinoic acid-binding protein II is regulated by retinoic acid-controlled SUMOylation', *J Biol Chem*, 286: 42749-57.

Makishima, M., A. Y. Okamoto, J. J. Repa, H. Tu, R. M. Learned, A. Luk, M. V. Hull, K. D. Lustig, D. J. Mangelsdorf, and B. Shan. 1999. 'Identification of a nuclear receptor for bile acids', *Science*, 284: 1362-5.

Makowski, L., K. C. Brittingham, J. M. Reynolds, J. Suttles, and G. S. Hotamisligil. 2005. 'The fatty acid-binding protein, aP2, coordinates macrophage cholesterol trafficking and inflammatory activity. Macrophage expression of aP2 impacts peroxisome proliferator-activated receptor gamma and IkappaB kinase activities', *J Biol Chem*, 280: 12888-95.

Mazaira, G. I., N. R. Zgajnar, C. M. Lotufo, C. Daneri-Becerra, J. C. Sivils, O. B. Soto, M. B. Cox, and M. D. Galigniana. 2018. 'The Nuclear Receptor Field: A Historical Overview and Future Challenges', *Nucl Receptor Res*, 5.

McIntosh, A. L., B. P. Atshaves, H. A. Hostetler, H. Huang, J. Davis, O. I. Lyuksyutova, D. Landrock, A. B. Kier, and F. Schroeder. 2009. 'Liver type fatty acid binding protein (L-FABP) gene ablation reduces nuclear ligand distribution and peroxisome proliferator-activated receptor-alpha activity in cultured primary hepatocytes', *Arch Biochem Biophys*, 485: 160-73.

McIntosh, A. L., A. D. Petrescu, H. A. Hostetler, A. B. Kier, and F. Schroeder. 2013. 'Liver-type fatty acid binding protein interacts with hepatocyte nuclear factor 4α', *FEBS Lett*, 587: 3787-91.

Morgan, E., P. Kannan-Thulasiraman, and N. Noy. 2010. 'Involvement of Fatty Acid Binding Protein 5 and PPARβ/δ in Prostate Cancer Cell Growth', *PPAR Res*, 2010.

Mossad, Omar, Elisa Nent, Sabrina Woltemate, Shani Folschweiller, Joerg M Buescher, Daniel Schnepf, Daniel Erny, Peter Staeheli, Marlene Bartos, and Antal Szalay. 2021. 'Microbiota-dependent increase in δ-valerobetaine alters neuronal function and is responsible for age-related cognitive decline', *Nature Aging*, 1: 1127-36.

Mukherjee, S., and S. Mani. 2010. 'Orphan nuclear receptors as targets for drug development', *Pharm Res*, 27: 1439-68.

Nagy, L., and J. W. Schwabe. 2004. 'Mechanism of the nuclear receptor molecular switch', *Trends Biochem Sci*, 29: 317-24.

Nakahara, M., N. Furuya, K. Takagaki, T. Sugaya, K. Hirota, A. Fukamizu, T. Kanda, H. Fujii, and R. Sato. 2005. 'Ileal bile acid-binding protein, functionally associated with the farnesoid X receptor or the ileal bile acid transporter, regulates bile acid activity in the small intestine', *J Biol Chem*, 280: 42283-9.

Neels, Jaap G, and Paul A Grimaldi. 2014. 'Physiological functions of peroxisome proliferator-activated receptor β', *Physiological reviews*, 94: 795-858.

O'Malley, B. W., M. R. Sherman, and D. O. Toft. 1970. 'Progesterone "receptors" in the cytoplasm and nucleus of chick oviduct target tissue', *Proc Natl Acad Sci U S A*, 67: 501-8.

Patil, R., B. Mohanty, B. Liu, I. R. Chandrashekaran, S. J. Headey, M. L. Williams, C. S. Clements, O. Ilyichova, B. C. Doak, P. Genissel, R. J. Weaver, L. Vuillard, M. L. Halls, C. J. H. Porter, and M. J. Scanlon. 2019. 'A ligand-induced structural change in fatty acid-binding protein 1 is associated with potentiation of peroxisome proliferator-activated receptor alpha agonists', *J Biol Chem*, 294: 3720-34.

Pawlak, M., P. Lefebvre, and B. Staels. 2012. 'General molecular biology and architecture of nuclear receptors', *Curr Top Med Chem*, 12: 486-504.

Petrescu, A. D., H. Huang, G. G. Martin, A. L. McIntosh, S. M. Storey, D. Landrock, A. B. Kier, and F. Schroeder. 2013. 'Impact of L-FABP and glucose on polyunsaturated fatty acid induction of PPARα-regulated β-oxidative enzymes', *Am J Physiol Gastrointest Liver Physiol*, 304: G241-56.

Petrescu, A. D., A. L. McIntosh, S. M. Storey, H. Huang, G. G. Martin, D. Landrock, A. B. Kier, and F. Schroeder. 2013. 'High glucose potentiates L-FABP mediated fibrate induction of PPARα in mouse hepatocytes', *Biochim Biophys Acta*, 1831: 1412-25.

Qiu, X., A. Mistry, M. J. Ammirati, B. A. Chrunyk, R. W. Clark, Y. Cong, J. S. Culp, D. E. Danley, T. B. Freeman, K. F. Geoghegan, M. C. Griffor, S. J. Hawrylik, C. M. Hayward, P. Hensley, L. R. Hoth, G. A. Karam, M. E. Lira, D. B. Lloyd, K. M. McGrath, K. J. Stutzman-

Engwall, A. K. Subashi, T. A. Subashi, J. F. Thompson, I. K. Wang, H. Zhao, and A. P. Seddon. 2007. 'Crystal structure of cholesteryl ester transfer protein reveals a long tunnel and four bound lipid molecules', *Nat Struct Mol Biol*, 14: 106-13.

Raghuram, S., K. R. Stayrook, P. Huang, P. M. Rogers, A. K. Nosie, D. B. McClure, L. L. Burris, S. Khorasanizadeh, T. P. Burris, and F. Rastinejad. 2007. 'Identification of heme as the ligand for the orphan nuclear receptors REV-ERBalpha and REV-ERBbeta', *Nat Struct Mol Biol*, 14: 1207-13.

Ringold, G. M., K. R. Yamamoto, G. M. Tomkins, M. Bishop, and H. E. Varmus. 1975. 'Dexamethasone-mediated induction of mouse mammary tumor virus RNA: a system for studying glucocorticoid action', *Cell*, 6: 299-305.

Sablin, E. P., A. Woods, I. N. Krylova, P. Hwang, H. A. Ingraham, and R. J. Fletterick. 2008. 'The structure of corepressor Dax-1 bound to its target nuclear receptor LRH-1', *Proc Natl Acad Sci U S A*, 105: 18390-5.

Schug, T. T., D. C. Berry, N. S. Shaw, S. N. Travis, and N. Noy. 2007. 'Opposing effects of retinoic acid on cell growth result from alternate activation of two different nuclear receptors', *Cell*, 129: 723-33.

Schug, T. T., D. C. Berry, I. A. Toshkov, L. Cheng, A. Y. Nikitin, and N. Noy. 2008. 'Overcoming retinoic acid-resistance of mammary carcinomas by diverting retinoic acid from PPARbeta/delta to RAR', *Proc Natl Acad Sci U S A*, 105: 7546-51.

Schulman, I. G. 2010. 'Nuclear receptors as drug targets for metabolic disease', *Adv Drug Deliv Rev*, 62: 1307-15.

Sessler, R. J., and N. Noy. 2005. 'A ligand-activated nuclear localization signal in cellular retinoic acid binding protein-II', *Mol Cell*, 18: 343-53.

Sever, R., and C. K. Glass. 2013. 'Signaling by nuclear receptors', *Cold Spring Harb Perspect Biol*, 5: a016709.

Sharma, A., and A. Sharma. 2011. 'Fatty acid induced remodeling within the human liver fatty acid-binding protein', *J Biol Chem*, 286: 31924-8.

Sladek, F. M. 2003. 'Nuclear receptors as drug targets: new developments in coregulators, orphan receptors and major therapeutic areas', *Expert Opin Ther Targets*, 7: 679-84.

Smith, U. 2001. 'Pioglitazone: mechanism of action', *International journal of clinical practice. Supplement*: 13-18.

Soliman, Sameh, MoezAlIslam E Faris, Zakaria Ratemi, and Rabih Halwani. 2020. 'Switching host metabolism as an approach to dampen SARS-CoV-2 infection', *Annals of Nutrition and Metabolism*, 76: 297-303.

Sommars, Meredith A, Krithika Ramachandran, Madhavi D Senagolage, Christopher R Futtner, Derrik M Germain, Amanda L Allred, Yasuhiro Omura, Ilya R Bederman, and Grant D Barish. 2019. 'Dynamic repression by BCL6 controls the genome-wide liver response to fasting and steatosis', *Elife*, 8: e43922.

Soprano, D. R., P. Qin, and K. J. Soprano. 2004. 'Retinoic acid receptors and cancers', *Annu Rev Nutr*, 24: 201-21.

Spiegelman, Bruce M. 1998. 'PPAR-gamma: adipogenic regulator and thiazolidinedione receptor', *Diabetes*, 47: 507-14.

Stehlin-Gaon, C., D. Willmann, D. Zeyer, S. Sanglier, A. Van Dorsselaer, J. P. Renaud, D. Moras, and R. Schüle. 2003. 'All-trans retinoic acid is a ligand for the orphan nuclear receptor ROR beta', *Nat Struct Biol*, 10: 820-5.

Takase, S., D. E. Ong, and F. Chytil. 1986. 'Transfer of retinoic acid from its complex with cellular retinoic acid-binding protein to the nucleus', *Arch Biochem Biophys*, 247: 328-34.

Tamori, Y., J. Masugi, N. Nishino, and M. Kasuga. 2002. 'Role of peroxisome proliferator-activated receptor-gamma in maintenance of the characteristics of mature 3T3-L1 adipocytes', *Diabetes*, 51: 2045-55.

Tan, N. S., N. S. Shaw, N. Vinckenbosch, P. Liu, R. Yasmin, B. Desvergne, W. Wahli, and N. Noy. 2002. 'Selective cooperation between fatty acid binding proteins and peroxisome proliferator-activated receptors in regulating transcription', *Mol Cell Biol*, 22: 5114-27.

Thorsell, A. G., W. H. Lee, C. Persson, M. I. Siponen, M. Nilsson, R. D. Busam, T. Kotenyova, H. Schuler, and L. Lehtio. 2011. 'Comparative structural analysis of lipid binding START domains', *PLoS One*, 6: e19521.

Tillman, M. C., M. Khadka, J. Duffy, M. C. Wang, and E. A. Ortlund. 2019. 'Structural characterization of life-extending Caenorhabditis elegans Lipid Binding Protein 8', *Sci Rep*, 9: 9966.

Tomas, Julie, Céline Mulet, Azadeh Saffarian, Jean-Baptiste Cavin, Robert Ducroc, Béatrice Regnault, Chek Kun Tan, Kalina Duszka, Rémy Burcelin, and Walter Wahli. 2016. 'High-fat diet modifies the PPAR-γ pathway leading to disruption of microbial and physiological ecosystem in murine small intestine', *Proceedings of the National Academy of Sciences*, 113: E5934-E43.

Tsukahara, R., H. Haniu, Y. Matsuda, and T. Tsukahara. 2014. 'Heart-type fatty-acid-binding protein (FABP3) is a lysophosphatidic acid-binding protein in human coronary artery endothelial cells', *FEBS Open Bio*, 4: 947-51.

Tsukahara, T., R. Tsukahara, Y. Fujiwara, J. Yue, Y. Cheng, H. Guo, A. Bolen, C. Zhang, L. Balazs, F. Re, G. Du, M. A. Frohman, D. L. Baker, A. L. Parrill, A. Uchiyama, T. Kobayashi, K. Murakami-Murofushi, and G. Tigyi. 2010. 'Phospholipase D2-dependent inhibition of the nuclear hormone receptor PPARgamma by cyclic phosphatidic acid', *Mol Cell*, 39: 421-32.

Uysal, K. T., L. Scheja, S. M. Wiesbrock, S. Bonner-Weir, and G. S. Hotamisligil. 2000. 'Improved glucose and lipid metabolism in genetically obese mice lacking aP2', *Endocrinology*, 141: 3388-96.

Vanier, M. T. 2015. 'Complex lipid trafficking in Niemann-Pick disease type C', *J Inherit Metab Dis*, 38: 187-99.

Velkov, T. 2013. 'Interactions between Human Liver Fatty Acid Binding Protein and Peroxisome Proliferator Activated Receptor Selective Drugs', *PPAR Res*, 2013: 938401.

Wang, D., H. Wang, Y. Guo, W. Ning, S. Katkuri, W. Wahli, B. Desvergne, S. K. Dey, and R. N. DuBois. 2006. 'Crosstalk between peroxisome proliferator-activated receptor delta and VEGF stimulates cancer progression', *Proc Natl Acad Sci U S A*, 103: 19069-74.

Wang, H., J. Chen, K. Hollister, L. C. Sowers, and B. M. Forman. 1999. 'Endogenous bile acids are ligands for the nuclear receptor FXR/BAR', *Mol Cell*, 3: 543-53.

Wang, Y., N. Kumar, C. Crumbley, P. R. Griffin, and T. P. Burris. 2010. 'A second class of nuclear receptors for oxysterols: Regulation of RORalpha and RORgamma activity by 24S-hydroxycholesterol (cerebrosterol)', *Biochim Biophys Acta*, 1801: 917-23.

Weikum, E. R., X. Liu, and E. A. Ortlund. 2018. 'The nuclear receptor superfamily: A structural perspective', *Protein Sci*, 27: 1876-92.

Wikoff, William R, Andrew T Anfora, Jun Liu, Peter G Schultz, Scott A Lesley, Eric C Peters, and Gary Siuzdak. 2009. 'Metabolomics analysis reveals large effects of gut microflora on

mammalian blood metabolites', *Proceedings of the National Academy of Sciences*, 106: 3698-703.

Wirtz, K. W., and D. B. Zilversmit. 1968. 'Exchange of phospholipids between liver mitochondria and microsomes in vitro', *J Biol Chem*, 243: 3596-602.

Wolfrum, C., C. M. Borrmann, T. Borchers, and F. Spener. 2001. 'Fatty acids and hypolipidemic drugs regulate peroxisome proliferator-activated receptors alpha - and gamma-mediated gene expression via liver fatty acid binding protein: a signaling path to the nucleus', *Proc Natl Acad Sci U S A*, 98: 2323-8.

Wolfrum, C., P. Ellinghaus, M. Fobker, U. Seedorf, G. Assmann, T. Börchers, and F. Spener. 1999. 'Phytanic acid is ligand and transcriptional activator of murine liver fatty acid binding protein', *J Lipid Res*, 40: 708-14.

Wong, L. H., A. Copic, and T. P. Levine. 2017. 'Advances on the Transfer of Lipids by Lipid Transfer Proteins', *Trends Biochem Sci*, 42: 516-30.

Wurtz, J. M., W. Bourguet, J. P. Renaud, V. Vivat, P. Chambon, D. Moras, and H. Gronemeyer. 1996. 'A canonical structure for the ligand-binding domain of nuclear receptors', *Nat Struct Biol*, 3: 87-94.

Yoo, Seong Ho, Mohamed A Abdelmegeed, and Byoung-Joon Song. 2013. 'Activation of PPARα by Wy-14643 ameliorates systemic lipopolysaccharide-induced acute lung injury', *Biochemical and biophysical research communications*, 436: 366-71.

Yu, S., L. Levi, G. Casadesus, G. Kunos, and N. Noy. 2014. 'Fatty acid-binding protein 5 (FABP5) regulates cognitive function both by decreasing anandamide levels and by activating the nuclear receptor peroxisome proliferator-activated receptor β/δ (PPARβ/δ) in the brain', *J Biol Chem*, 289: 12748-58.

Zhao, Lele, Gang Wang, Paul Siegel, Chuan He, Hezhong Wang, Wenjing Zhao, Zhengxiao Zhai, Fengwei Tian, Jianxin Zhao, and Hao Zhang. 2013. 'Quantitative genetic background of the host influences gut microbiomes in chickens', *Scientific reports*, 3: 1-6.

Zomer, A. W., B. van Der Burg, G. A. Jansen, R. J. Wanders, B. T. Poll-The, and P. T. van Der Saag. 2000. 'Pristanic acid and phytanic acid: naturally occurring ligands for the nuclear receptor peroxisome proliferator-activated receptor alpha', *J Lipid Res*, 41: 1801-7.

Chapter 2: Ligand-dependent interaction between phosphatidylcholine transfer protein and PPARδ: Implications for metabolic syndrome.

Samuel A. Druzak [1*], Matteo Tardelli [2*], Suzanne G. Mays [1], Mireille El Bejjani [1], Xulie Mo [4], Kristal M. Maner-Smith[5], Thomas Bowen[5], Michael L. Cato[1], Matthew C. Tillman[1], Akiko Sugiyama [2,3], Yang Xie[2,3] ,Haian Fu [4], David E. Cohen [2,3], Eric A. Ortlund[1]

From the [1]Department of Biochemistry, Emory University School of Medicine, 1510 Clifton Road, Atlanta, GA 30322; [2]Joan & Sanford I. Weill Department of Medicine, Weill Cornell Medical College, New York, NY. [3]Division of Gastroenterology, Hepatology and Endoscopy, Brigham and Women's Hospital, Harvard Medical School, Boston, MA. [4]Department of Chemical Biology and Pharmacology, Emory University School of Medicine, 1510 Clifton Road, Atlanta, GA 30322. [5]Emory Integrated Lipidomics and Metabolomics Core, Emory University School of Medicine, 1510 Clifton Road, Atlanta, GA 30322

This chapter is currently under review at Nature communications.

Author Contributions: S.A.D., S.G.M., M.T., D.E.C., and E.A.O. designed research; S.A.D., S.G.M., M.T. M.L.C., X.M., M.B., K.M.S., and A.S. performed research; M.T., and D.E.C. Contributed tissue for analysis; S.A.D., S.G.M., and M.T. analyzed data; S.A.D., and E.A.O. wrote the chapter; S.A.D made figures; S.A.D., M.T., S.G.M., D.E.C., Y.X., and E.A.O. edited the chapter.

2.1 Summary:

Phosphatidylcholine transfer protein (PC-TP; synonym StarD2) is a soluble lipid binding protein that transports phosphatidylcholine (PC) between cellular membranes. PC-TP knockout mice are more sensitive to glucose and insulin, have increased beta oxidation and improved liver health compared to wild-type mice. To better understand the protective metabolic effects associated with PC-TP deletion, we investigated how hepatic PC-TP affects lipid metabolism, sensitivity to glucose and insulin, and energy homeostasis in a mouse model of diet-induced obesity. We generated a hepatocyte-specific PC-TP knockdown mouse (L-*Pctp*$^{-/-}$), which gains less weight and accumulates less liver fat compared to wild-type mice when challenged with a high fat diet. Hepatic deletion of PC-TP also reduced adipose tissue mass combined with decreases

in levels of triglycerides and phospholipids in skeletal muscle, liver and plasma suggesting that hepatic PC-TP activity influences whole body lipid homeostasis. Gene expression analyses suggest that the observed metabolic changes are related to transcriptional activity of peroxisome proliferative activating receptor (PPAR) family members. An in-cell protein complementation screen between lipid transfer proteins and PPARs uncovered a novel, direct interaction between PC-TP and PPARδ that was not observed for other PPAR family members. We confirmed the PC-TP– PPARδ interaction in HUH7 hepatoma cells, where it was found to repress PPARδ-mediated transactivation. Mutations of PC-TP residues implicated in PC binding and transfer reduce the PC-TP-PPARδ interaction and relieve PC-TP-mediated PPARδ repression. Reduction of exogenously supplied methionine and choline reduces the interaction while serum starvation enhances the interaction in cultured hepatocytes. Together our data points to a ligand sensitive PC-TP– PPARδ interaction that suppresses PPAR activity.

2.2 Introduction:

Steroidogenic acute regulatory lipid transport (START/STARd) domain-containing proteins bind and transport glycerophospholipids, ceramides, and sterols. This family is comprised of 15 members that are further classified based on sequence and ligand preferences. The STARD2 subfamily, containing STARD2, 7, and 10, bind glycerophospholipids species. The titular member of this family, phosphatidylcholine transfer protein (PC-TP a.k.a STARD2), specifically binds and transfers phosphatidylcholine (PC) generated in the endoplasmic reticulum throughout the cell to modulate plasma membrane, lipid, and thermal homeostasis. (Kang et al., 2009; Kang et al., 2010b; Scapa et al., 2008) Knockout of PC-TP (*Pctp*$^{-/-}$) in mice leads to beneficial alterations in fatty acid metabolism, glucose homeostasis, and liver health. In the context of high fat diet, *Pctp*$^{-/-}$ protects mice from diet-induced insulin and glucose intolerance as indicated by glucose tolerance test and increases in phosphorylation of important mediators of insulin signaling. (Krisko et al., 2017) *Pctp*$^{-/-}$ mice are also protected from hepatoxicity induced by a methionine and choline deficient (MCD) diet. (Nicholls et al., 2017) Therefore, PC-TP promotes pathological effects in multiple models of liver damage.

Many of the phenotypic effects observed in *Pctp*$^{-/-}$ mice have been rationalized in the context of its interaction with thioesterase superfamily member 2 (THEM2). In the cytoplasm near the mitochondrial membrane, THEM2 cleaves fatty acyl-CoA into free fatty acids which may then be conjugated and imported into the mitochondria by Carnitine palmitoyltransferase I (CPT1) – Acyl-CoA Synthetase Long Chain (ACSL). The PC-TP– THEM2 interaction increases the thioesterase activity of THEM2, resulting in increased fatty acid metabolism and improved glucose and insulin tolerance. (Kang et al., 2012) Interestingly, knockout of PC-TP, but not THEM2,

improves liver health and increases peroxisome proliferative activating receptor (PPAR) activity, suggesting THEM2 does not solely mediate the effects of PC-TP. (Kawano et al., 2014)

PPARs are part of a lipid-sensing nuclear receptor family comprised of three members: PPARα, γ, δ. Members of this family have the largest ligand binding pocket of any nuclear receptor allowing them to accommodate a variety of ligands from fatty acids to phosphatidylcholines (PCs) and their metabolites. (Chakravarthy et al., 2009b; Davies et al., 2001; Klingler et al., 2016; Sanderson et al., 2009; Zoete et al., 2007) PPARs are localized primarily in the nucleus and heterodimerize with retinoid x receptor alpha (RXRα) to bind DNA and control transcription of genes involved in metabolism, proliferation and inflammation. Ligand binding induces shedding of co-repressor complexes by inducing an allosteric shift in the activation function surface 2 (AF-2). This allows for coactivator association, which modulates transcription by recruiting enzymes involved in DNA methylation or histone acetylation, and altering chromatin accessibility for RNA pol 2. (IJpenberg et al., 2004) It is unknown how lipophilic ligands are transported to PPARs in the nucleus. One possible mechanism is through delivery by lipid transport proteins (LTPs). For example, fatty acid binding proteins (FABPs) have been shown to act as lipid chaperones delivering ligands to the PPAR family in an isoform-specific manner. (Adida and Spener, 2006; Armstrong et al., 2014b; De Gerónimo et al., 2010; Huang et al., 2004; Schug et al., 2007b; Wolfrum et al., 2001b) However, FABPs only bind a subset of reported PPAR ligands and it is unclear how PPARs access larger ligands such as glycerophospholipids.

We sought to characterize the role of PC-TP in the liver to determine the mechanism by which hepatic PC-TP modulates energy homeostasis. Transcriptomic analysis of livers isolated from *Pctp*$^{-/-}$ vs wild type mice fed an MCD diet to induce steatosis revealed PC-TP-dependent alterations in PPAR signaling that were enhanced upon methionine and choline restriction. We

generated a transducible, liver specific PC-TP knockout (L-*Pctp*$^{-/-}$) which had a mild phenotype under normal dietary conditions but reduced hepatic lipid accumulation, improved glucose and insulin homeostasis when given a high fat diet. Targeted gene expression analysis showed a strong induction of PPAR-controlled transcripts in L-*Pctp*$^{-/-}$ mice fed a high fat diet, suggesting PC-TP represses PPARδ during overnutrition. We demonstrate that PC-TP interacts directly with PPARδ to suppress its transcriptional activity, using a combination of cellular assays and binding assays with purified proteins. The PPARδ ligand binding domain (LBD) is sufficient for PC-TP and FABP5 interaction *in vitro*, though full-length PPARδ (FL-PPARδ) is required in cells. Mutations to the PC-TP lipid binding pocket abrogate PPARδ interaction and relieve the observed gene suppression. Taken together, these observations suggest a novel role for PC-TP in regulating PPARδ.

2.3 Results:

2.3.1 RNA-seq analysis of liver tissue from Pctp $^{-/-}$ mice

Previous work has shown positive metabolic effects associated with whole-body knockout (KO) of PC-TP in mice (*Pctp*$^{-/-}$). *Pctp*$^{-/-}$ mice are more sensitive to glucose and insulin, have increased beta oxidation and improved liver health compared to wild-type mice, suggesting an important role for this protein in regulation of glucose and insulin sensitivity.(Kang et al., 2010c; Krisko et al., 2017; Scapa et al., 2008) When given a methionine and choline-deficient (MCD) diet to induce liver damage, *Pctp*$^{-/-}$ mice develop steatosis but are protected from hepatotoxicity. (Nicholls et al., 2017) To better understand mechanisms underlying the protective effects associated with PC-TP deletion, we investigated changes in the transcriptome that occur in the livers of *Pctp*$^{-/-}$ mice on normal chow and on the MCD diet.

Pctp KO changes 97 genes by at least 1.5-fold in male mice given normal diet (ND) and 415 genes in mice on the MCD diet. Under both dietary conditions, we detected a large subset of genes known to be regulated via PPARs (Figure 2-1A-B). This observation was confirmed when cross referencing the differentially expressed genes (DEGs) with the ChIP Enrichment Analysis (CHEA) database (Figure 2-2A-B). (Kuleshov et al., 2016; Lachmann et al., 2010) Kyoto Encyclopedia of Genes and Genomes (KEGG) pathway analysis revealed increased perturbations in PPAR-associated processes in the MCD condition compared to ND (Figure 2-2C-D). (Kanehisa and Goto, 2000) Comparing the effect of diet within each genotype shows a reduction of differential PPAR regulation for both CHEA and KEGG analysis when comparing WT **(**Figure 2-1C-D) to *Pctp* $^{-/-}$ mice (Figure 2.11E-F) supporting a role for PC-TP in differential PPAR regulation resulting from MCD diet.

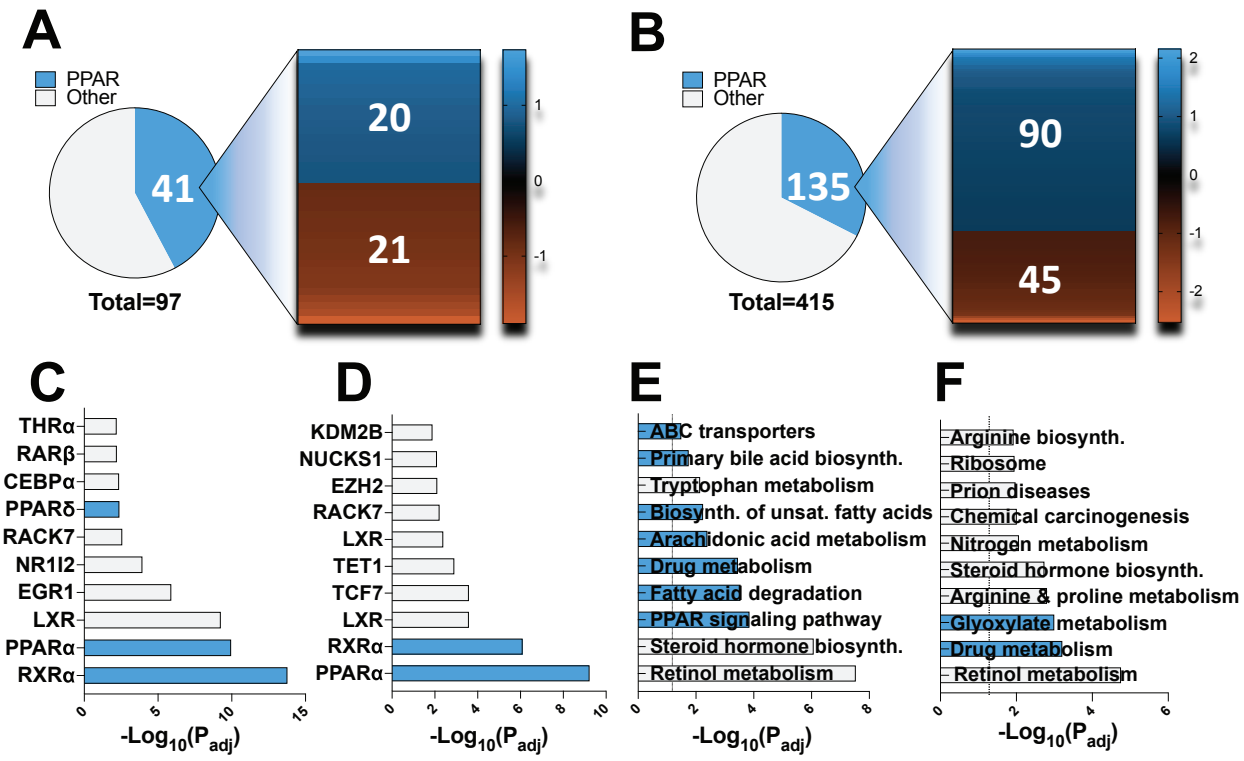

Figure 2- 1: RNAseq comparing Pctp-/- and WT chow and MCD fed mice reveal dysregulation of PPARs.

RNA from chow and MCD fed WT (n = 3) and *Pctp* $^{-/-}$ (n = 3) mouse livers was used for RNAseq analysis. **A & B**) Differentially expressed genes (DEGs) for chow fed and MCD fed mice respectively, comparing WT to PC-TP KO. Heat Map of PPAR controlled DEGs shows the distribution of PPARδ controlled DEGs **C & D)** Enrichr analysis of DEGs comparing the effect of diet on each genotype compared to transcription factor CHIP-seq databases (CHEA), for WT and *Pctp* -/- respectively.(Lachmann et al., 2010) (Kuleshov et al., 2016) **E & F)** Enrichment analysis of altered metabolic pathways (KEGG) determined by cross referencing the statistically significantly altered genes comparing the effect of diet on each genotype, for WT and *Pctp* -/- respectively. Blue denotes a PPAR related process. (Kuleshov et al., 2016) (Kanehisa and Goto, 2000)

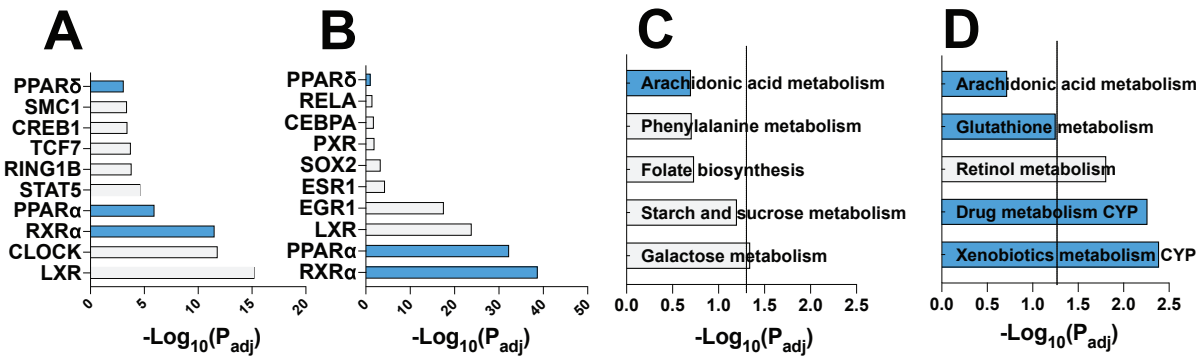

Figure 2- 2. RNAseq comparing Pctp-/- and WT chow and MCD fed mice.

RNA from chow and MCD fed WT (n = 3) and *Pctp* $^{-/-}$ (n = 3) mouse livers was used for RNAseq analysis. **A & B**) Enrichr analysis of DEGs from chow fed and MCD fed mice respectively, mice were compared to know transcription factor CHIP-seq databases (CHEA).**C & D)** Enrichment analysis of altered metabolic pathways (KEGG) determined by cross referencing the statistically significantly altered genes for chow and MCD fed mice respectively.

2.3.2 In vivo characterization of L-Pctp$^{-/-}$

We established an inducible hepatocyte specific PC-TP KD (L-*Pctp*$^{-/-}$) mice to avoid potential confounding developmental or compensatory effects from a whole-body deletion and to query the specific role of hepatic PC-TP. L-*Pctp*$^{-/-}$ mice were generated through i.v. injection of AAV8-TBG-Cre into *Pctp*$^{flox/flox}$ mice. AAV8 harboring CRE under the Thyroxine-binding globulin (TBG) promoter ensures hepatocyte-specific deletion (Figure 2-3 A). Mice were challenged with either high fat diet (HFD) or normal diet (ND) (Figure 2-3A-B). When given a ND, L-*Pctp*$^{-/-}$ mice showed no significant change in body weight, glucose or insulin tolerance compared to WT mice (Figure 2-3C-E). L-*Pctp*$^{-/-}$ mice displayed increased gluconeogenesis in the liver (Figure 2-3F) and only minor alterations in the composition of liver and serum and liver lipids (Figure 2-4A-J).

Under HFD feeding, L-*Pctp*$^{-/-}$ mice gained less weight and had reduced adipose tissue mass relative to their WT counterparts (Figure2-3C). This change in weight started on week 5 and continued throughout the assay period (Figure 2-5A). Food and water intake between HFD-fed mice were not significantly different for WT or L-*Pctp*$^{-/-}$ mice, suggesting these effects are independent of nutrient consumption (Figure 2-5B-C). We also observed improved glucose tolerance (Figure 2-3D) and insulin sensitivity (Figure 2-3E). Traces for these tolerance tests can be found in Figure 2-5 D-F. These changes in glucose and insulin homeostasis were also reflected in decreased fasting levels of both glucose and insulin (Figure 2-5 G-H).

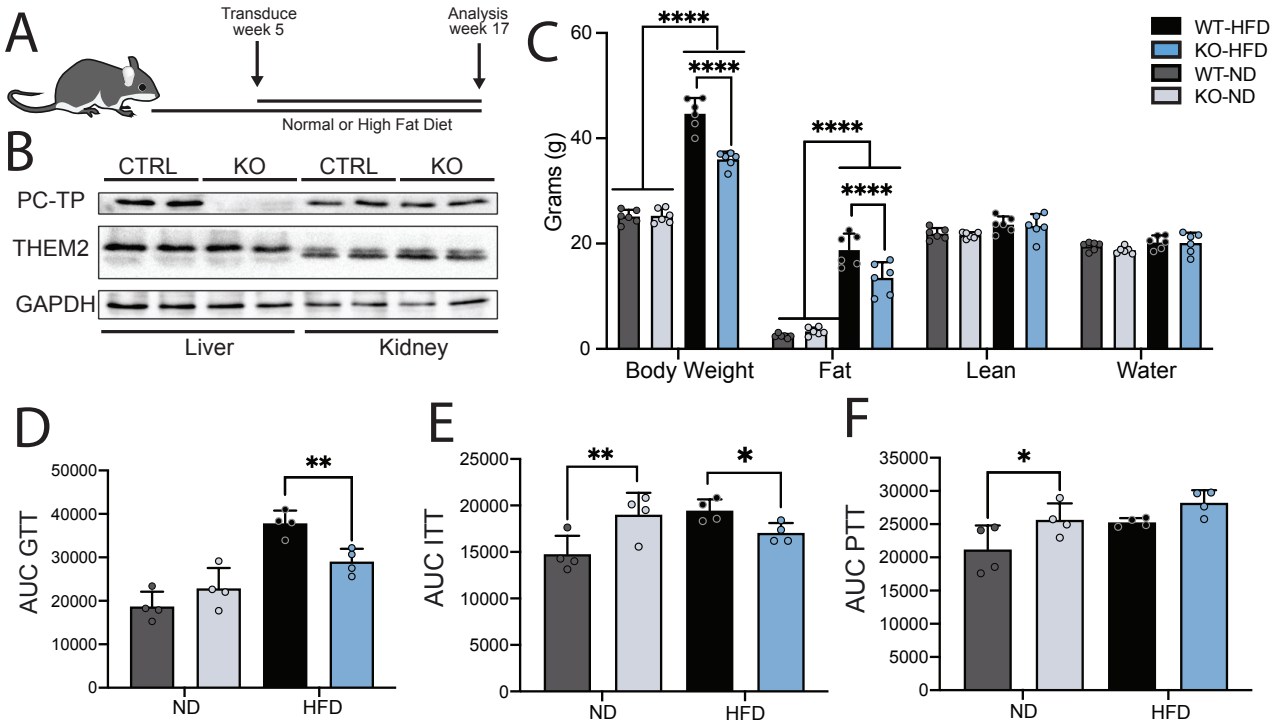

Figure 2- 3:Characterization of the L-Pctp-/- mouse.

A) L-*Pctp*$^{-/-}$ male mice were generated through i.v. injection of AAV8-TBG-Cre into *Pctp*$^{flox/flox}$ mice. AAV8 harboring CRE under the TBG promoter ensures hepatocyte-specific deletion. Control mice (WT) were *Pctp*$^{flox/flox}$ mice treated with AAV8-TBG-LacZ through i.v. injection. Following AAV8 injection, mice were fed either ND or HFD for an additional 12 weeks prior to analysis. **B)** Representative western blot showing hepatocyte-specific knockdown of Pctp in L-*Pctp*$^{-/-}$ group. **C)** Echo-RI of L-*Pctp*$^{-/-}$ and WT mice on ND or HFD (n=6, Two-way ANOVA, SEM). **D)** Area under the curve (AUC) for glucose tolerance test (GTT) (n=4, T-test, SEM) **E)** Area under the curve for insulin tolerance test (ITT) (n=4, T-test, SEM). **F)** Area under the curve for pyruvate tolerance test (PTT) (N=4, T-test, SEM).

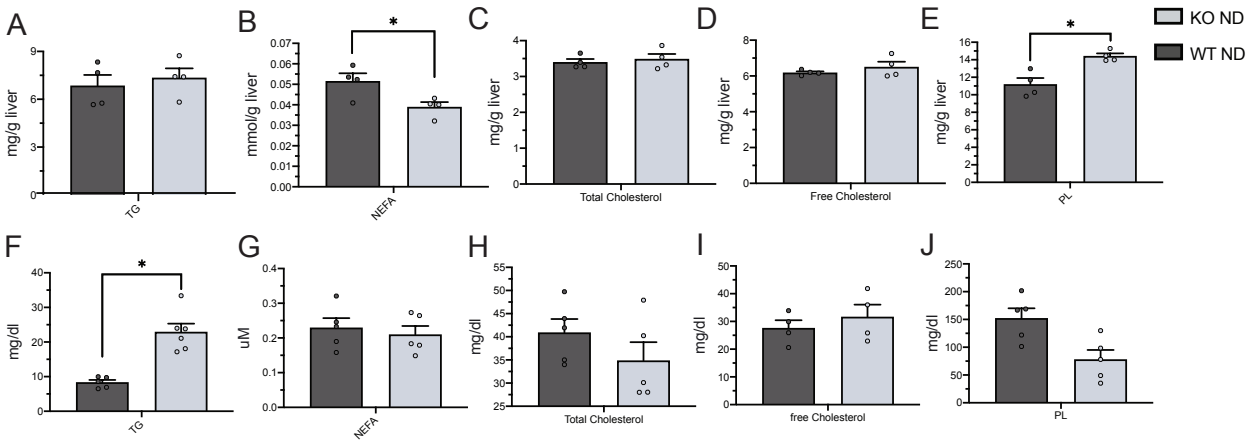

Figure 2- 4: Characterization of liver and plasma the L-Pctp-/- mouse fed ND.

A-E) Quantification of liver composition of triglycerides (TG), free fatty acids (FFA), phospholipids (PL), as well as total and free cholesterol for L-*Pctp*$^{-/-}$ and WT mice (n=4-5, T-test, SEM). **F-J)** Quantification of Plasma composition of triglycerides (TG), Non-esterified fatty acids (NEFA), as well as total and free cholesterol and phospholipid for L-*Pctp*$^{-/-}$ and WT mice (n=4-5, T-test, SEM).

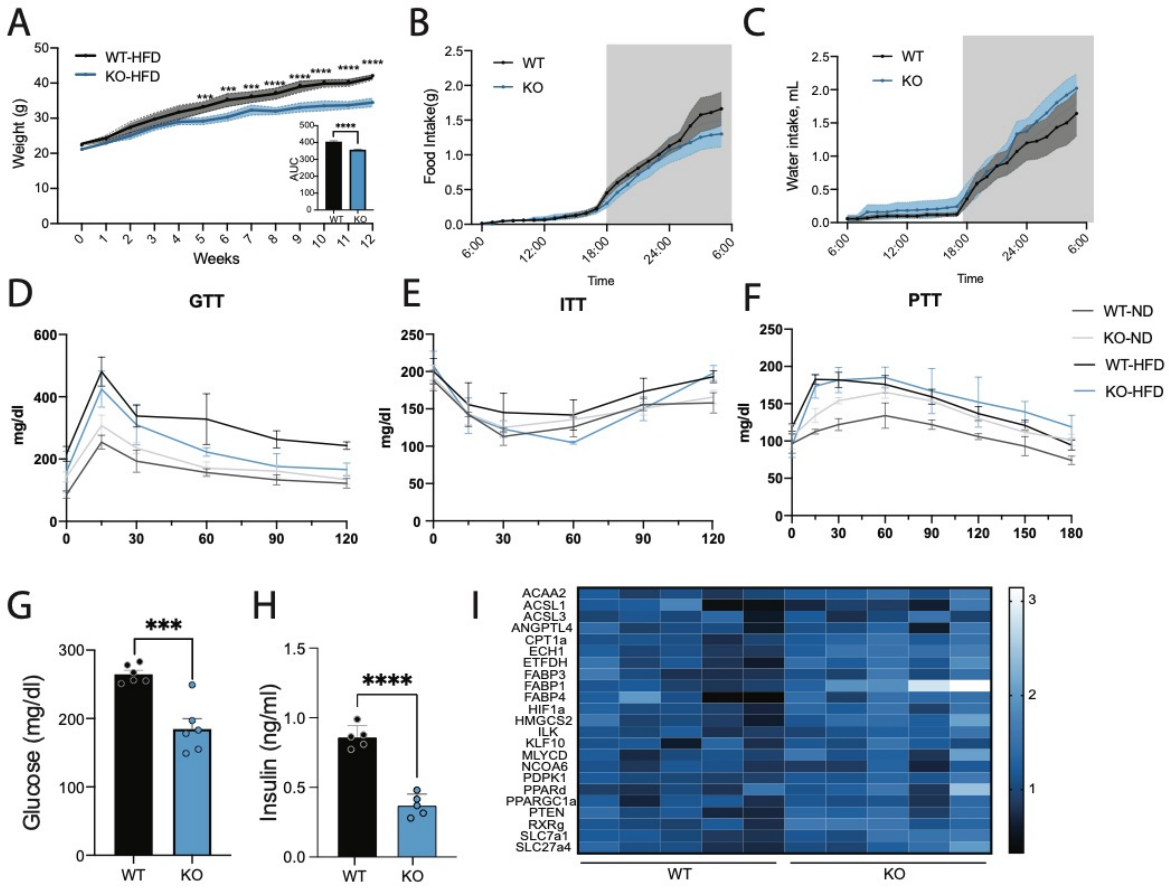

Figure 2- 5: Additional characterization of the L-Pctp-/- mouse fed HFD.

A) Growth curve of L-*Pctp*$^{-/-}$ (KD) and WT mice on HFD throughout the period of diet intervention, with quantification of area under the curve provided in the insert (n=15, T-Test, SEM). **B & C)** Food intake and water intake of HFD cohort measured over one day following 12 weeks of diet intervention show no significant difference in nutrient consumption to explain changes in weight (n=6, T-Test, SEM). **D-F)** Curves for the GTT, ITT and PTT used for measuring area under the curves (n=4,SEM) **G & H)** Fasting glucose and insulin in KD and WT mice on HFD following 6 hour fast or 1.5 hour fast respectively (n=6, T-test, SEM). **I)** qRT-PCR of cDNA generated from the livers of WT and KD mice fed HFD shows significant alteration in several genes known to be regulated by PPARs. (n=5).

In addition to a reduction in fat mass and total body weight, we also observed a significant decrease in liver weight for L-*Pctp*$^{-/-}$ mice fed HFD compared to WT HFD mice (Figure 2-6A). Under HFD, deletion of hepatic PC-TP normalized liver size to a weight comparable to WT mice fed ND. In line with this, we also observed reduced lipid droplet formation in L-*Pctp*$^{-/-}$ mice fed HFD relative to WT HFD mice (Figure 2-6B-C), accompanied by decreases in hepatic triglyceride (TG) content (Figure 2-6D-E). Taken together, this data points to a role for PC-TP in the progression of liver lipotoxicity driven by a state of overnutrition.

We next investigated whether the decreased liver cholesterol and TG could be a result of increased export of these lipid species into the serum. Serum lipid profiling reveals similar levels of TGs, PLs, and non-esterified free fatty acids (NEFA) for all groups. However, there is an increase in total serum cholesterol levels in KO HFD, likely due to changes in the composition of lipoprotein particles (Figure 2-6F-J). Supporting this idea, we see more cholesterol packaged into the lipoprotein particles as well as less triglyceride content (Figure 2-6K-L).

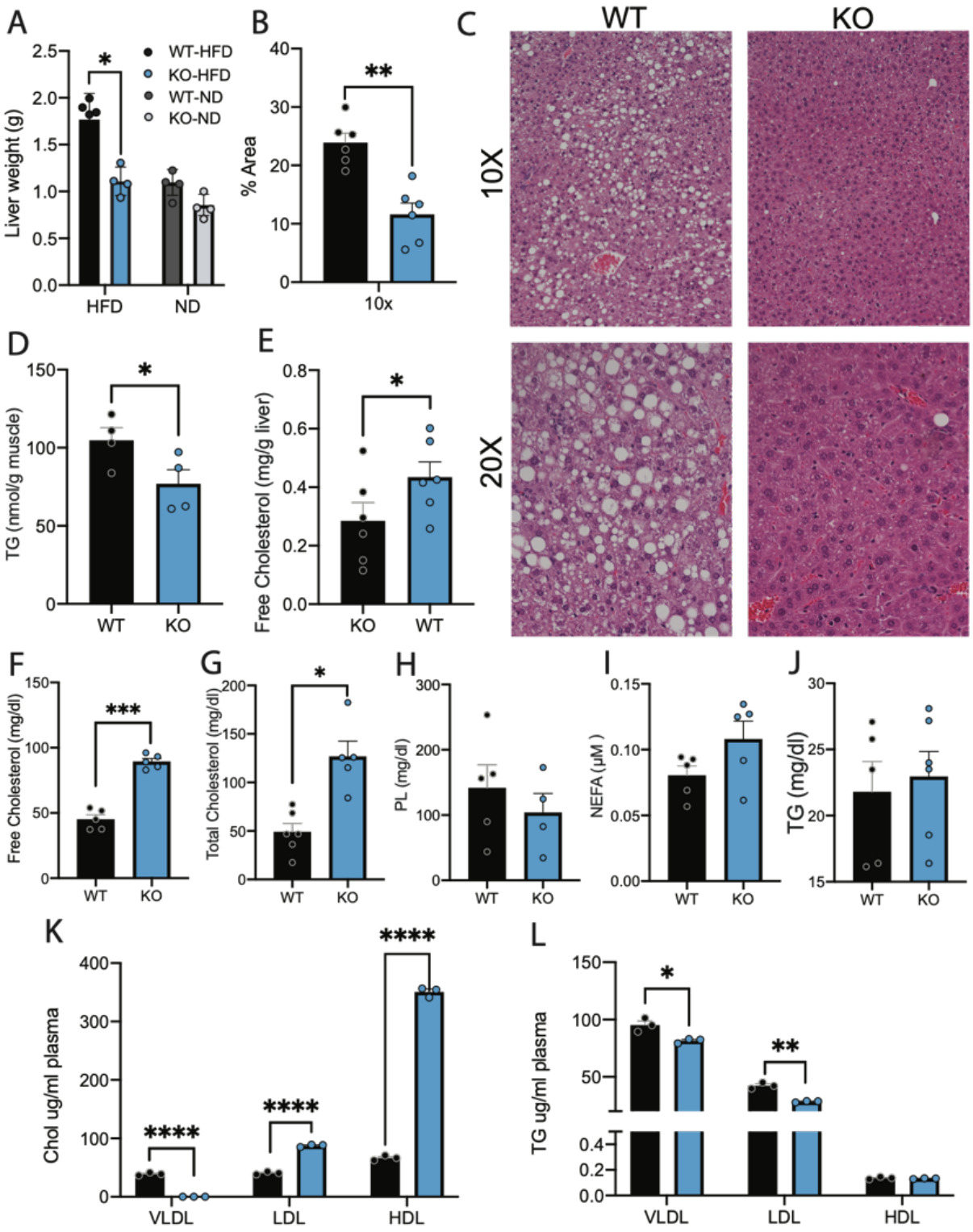
A
Liver weight (g)
WT-HFD
KO-HFD
WT-ND
KO-ND
HFD
ND
B
% Area
10x
C
WT
KO
10X
20X
D
TG (nmol/g muscle)
WT
KO
E
Free Cholesterol (mg/g liver)
KO
WT
F
Free Cholesterol (mg/dl)
G
Total Cholesterol (mg/dl)
H
PL (mg/dl)
I
NEFA (μM)
J
TG (mg/dl)
K
Chol ug/ml plasma
VLDL
LDL
HDL
L
TG ug/ml plasma

Figure 2- 6: Decreased hepatic lipotoxicity in L-Pctp-/- mice on HFD.

A) Decreased liver weight in mice KO mice fed HFD compared to WT control (n=4-6, T-test, SEM). **B)** Quantification of lipid droplet area for histology (n=6, T-test, SEM). **C)** Representative histological sections of HFD fed KO and WT mice with H&E staining. **D & E)** Quantification of liver composition of triglycerides (TG) and free cholesterol for KO and WT mice (n=4-6, T-test, SEM). **F-J)** Quantification of Plasma composition of cholesterol, PL, NEFA and TG for KO and WT mice (n=4-6, T-test, SEM). **K & L)** Amount of cholesterol and TG packaged into lipoprotein particles as determined by size exclusion chromatography (n=3, T-test, SEM).

The HFD L-*Pctp*$^{-/-}$ mice do not have alterations in energy expenditure, respiration exchange ratio or beta-hydroxybutyrate levels (Figure 2-7A-C). We also interrogated the lipid profile of muscle isolated from HFD mice and found that L-*Pctp*$^{-/-}$ HFD mice had decreased levels of TG, NEFA and phospholipid species compared to WT HFD mice (Figure 2-7D-F). Taken together these observations point to alterations in lipid homeostasis without affecting substrate utilization, energy expenditure or food intake. HFD L-*Pctp*$^{-/-}$ mice displayed an increase in distance traveled during voluntary wheel running when compared to WT mice (Figure 2-7G). Follow up endurance running tests showed ND L-*Pctp*$^{-/-}$ ran further and longer than control mice (Figure 2-7H-I).

Taken together our data suggest a role for PC-TP in regulating PPARs as our L-*Pctp* $^{-/-}$ mouse on HFD displayed an opposing phenotype to hepatic deletion of PPARs. Deletion of hepatic PPARα resulted in decreased beta oxidation, insulin resistance and increased liver lipid accumulation. Similarly liver specific PPARδ KO presented with insulin resistance, dyslipidemia and steatosis. (Liu et al., 2013; Montagner et al., 2016) While seemingly redundant, PPARα is thought to control these processes in the fasted state, with PPARδ playing a more important role in the fed state. (Sommars et al., 2019) To test this, we performed a PPAR qRT-PCR array on livers from HFD animals which shows an increase in PPAR regulated transcripts in L-*Pctp*$^{-/-}$ mice (Figure 2-7J) (Figure 2-5F).

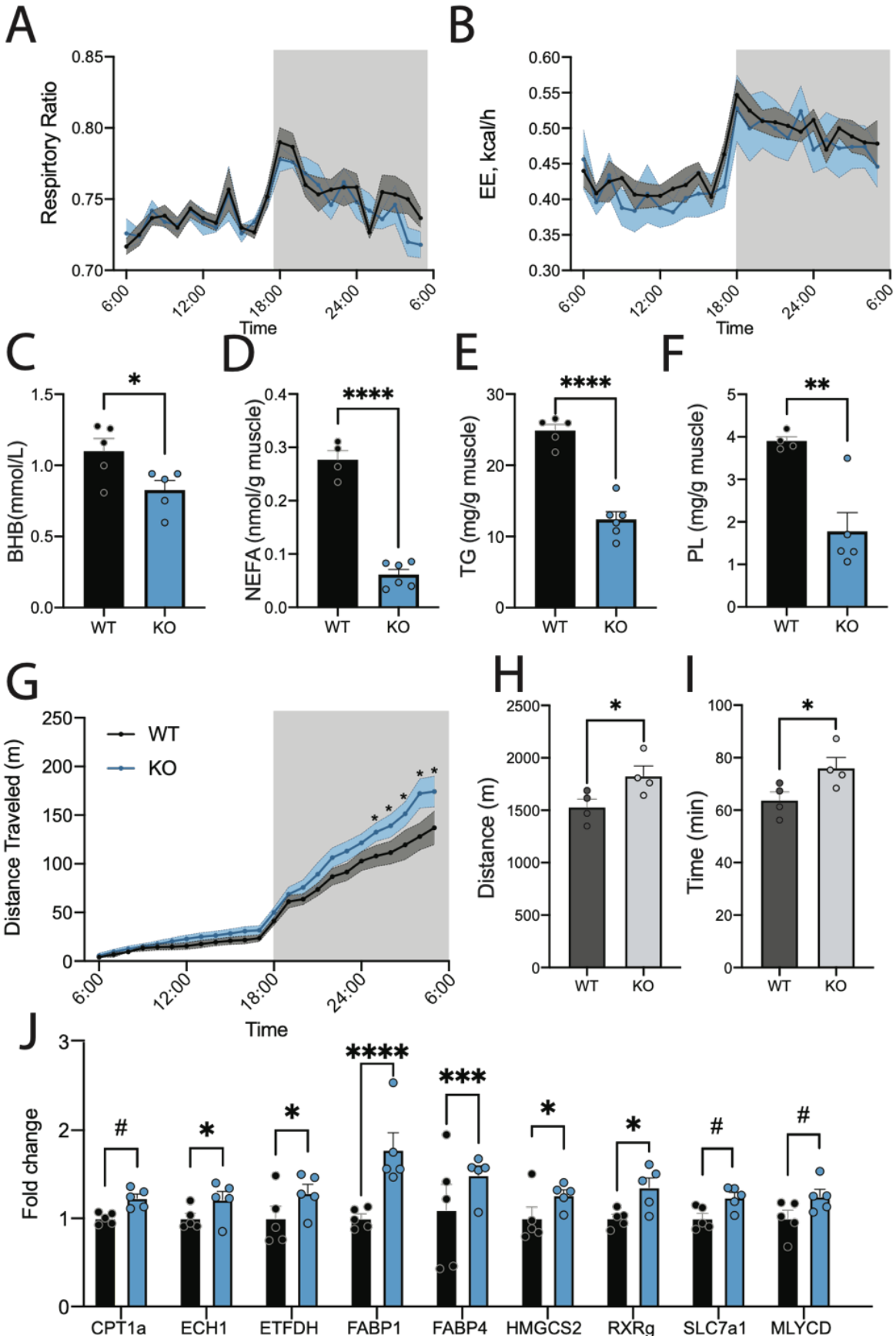
A
Respirtory Ratio
0.85
0.80
0.75
0.70
6:00
12:00
18:00
24:00
6:00
Time
B
EE, kcal/h
0.60
0.55
0.50
0.45
0.40
0.35
0.30
6:00
12:00
18:00
24:00
6:00
Time
C
BHB(mmol/L)
1.5
1.0
0.5
0.0
*
WT
KO
D
NEFA (nmol/g muscle)
0.4
0.3
0.2
0.1
0.0
****
WT
KO
E
TG (mg/g muscle)
30
20
10
0
****
WT
KO
F
PL (mg/g muscle)
5
4
3
2
1
0
**
WT
KO
G
Distance Traveled (m)
250
200
150
100
50
0
WT
KO
6:00
12:00
18:00
24:00
6:00
Time
H
Distance (m)
2500
2000
1500
1000
500
0
*
WT
KO
I
Time (min)
100
80
60
40
20
0
*
WT
KO
J
Fold change
3
2
1
0
#
*
*
****
***
*
*
#
#
CPT1a
ECH1
ETFDH
FABP1
FABP4
HMGCS2
RXRg
SLC7a1
MLYCD

Figure 2- 7: L-Pctp-/- drives beneficial metabolic alterations through muscle-liver axis.

A & B) Promethion cage tracking of the respiration ratio and energy expenditure (n=6, T-Test, SEM). **C)** Quantification of plasma beta-hydroxybutyrate levels using ELISA (n=5, T-test, SEM). **D-F)** Quantification of muscle lipid content (n=4-6, T-test, SEM). **G)** Promethion cage of free running for HFD L-*Pctp*$^{-/-}$ mice show a significantly different trend toward increased movement at later time points (n=6, T-test, SEM). **H & I)** quantification of endurance stress test of WT and PC-TP KO mice (n=6, T-test, SEM). **J)** Relative gene expression in the livers of WT and KD mice fed HFD shows significant alteration in several genes known to be regulated by PPARs. # denotes p value <0.07 but >0.05 (n=5, Two-way ANOVA, SEM).

2.3.3 Defining the PC-TP – PPAR interactome; discovery of a repressive interaction between PC-TP and PPARδ

We systematically interrogated the ability of PPARs to interact with STARD and FABP proteins using a split nano luciferase protein complementation assay (nano-PCA) (Figure 2-8A) developed within the Emory Chemical Biology Discovery Center. (Mo et al., 2017) This in-cell approach relies on the reversible interaction between two fragments of nano-luciferase whereby two proteins containing either the N- or C-terminal portion of nano-luciferase interact to permit reconstitution of the intact enzyme. We observed a PC-TP–PPARδ interaction signal that is stronger in this assay than literature-reported interactors for both PC-TP (PAX3, Them2) and PPARδ (FABP5) (Figure 2-8 B-C). (Armstrong et al., 2014b; Kanno et al., 2007) In agreement with *in vivo* studies, transient knockdown of PC-TP in HUH7 cells led to an increase in the PPARδ target genes *ANGPLT4*, *HMGCS2*, *ADRP*, and *MCAD* implying an inhibitory role for PC-TP (Figure 2-8D). Knockdown efficiency was measured via qPCR and Western blot (Figure 2-9A-C). We verified the repressive effect of PC-TP on PPARδ using luciferase reporter. Consistent with qPCR analysis, we observed increased luciferase reporter activity (Figure 2-8E) upon knockdown of PC-TP.

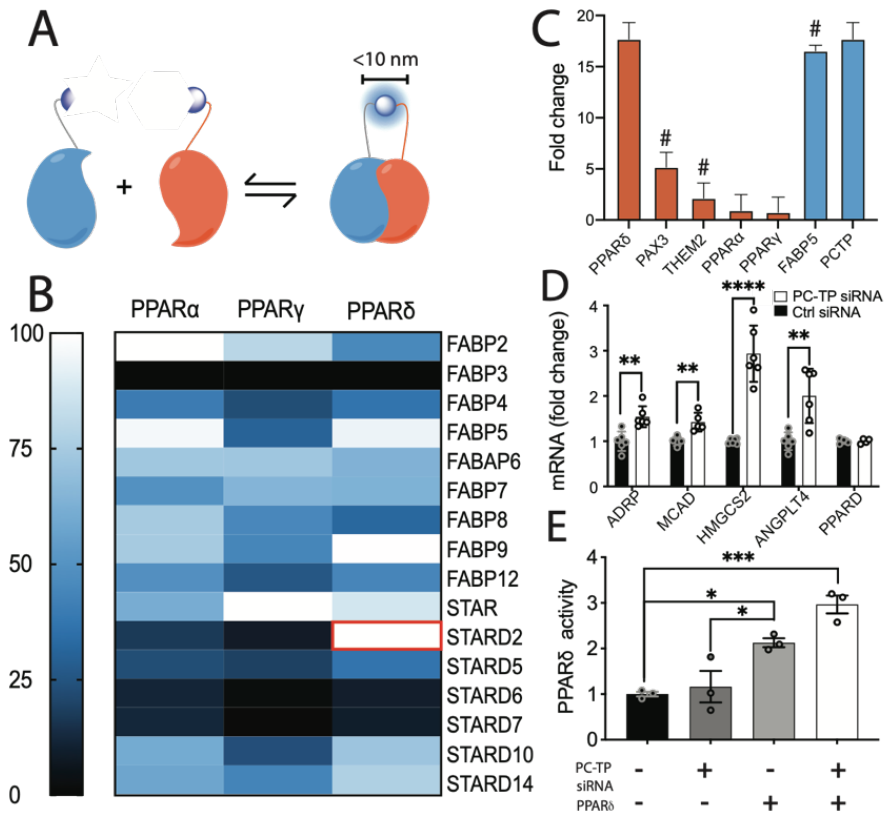

Figure 2- 8: Discovery of a repressive PC-TP–PPARδ complex.

A) Depiction of the nano-PCA assay **B)** Heat map of nano-PCA data from HEK293T cells, for each PPAR isoform and LTP (n=1). z' and S/B noise suggest that this assay is robust using Them1-Them1, as a positive control, and beta-catenin with FABP3 as a negative control (z'=0.795 S/B=7.03) **C)** Bar graph showing the quantification from the nano-PCA screen. PPARδ (blue) interacts with PC-TP (orange) stronger than known partners (#) of either protein (SEM). **D)** To evaluate the effect of PC-TP on the activity of PPARδ, siRNA knockdown of PC-TP was performed in HUH7 cells using targeted and scrambled siRNA. Knockdown (KD) efficiency was confirmed by Western blot. Target mRNA expression levels at 48H post KD was quantified by qRT-PCR and showed increased PPARδ transactivation when PC-TP is transiently KD. (n=6, One way ANOVA, SEM) **E)** Luciferase reporter assay in conjunction with siRNA of PC-TP's confirms PC-TP negatively regulates PPARδ's transactivation (n=3, Two-way ANOVA, SEM)

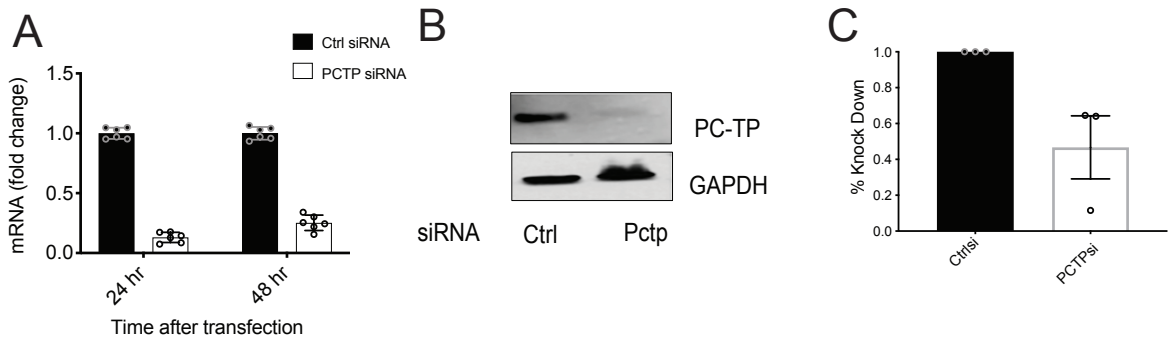

Figure 2- 9: Validation of siRNA mediated knockdown in HUH7.

A) qPCR shows efficient knockdown of gene expression of PC-TP at 24 and 48 hours (n=6). **B)** Representative western blot further demonstrates loss of steady state protein levels. **C)** Quantification of intensities of western blot analysis of PC-TP KD (n=3)

2.3.4 Domain mapping of the PPARδ–PC-TP and PPARδ–FABP5 complex

There are four functionally important surfaces that FABP5 or PC-TP could bind to affect PPARδ transactivation: the DNA binding domain, N-terminal activation function domain 1 (AF-1), activation function surface (AF-S), or the heterodimer interface (Figure 2-10A). The AF-1 and AF-S are implicated in ligand-independent and ligand-dependent activation, respectively, whereas the DNA binding and heterodimer interface are where PPARδ binds DNA or RXRα, respectively. In-cell PCA assays showed that full length PPARδ generates the strongest interactions with PC-TP and FABP5 compared to any isolated domain, suggesting the interaction between LTP and PPARs is multivalent or cooperative (Figure 2-10B). Previous reports suggest that FABPs modulate PPAR in a ligand-dependent manner involving direct ligand transfer. (De Gerónimo et al., 2010) We therefore expected the main interaction interface to be located somewhere within the ligand binding domain (LBD). Instead, FABP5 interacts more strongly with the PPARδ N-terminal AF-1-DBD than the LBD alone, though still at levels lower than observed for the full-length protein (Figure 2-10D). To characterize these interactions *in vitro* we monitored the ability of purified Cy5-labeled PPARδ LBD or full-length (FL) PPARδ to bind purified PC-TP or FABP5 using temperature related intensity change (TRIC) on a Dianthus Pico 2.3 (NanoTemper) (Figure 2-10C and 2.10E). (Hatty et al.) Both FABP5 and PC-TP interact with FL-PPARδ with binding affinities (Kd) of ~150 nM and ~4uM, respectively. In contrast to in cell domain mapping, there was no significant difference in binding affinities between PPARδ-LBD or FL-PPARδ with either PC-TP or FABP5.

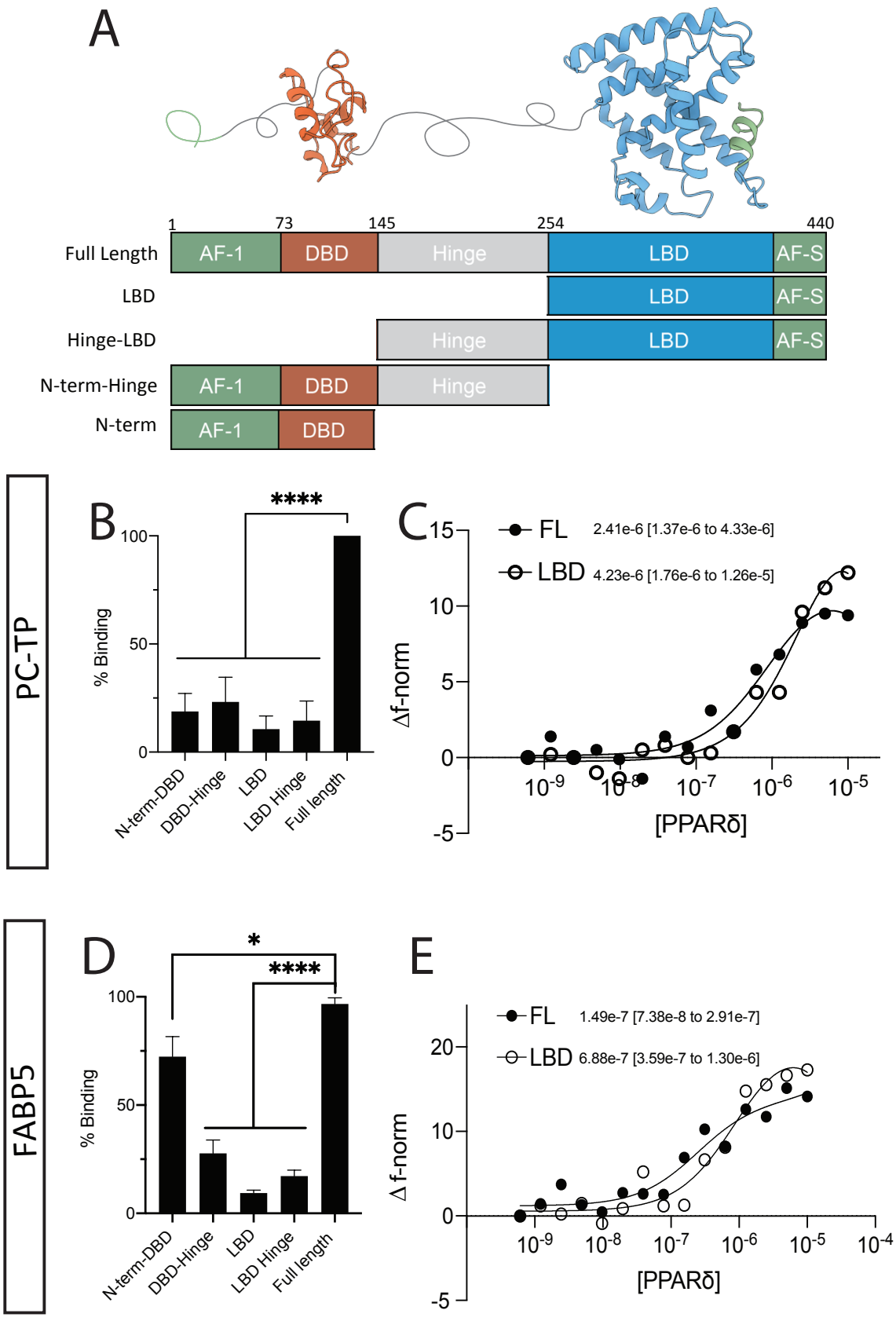
A
1
73
145
254
440
Full Length
AF-1
DBD
Hinge
LBD
AF-S
LBD
Hinge-LBD
N-term-Hinge
N-term
PC-TP
B
****
% Binding
100
50
0
N-term-DBD
DBD-Hinge
LBD
LBD Hinge
Full length
C
FL 2.41e-6 [1.37e-6 to 4.33e-6]
LBD 4.23e-6 [1.76e-6 to 1.26e-5]
Δf-norm
15
10
5
0
-5
10-9
10-8
10-7
10-6
10-5
[PPARδ]
FABP5
D
*
****
% Binding
100
50
0
N-term-DBD
DBD-Hinge
LBD
LBD Hinge
Full length
E
FL 1.49e-7 [7.38e-8 to 2.91e-7]
LBD 6.88e-7 [3.59e-7 to 1.30e-6]
Δ f-norm
20
10
0
-5
10-9
10-8
10-7
10-6
10-5
10-4
[PPARδ]

Figure 2- 10: Mapping the PC-TP/FABP5 – PPARδ interacting domains.
A) Homology model of full length PPARδ generated using the structure of full length PPARy. Schema of the modular structure of PPARδ with representative domain truncations used in subsequent PCA experiments **B & D)** To determine the locus of PPARδ interaction with PC-TP or FABP5 respectively we utilized our nano-PCA in HUH7 cells. (n= 6, One-way ANOVA, SEM). **C & E)** Temperature related intensity changes (TRIC) traces on 50 nm Cy5 NHS labeled PC-TP or FABP5 titrating in PPARδ Full length (FL) or ligand binding domain (LBD) (n=3).

2.3.5 Altered lipid levels modulate the interaction between PC-TP or FABP5 with PPARδ

As shown using purified components, the PPARδ-LBD is required for PC-TP interaction, and our *in vivo* data suggests modulation of hepatic PPARδ could be dependent on lipid availability. This is in line with idea that PC-TP may sense or channel a ligand to PPARδ, and we hypothesized that the interaction could be dependent on PC-TP binding to a lipid ligand. To test this, we either lowered the concentration of exogenously supplied lipids via serum starvation or grew cells in media depleted of methionine and choline and interrogated complex formation by performing Bioluminescence Resonance Energy Transfer (BRET) assays. (Mo and Fu, 2016) The PC-TP–PPARδ interaction was increased in the serum restricted condition when compared to cells cultured in full media (Figure 2-11A). This increase in the PC-TP–PPARδ interaction is juxtaposed by a decrease in the interaction between FABP5 and PPARδ (Figure 2-12A). In line with our hypothesis that the interaction between PC-TP and PPARδ is modulated by ligand, we see enhanced repression of PPARδ activity when cells are restricted of serum (Figure 2-12B). While serum starvation increased PC-TP–PPARδ complex formation, culturing cells in MCD media ablated the interaction (Figure 2-11A). PC-TP preferentially binds PCs with medium-length, saturated SN1 acyl chains and long, polyunsaturated SN2 acyl-chains. (Kasurinen et al., 1990; Roderick et al., 2002) We therefore used targeted lipidomic analysis to profile PC levels in ER from livers isolated from *Pctp*$^{-/-}$ fed either HFD or ND which showed PC-TP dependent PC changes, in particular PC (36:4) (Figure 2-11B) (Figure 2-12C).

1.3.5 Ligand binding and transfer enhance PC-TP–PPARδ complex formation

To understand how PC-TP interacts with its preferred ligand, we solved the structure of PC-TP bound to PC (16:0/20:4) to 2.18 Å, which contains an arachidonoyl acyl chain in the SN2 position (PDB:7U9D) (Table 2-1). PC-TP adopted the expected STARD fold consisting of nine antiparallel

beta sheets with four alpha helices. Our structure revealed clear electron density to guide the modeling of the bound ligand (Figure 2-11 C-D). The PC (16:0/20:4) phosphate group is coordinated by Tyr72, Arg78, and Gln157. Whereas the quaternary ammonium on the choline head group is stabilized by an aromatic cage consisting of Trp101, Tyr114, Tyr116, and Tyr155 (Figure 2-11 E). Using this structure, we designed mutations to reduce phospholipid binding (R78E, R78A and Y114R). Mutating Arg78 to glutamic acid (R78E) introduces a charge repulsion with the lipid phosphate group that would displace PL binding, where mutation of Arg78 to alanine (R78A) may have a more subtle effect by neutralizing the charge rather than introducing charge repulsion. We also mutated Y114 to an arginine to disfavor PC binding through charge repulsion. In addition to the structure guided mutations, we also tested a mutation previously shown to reduce PC transfer (R120H).(Joost, 2011; Pan et al., 2006)

Protein complementation assays in HUH7 cells, Y114R, R78E, and R120H all decrease the interaction between PC-TP and PPARδ by ~45% relative to wild-type PC-TP. The R78A mutation has a lesser effect, maintaining ~85% interaction compared to WT PC-TP (Figure 2-11F). Using in-cell luciferase reporter assays, we assessed the ability of these mutants to suppress PPARδ-driven transactivation. In agreement with our nano-PCA data, mutants that retained PC binding demonstrate similar levels of repression to that of WT PC-TP, while mutations that attenuate the PC binding have an attenuated affect (Figure 2-11G).

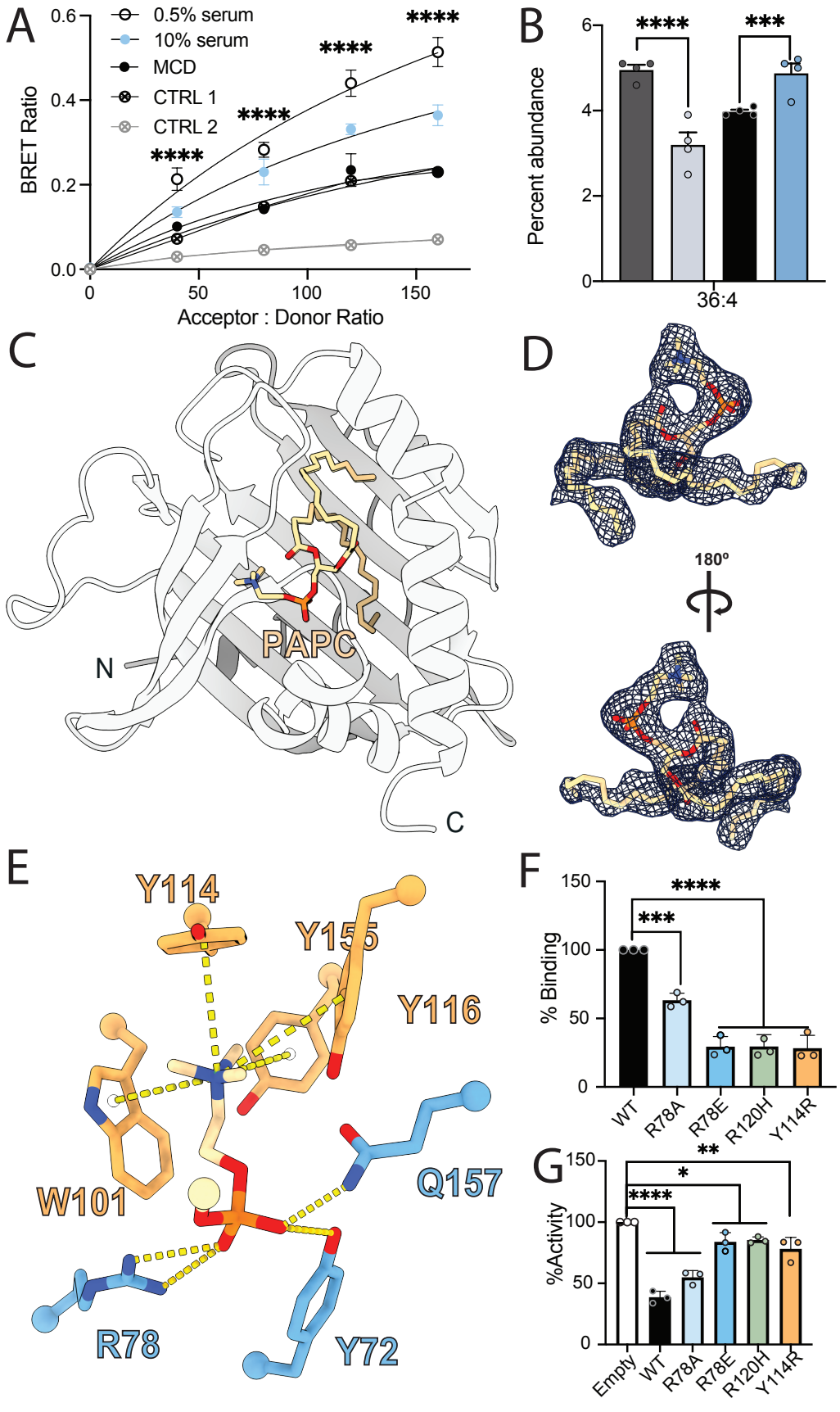
A
0.5% serum
10% serum
MCD
CTRL 1
CTRL 2
BRET Ratio
Acceptor : Donor Ratio
****
B
Percent abundance
36:4
****
***
C
PAPC
N
C
D
180°
E
Y114
Y155
Y116
W101
Q157
R78
Y72
F
% Binding
WT
R78A
R78E
R120H
Y114R
G
%Activity
Empty
WT
R78A
R78E
R120H
Y114R

Figure 2- 11: Lipid dependence of PC-TP – PPARδ interaction.

A) BRET data performed in HUH7 cells confirms the PC-TP- PPARδ complex formation and a slight increase in serum starved HUH7 cells (n=3, 2-way ANOA, SEM). CTRL 1 corresponds to Venus-PPARδ with empty N-Luc, CTRL 2 corresponds to N-Luc-PC-TP with empty Venus. **B)** Lipidomic profiling of the PC species isolated from ERs of livers from *Pctp*$^{-/-}$ on normal diet (ND) or high fat diet (HFD) reveals changes in PC 36:4 (PAPC) (n=4, Two-way ANOVA, SEM). **C)** 2.18 Å structure of PC-TP in complex with PC 36:4 (PAPC) used to design proposed mutations to alter PC-TP PC binding. **D)** Polder map (sigma=3) showing ligand density associated with PC36:4 (PAPC) bound to PC-TP **E)** Sidechains known to form an aromatic cage around the choline head group (shown in melon) and residues that coordinate the phosphate backbone (baby blue) hydrogen bonds (cut off of 3.5 Å) **F)** To determine the requirement of PC-TP PC binding on the interaction with PPARδ interaction with PC-TP, Nano-PCA was performed in HUH7 cells cultured in 0.5% serum using mutants under serum starvation conditions to show a dependence on PC-TP PC binding and transfer (n=3, One-way ANOVA, SEM). **G)** To determine if mutants retain the ability to inhibit PPARδ, we performed luciferase reporter assays in HUH7 cells cultured in serum starvation conditions suggesting that reducing PC-TP PC binding or transfer ablates the ability to suppress the activity of PPARδ (n=3, One-way ANOVA, SEM).

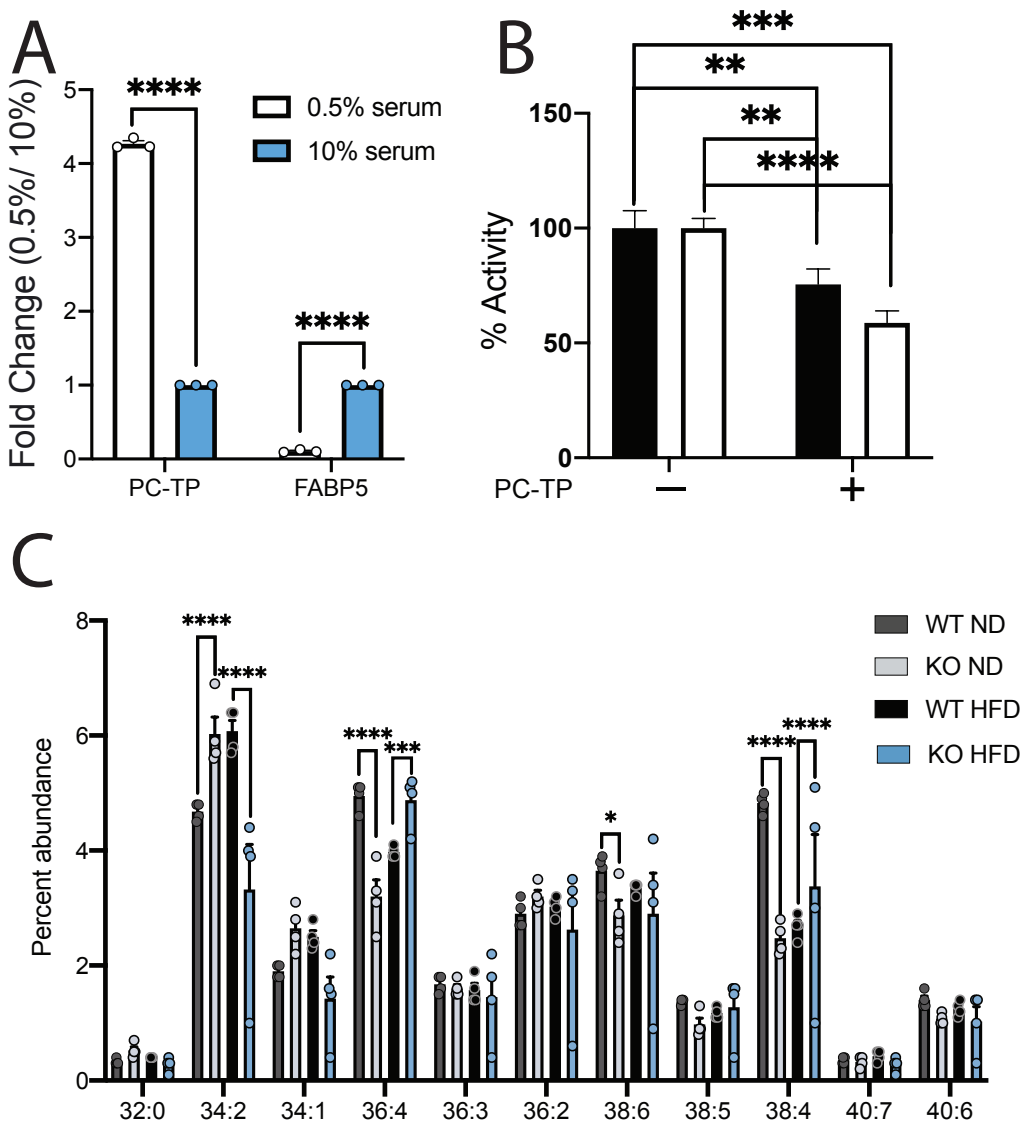

Figure 2- 12: Additional evidence of ligand mediated repressive complex.

A) PC-TP-PPARδ or FABP5- PPARδ interaction detected in HUH7 cells using nano-PCA, was significantly altered by restricting serum (n=4, T-Test, SEM.) **B)** Luciferase reporter data performed in HUH7 cells confirms the PC-TP repression of PPARδ activity with a slight decrease in PPARδ activity in serum starved HUH7 cells (n=4, T-Test, SEM.). **C)** Lipidomic profiling of the PC species isolated from livers of *Pctp*$^{-/-}$ on normal diet (ND) or high fat diet (HFD) reveals changes in select PCs (n=4, Two-way ANOVA, SEM)

Table 2- 1 Data collection and refinement statistics.

Data Collection	
Resolution range (Å)	50.000 - 2.185 (2.263 - 2.185)
Space group	I 4 2 2
Unit cell **a,b,c (Å)** **A,B,C (°)**	 133.1, 133.1, 83.2 90, 90, 90
Total reflections	5074487
Unique reflections	19663 (1906)
Completeness (%)	99.5 (98.1)
Mean I/sigma(I)	27.2 (1.7)
Wilson B-factor	61.4
CC1/2	1.0 (0.75)
Refinement	
Resolution	50.0 -2.18
Reflections used in refinement	19605 (1888)
Reflections used for R-free	980 (93)
R-work	0.2322 (0.50)
R-free	0.2433 (0.48)
Number of non-hydrogen atoms	1767
macromolecules	1667
ligands	60
solvent	40
Protein residues	203
RMS (Å)	0.01
RMS(°)	1.6
Ramachandran favored (%)	94%
Ramachandran allowed (%)	6%
Ramachandran outliers (%)	0%
Rotamer outliers (%)	8%
Clashscore	7
Average B-factor	85.3
macromolecules	86.1
ligands	74.3
solvent	76.6

Statistics for the highest-resolution shell are shown in parentheses.

2.4 Discussion:

Our transcriptomic analysis of livers isolated from the previously established *Pctp*$^{-/-}$ mouse fed either normal diet (ND) or methionine and choline depleted (MCD) diet demonstrates a clear effect of both the knockout and MCD diet on PPAR activity. This analysis also suggests that PC-TP regulation of PPARδ is altered depending on diet, as MCD led to a more dramatic change in the transcriptome compared to ND fed mice. Pathway analysis comparing the effect of diet within each genotype showed changes in PPARδ controlled processes for both CHEA and KEGG analysis that was not present in PCTP $^{-/-}$ mice, suggesting that differential PPARδ regulation in response to dietary changes requires the presence of PC-TP. Given that PPARα and PPARδ share a highly conserved DNA binding element and have differential occupancy at overlapping gene targets depending on nutrient status, ontology analysis may be skewed to show PPARα as a result of being the more thoroughly studied member of the PPAR family.(Sommars et al., 2019)

Hepatic *Pctp* KD resulted in increased insulin and glucose sensitivity with decreases in weight gain, and lipid accumulation in the liver and skeletal muscle under high fat diet feeding. This change occurred in absence of any significant alteration in food or water intake. Our characterization of the L-*Pctp*$^{-/-}$ showed that a reduction in PC-TP levels not only improved liver health but also had an effect on the muscle lipid content in line with previous reports of a hepatic PPARδ-PC-muscle axis. In the liver, PPARδ controls autophagy and metabolism in the fed state and inflammatory response.(Fan et al., 2017; Gou et al., 2020) However, many of the beneficial metabolic effects associated with activation of hepatic PPARδ has been ascribed to its role in modulating liver-skeletal muscle communication. This phenomenon is regulated by a specific PC (PC (18:0/18:1)) known to be generated in the liver by processes transcriptionally controlled by PPARδ.(Liu et al., 2013) In the muscle, PC 18:0/18:1 activates PPARα, culminating in increased

fatty acid uptake and utilization. The consequences of this liver-skeletal muscle axis controlled by PPARδ is increased endurance during exercise, sensitization to glucose and insulin, and a decrease in lipid content in both the liver and the muscle. (Fan et al., 2017; Liu et al., 2013)

While much of our mouse model phenocopied aspects of PPAR activation, we did not observe a characteristic increase in fatty acid oxidation as indicated by the respiratory ratio, or energy expenditure. However, we observed a decrease in lipid accumulation in all tissues as determined via EchoMRI and lipid profiling of liver, muscle and serum. This global decrease in lipid accumulation indicates that fatty acid homeostasis has been altered in ways that may mitigate hepatic lipotoxicity.

We show using both nanoPCA and BRET, that PC-TP and FABP5 interact directly with PPARδ in cells and that the PPARδ LBD is sufficient for this interaction *in vitro* as measured by TRIC. In cells, both PC-TP and FABP5 interact with intact PPARδ greater than the isolated LBD; however, this could be partly explained by differences in PPARδ LBD localization since it lacks a nuclear localization sequence. In cell, PPARδ-LTP interaction may also be stabilized by PTMs, endogenous ligands or other interacting partners that are not recapitulated with the bacterially expressed and purified proteins. Combining these observations with luciferase reporter and qPCR assays, we show PC-TP negatively regulates PPARδ mediated transactivation. We hypothesized that ligand binding and possibly transfer are required for productive interaction between PC-TP and PPARδ. This hypothesis is supported by our mutants aimed at altering PC binding (R78A, R78E, Y114R) and transfer (R120H), as these mutants attenuated the interaction and the complimentary repressive phenotype. Serum starvation increased formation of the PC-TP–PPARδ complex and enhanced PPARδ repression suggesting that this interaction is sensitive to nutrient availability. Serum starvation had the opposite effect on the FABP5 – PPARδ interaction. This

result suggests that these two LTPs play opposing roles in modulating PPAR function. Taken together our data points to a new role of PC-TP in regulating liver health via modulating PPARδ in a ligand dependent manner. Further studies investigating which ligand modulates this interaction as well as the effect of these ligands on PC-TP/ PPARδ biology could shed light on the role of this complex in the pathogenesis of obesity.

The STARd family of proteins are characterized by their unique fold and ability to bind and transfer hydrophobic ligands. Members of this family range in complexity from the minimal start domain (e.g. PC-TP) to multidomain proteins, such as STARD14 (THEM1). In these complex multidomain proteins, the start domain acts as a sensor that is capable of relaying ligand binding information to other domains to tune activity. (Tillman et al., 2020) PC-TP is capable of relaying ligand binding information to control the activity of interacting proteins such as THEM2 or PAX3. (Kanno et al., 2007) PC-TP increases the thioesterase activity of THEM2 which antagonizes fatty acid shuttling into the mitochondria by cleaving activated fatty-acyl-CoA species into NEFA. (Kang et al., 2012; Kang et al., 2009) Interestingly, knockout of PC-TP, but not THEM2, increases the expression of PPAR target genes, suggesting repression of PPAR activity is PC-TP specific.(Kawano et al., 2014)

Our data suggests that PC-TP interacts with PPARδ and regulates transcriptional activation in response to dietary alterations (Figure 8). Further work is required to characterize the consequence of the PC-TP–PPARδ signaling in other tissues as well as the role of other START domain-containing proteins in modulating PPARs, or other lipid binding nuclear receptors.

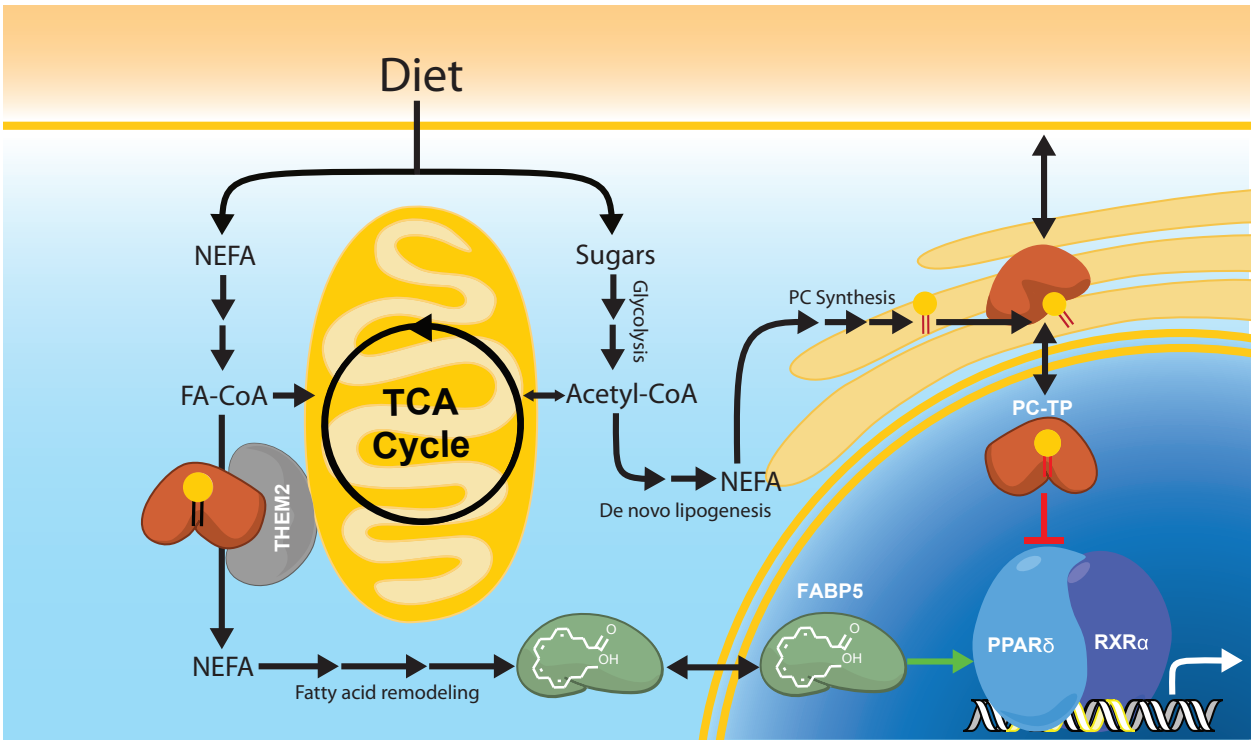

Figure 2- 13: Cellular context for a LTP-PPARδ Axis.

Here we outline the novel mechanism by which PC-TP may regulate PPARδ activity. Diet supplies a myriad of nutrients from carbohydrates to lipids. Fats from diet are transported throughout the body in lipoprotein particles. Once liberated by various lipases these non-esterified fatty acids (NEFA) are then absorbed by cells where they are either used as an energy source, incorporated into other fatty acid species, or remodeled into signaling moieties such as eicosanoids, leukotriene, and thromboxane. Sugars are broken down in the cytosol via glycolysis, the products of which can be utilized as building blocks for a number of macromolecules or further metabolized in the mitochondria to produce more energy. FABP5 (shown in green) binds polyunsaturated fatty acids, derived from diet, which can lead to nuclear localization where it increases PPARδ transactivation of genes. PC-TP (shown in orange) regulates membrane fluidity via the transfer of PCs synthesized in the ER, metabolism through increasing the thioesterase activity of THEM2(shown in grey), and transcription through its novel interaction with PPARδ, characterized

here. PCs generated via de novo lipogenesis contain medium chain saturated fatty acyl chains. Whereas essential fatty acid obtained from diet contain unique desaturation states, capable of altering FABP5 localization. We hypothesize that these uniquely generated PCs species can perturb the homeostatic regulation of PPARδ culminating aspects of metabolic syndrome.

2.5 Materials and Methods:

2.5.1 Reagents

Buffers and reagents for crystallography were purchased from Sigma, Fisher, Polysciences, or Cayman, Inc. The pMCSG7-His plasmid was a gift from Dr. John Sondek (University of North Carolina, Chapel Hill), whereas Nano-PCA and BRET vectors were graciously given by Dr. Haian Fu (Emory University, Atlanta, GA).

2.5.2 Expression of PC-TP, FABP5 and PPARδ LBD and FL PPARδ

Following sequencing, vectors containing coding regions of either the PPARδ ligand binding domain (LBD) in pRSET vector, full length PPARδ in PSMT3 vector or FABP5 /PC-TP in pMCSG7 were transformed into BL21 DE3 *E. coli.* Cultures were grown in terrific broth (TB; 6 × 1.3 L) at 37°C with gentle shaking to an OD600 of 0.6, cooled to 18°C, induced with 0.5 mM isopropyl-1-thio-D-galactopyranoside (IPTG), and allowed to grow overnight. 0.01% soy lecithin was added to PC-TP cultures at induction to help increase protein yield. Similarly, 100 mM ZnSO4 was added to growths of full length PPARδ to aid in correct folding of zinc finger domain. The next morning cells were spun down at 3500 x g for 20 min. Pellets were frozen at -80 °C until purification.

2.5.3 Purification of PC-TP and FABP5

Pellets were thawed, homogenized, and lysed in 150 mM NaCl, Tris–HCl pH 7.4 supplemented with 5% glycerol, 25 mM imidazole, 5 mM β-mercaptoethanol, 100 μM PMSF, DNAse A, and lysozyme. The lysate was then spun down at 18,000 x g for 60 min and the supernatant was isolated before being loaded onto an immobilized metal affinity chromatography (IMAC) column with the following buffers: buffer A (150 mM NaCl, 20 mM Tris, 20 mM imidazole, 5% glycerol, pH 7.5) and buffer B (150 mM NaCl, 20 mM Tris 250mM imidazole, 5

% glycerol, pH7.5). Fractions containing PC-TP or FABP5 were then pooled, run on a superdex 75pg 16/60 size exclusion column (20 mM HEPES, pH 8.2, 200 mM NaCl, 0.05% tween-20 and 0.5 mM TCEP), and frozen at -80 °C.

2.5.4 Purification of PPARδ

PPARδ was expressed in *E. coli.* and purified as previously described.(Wu et al., 2017) Growth conditions and pellet processing were identical to PC-TP, except PPARδ pellets were lysed with a buffer containing 50 mM HEPES, pH 8.0, 500 mM ammonium acetate, 20 mM imidazole, 1% triton x100, 10% [v/v] glycerol and 10 mM β-mercaptoethanol. IMAC purification was performed using buffer A (50 mM Tris-HCl, pH 8.0, 500 mM ammonium acetate, 20 mM imidazole, 10% [v/v] glycerol and 10 mM β-mercaptoethanol) and buffer B (50 mM Tris-HCl, pH 8.0, 500 mM ammonium acetate, 250 mM imidazole, 10% [v/v] glycerol and 10 mM β-mercaptoethanol). The full length PPARδ was further purified using ion affinity chromatography. Briefly, following IMAC column fractions containing full length PPARδ were diluted to a salt concentration of ~150 mM and further purified using tandem Capto S and Capto Q columns, collecting fractions from the Q column. Both full length PPARδ and the LBD were then further purified using exclusion chromatography via Superdex 75pg 16/60 with a running buffer containing 20 mM HEPES, pH 8.3, 200 mM NaCl, 0.05% tween-20 and 0.5 mM TCEP.

2.5.5 Protein crystallization, data collection, and structure determination

PC-TP was concentrated to 15 mg/mL. Crystals were grown by hanging drop vapor diffusion at 18 °C in drops containing 1 µL of PC-TP and 1-2 µL of well buffer containing 3.4-3.8 M sodium formate and 0.1 mM sodium acetate, pH 5.7. Crystals grew rapidly, often with significant growth overnight. Crystals were cryoprotected in well solution containing 15% glycerol and flash frozen in liquid nitrogen. Data was remotely collected from the Southeast Regional

Collaborative Access Team (SER-CAT) at the Advanced Photon Source (APS), 22ID beamline (Argonne National Laboratories, Chicago, IL). Data was processed and scaled using HKL-2000(Otwinowski and Minor, 1997) and phased by molecular replacement using Phaser-MR(Adams et al., 2010) using a previously published PC-TP structure as a reference model (PDB: 1LN1). (Roderick et al., 2002) Models were built using COOT(Adams et al., 2010; Emsley et al., 2010) and refined using PHENIX and PDB_REDO.(Joosten et al., 2009) Structures were visualized using PyMOL (Schrödinger, LLC).

2.5.6 Cloning and mutagenesis

Full length, wild-type human PC-TP (residues 1–220) was subcloned into pDONR201. Mutants R78E, R78A, Y114R, and R120H mutants were established in pDONR201 prior to subcloning into pDEST26 Nluc-PCA for luciferase reporter or Nano-PCA, respectively. Similarly, wild-type human PPARδ (residues 1-470) was subcloned into pDonr223. PPARδ truncations were first cloned into pDONR201 using BP clonase and subsequently cloned into Nano-PCA vector via LR clonase. All mutagenesis was performed using NEB Q5 site directed mutagenesis kit (New England biosciences).

2.5.7 In-vitro binding assays

PPARδ LBD or full length PPARδ was purified in assay buffer (20 mM Hepes pH 8.3, 200 mM NaCl, 5% glycerol, 0.05% tween-20, 0.5 mM TCEP) and labeled using the NHS-CY5 dye as per companies instructions.(Hatty et al.) Proteins were labeled with a Cy5 fluorophore through covalent linkage to lysine amines using the Monolith NT.115 Protein Labeling Kit RED-NHS (NanoTemper Technologies, München, Germany). PC-TP and FABP5 were exchanged into in assay buffer via dialysis. LTPs (10 μM- 610 pM) were then incubated with 50 nM Cy5-labeled full length PPARδ or PPARδ LBD over night at 4 °C before assessing binding. TRIC

measurements were taken using a Dianthus NT.23 Pico (NanoTemper Technologies, München, Germany) instrument. Data for three independent measurements were fitted with a non-linear regression model in GraphPad Prism 8.0.

2.5.8 PC-TP knockdown

SMARTpool siRNA against human PC-TP and scrambled control siRNA were purchased from Dharmacon. HUH7 cells were seeded at 35,000 cells/ well in 24-well plates and allowed to adhere overnight. Cells were transfected with siRNA using Dharmafect transfection reagent 4, at a final concentration of 25 nM siRNA and 0.6 µl transfection reagent per well. Cells were harvested 24 hrs after transfection in Trizol reagent (Invitrogen), and RNA was purified using the RNAeasy kit (Qiagen). RNA was reversed transcribed into cDNA using the High-Capacity RT kit (Applied Biosystems) prior to analysis by qPCR as described below.

For siRNA experiments with luciferase reporter assays, HUH7 cells were seeded at 7,000 cells/ well in clear-bottomed, white-welled 96 well culture plates in DMEM F12 medium supplemented with 10% charcoal-stripped FBS and allowed to adhere overnight. Cells were transfected with the siRNA described above (25 nM) together with a luciferase reporter expressing firefly luciferase under the control of a 6 x PPAR response element (100 ng) and a constitutive luciferase reporter expressing Renilla luciferase under the control of the CMV promoter (20 ng). Some cells were also transfected with full-length human PPARδ in a pSG5 vector (100 ng). Transfections used Dharmafect Duo transfection reagent (0.2 µl per well). Luciferase signal was measured 24 hrs after transfection using the Dual-Glo kit as described below.

2.5.9 In cell activation assays

HUH7 cells were grown and maintained in DMEM F-12 containing L-glutamine, sodium pyruvate, and phenol red (Invitrogen) supplemented with 10% FBS (Invitrogen). Cells were

transferred into a 96-well plate and allowed to grow for one day prior to transfection. 100 ng/well pSG5 vector harboring full-length human PPARδ receptor, 100 ng/well PPAR-response element-driven firefly luciferase reporter (PPAR-response element X3-TK-luc), and 20 ng /well constitutive Renilla luciferase reporter (phRLtk) in the presence or absence of 25 ng/ well wild-type or mutant variant human PC-TP cloned into the pDEST26 vector was added to FuGENE HD in Opti-MEM (Invitrogen). 4 µl of this solution was used to transfect 60-70% confluent cells overnight. 24 hrs post transfection, media was changed to either fresh culture media, DMEM F-12 containing either 10% serum or 0.5% serum and assayed with Dual-Glo luciferase substrate (Promega). Cells that were starved of serum were grown in culture media containing 0.5% FBS for 24 hrs before reading. Firefly activity was divided by Renilla activity to account for cell number, viability, and transfection efficiency. Data was collected on a NEO plate reader from BioTek(Winooski, VT, USA) using the Gen 5 software and processed in Graphpad prisim.

2.5.10 RNAseq analysis and Quantitative PCR

Total RNA was isolated from liver (10 µg) or cells using miRNeasy (QIAGEN, Hilden, Germany) following manufacturer's instructions. cDNA was synthesized with a High-Capacity cDNA Reverse transcription Kit (Applied Biosystems, Foster City, CA, USA). RNA quality was assessed via agarose gel and nanodrop prior to library preparation and transcriptome sequencing was conducted by Novogene Co., LTD (Beijing, China). Genes with adjusted p-value < 0.05 and $|\log2(\text{FoldChange})| > 0$ were considered as differentially expressed. Relative mRNA expression was also determined by quantitative PCR using SYBR Green Real-Time PCR Master Mix (QIAGEN, Hilden, Germany). Equal amounts of cDNA samples were subjected to qPCR a using StepOnePlus (Applied Biosystems, Foster City, CA, USA) in a 96-well plate. mRNA isolated from cells were analyzed relative to Thyroxine-binding globulin (TBG), whereas, arrays were analyzed

per manufactures instruction.(Arikawa et al., 2010) Qiagen RT2 custom arrays (CLAM28936C) layout and information is presented in Table 2-2. The nucleotide sequences of oligonucleotides used for qPCR are presented in Table 2-3.

Table 2- 2: Layout of custom RT2 microarray CLAM28936C.

	1	**2**	**3**	**4**	**5**	**6**	**7**	**8**	**9**	**10**	**11**	**12**
A	Acaa2	Acsl1	Acsl3	Angptl4	Acaa2	Acsl1	Acsl3	Angptl4	Acaa2	Acsl1	Acsl3	Angptl4
B	Cpt1a	Ech1	Etfdh	Fabp3	Cpt1a	Ech1	Etfdh	Fabp3	Cpt1a	Ech1	Etfdh	Fabp3
C	Fabp1	Fabp4	Hif1a	Hmgcs2	Fabp1	Fabp4	Hif1a	Hmgcs2	Fabp1	Fabp4	Hif1a	Hmgcs2
D	Ilk	Klf10	Mlycd	Ncoa6	Ilk	Klf10	Mlycd	Ncoa6	Ilk	Klf10	Mlycd	Ncoa6
E	Pdpk1	Ppard	Ppargc1a	Pten	Pdpk1	Ppard	Ppargc1a	Pten	Pdpk1	Ppard	Ppargc1a	Pten
F	Rxrg	Slc7a1	Slc27a4	Scd1	Rxrg	Slc7a1	Slc27a4	Scd1	Rxrg	Slc7a1	Slc27a4	Scd1
G	Actb	B2m	Gapdh	Gusb	Actb	B2m	Gapdh	Gusb	Actb	B2m	Gapdh	Gusb
H	Hsp90ab1	GDC	RTC	PPC	Hsp90ab1	GDC	RTC	PPC	Hsp90ab1	GDC	RTC	PPC

Table 2- 3: Sequences of oligonucleotides used for qPCR are presented.

Gene	Primer direction	Sequence (5'-3')
ADRP	forward	TGTGAGATGGCAGAGAACGGT
ADRP	reverse	CTGCTCACGAGCTGCATCATC
HMGCS2	forward	GGAACCCATATGGAGAATGTGT
HMGCS2	reverse	ATCGCTGCCAGCTTGCTT
PPARD	forward	GTCACACAACGCTATCCGTTT
PPARD	reverse	AGGCATTGTAGATGTGCTTGG
MCAD	forward	TTCCAGAGAACTGTGGAGGTCTT
MCAD	reverse	TCAATAGCAGTCTGAACCCCTGT
PEPCK	forward	TGCATGAAAGGTCGCACCA
PEPCK	reverse	CACAGAATGGAGGCATTTGACA
ANGPLT4	forward	GATGGCTCAGTGGACTTCAACC
ANGPLT4	reverse	CCCGTGATGCTATGCACCTTC
LPCAT3	forward	TGGGCCGCACCATCAC
LPCAT3	reverse	AGTTGCCGGTGGCAGTGTA
ACSL4	forward	CCCTGAAGGATTTGAGATTCACA
ACSL4	reverse	CCTTAGGTCGGCCAGTAGAAC

2.5.11 In cell protein complementation assays

HUH7 cells were maintained in DMEM F-12 containing 10% FBS. Cells were then transferred into a 96-well plate and grown for 24 hrs. For nano-PCA assays, cells were then transfected with 100 ng/well of WT or mutant human PC-TP or FABP5 in a Nluc-PCA vector, 100 ng/well of WT or mutant PPARδ were added to FUGENE HD in Opti-MEM. 24 hrs post transfection, media was changed to either fresh culture media, DMEM F-12 containing 0.5% serum and assayed using nano-glo luciferase substrate (Promega). Controls include empty Nluc-PCA vector mixed with either LTP or PPARδ to account for nonspecific interaction. Signal from the interaction was normalized to the highest signal from a negative control.

2.5.12 Animals and diets

Tissue specific knockdown mice were created (Institute of Model Animal, School of Medicine, Wuhan University, Wuhan, China; Dr. Hongliang Li, Director) using a LoxP/Cre system C56BL6 background mice with *Pctp* flanked by two LoxP sites ($Pctp^{flox/flox}$) using a CRISPR/Cas9 set up (Supplemental Figure 5). $Pctp^{flox/flox}$ were transduced with AAV8 harboring a vector for Cre recombinase driven by the TBG promoter to generate hepatocyte specific deletion of $Pctp^{-/-}$ ($L\text{-}Pctp^{-/-}$). Similarly, control mice were treated with equivalent titer of empty AAV8. These mice were viable and displayed no apparent developmental abnormalities. Knockdown efficiency was assayed via western blot, comparing liver and kidney isolated from KO and control mice. Mice were housed in a barrier facility on a 12 hr light/dark cycle with free access to water and diet. Male mice were weaned at 4 weeks of age and fed chow (PicoLab Rodent Diet 20; LabDiet, St. Louis, MO, USA). Alternatively, 5 week-old-male mice were fed a HFD (D12492: protein 20 % kcal, fat 60 % kcal, carbohydrate 20 % kcal, energy density 5.21 kcal/g; Research

Diets Inc., New Brunswick, NJ, USA) for 12 weeks. Following 6 hr fasting (9:00 AM to 3:00 PM) or 18 hr fasting (6:00 PM to 12:00 PM), 17-week-old mice were euthanized and plasma was collected by cardiac puncture. Tissues were harvested for immediate use or snap frozen in liquid nitrogen and stored at -80 °C. Mice were monitored by daily health status observation by technicians supported by veterinary care. Housing and husbandry were conducted in facilities with a sentinel colony health monitoring program and strict biosecurity measures to prevent, detect, and eradicate adventitious infections. Animal use and euthanasia protocols were approved by the Institutional Animal Care and Use Committee of Weill Cornell Medical College.

A

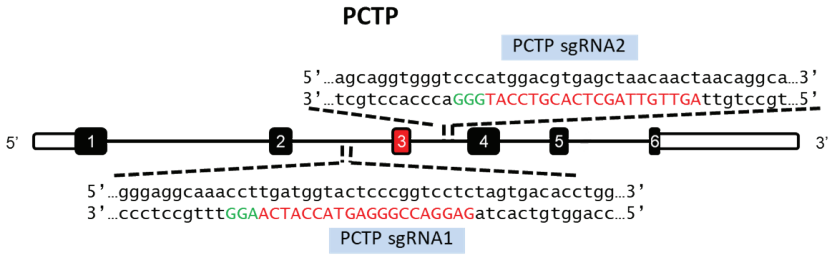

B

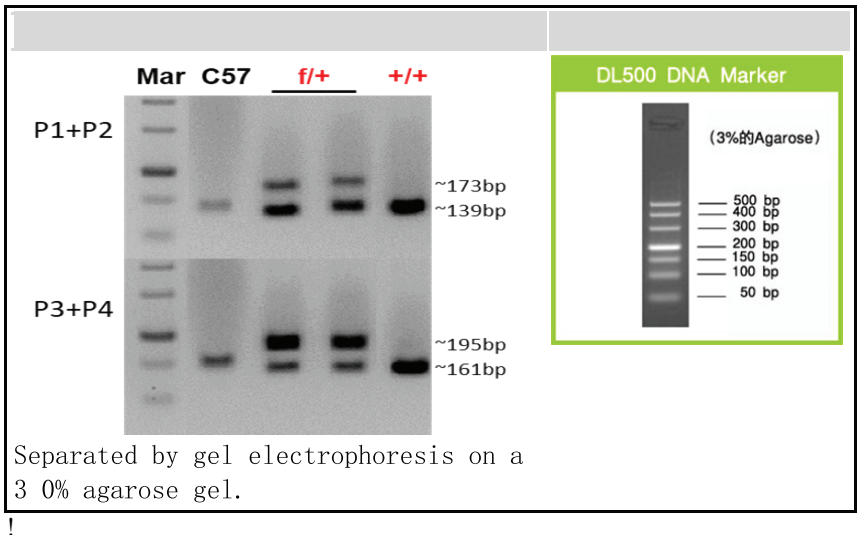

!

Primer	Expected Results:
P1+P2	Wild type = ~139 bp; Heterozygote = ~139 bp & 173 3=; Mutant = ~229 3=
P3+P4	Wild type = ~161 bp; Heterozygote = ~161 bp & 195 3=; Mutant = ~195 3=

Figure 2- 14: Generation of the Pctpflox/flox mouse.

A)The guide RNAs targeting specific loci in the genome will guide Cas9 enzyme to the locus and cause DNA double strain break (DSB). Homologous recombination (HR) will enable the donor fragment (single-stranded DNA oligos) which contains loxP sites to integrate into the breaking

locus. These mice possess loxP sites on either side of exon 3, which encodes the DNA binding domain. Mice that are homozygous for this allele are viable, fertile, normal in size and do not display any gross physical or behavioral abnormalities. When these mutant mice are bred to mice that express Cre recombinase, resulting offspring will have exon 3 deleted in the cre-expressing tissue(s).A pair of crispr/cas9 guideRNA constructs that were specifically targeted to PCTP intron 2 **B)** Validation of generation of the *Pctp*$^{flox/flox}$ mouse.

2.5.13 Endurance stress test

Male mice were acclimated to treadmill running tracks incrementally for 5 days starting from 10 min at 0.3 km/hr to 60 min at 1.2 km/hr. To determine maximal exercise capacity, treadmill speed was started at 0.3 km/hr and increased 0.3 km/hr every 3 min until the speed reached 1.2 km/hr. The speed was kept constant (1.2 km/hr) until mice reached exhaustion. Measuring the time and distance mice ran till they fell off the treadmill.

2.5.14 Metabolic monitoring

Mice were housed in individual cages for 1 week for acclimation prior to metabolic monitoring(Krisko et al., 2020) Mice were then housed in temperature-controlled cabinets with a 12 hr light/dark cycle and monitored using the Promethion Metabolic Screening System (Sable Systems International, North Las Vegas, NV). Rates of O_2 consumption (VO_2) and CO_2 production (VCO_2) were determined at 5 min intervals. Values of respiratory exchange ratio (RER) were calculated as VCO_2/VO_2. After 2 days acclimation, metabolic parameters were recorded over 24 hrs with or without a running wheel inside the cage. Physical activities and voluntary running on wheel were determined according to beam breaks within a grid of photosensors built outside the cages. Energy expenditure was calculated by indirect calorimetry and adjusted by ANCOVA using VassarStats to adjust for differences in lean body mass using lean body composition determined by magnetic resonance imaging EchoMRI (EchoMRI, Houston, TX).

2.5.15 Tolerance tests

Glucose tolerance tests (GTT), insulin tolerance tests (ITT), and pyruvate tolerance tests (PTT) were performed with minor modifications. In brief, mice were fasted 6 hr for GTT, 4 hr for ITT, and overnight (16 hr) for PTT. A drop of blood from the tail tip was subjected to glucose measurement at baseline and at regular intervals using GE 100 Blood Glucose Monitor (General

Electric, Ontario, CA). Glucose solution was administered by oral gavage with 1.5 g/kg for *L-Pctp*$^{-/-}$ mice and their littermate controls. Insulin solution was administered by intraperitoneal injection with 0.75 U/kg for *L-Pctp*$^{-/-}$ mice, and littermate controls. Pyruvate solution was administered by Gavage with 2 g/kg for *L-Pctp*$^{-/-}$ mice and littermate controls.

2.5.16 Immunoblot analysis

Immunoblot analyses were performed by standard techniques. Briefly, tissues or cells were homogenized in a RIPA buffer containing cOmplete Protease Inhibitor Cocktail and PhosphoSTOP Phosphate Inhibitor Cocktail Tablets (Roche, Indianapolis, IN, USA) using a Bead Ruptor 24 Elite bead mill homogenizer (Omni International, Kennesaw, GA, USA). Protein concentrations were determined by using a BCA reagent (Thermo Fisher Scientific, Springfield Township, NJ). Equal amounts of protein samples were separated by SDS-PAGE and transferred to nitrocellulose membranes for immunoblot analysis. Membranes were incubated with primary antibodies (Suppl. Table 3) overnight and probed with respective secondary antibodies (Dako-Agilent, Santa Clara, CA, USA) for 1 hr. Bands were then developed using enhanced chemiluminescence (SuperSignal West DURA, Thermo Fisher Scientific, Springfield Township, NJ, USA) and imaged by ChemiDoc XRS+ (BioRad, Hercules, CA, USA).

2.5.17 Histopathology

Freshly harvested tissues from 17-week old mice were immersed in 10% neutralized formaldehyde for 2 days. Following a paraffin embedding, sectioned tissues were stained with Hematoxylin and Eosin by the Laboratory of Comparative Pathology, Memorial Sloan Kettering Cancer Center, NY, USA. Slides were visualized using an Eclipse Ti microscope (Nikon, Tokyo, Japan).

2.5.18 Tissue triglyceride concentrations

Lipids were extracted from frozen specimens with a mixture of chloroform/methanol (2:1) using Folch's method as previously described.(Alves-Bezerra et al., 2019) Concentrations of triglycerides were assayed enzymatically (FUJIFILM Wako Diagnostics, Mountain View, CA).

2.5.19 Plasma assays and fast protein liquid chromatography

Enzymatic assay kits were used to measure plasma concentrations of triglycerides, free fatty acids, total cholesterol, free cholesterol, phospholipid (FUJIFILM Wako Diagnostics, Mountain View, CA), ß-hydroxybutyrate (Stanbio Laboratories, Boerne, TX), aspartate aminotransferase, alanine aminotransferase (Infinity AST/ALT, Thermo Scientific, Waltham, MA, USA) and creatine kinase (Stanbio CK Liqui-UV Test, EKF Diagnostics, Cardiff, UK). Plasma concentrations of insulin were measured by using an ELISA kit (Crystal Chem, Downers Grove, IL), according to the manufacturer's protocol. Equal volumes of plasma were pooled from 5 mice and lipoproteins were fractionated by fast protein liquid chromatography (ÄKTA pure FPLC system, GE Healthcare, Pittsburgh, PA, USA) and triglyceride and cholesterol in fractions quantified with reagent kits (Wako Diagnostics, Mountain View, CA) as previously performed.

2.5.20 Lipidomic analysis on isolated endoplasmic reticulum

To characterize phospholipids in mouse liver endoplasmic reticulum (ER), ER was first isolated by density centrifugation according to a Nature Protocols method.(Wieckowski et al., 2009) Briefly, 500 mg of mouse liver was homogenized in 1 mL ice cold PBS, pH 7.4 using a glass, mortar and pestle style homogenizer. The homogenate was then centrifuged for 5 min at 740 x g and the pellet was discarded. The resulting supernatant was collected and further centrifuged for 10 min at 9,000 x g. The pellet, containing crude mitochondria was discarded, and the supernatant, which contains the ER, was centrifuged for 30 min at 20,000 x g. In the final step, the resulting supernatant was centrifuged for 1 hr at 100,000 x g to pellet purified ER. All

centrifugation steps were performed at 4 °C. Lipids were then extracted from the ER fraction. For this, the pellet was resuspended in 1 mL 2:1 methanol:chloroform [v/v]. The sample was then mixed in a stand vortexer for 15 min. To separate phases and aid in the partition of zwitterionic lipids to the organic phase, 0.5 mL 0.1 mM NaCl was added. The aqueous phase was removed, and the organic phase was retained then subsequently dried under a gentle nitrogen stream. Extracted lipids were reconstituted in 500 µL 1:1 methanol:chloroform.

Targeted lipidomics was performed using a Sciex QTrap 3000 (Framingham, MA, USA), whereby lipids were directly infused into the mass spectrometer using a syringe pump at a flow rate of 5 µL /min. Instrumental parameters, were electrospray voltage (-3500 kV), collision energy (-30 eV), and declustering potential (-70 arb units) were optimized using analytical grade standards, di17:0 phosphatidylcholine (PC) and phosphatidylethanolamine (PE), both purchased from Avanti Polar Lipids. The distribution of lipids in ER was determined by shotgun lipidomics. For this, phosphatidylcholine species were identified by conducting precursor ion scanning for m/z 184 in the positive ion mode, which corresponds to the mass of the phosphocholine head group. Similarly, PE was detected by precursor ion scanning for m/z 196 in the negative ion mode. For each precursor ion scan, resulting peaks with signal to noise ratio greater than 5 were fragmented for characterization. However, quantification of identified species was achieved using the area under the curve from precursor ion scans. A phospholipid profile was then generated and used to establish differences in distributions.

2.5.21 Rates of fatty acid oxidation

Rates of fatty acid oxidation in muscle tissues were measured by degradation of ^{14}C-palmitate (American Radiolabeled Chemicals; St. Louis, MO, USA) into ^{14}C acid soluble metabolites (ASM) and ^{14}C-labeled CO_2(Alves-Bezerra et al., 2019),(Huynh et al., 2014) Briefly,

gastrocnemius muscle strips were collected from 6 hr fasted mice. Tissues were kept on ice no longer than 30 min. Muscle tissues were minced and homogenized in a Dounce homogenizer followed by centrifugation for 10 min at 420 x g. Supernatants were transferred to microtubes containing 0.4 μCi ^{14}C-palmitate / 500 μM palmitate conjugated with 0.7 % fatty acid-free BSA and incubated at 37 °C for 30 min. ^{14}C-labeled CO_2 produced by TCA cycle was captured onto filter paper soaked with 1 M NaOH and ^{14}C-labeled ASM were separated with 1 M perchloric acid. ^{14}C-labeled CO2 in the filter paper and ^{14}C-labeled ASM in the supernatant were dissolved in Ecoscint H (National Diagnostics; Atlanta, GA, USA) and were counted using a liquid scintillation counter (Beckman Coulter; Danvers, MA).

2.5.22 Hepatic triglyceride secretion rates

Following a 12 hr fast, the lipoprotein lipase inhibitor Tyloxapol (500 mg/kg of body weight) (Sigma-Aldrich) was administered through retro-orbital injection. (Alves-Bezerra et al., 2019) Tail tip blood samples (25 μL) were collected into microtubes before Tyloxapol injection and at regular intervals for up to 2 hrs. Serum triglyceride concentrations were determined using the enzymatic assay described above. Rates of hepatic triglyceride secretion were calculated from the time-dependent linear increases in serum triglyceride concentration.

2.5.23 Statistical analyses

Data are presented as mean values with error bars representing SEM. Statistical significance was determined by using two-tailed unpaired Student's t-tests when two groups were compared. Correlations were evaluated by Pearson's correlation coefficient analysis. Threshold values were determined by segmental linear regression. Multiple group comparisons were performed using one- or two-factor ANOVA, and individual comparisons were made with Tukey HSD or Bonferroni post hoc tests. Differences were considered significant for *, $p<0.05$; **,

p<0.01; *** p<0.001;****p<0.0001. (GraphPad Prism 8, GraphPad Software, La Jolla, CA, USA).

2.6 Reference:

Adams, Paul D, Pavel V Afonine, Gábor Bunkóczi, Vincent B Chen, Ian W Davis, Nathaniel Echols, Jeffrey J Headd, L-W Hung, Gary J Kapral, and Ralf W Grosse-Kunstleve. 2010. 'PHENIX: a comprehensive Python-based system for macromolecular structure solution', *Acta Crystallographica Section D: Biological Crystallography*, 66: 213-21.

Adida, Anne, and Friedrich Spener. 2006. 'Adipocyte-type fatty acid-binding protein as inter-compartmental shuttle for peroxisome proliferator activated receptor γ agonists in cultured cell', *Biochimica et Biophysica Acta (BBA)-Molecular and Cell Biology of Lipids*, 1761: 172-81.

Alves-Bezerra, Michele, Yingxia Li, Mariana Acuña, Anna A Ivanova, Kathleen E Corey, Eric A Ortlund, and David E Cohen. 2019. 'Thioesterase superfamily member 2 promotes hepatic VLDL secretion by channeling fatty acids into triglyceride biosynthesis', *Hepatology*, 70: 496-510.

Arikawa, Emi, George Quellhorst, Ying Han, Hongguang Pan, and Jingping Yang. 2010. 'RT2 Profiler PCR Arrays: Pathway-focused gene expression profiling with qRT-PCR', *SA Biosciences Technical Article*, 11.

Armstrong, Eric H, Devrishi Goswami, Patrick R Griffin, Noa Noy, and Eric A Ortlund. 2014. 'Structural basis for ligand regulation of the fatty acid-binding protein 5, peroxisome proliferator-activated receptor β/δ (FABP5-PPARβ/δ) signaling pathway', *Journal of Biological Chemistry*, 289: 14941-54.

Chakravarthy, Manu V, Irfan J Lodhi, Li Yin, Raghu RV Malapaka, H Eric Xu, John Turk, and Clay F Semenkovich. 2009. 'Identification of a physiologically relevant endogenous ligand for PPARα in liver', *Cell*, 138: 476-88.

Davies, Sean S, Aaron V Pontsler, Gopal K Marathe, Kathleen A Harrison, Robert C Murphy, Jerald C Hinshaw, Glenn D Prestwich, Andy St Hilaire, Stephen M Prescott, and Guy A Zimmerman. 2001. 'Oxidized alkyl phospholipids are specific, high affinity peroxisome proliferator-activated receptor γ ligands and agonists', *Journal of Biological Chemistry*, 276: 16015-23.

De Gerónimo, Eduardo, Robert M Hagan, David C Wilton, and Betina Córsico. 2010. 'Natural ligand binding and transfer from liver fatty acid binding protein (LFABP) to membranes', *Biochimica et Biophysica Acta (BBA)-Molecular and Cell Biology of Lipids*, 1801: 1082-89.

Emsley, Paul, Bernhard Lohkamp, William G Scott, and Kevin Cowtan. 2010. 'Features and development of Coot', *Acta Crystallographica Section D: Biological Crystallography*, 66: 486-501.

Fan, Weiwei, Wanda Waizenegger, Chun Shi Lin, Vincenzo Sorrentino, Ming-Xiao He, Christopher E Wall, Hao Li, Christopher Liddle, T Yu Ruth, and Annette R Atkins. 2017. 'PPARδ promotes running endurance by preserving glucose', *Cell metabolism*, 25: 1186-93. e4.

Gou, Qian, Yidan Jiang, Runyun Zhang, Ying Xu, Huihui Xu, Wenbo Zhang, Juanjuan Shi, and Yongzhong Hou. 2020. 'PPARδ is a regulator of autophagy by its phosphorylation', *Oncogene*, 39: 4844-53.

Hatty, Claire, Anne Neumann, Alina Neumann, Tanja Bartoschik, Johannes Rieger, Amit J Gupta, Peter Cherepanov, and Matthew J Fuchter. 'Application of Temperature Related Intensity Change (TRIC) in biophysical drug discovery projects with Dianthus', *Target*, 2: 3.

Huang, Huan, Olga Starodub, Avery McIntosh, Barbara P Atshaves, Gebre Woldegiorgis, Ann B Kier, and Friedhelm Schroeder. 2004. 'Liver fatty acid-binding protein colocalizes with peroxisome proliferator activated receptor α and enhances ligand distribution to nuclei of living cells', *Biochemistry*, 43: 2484-500.

Huynh, Frank K, Michelle F Green, Timothy R Koves, and Matthew D Hirschey. 2014. 'Measurement of fatty acid oxidation rates in animal tissues and cell lines.' in, *Methods in enzymology* (Elsevier).

IJpenberg, Annemieke, Nguan Soon Tan, Laurent Gelman, Sander Kersten, Josiane Seydoux, Jianming Xu, Daniel Metzger, Laurence Canaple, Pierre Chambon, and Walter Wahli. 2004. 'In vivo activation of PPAR target genes by RXR homodimers', *The EMBO journal*, 23: 2083-91.

Joost, Hans-Georg. 2011. 'The genetic basis of obesity and type 2 diabetes: lessons from the New Zealand obese mouse, a polygenic model of the metabolic syndrome', *Sensory and Metabolic Control of Energy Balance*: 1-11.

Joosten, Robbie P, Jean Salzemann, Vincent Bloch, Heinz Stockinger, A-C Berglund, Christophe Blanchet, Erik Bongcam-Rudloff, Christophe Combet, Ana L Da Costa, and Gilbert Deleage. 2009. 'PDB_REDO: automated re-refinement of X-ray structure models in the PDB', *Journal of applied crystallography*, 42: 376-84.

Kanehisa, Minoru, and Susumu Goto. 2000. 'KEGG: kyoto encyclopedia of genes and genomes', *Nucleic acids research*, 28: 27-30.

Kang, Hye Won, Michele W Niepel, Shuxin Han, Yuki Kawano, and David E Cohen. 2012. 'Thioesterase superfamily member 2/acyl-CoA thioesterase 13 (Them2/Acot13) regulates hepatic lipid and glucose metabolism', *The FASEB Journal*, 26: 2209-21.

Kang, Hye Won, Scott Ribich, Brian W Kim, Susan J Hagen, Antonio C Bianco, and David E Cohen. 2009. 'Mice lacking Pctp/StarD2 exhibit increased adaptive thermogenesis and enlarged mitochondria in brown adipose tissue [S]', *Journal of lipid research*, 50: 2212-21.

Kang, Hye Won, Jie Wei, and David E Cohen. 2010a. 'PC-TP/StARD2: Of membranes and metabolism', *Trends in Endocrinology & Metabolism*, 21: 449-56.

. 2010b. 'Regulation of lipid and glucose metabolism by phosphatidylcholine transfer protein', *Trends in endocrinology and metabolism: TEM*, 21: 449.

Kanno, Keishi, Michele K Wu, Diana S Agate, Brandon J Fanelli, Neil Wagle, Erez F Scapa, Chinweike Ukomadu, and David E Cohen. 2007. 'Interacting proteins dictate function of the minimal START domain phosphatidylcholine transfer protein/StarD2', *Journal of Biological Chemistry*, 282: 30728-36.

Kasurinen, Juha, Peter A Van Paridon, Karel WA Wirtz, and Pentti Somerharju. 1990. 'Affinity of phosphatidylcholine molecular species for the bovine phosphatidylcholine and phosphatidylinositol transfer proteins. Properties of the sn-1 and sn-2 acyl binding sites', *Biochemistry*, 29: 8548-54.

Kawano, Yuki, Baran A Ersoy, Yingxia Li, Shin Nishiumi, Masaru Yoshida, and David E Cohen. 2014. 'Thioesterase superfamily member 2 (Them2) and phosphatidylcholine transfer protein (PC-TP) interact to promote fatty acid oxidation and control glucose utilization', *Molecular and cellular biology*, 34: 2396-408.

Klingler, Christian, Xinjie Zhao, Till Adhikary, Jia Li, Guowang Xu, Hans-Ulrich Häring, Erwin Schleicher, Rainer Lehmann, and Cora Weigert. 2016. 'Lysophosphatidylcholines activate PPARδ and protect human skeletal muscle cells from lipotoxicity', *Biochimica et Biophysica Acta (BBA)-Molecular and Cell Biology of Lipids*, 1861: 1980-92.

Krisko, Tibor I, Katherine B LeClair, and David E Cohen. 2017. 'Genetic ablation of phosphatidylcholine transfer protein/StarD2 in ob/ob mice improves glucose tolerance without increasing energy expenditure', *Metabolism*, 68: 145-49.

Krisko, Tibor I, Hayley T Nicholls, Curtis J Bare, Corey D Holman, Gregory G Putzel, Robert S Jansen, Natalie Sun, Kyu Y Rhee, Alexander S Banks, and David E Cohen. 2020. 'Dissociation of adaptive thermogenesis from glucose homeostasis in microbiome-deficient mice', *Cell metabolism*, 31: 592-604. e9.

Kuleshov, Maxim V, Matthew R Jones, Andrew D Rouillard, Nicolas F Fernandez, Qiaonan Duan, Zichen Wang, Simon Koplev, Sherry L Jenkins, Kathleen M Jagodnik, and Alexander Lachmann. 2016. 'Enrichr: a comprehensive gene set enrichment analysis web server 2016 update', *Nucleic acids research*, 44: W90-W97.

Lachmann, Alexander, Huilei Xu, Jayanth Krishnan, Seth I Berger, Amin R Mazloom, and Avi Ma'ayan. 2010. 'ChEA: transcription factor regulation inferred from integrating genome-wide ChIP-X experiments', *Bioinformatics*, 26: 2438-44.

Liu, Sihao, Jonathan D Brown, Kristopher J Stanya, Edwin Homan, Mathias Leidl, Karen Inouye, Prerna Bhargava, Matthew R Gangl, Lingling Dai, and Ben Hatano. 2013. 'A diurnal serum lipid integrates hepatic lipogenesis and peripheral fatty acid use', *Nature*, 502: 550-54.

Mo, Xiu-Lei, and Haian Fu. 2016. 'BRET: NanoLuc-based bioluminescence resonance energy transfer platform to monitor protein-protein interactions in live cells.' in, *High Throughput Screening* (Springer).

Mo, Xiulei, Qi Qi, Andrei A Ivanov, Qiankun Niu, Yin Luo, Jonathan Havel, Russell Goetze, Sydney Bell, Carlos S Moreno, and Lee AD Cooper. 2017. 'AKT1, LKB1, and YAP1 revealed as MYC interactors with NanoLuc-based protein-fragment complementation assay', *Molecular pharmacology*, 91: 339-47.

Montagner, Alexandra, Arnaud Polizzi, Edwin Fouché, Simon Ducheix, Yannick Lippi, Frédéric Lasserre, Valentin Barquissau, Marion Régnier, Céline Lukowicz, and Fadila Benhamed. 2016. 'Liver PPARα is crucial for whole-body fatty acid homeostasis and is protective against NAFLD', *Gut*, 65: 1202-14.

Nicholls, Hayley T, Jason L Hornick, and David E Cohen. 2017. 'Phosphatidylcholine transfer protein/StarD2 promotes microvesicular steatosis and liver injury in murine experimental steatohepatitis', *American Journal of Physiology-Gastrointestinal and Liver Physiology*, 313: G50-G61.

Otwinowski, Zbyszek, and Wladek Minor. 1997. '[20] Processing of X-ray diffraction data collected in oscillation mode.' in, *Methods in enzymology* (Elsevier).

Pan, Huei-Ju, Diana S Agate, Benjamin L King, Michele K Wu, Steven L Roderick, Edward H Leiter, and David E Cohen. 2006. 'A polymorphism in New Zealand inbred mouse strains that inactivates phosphatidylcholine transfer protein', *FEBS letters*, 580: 5953-58.

Roderick, Steven L, Wayne W Chan, Diana S Agate, Laurence R Olsen, Matt W Vetting, KR Rajashankar, and David E Cohen. 2002. 'Structure of human phosphatidylcholine transfer protein in complex with its ligand', *Nature structural biology*, 9: 507-11.

Sanderson, Linda M, Tatjana Degenhardt, Arjen Koppen, Eric Kalkhoven, Beatrice Desvergne, Michael Müller, and Sander Kersten. 2009. 'Peroxisome proliferator-activated receptor β/δ (PPARβ/δ) but not PPARα serves as a plasma free fatty acid sensor in liver', *Molecular and cellular biology*, 29: 6257-67.

Scapa, Erez F, Alessandro Pocai, Michele K Wu, Roger Gutierrez-Juarez, Lauren Glenz, Keishi Kanno, Hua Li, Sudha Biddinger, Linda A Jelicks, and Luciano Rossetti. 2008. 'Regulation of energy substrate utilization and hepatic insulin sensitivity by phosphatidylcholine transfer protein/StarD2', *The FASEB Journal*, 22: 2579-90.

Schug, Thaddeus T, Daniel C Berry, Natacha S Shaw, Skylar N Travis, and Noa Noy. 2007. 'Opposing effects of retinoic acid on cell growth result from alternate activation of two different nuclear receptors', *Cell*, 129: 723-33.

Sommars, Meredith A, Krithika Ramachandran, Madhavi D Senagolage, Christopher R Futtner, Derrik M Germain, Amanda L Allred, Yasuhiro Omura, Ilya R Bederman, and Grant D Barish. 2019. 'Dynamic repression by BCL6 controls the genome-wide liver response to fasting and steatosis', *Elife*, 8: e43922.

Tillman, Matthew C, Norihiro Imai, Yue Li, Manoj Khadka, C Denise Okafor, Puneet Juneja, Akshitha Adhiyaman, Susan J Hagen, David E Cohen, and Eric A Ortlund. 2020. 'Allosteric regulation of thioesterase superfamily member 1 by lipid sensor domain binding fatty acids and lysophosphatidylcholine', *Proceedings of the National Academy of Sciences*, 117: 22080-89.

Wieckowski, Mariusz R, Carlotta Giorgi, Magdalena Lebiedzinska, Jerzy Duszynski, and Paolo Pinton. 2009. 'Isolation of mitochondria-associated membranes and mitochondria from animal tissues and cells', *Nature protocols*, 4: 1582-90.

Wolfrum, Christian, Carola M Borrmann, Torsten Börchers, and Friedrich Spener. 2001. 'Fatty acids and hypolipidemic drugs regulate peroxisome proliferator-activated receptors α-and γ-mediated gene expression via liver fatty acid binding protein: a signaling path to the nucleus', *Proceedings of the National Academy of Sciences*, 98: 2323-28.

Wu, Chyuan-Chuan, Thomas J Baiga, Michael Downes, James J La Clair, Annette R Atkins, Stephane B Richard, Weiwei Fan, Theresa A Stockley-Noel, Marianne E Bowman, and Joseph P Noel. 2017. 'Structural basis for specific ligation of the peroxisome proliferator-activated receptor δ', *Proceedings of the National Academy of Sciences*, 114: E2563-E70.

Zoete, Vincent, Aurelien Grosdidier, and Olivier Michielin. 2007. 'Peroxisome proliferator-activated receptor structures: ligand specificity, molecular switch and interactions with regulators', *Biochimica et Biophysica Acta (BBA)-Molecular and Cell Biology of Lipids*, 1771: 915-25.

Chapter 3: Molecular mechanisms of the gut microbiome-derived obesogen delta-valerobetaine

Ken H. Liu[1]*†, Samuel Druzak[2], Choon Lee[1], William Crandall[1], Jaclyn Weinberg[1], Joshua A. Owens[1], Bejan Saeedi[1], Edward Morgan[3], Young-Mi Go[1], Eric Ortlund[2], Dean P. Jones[1]

From the[1] Division of Pulmonary, Allergy, Critical Care and Sleep Medicine, Department of Medicine, Emory University School of Medicine, Atlanta GA [2]Department of Biochemistry, Emory University School of Medicine, 1510 Clifton Road, Atlanta, GA 30322; [3]Department of Chemical Biology and Pharmacology, Emory University School of Medicine, 1510 Clifton Road, Atlanta, GA 30322.

*Corresponding Author

Author Contributions: S.A.D., and K.L. designed research; K.L. and S.A.D performed research; S.A.D., and K.L. analyzed data; S.A.D. wrote the chapter; S.A.D made figures; S.A.D., K.L. and E.A.O. edited the chapter.

3.1 Summary:

Mitochondrial fatty acid oxidation relies on carnitine for transport of fatty acyl groups across the outer mitochondrial membrane. Previously, we characterized delta-valerobetaine (VB), a gut microbiome derived metabolite known to decrease lipid metabolism by altering carnitine signaling. Here, we report the existence of homocarnitine (HC), a 5-carbon carnitine analogue, in mice treated with VB. *In silico* modeling suggests VB and HC could exert negative effects on metabolism by engaging with the same suite of enzymes as gamma butyrobetaine (γBB) or carnitine. Isotope tracer studies confirm that that HC is produced from VB in a butyrobetaine dioxygenase (BBOX) dependent manner. Preliminary biochemical characterization of BBOX shows that VB can stabilize this enzyme, but to a lesser extent than carnitine. We hypothesized that the mechanism by which VB alters lipid metabolism could be driven, in part, through HC. Addition of labeled palmitate to BBOX-overexpressing HUH7 cells produced acyl-homocarnitne in a carnitine palmitoyltransferase I (CPT1)-dependent manner. Biochemical and structural

characterization of VB show that this metabolite can compete with carnitine for carnitine O-acetyltransferase (CRAT) and likely CPT1. Finally, we detect homocarnitine in human samples and show it tightly correlates to VB levels suggesting relevance for these findings in the human population. Further studies are needed to characterize the role these carnitine-related analogues play in modulating host metabolism.

3.2 Introduction:

Metabolic disease is an epidemic that continues to grow, and it is estimated that 50% of the US population will be obese by 2030. (Ward et al., 2019) Obesity is associated with the development of metabolic syndrome (MetS), which includes co-morbidities such as non-alcoholic fatty liver disease (NAFLD), dyslipidemia, and diabetes. While many therapies have been developed to treat the symptoms of various co-morbidities associated with MetS, there is a lack of understanding surrounding the metabolic adaptations associated with obesity and the development of MetS. (Fothergill et al., 2016) The development of MetS is thought to be driven by interaction between diet, host genetics, and environment. (Kaur, 2014)

Emerging evidence suggests that altered gut microbiome composition is sufficient to drive many of the negative effects associated with overnutrition including weight gain, NAFLD and diabetes. (Bibbò et al., 2018; Devaraj et al., 2013; Turnbaugh et al., 2006) Our lab has previously characterized a role for the gut microbiome derived metabolite, delta-valerobetaine (VB), in driving the development of aspects of MetS. (Liu et al., 2021) VB is a product of bacteria known to have detrimental effects on host metabolism. Treatment of mice with VB led to increased weight gain and hepatic lipid accumulation under high fat diet feeding. This was thought to be driven via dysregulation of two essential processes that control lipid metabolism. First VB regulates lipid metabolism through perturbing carnitine homeostasis, this results in a build up of free fatty acids in the cell. Second, this buildup of free fatty acids can then alter PPAR activity leading to further dysregulation of lipid.

Carnitine is essential for ubiquitous metabolic processes present in all metazoans. In the cell near the mitochondrial membrane carnitine is coupled to activated fatty acyl CoA via carnitine

palmitoyltransferase I (CPT1a) which then shuttles these species into the inner mitochondrial space. Once there, these carnitine conjugates are transported into the mitochondrial matrix via carnitine-acylcarnitine translocase (CACT). In the mitochondrial matrix carnitine, is decoupled from fatty acids via carnitine palmitoyltransferase II (CPT2) and is recycled. Free fatty acids have two fates once in the mitochondrial matrix: they are subject to metabolism in a process termed beta oxidation or excreted back into the cytosol following recoupling to carnitine via Carnitine O-acetyltransferase (CRAT).

The direct biosynthetic precursor to carnitine is gamma butyrobetaine (γBB), which is derived from trimethyllysine (TML). (Cox and Hoppel, 1973) gamma-butyrobetaine hydroxylase (BBOX), which is highly expressed in liver, catalyzes the hydroxylation of γBB to form carnitine with alpha-ketoglutarate, iron and ascorbate as co-factors. VB is a structural analogue of γBB, which distributes to host tissues and is linked to obesity and aging in humans.(Go et al., 2020; Mossad et al., 2021) The structural similarity between delta-valerobetaine and gamma-butyrobetaine raised the possibility that delta-valerobetaine could similarly be hydroxylated to form a structural analogue of carnitine.

Here, we report, for the first time, the existence of homocarnitine in living systems. Homocarnitine is present in conventional mice, where VB is a microbiome-derived metabolite. Homocarnitine increases with VB treatment in mice. *In silico* modeling suggests that VB and HC are capable of decreasing the biosynthesis of carnitine and affecting carnitines' role in facilitating lipid metabolism through engaging a similar suit of enzymes. We confirm this and show that HC is generated from VB in a BBOX-dependent manner. Biochemical characterization of VB with CRAT and BBOX suggest and interaction is capable of affecting normal enzymatic function. Crystal structures of VB bound to CRAT suggest that VB could compete with carnitine for this

enzyme. Attempts to co-crystalize VB with BBOX have been unsuccessful thus far. We also demonstrate that HC, similar to carnitine, conjugates palmitic acid in a CPT1-dependent manner. Importantly homocarnitine is found to correlate with VB in the human population. Following definitive structural characterization of HC, we plan to synthesize HC to facilitate further biochemical and structural characterization. Future work is required to determine the role homocarntine plays in altering host lipid metabolism independent of VB.

3.3 Results:

3.3.1 Uncovering the biosynthetic pathway of valerobetaine and homocarnitne

Following the discovery and characterization of valerobetaine, we sought to characterize the molecular mechanism by which VB alters host metabolism. We first wanted to determine possible precursors of VB. We hypothesized that VB is generated by fermentation of lysine in the gut. To test this we performed targeted mass spectrometry (MS) analysis on livers from mice fed either Trimethyllysine (TML) or ^{13}C-labeled Trimethyllysine (LTML). Mice fed LTML and TML led to the generation of a mass at 163.1431 m/z (labeled VB) or 160.1332 m/z (unlabeled VB) respectively, suggesting that TML is the precursor (Figure 3.1 A). Following this, we sought to determine if VB was further metabolized via host metabolic processes. MS analysis from livers of mice fed LTML show the formation of a mass at 179.1383 m/z, which corresponds to the addition of a hydroxyl group (Figure 3.1 B). From here forward we will refer to this mass as homocarnitine.

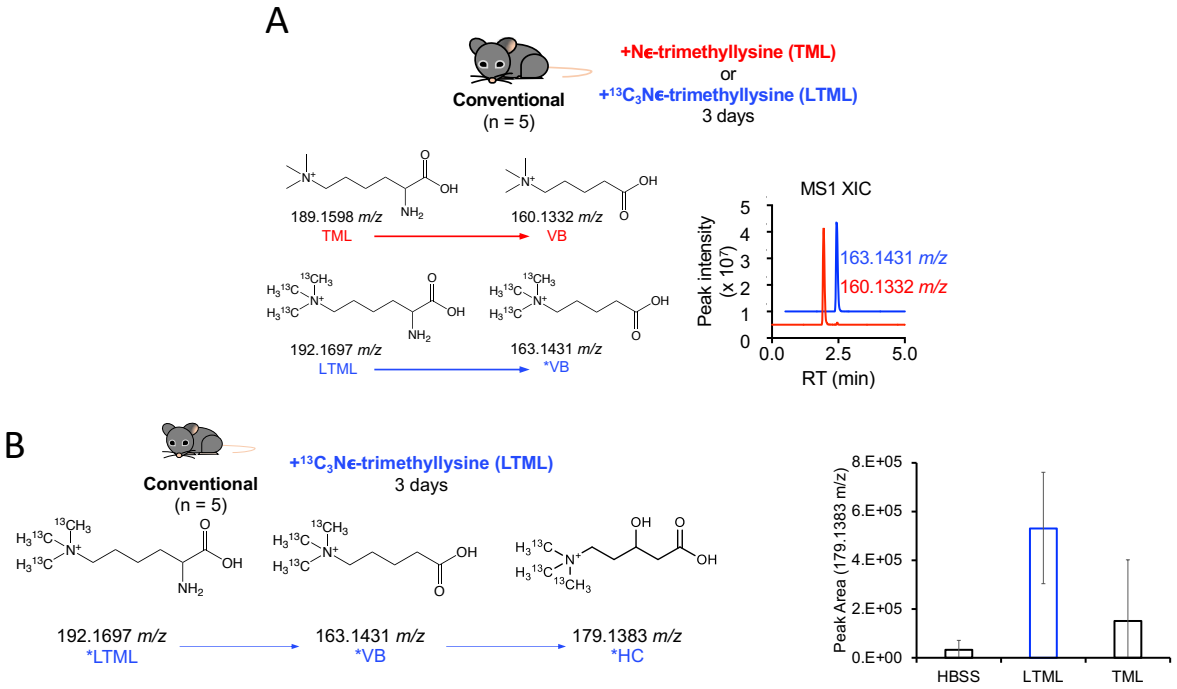

Figure 3 - 1: Characterization of the homocarnitine biosynthetic pathway.

A.) Tracer studies of mice treated with trimethyl lysine or ^{13}C-labeled trimethyl lysine confirm the presence and precursor of VB *in vivo*. **B.)** Mice treated with ^{13}C-labeled TML show generation of a mass at 179.1383 m/z , predicted to be homocarnitine.

3.3.2 BBOX catalyzes the formation of homocarnitine

To identify enzymes capable of explaining the phenotype associated with VB treatment we assessed potential overlap between VB and HC with endogenous molecules using similarity ensemble approach (SEA). SEA works by comparing molecules of unknown function to a curated data base of proteins and small molecules that are known to interact. Similarity scores are determined by chemical resemblance between ligands and then ranked. SEA modeling suggests that VB (Figure 3.2A) and HC (Figure 3.2B) can interact with a similar suite of proteins as carnitine. This was unsurprising due to the similar structure of γBB, carnitine, delta-valerobetaine, and homocarnitine (Figure 3.2 C & D). We hypothesized that, similar to the hydroxylation of γBB by BBOX to form carnitine, VB could undergo biotransformation via BBOX to form homocarnitine . Evidence using BBOX-overexpressing HUH7 cells supports a link between VB and homocarnitine, dependent on BBOX (Figure 3.2E).

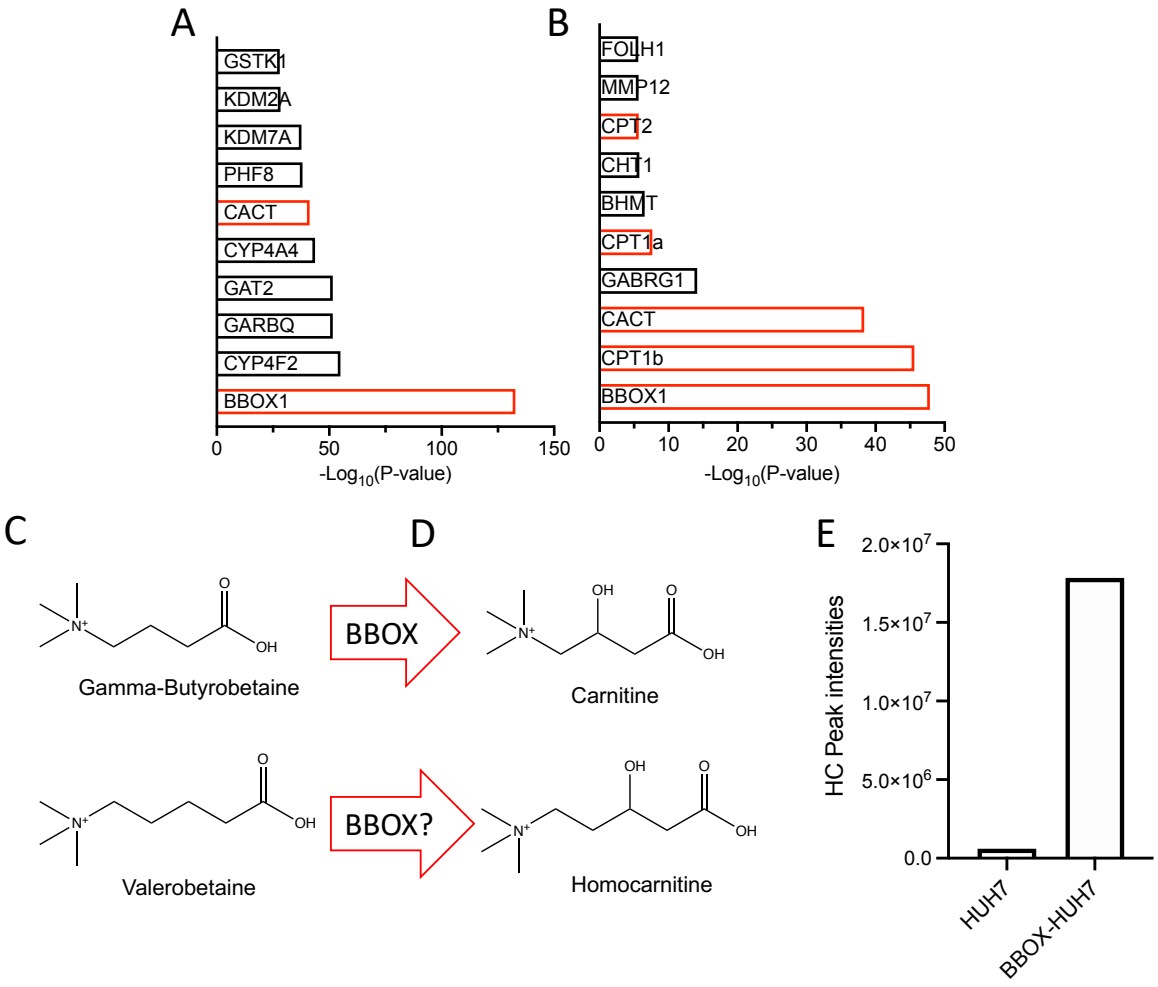

Figure 3 - 2: Carnitine analogues engage with enzymes related to biosynthesis and lipid shuttling

A.) Similarity ensemble approach (SEA) results for VB suggest an interaction between VB and BBOX **B.)** SEA results for HC suggest important role of this metabolite in regulating carnitine homeostasis **C.)** Structural and chemical similarities between γBB and VB **D.)** Structural chemical similarities between carnitine and HC **E.)** Production of homocarnitine for HUH7 cells show a dependance on BBOX.

3.3.3 Biochemical and structural characterization of VB-BBOX complex

We next sought to biochemically characterize the consequence of the interaction between VB and BBOX, the rate limiting enzyme in the synthesis of carnitine. Thermal melting studies show that VB stabilized BBOX, although to a lesser extent compared to carnitine (Figure 3.3 A). Following this evidence, we sought to structurally characterize the interaction between VB and BBOX. BBOX was preincubated with N-Oxalylglycine, a nonhydrolyzable alpha ketoglutarate, zinc, and VB prior to setting trays. Crystals were obtained in two previously reported conditions - one in high salt and one in low salt high polyethylene glycol (PEG) condition. The high salt condition - derived crystals were optimized first, however, structure determination revealed this crystal form is incompatible with VB binding (Figure 3.3 B). Specifically, the loops which coordinate the endogenous ligand, γBB within the catalytic pocket were disordered and attempts to build the loops into weak density using the active BBOX- 4 -(Ethyldimethylammonio)butanoate complex as a guide generated steric clashes with a symmetry mate. (Tars et al., 2014) This is consistent with the apo BBOX crystal form reported in similar conditions. (Leung et al., 2010) Rescreening strategies are currently underway, in an attempt to find a new condition to allow for visualization of this complex. Further characterization with BBOX in complex with its endogenous ligand γBB would allow for more mechanistic insight and will be a valuable point of comparison for future assessment.

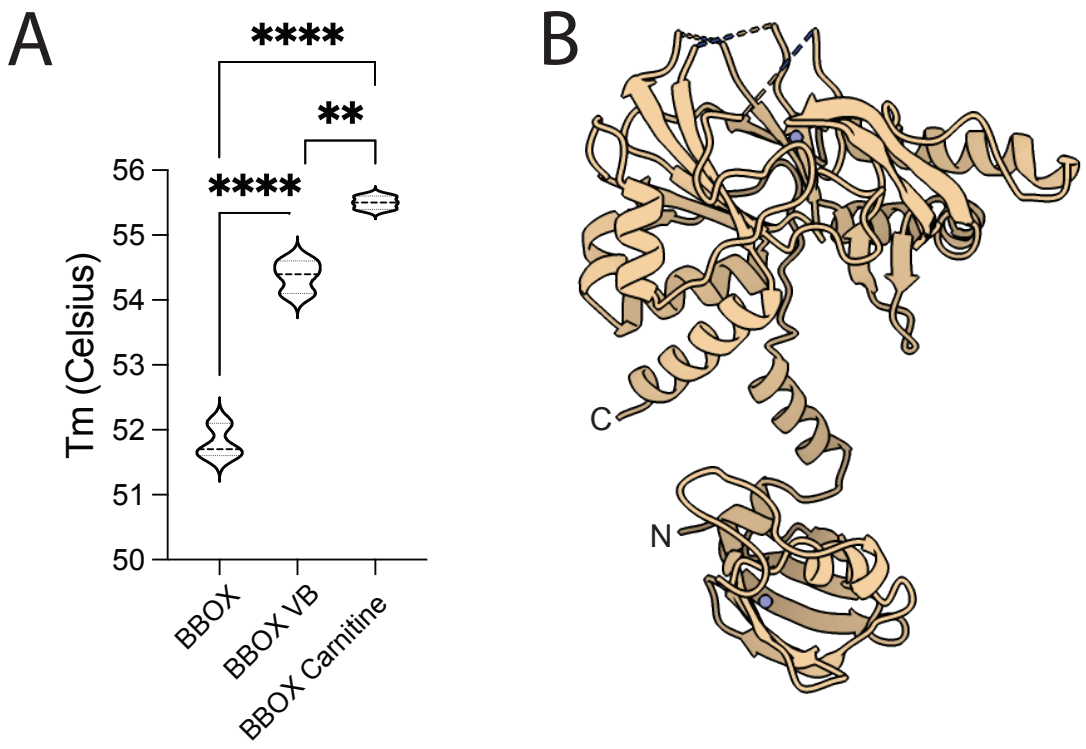

Figure 3 - 3: Characterization of the VB-BBOX complex.

A.) Thermal melting show a stabilization of BBOX with carnitine and VB (n=3, One-way ANOVA) **B.)** 2.8 Å structure of BBOX in a crystal packing not amenable to visualization of substrate binding.

Table 3 - 1: Data collection and refinement statistics for BBOX.

Data collection	
Resolution range (Å)	50.0 - 2.85 (2.95 - 2.85)
Space group	P 65 2 2
Cell Dimensions **a,b,c(Å)** **A,B,C (°)**	 165.1, 165.1, 97.5 90.0, 90.0, 120.0
No. reflections	19825 (1935)
Completeness (%)	99.8 (100.0)
Redundancy	32.6 (34.1)
Mean I/sigma(I)	13.3 (1.4)
Wilson B-factor	69.69
CC1/2	0.999 (0.78)
Refinement	
Resolution	50.0 - 2.8
R-work/R-free	0.22/0.25
Protein residues	365
RMS(Å)	0.01
RMS(°)	1.1
Ramachandran favored (%)	96.6
Ramachandran allowed (%)	3.4
Ramachandran outliers (%)	0.0
Rotamer outliers (%)	0.0
Clashscore	5.7
Average B-factor	67.7
Protein	67.7
ligands	71.0
solvent	62.0

Statistics for the highest-resolution shell are shown in parentheses.

3.3.4 Homocarnitne can engage with enzymes to form acyl homocarntines

SEA modeling of homocarnitine also identified many enzymes in the fatty acid- carnitine shuttling pathway, specifically CPT1, CACT, and CPT2 (Figure 3.2 and 3.4 A). We hypothesized that following generation of homocarnitine from BBOX, HC can interact with CPT1 leading to a decrease in fatty acid shuttling into the mitochondria. Treating BBOX overexpressing cells with ^{13}C-labeled palmitate for 4 hours led to the formation of a palmitoyl-carnitine conjugate. Cells treated with etomoxir, and inhibitor of CPT1, show a dependence on CPT1a as the conjugation was lost (Figure 3.4 B). Similarly, cells pretreated with 200 μM VB showed the formation of a palmitoyl-homocarnitine conjugate, that was also dependent on CPT1 (Figure 3.4 C). The kinetics and consequences of these interaction need to be explored further, looking at mitochondrial respiration of cells treated with HC using seahorse assays and how this metabolite could affect the functions of enzymes involved in these processes *in vitro*.

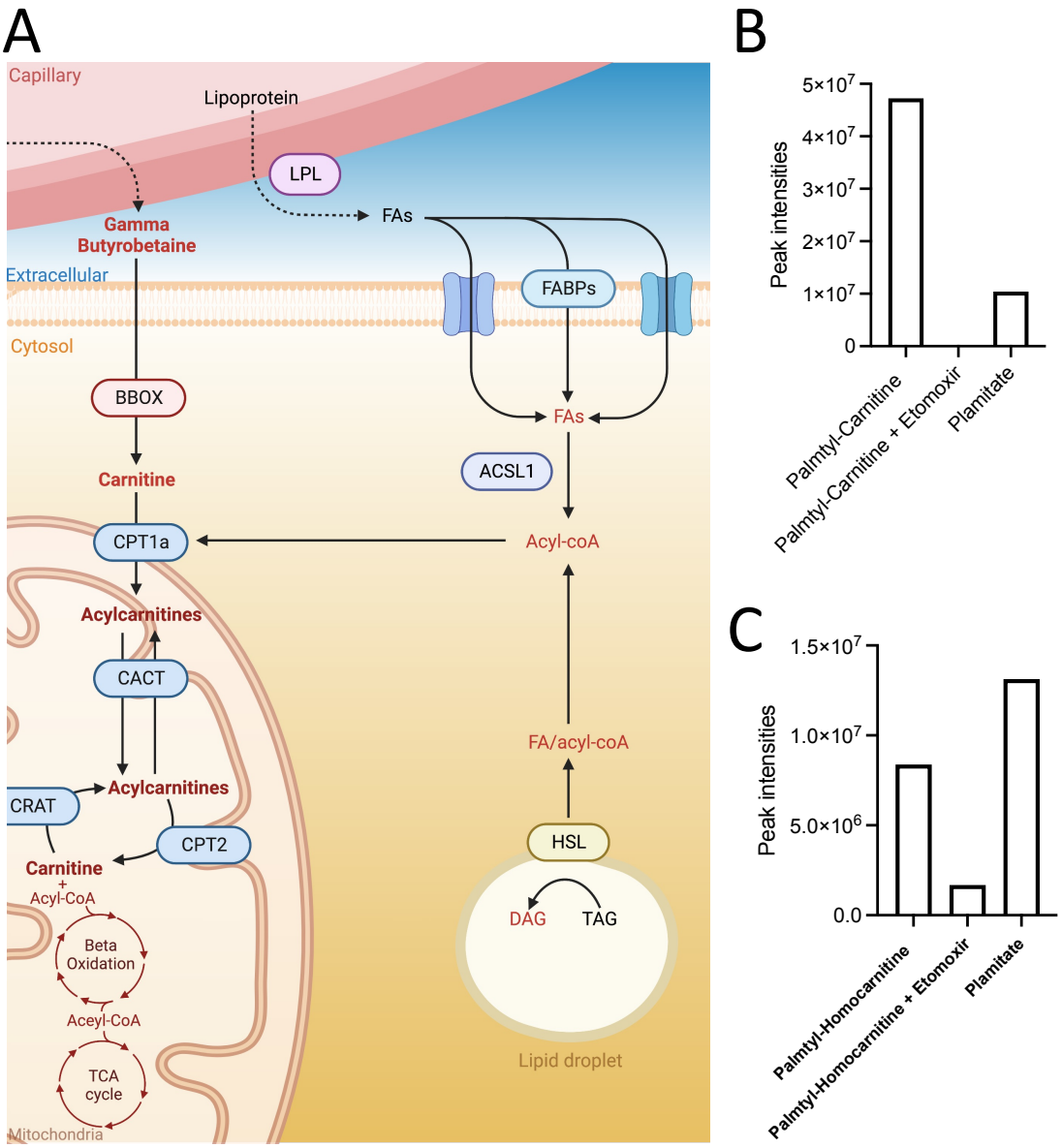

Figure 3 - 4: Tracer studies in HUH7 cells suggest the formation acyl-homocarnitine.

A.) Diagram of mitochondrial beta oxidation elaborates on the process by which palmitate is metabolized highlighting a role for the various enzymes involved, most of which were identified by our *in silico* modeling. **B.)** Relative peak intensities of palmitoyl -carnitine for HUH7 cell treated with ^{13}C-labeled palmitate for 4 hours **C.)** Relative peak intensities of palmitoyl-homocarnitine for BBOX over expressing HUH7 cell pretreated with 200µM valerobetaine, then treated with ^{13}C-labeled palmitate for 4 hours.

3.3.5 Biochemical and structural characterization of VB-CRAT complex

Formation of acyl-homocarnitine species appeared to be CPT1a-dependent process. The endogenous ligand for CPT1a is carnitine, which contains a hydroxyl in the 3 position and is one carbon shorter than VB. While we would like to characterize the interaction between CPT1a and homocarninte, we have not been able to successfully isolate HC. Additionally, CPT1a is a membrane anchored enzyme that has resisted prior attempts at purification and crystallization. Previous studies have instead used the closely related homologue, CRAT, as a surrogate to study carnitine transferase mechanisms. (Morillas et al., 2004) In the mitochondria matrix CRAT performs a similar enzymatic function as CPT1, except instead of facilitating import of fatty acids into the mitochondria by conjugation to carnitine, CRAT facilitates excretion of these species. Given this, we instead began with biochemical characterization of the VB-CRAT interaction. This also allows for visualization of the interactions between VB and CRAT. Thermal melting studies of the CRAT- carnitine complex show a dramatic increase in the thermal stability of CRAT when bound to its endogenous substrate. Unlike CRAT- carnitine complex, the CRAT–valerobetaine complex slightly destabilized CRAT (Figure 3.5A). Previous studies have shown that VB exists within the mitochondria which suggests these finding may still be a part of the mechanism by which VB inhibits fatty acid oxidation. While likely a weaker inhibitor than HC, VB may bind and interfere with CPT1a/ CRAT-carnitine interaction.

The crystal structure of CRAT bound to valerobetaine (Figure 3.5 B) suggests that VB could block binding of CPT1a to carnitine as VB occupied the same space as carnitine within the active site. Interestingly, VB adopts two confirmations within the ligand binding pocket as shown via a feature enhanced map (FEM) and a polder map (Figure 3.5 C &D). This data suggests that dysregulation of CPT1a could be due to competition between these two ligands. Compared to

carnitine, VB lacks a hydroxyl and has an elongated acyl chain. These difference would add strain to the ligand binding pocket, expanding the active state, explaining reduced thermal stability. These chemical differences would also lead to weaker association with CRAT and could allow for higher mobility in the ligand binding pocket resulting in slowed catalytic efficiency.

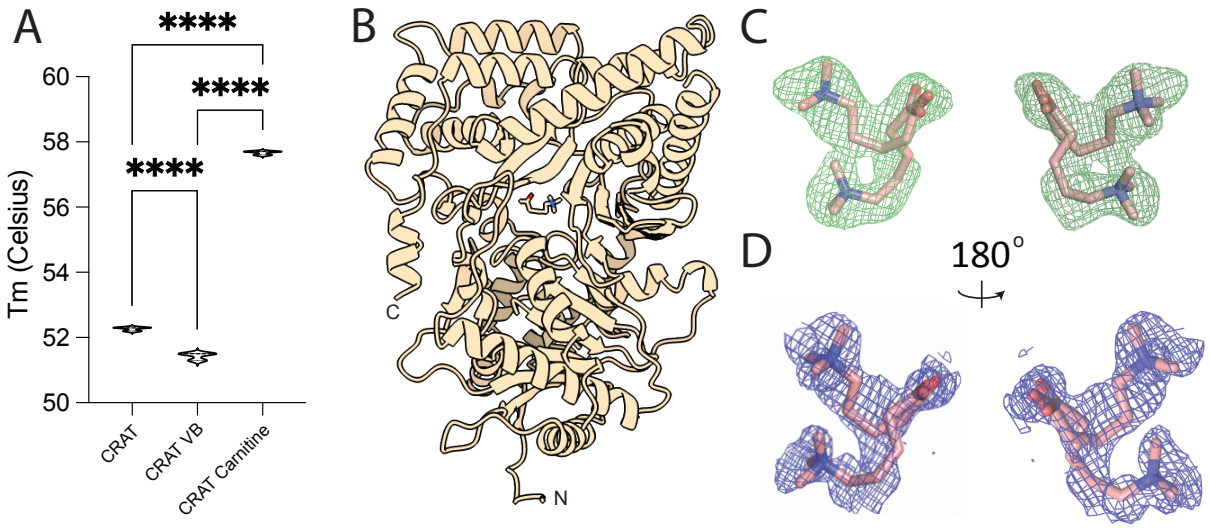

Figure 3 - 5: VB-CRAT complex inform mechanism of inhibition of lipid metabolism.

A.) Thermal melting shows a stabilization of CRAT with carnitine and a destabilizing effect of VB on CRAT (n=3, One-way ANOVA) **B.)** 1.65 Å structure of CRAT VB complex suggests a competitive mechanism as VB occupies a similar location withing the catalytic pocket **C.)** Electron density supports the binding of VB in two distinct modes withing the catalytic pocket supported by a polder map (4 sigma) **D.)** Binding of VB in the catalytic pocket of CRAT is further supported by electron density visualized via the FEM map (1 sigma).

Table 3 - 2: Data collection and refinement statistics for VB-CRAT complex.

Data collection	
Resolution range Å	50.0 - 1.651 (1.71 - 1.65)
Space group	C 1 2 1
Cell Dimensions **a,b,c (Å)** **A,B,C (°)**	 157.5, 89.0, 118.9 90, 126.9, 90
No. reflections	155277 (14915)
Completeness (%)	98.34 (94.6)
Redundancy	6.4 (5.2)
CC1/2	0.95 (0.46)
Mean I/sigma(I)	8.54 (1.1)
Wilson B-factor	27.5
Refinement	
Resolution	50.0-1.65
Reflections used in refinement	155191 (14853)
Reflections used for R-free	1995 (190)
R-work/ R-free	0.17/0.19
Protein residues	1188
RMS(Å)	0.01
RMS(°)	0.94
Ramachandran favored (%)	98.6
Ramachandran allowed (%)	1.4
Ramachandran outliers (%)	0.0
Rotamer outliers (%)	1.2
Clashscore	3.1
Average B-factor	34.2
Protein	33.3
Ligands	39.3
Solvent	43.1

Statistics for the highest-resolution shell are shown in parentheses.

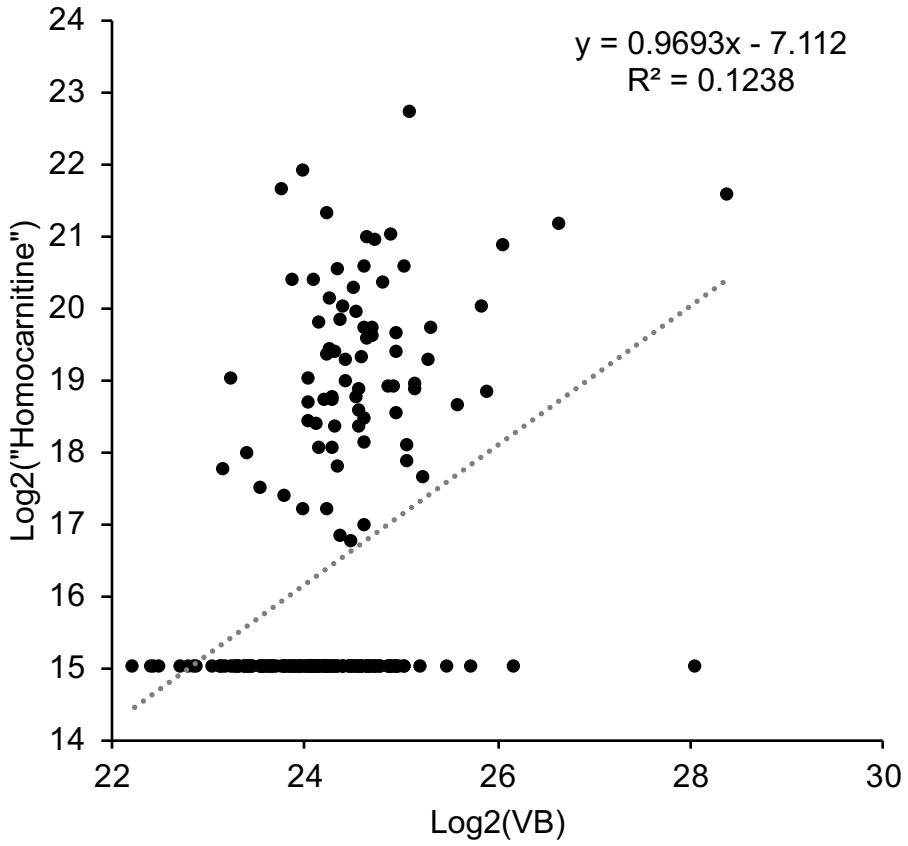

Figure 3 - 6: Homocarnitine is detected in human samples.

A.) Homocarnitne is detected within the human population and correlates with the presence of valerobetaine.

3.4 Discussion:

Carnitine was discovered over a century ago (Bremer, 1983) and its fundamental role in lipid metabolism was elucidated approximately fifty years after. (Friedman S Fau - Fraenkel and Fraenkel; Fritz; Fritz, 1959) Despite thorough research on carnitine there have been no reports on the existence of homocarnitine. Here we outline the biosynthetic route of homocarnitine using isotope tracer studies in conventionalized mice. Follow up characterization from hits identified via *in silico* modeling suggest both VB and HC are capable of altering carnitine homeostasis through competitive binding to BBOX and CRAT/CPT1a. Biochemical characterization of VB supports these interactions. Structural characterization of VB and CRAT show that VB could compete with carnitine for CRAT and likely CPT1a. Together these findings open the possibility that these metabolites affects host biology by multiple perturbations, from the synthesis of carnitine to its role in regulating lipid catabolism. In line with this hypothesis, our analysis also uncovered CPT1a dependent formation of acyl- homocarnitine. Our *in vitro* and murine studies appear to be relevant to human health as we see a correlation between VB and HC in human samples (Figure 3.6). Further investigation into the distinct roles VB, HC and HC-fatty acid conjugates play in regulating host metabolism will offer insight into the mechanism by which VB decreases fatty acid oxidation resulting in weight gain and hepatic steatosis. While exciting these findings could benefit from further characterization looking into the physiological and kinetic consequences of the actions of VB and HC engaging with host metabolic machinery.

While the mass and dependence on BBOX for the formation of HC suggests that this metabolite is a hydroxylated product of VB, the exact location of this moiety is unknown. The most likely location for this hydroxyl group is either in the 3 or 4 position. Isolation of these species is ongoing and planned to occur via two workflows. First, HC can be isolated from the

aforementioned BBOX over-expressing cell line. Second HC can be synthesized. Thus far, isolation of these species have proven challenging and only resulted in a crude product. Once sufficiently pure, NMR studies will be able to determine the definitive structure of HC. Following this, synthesis of HC using the suggested synthetic routes will allow for sufficient material to enable detailed *in vitro* and *in vivo* studies. Of particular relevance to this chapter are the characterization of HC with BBOX and CRAT. These analysis would also benefit from investigating how γBB affects BBOX and CRAT, as this would allow for better comparison between the non-hydroxylated carnitine analogues. Further studies should also focus on the potential perturbation of theses species on carnitine shuttling via CACT. In line with this, investigating the effect of mitochondrial beta oxidation on cells treated with HC would provide evidence to support VB or HC as sufficient to drive the aforementioned metabolic phenotypes.

While not characterized in this study, our findings open the possibility that, like VB, HC can regulate members of the PPAR family through altering metabolism. Prior studies performed in collaboration with the Jones lab infer an indirect regulation of PPAR transactivation. Further studies investigating the possibility of direct regulation of PPARs via VB or HC would allow for more mechanistic insight as to how microbiome derived metabolites can host alter metabolism. Finally, similar to previous characterization of mice fed VB, HC should be investigated for its ability to drive weight gain and hepatic steatosis.

Conflicting reports have also identified the existence of 3-methyl-4-(trimethylammonio)butanoate, a gut microbiome derived, structural analogue to VB. (Hulme et al., 2020) Instead of containing an extended acyl chain, 3-methyl-4-(trimethylammonio)butanoate contains a methyl group in the 3 position. While not necessarily exclusive, this report opens the possibility that initial characterization of the structure of VB could be erroneous. One piece of

evidence that supports the existence of both molecules, surrounds the hydroxylation of VB to HC. Based on the interaction between γBB and BBOX, the addition of a methyl group in the 3 position should inhibit the formation of HC. Previous studies investigating BBOX inhibitors support this, as addition of a methyl in the 4 position or a covalently linked chlorine in the 3-position resulted in a 340 μM and 450 μM IC50 respectively. (Tars et al., 2014) Finally, determining the potential overlap of VB and 3-methyl-4-(trimethylammonio)butanoate play in regulating host metabolism will enable proper interpretation for future studies.

Carnitine and it associated enzymes are thought to have co-evolved. This opens the possibility that perhaps homocarnitine and its precursor valerobetaine represents an ancient relic of an alternative carnitine shuttling system. The observed phenotype of VB treated mice suggest that VB and HC did not perform as efficiently as butyrobetaine or carnitine in facilitating fatty acids mobilization into the mitochondria for the generation of fuel. An alternative hypothesis that the presence of molecules that slow our ability to burn fats could afford an evolutionary advantage allowing for longer term storage of fat depots. Either scenario highlights the role that our holobiome has to shape host metabolic processes and possibly influence our own evolution.

3.5 Material and Methods:

3.5.1 Reagents

Buffers and reagents for crystallography were purchased from Sigma, Fisher, Polysciences, or Cayman, Inc. The murine CRAT pET28a plasmid was a gift from Dr. Tong (Columbia University, New York, Ny), whereas the BBOX pFX729 vector were graciously given by Dr. Dambrova (Rīga Stradiņš University, Riga, Latvia).

3.5.2 In silico modeling of putative targets:

In silico modeling was performed using the similarity ensemble approach (SEA) webserver. (Keiser et al., 2007) This method works by comparing the chemical structure of an

input to a curated database of known ligand-protein interactions. The similarity score between each set was calculated using ligand topology. A statistical model is then used to determine and rank the significance of the resulting similarity scores.

3.5.3 Expression of CRAT and BBOX

Following sequencing, pET28a vector containing coding regions of CRAT were transformed into BL21 DE3 *E. coli.* Cultures were grown in terrific broth (TB; 6 × 1.3 L) at 37°C with gentle shaking to an OD_{600} of 0.6, cooled to 18°C, induced with 0.5 mM isopropyl-1-thio-D-galactopyranoside (IPTG), and allowed to grow overnight. The next morning cells were spun down at 3500 x g for 20 min. Pellets were frozen at -80 °C until they were purified.

BBOX in the pFX729 vector was transformed into MAH22 yeast. Cells were then plated onto agarized YFPD supplemented with 3% formaldehyde. This plate was then sent to the bioexpression and fermentation facility at University of Georgia for large scale fermentation. Cells were washed once with distilled water and pelleted. The resulting ~200 g of yeast pellet was then stored at -80 °C until lysis.

3.5.4 Purification of CRAT and BBOX

CRAT pellets were thawed, homogenized, and lysed in 150 mM NaCl, Tris–HCl pH 7.4 supplemented with 5% glycerol, 25 mM imidazole, 5 mM β-mercaptoethanol, 100 μM PMSF, DNAse A, and lysozyme. The lysate was then spun down at 18,000 g for 60 min, the supernatant was isolated and loaded onto a immobilized metal affinity chromatography (IMAC) column with the following buffers: buffer A (150 mM NaCl, 20 mM Tris, 20 mM imidazole, 5% glycerol, pH 7.5) and buffer B (150 mM NaCl, 20 mM TRIS 250mM imidazole, 5 % glycerol, pH7.5). Fractions containing CRAT were then pooled, and further purified against a Superdex 75pg 16/60 size

exclusion column (20 mM HEPES, pH 8.2, 200 mM NaCl, 0.05% Tween-20 and 0.5 mM TCEP), and frozen at -80 ° C.

Yeast cells were then resuspended 1:1 with lysis buffer: 20 mMTris-HCl and 300 mM NaCl at pH 8.0 supplemented with lysozyme, and PMSF. Following 1 minute of vortexing, the resuspended yeast pellet was then frozen in liquid nitrogen. Frozen yeast breads were then subjected to mechanical disruption using a mortar and pestle. This process was repeated 5 times. Lysate was then spun down at 18,000 x g for 1 hour. The supernatant was isolated and loaded onto an immobilized metal affinity chromatography (IMAC) column with the following buffers: buffer A (300 mM NaCl, 20 mM Tris, 20 mM imidazole, 5% glycerol, pH 8) and buffer B (300 mM NaCl, 20 mM TRIS 500mM imidazole, 5 % glycerol, pH 8). Fractions containing BBOX were pooled and subject to TEV cleavage over the weekend. To remove the 6X His tag, the recombinant TEV protease (100 μg of protease/2 mg of protein) in 0.5 mM ethylenediaminetetraacetic acid (EDTA) and 1 mM dithiothreitol (DTT) was added and cleavage was performed for 72 h at 4 °C. Cleaved BBOX was isolated from His-TEV using via IMAC. Flow through containing BBOX was further purified using an HiTrap Q ion exchange column using a linear gradient (20 CV) and the following buffers: buffer A (20 mM Tris, 5% glycerol, pH 8) buffer B: (1M NaCl, 20 mM Tris, 5% glycerol, pH 8). Fractions were concentrated to 10 mg/ml, flash frozen and stored at -80 °C. Finally, BBOX was ran on a Enrich SEC70 gel filtration column into 20 mM Tris-HCl (pH = 8.0) before setting trays.

3.5.5 Protein crystallization, data collection, and structure determination

CRAT was concentrated to 30 mg/mL and supplemented with 2 mM VB. Crystals were grown using IP2 plates by sitting drop vapor diffusion at 4 °C in drops containing 1 μL of CRAT and 1-2 μL of well buffer containing: 100 mM Tris (pH 8.5), 100 mM NaCl, 14% (w/v) PEG 3350,

and 2.3 mM VB. Crystals grew rather quickly reaching their maximum size over the weekend. These crystals were cryoprotected in well solution containing 10% glycerol and flash frozen in liquid nitrogen.

BBOX was concentrated using Amicon centrifugation units to 3 mg/mL. Following this, 10 mM N-Oxalylglycine and 10 mM VB were added and allowed to incubate at room temperature for 20 min. Samples were spun down and transferred to a new tube before setting trays. Crystals were grown by hanging drop vapor diffusion at 4 °C. Drops contained 1 µL of BBOX and 1-2 µL of well buffer containing 1.2 M ammonium sulfate, 100 mM sodium acetate, pH 4.5. Crystals grew slowly, taking about 1 week to appear. Crystal growth halted 2 weeks after the tray was set. Crystals were cryoprotected in well solution containing 15% glycerol and flash frozen in liquid nitrogen.

Data were remotely collected from the Southeast Regional Collaborative Access Team (SER-CAT) at the Advanced Photon Source (APS), 22ID beamline (Argonne National Laboratories, Chicago, IL). Data were processed and scaled using HKL-2000 (Otwinowski and Minor) and phased by molecular replacement using Phaser-MR (Adams et al.) using a previously published BBOX and CRAT structures as a reference model (CRAT-PDB:2H3U) (BBOX-PDB: 3O2G). Models were built using COOT (Adams et al.) (Emsley et al., 2010) and refined using PHENIX and PDB_REDO. (Joosten et al., 2009) Structures were visualized using PyMOL (Schrödinger, LLC).

3.5.6 Thermal Stability

Alterations in thermal stability of both BBOX and CRAT were performed using the Tycho (Nanotemper technologies, Munich Germany). BBOX and CRAT at 30 µM were incubated overnight with 5 molar excess of valerobetaine or carnitine. The next day ~10 µl of solution was

loaded into capillaries and loaded into the Tycho. Thermal melting (Tm) was determined using the first derivative of these data, and performed in triplicate.

3.5.7 Chemical characterization of HC:

$^{13}C_{16}$-palmitic acid (Sigma-Aldrich 605573) was dissolved in 150 mM NaCl after heating to 70 °C and slowly mixed with prewarmed (37 °C) FFA-free bovine serum albumin (BSA) (Sigma-Aldrich A4602) solution in 150 mM NaCl with stirring to produce a 1 mM palmitate to 0.17 mM BSA ratio. HUH7 cells were grown in 6-well cell culture plates to 100% confluence. Cell media was replaced with EMEM containing 0.5% FBS for 12 h ± VB before treatment with labelled palmitic acid. Cells were washed twice with prewarmed HBSS and media was replaced with EMEM containing 0.5% FBS, 200 µM labelled palmitate and either vehicle, 50 µM VB, 40 µM etomoxir or 50 µM carnitine. At each time point, cells were washed once with ice-cold HBS-S and collected by scraping on ice using 200 µl of ice-cold 20:80 water:acetonitrile and centrifuged at 14,000 x *g* for 10 min at 4 °C. Supernatants were transferred to autosampler vials and maintained at 4 °C until analysis. Data were analysed using xCalibur (v.4.2) QuanBrowser for carnitine and labelled palmitate, palmitoyl-CoA, palmitoylcarnitine, acetyl-CoA and acetylcarnitine.

3.5.8 MS analysis of BBOX overexpressing HUH7 Cells

Metabolites from BBOX, HUH7 cell lines were extracted by the addition of 200 uL of 80% Acetonitrile:20% water to 6 well cell culture plates with scraping. Extracts were centrifuged at 14,000g for 10 minutes and the supernatants were transferred to autosampler vials for LC-HRMS analysis with a Vanquish Duo UHPLC coupled to an Orbitrap ID-X mass spectrometer.

3.6 References:

Adams, Paul D, Pavel V Afonine, Gábor Bunkóczi, Vincent B Chen, Ian W Davis, Nathaniel Echols, Jeffrey J Headd, L-W Hung, Gary J Kapral, and Ralf W Grosse-Kunstleve. 2010. 'PHENIX: a comprehensive Python-based system for macromolecular structure solution', *Acta Crystallographica Section D: Biological Crystallography*, 66: 213-21.

Bibbò, Stefano, Gianluca Ianiro, Maria Pina Dore, Claudia Simonelli, Estelle E Newton, and Giovanni Cammarota. 2018. 'Gut microbiota as a driver of inflammation in nonalcoholic fatty liver disease', *Mediators of inflammation*, 2018.

Bremer, J. 1983. 'Carnitine - Metabolism and Functions', *Physiological Reviews*, 63: 1420-80.

Cox, R. A., and C. L. Hoppel. 1973. 'Biosynthesis of carnitine and 4-N-trimethylaminobutyrate from 6-N-trimethyl-lysine', *The Biochemical journal*, 136: 1083-90.

Devaraj, Sridevi, Peera Hemarajata, and James Versalovic. 2013. 'The human gut microbiome and body metabolism: implications for obesity and diabetes', *Clinical chemistry*, 59: 617-28.

Emsley, Paul, Bernhard Lohkamp, William G Scott, and Kevin Cowtan. 2010. 'Features and development of Coot', *Acta Crystallographica Section D: Biological Crystallography*, 66: 486-501.

Fothergill, Erin, Juen Guo, Lilian Howard, Jennifer C Kerns, Nicolas D Knuth, Robert Brychta, Kong Y Chen, Monica C Skarulis, Mary Walter, and Peter J Walter. 2016. 'Persistent metabolic adaptation 6 years after "The Biggest Loser" competition', *Obesity*, 24: 1612-19.

Friedman S Fau - Fraenkel, G., and G. Fraenkel. 'Reversible enzymatic acetylation of carnitine'.

Fritz, I. 'The effect of muscle extracts on the oxidation of palmitic acid by liver slices and homogenates'.

Fritz, I. B. 1959. 'Action of carnitine on long chain fatty acid oxidation by liver', *Am. J. Physiol.*, 197: 297-304.

Go, Young-Mi, Ken Liu, Zachery Jarrell, Moriah Bellissimo, and Dean Jones. 2020. 'Association of Microbiome Metabolite Valerobetaine with Aging', *Current Developments in Nutrition*, 4: 26-26.

Hulme, Heather, Lynsey M Meikle, Nicole Strittmatter, Justin JJ van der Hooft, John Swales, Ryan A Bragg, Victor H Villar, Michael J Ormsby, Stephanie Barnes, and Sheila L Brown. 2020. 'Microbiome-derived carnitine mimics as previously unknown mediators of gut-brain axis communication', *Science advances*, 6: eaax6328.

Joosten, Robbie P, Jean Salzemann, Vincent Bloch, Heinz Stockinger, A-C Berglund, Christophe Blanchet, Erik Bongcam-Rudloff, Christophe Combet, Ana L Da Costa, and Gilbert Deleage. 2009. 'PDB_REDO: automated re-refinement of X-ray structure models in the PDB', *Journal of applied crystallography*, 42: 376-84.

Kaur, Jaspinder. 2014. 'A comprehensive review on metabolic syndrome', *Cardiology research and practice*, 2014.

Keiser, Michael J, Bryan L Roth, Blaine N Armbruster, Paul Ernsberger, John J Irwin, and Brian K Shoichet. 2007. 'Relating protein pharmacology by ligand chemistry', *Nature biotechnology*, 25: 197-206.

Leung, Ivanhoe KH, Tobias J Krojer, Grazyna T Kochan, Luc Henry, Frank von Delft, Timothy DW Claridge, Udo Oppermann, Michael A McDonough, and Christopher J Schofield.

2010. 'Structural and mechanistic studies on γ-butyrobetaine hydroxylase', *Chemistry & biology*, 17: 1316-24.

Liu, Ken H, Joshua A Owens, Bejan Saeedi, Catherine E Cohen, Moriah P Bellissimo, Crystal Naudin, Trevor Darby, Samuel Druzak, Kristal Maner-Smith, and Michael Orr. 2021. 'Microbial metabolite delta-valerobetaine is a diet-dependent obesogen', *Nature Metabolism*, 3: 1694-705.

Morillas, Montserrat, Eduardo López-Viñas, Alfonso Valencia, Dolors Serra, Paulino Gómez-Puertas, Fausto G Hegardt, and Guillermina Asins. 2004. 'Structural model of carnitine palmitoyltransferase I based on the carnitine acetyltransferase crystal', *Biochemical Journal*, 379: 777-84.

Mossad, Omar, Elisa Nent, Sabrina Woltemate, Shani Folschweiller, Joerg M Buescher, Daniel Schnepf, Daniel Erny, Peter Staeheli, Marlene Bartos, and Antal Szalay. 2021. 'Microbiota-dependent increase in δ-valerobetaine alters neuronal function and is responsible for age-related cognitive decline', *Nature Aging*, 1: 1127-36.

Otwinowski, Zbyszek, and Wladek Minor. 1997. '[20] Processing of X-ray diffraction data collected in oscillation mode.' in, *Methods in enzymology* (Elsevier).

Tars, Kaspars, Janis Leitans, Andris Kazaks, Diana Zelencova, Edgars Liepinsh, Janis Kuka, Marina Makrecka, Daina Lola, Viktors Andrianovs, and Daina Gustina. 2014. 'Targeting carnitine biosynthesis: discovery of new inhibitors against γ-butyrobetaine hydroxylase', *Journal of medicinal chemistry*, 57: 2213-36.

Turnbaugh, P. J., R. E. Ley, M. A. Mahowald, V. Magrini, E. R. Mardis, and J. I. Gordon. 2006. 'An obesity-associated gut microbiome with increased capacity for energy harvest', *Nature*, 444: 1027-31.

Ward, Zachary J, Sara N Bleich, Angie L Cradock, Jessica L Barrett, Catherine M Giles, Chasmine Flax, Michael W Long, and Steven L Gortmaker. 2019. 'Projected US state-level prevalence of adult obesity and severe obesity', *New England Journal of Medicine*, 381: 2440-50.

Chapter 4: Discussion

4.1 General Discussion:

In order for nuclear receptors to regulate transcription they must bind hydrophobic ligands often generated in distal tissues or cellular locations outside of the nucleus. PPARs contain the largest ligand binding pocket of any nuclear receptor, allowing their activity to be affected by changes in the composition of fatty acids, glycerophospholipids, and sterols. The abundance of these ligands can be altered by multiple factors from tissue specific abundances to dietary influx. Pathological processes such as gut dysbiosis, and viral infections can alter host metabolism, leading to dysregulation of NRs. Here I've outline two separate mechanisms by which host lipid transport proteins, and gut microbiome can alter host metabolism and influence the activity of member of the PPAR family. In the appendix I have characterized metabolic changes that occur upon COVID infection, elucidating a driver of disease severity unique to adults.

4.2 Can STARDs modulate PPAR activity?

While not as well characterized as the FABP family, there is evidence to support a role of the steroidogenic acute regulatory (StAR) related transfer domains (STARDs) family of proteins in regulating the NRs, in particular members of the PPAR family. For one, many NRs are activated by the cargo of STARDs. Second, the activity of some NRs is altered in the presence of STARDs. (Kang et al., 2010; Kohn) Third, there is a close link between STARDs and regulation of transcription, demonstrated by mammalian STARDs activating transcription when fused to a DNA binding domain in yeast. (Schrick et al., 2014) Furthermore, in plants, STARDs serve as transcription factors, analogous to the role of the NR LBD in animals. (Schrick et al., 2004) My work is the first report of a direct interaction between STARDs and members of the PPAR family,

that results in repression of PPAR activity. The literature supports a role for other members of this family possibly regulating PPAR activity, and merits further investigation (Figure 4-1).

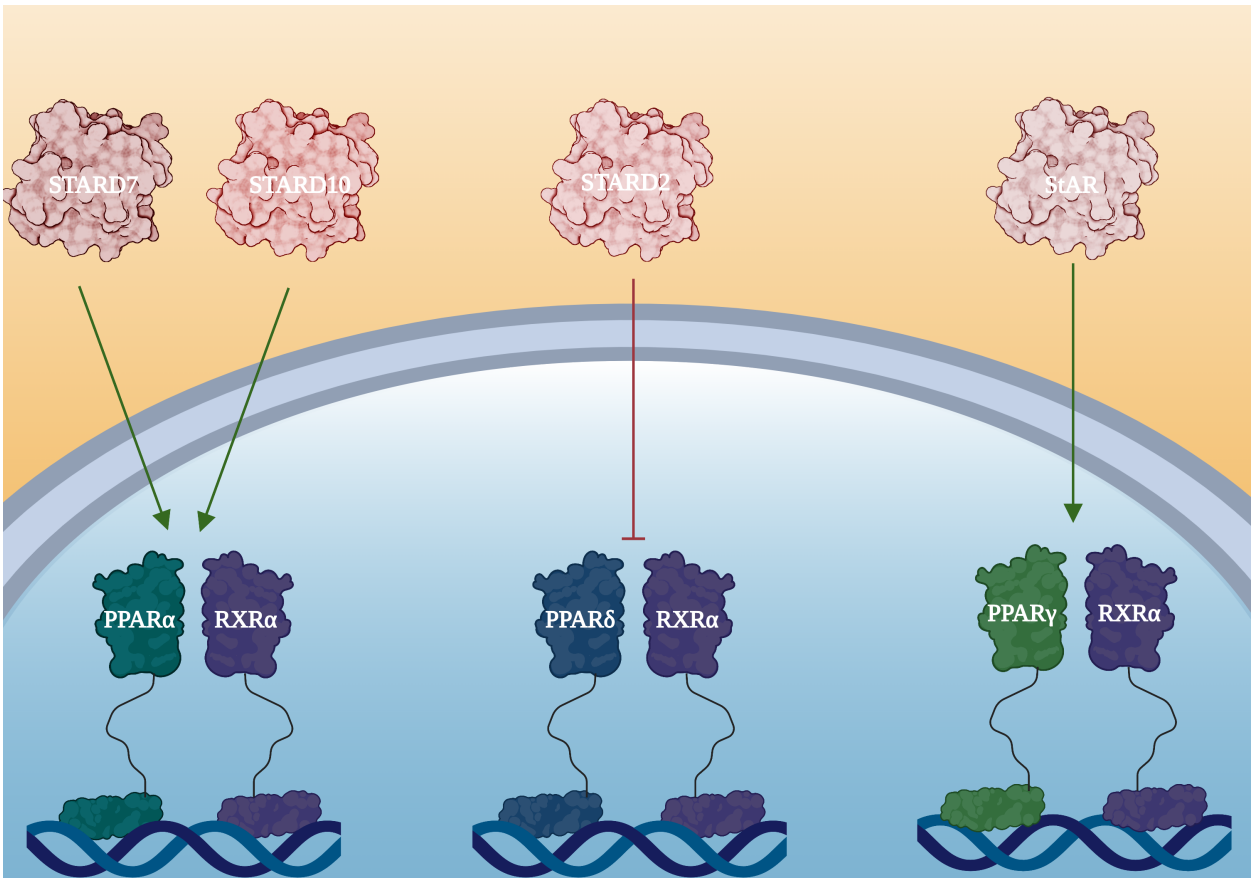

Figure 4- 1: Schematic of experimentally established STARD-PPAR interactions

STARDs (colored in red) interact with and regulate the activity of specific PPARs (colored in hues of blue). Green arrows represent LTP enhancement of NR transcriptional activity, while red lines depict suppression of transcriptional activity.

4.2.1 STARD2—PPARδ

STARD2 (aka phosphatidylcholine transfer protein PC-TP) represents the minimal STARD containing protein. STARD2 modulates membrane and metabolic homeostasis through transfer of PCs synthesized in the ER throughout the cell. Initial characterization of PC-TP deletion showed no defect in alveolar or biliary secretion of PCs leaving many researchers perplexed. Since this initial discovery, much of the actions of PC-TP have been rationalized through its interacting partners, PAX3 and THEM2. The most well characterized of these interacting partners is THEM2, a thioesterase protein whose catalytic activity is responsible for controlling the levels of fatty acyl-CoA in the cell. Previous studies have demonstrated that PC-TP can modulate the activity of PPARα and HNF4α. PC-TP activation of THEM2 thioesterase activity increases the concentration of non-esterified fatty acids, known ligands for both PPARα and HNF4α. Later studies performed in our lab using a high throughput split protein complementation screen between PPARs and LTPs suggest this is likely the mechanism by which PC-TP modulated these nuclear receptors, as PC-TP was shown to interact with PPARδ, but not PPARα or PPARγ.

Our lab previously characterized the role of polyunsaturated fatty acid binding in regulating FABP5 mediated enhancement of PPARδ activity. While the interaction between FABP5 and PPARδ was shown to activate PPARδ, we've now demonstrated that the interaction between PC-TP and PPARδ is repressive. We confirmed this observation by both knockdown and overexpression studies in cells. This interaction seemed to explain aspects of the phenotype observed in a liver specific deletion of PC-TP such as decreased weight gain, improved glucose homeostasis and decreased hepatic lipotoxicity. Similar to the ligand sensitive interaction between FABP5 and PPARδ we hypothesized that PC-TP-PPARδ complex also was sensitive to ligand. To test this, we cultured cells in the serum restricted media, and methionine and choline depleted

(MCD) media. Serum restriction resulted in an increase in the interaction of PC-TP and PPARδ whereas MCD abrogated the interaction. This increase in the PC-TP- PPARδ interaction under serum starvation conditions was complimented by a decrease in the interaction between FABP5 and PPARδ. *In vitro* binding assays suggest the interaction between PC-TP and PPARδ is driven by the LBD, as there was no apparent difference in binding affinity when comparing truncated LBD to the full-length receptor. Domain mapping in cells required full length PPARδ suggesting a dependance on subcellular location, PTMs or ligands present in cells. Our data suggests a role for STARD2 in modulating the activity of PPARδ in an opposing manner to FABP5. Importantly, PPARδ controls many genes involved in the conversion of fatty acids to PC as well as lipid transport proteins, like PC-TP and FABP5. Taken together, this suggests a regulatory feedback loop by which PPARδ can be regulated by FA and PC ligands shuttled by either FABP5 or PC-TP culminating in activation or repression of PPARδ respectively. (Figure 4-1). While my work details the mechanism by which two LTPs are capable of modulating the activity of PPARs there are several other promising targets capable of modulating these receptors.

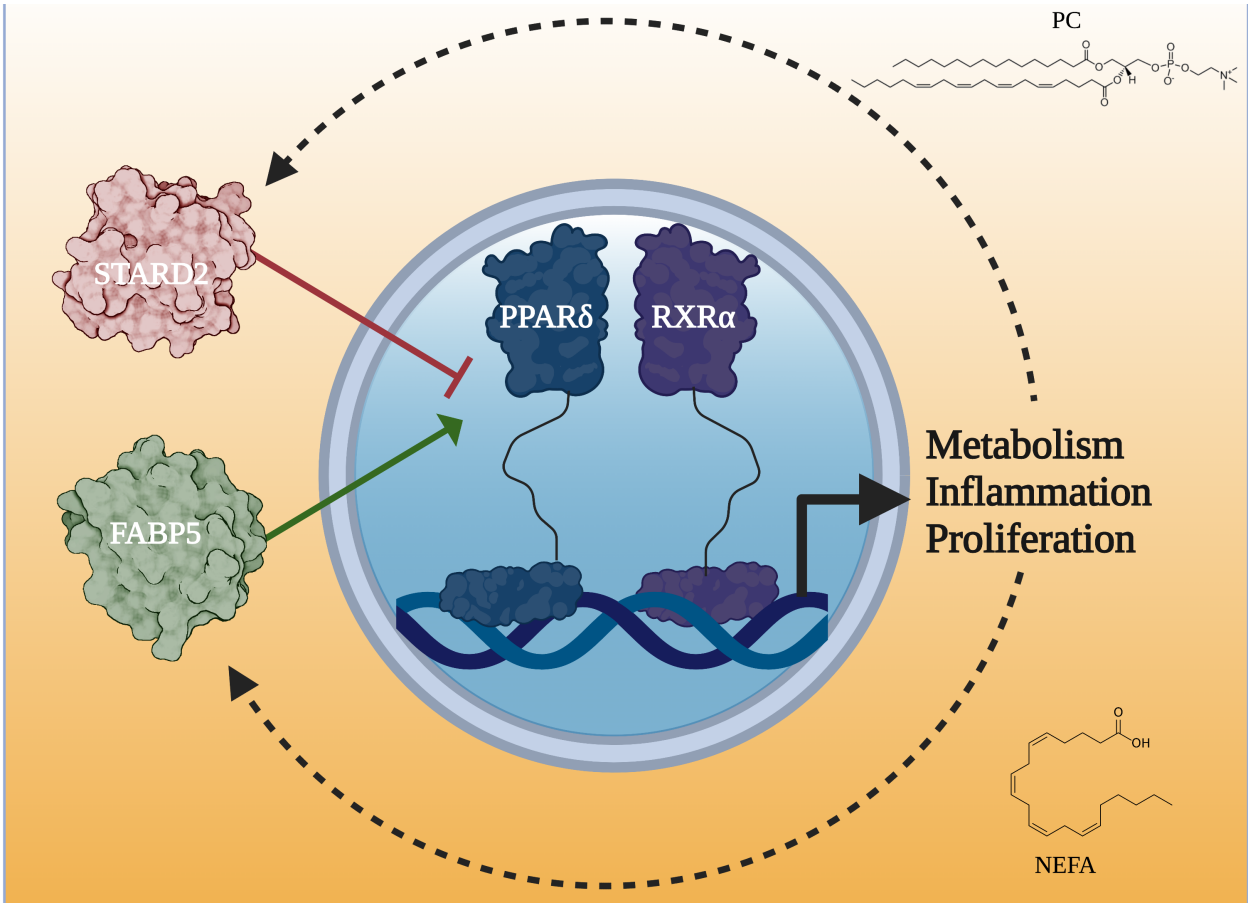

Figure 4- 2: Proposed PPARδ-PC-TP-FABP5 axis.

FABP5 is capable of binding PUFAs, shown in green, leading to an increase in PPARδ regulated transcripts, including FABP5 and PC-TP. In chapter 2 I've characterized the contribution of PCTP to PPARδ regulation. Similar to FABP5, PC-TP may modulate lipid homeostasis through repressing PPARδ signaling in response to altered membrane lipid composition leading to repression of PPARδ mediated transcription.

4.2.3 STARD10–PPARα

STARD10, previously known as PCTP-like-protein, is an intracellular lipid transport protein. Sequence similarity between STARD2 and STARD10 is approximately 50% with STARD10 containing small extensions flanking the START domain. Like PC-TP, a number of studies also support a role for STARD10 in regulating the transcriptional activity of PPARs, specifically PPARα. Similar to PC-TP knockout, mice lacking STARD10 did not show any changes in biliary secretion of PCs but did show changes lung surfactant excretion and the bile acid composition. (Lin et al., 2015) A shift toward taurine conjugated bile acids was observed and driven by increases in the mRNA levels of ACOTs, ASBT and CYP8b1, all of which are known PPARα targets. Unlike the interaction between PC-TP and PPARδ, the interaction between PPARα and STARD10 was shown to enhance rather than repress transactivation. (Ito et al., 2013) One possible explanation for this disparity could be a result of ligand preference, as PPARα has been shown to bind and be activated by PC species whereas the role of PCs in the regulation of PPARδ has yet to be elucidated. (Chakravarthy et al., 2009)

Follow up studies also implicate a role for STARD10 in regulating insulin signaling in beta cells. Generation of the beta cell specific deletion of STARD10 in mice support this, as mice lacking STARD10 presented with deficient insulin signaling. Consistent with these findings, RNAseq experiments on STARD10$^{-/-}$ mice show a number of DEGs known to be regulated by PPARα. (Carrat et al., 2020; Carrat et al., 2017) In addition to binding PC species, STARD10 has also been shown to bind phosphatidylinositol species. This opens the possibility that STARD10 could also affect the activity of other NRs, such as members of the NR5A family.

4.2.4 STARD7–PPAR

Given the implications of STARD2 and STARD10 in regulating PPAR activity, as well as the overlapping ligand specificity, it shouldn't come as a surprise that STARD7 has also been shown to affect PPAR transcription, though evidence of a direct interaction is lacking. Unlike STARD2 and STARD10, STARD7 is primarily localized to the mitochondria where it shuttles PCs. PC are the most prevalent phospholipid in the mitochondria; however, this organelle doesn't have the ability to produce its own PCs. Due to this vital role, homozygous deletion of STARD7 is embryonically lethal in animals. Importantly, STARD7 has been shown to have two isoforms. STARD7-I is the most abundantly expressed, contains a mitochondrial localization sequence, and is the most well characterized. STARD7-II is truncated and has been shown to be localized throughout the cell, including in the nucleus. (Flores-Martin et al., 2013; Horibata and Sugimoto, 2010; Leman et al., 2009)

Haploinsuffcient animals are viable albeit with severe deficiencies. These mice present with spontaneous dermatitis, an enhanced allergen response, increased IgE production and alterations in mucosal homeostasis in the lung. This effect could be partially recapitulated via transferring bone marrow derived cells from STARD7$^{+/-}$ and transferring them to WT mice, suggesting that immune cell dysfunction are sufficient to recapitulate much of the phenotype associated with STARD7$^{+/-}$ mice. (Yang et al., 2015) The resulting phenotype was hypothesized to be due to, in part, regulation of PPARs. Similar to STARD7$^{+/-}$, PPARα $^{-/-}$ in mice present with deficits in eosinophil mediated response to allergens, and increased IgE production. (Woerly et al., 2003)

4.2.5 StAR -PPARγ

StAR, the titular member of this family, is perhaps the most well characterized member due to its vital role in regulating steroidogenesis. In the aforementioned protein complementation

screen, a specific and selective interaction between StAR and PPARγ was detected. Similar to STARD7, StAR contains a mitochondrial localization sequence. Unlike STARD7, StAR is not known to have isoforms where the mitochondrial localization sequence is truncated. Taken together these data either suggests a role for cytosolic PPARγ or a yet to be discovered isoform of StAR, capable of translocating to the nucleus. While not yet characterized, there are several reports that support the ability for STAR to regulate a number of NRs including PPARγ and LXR. (Ning et al., 2009)

For example, over-expression of StAR affected transcripts of genes from a number of steroid binding nuclear receptors. Surprisingly alterations in steady state levels of STAR were also shown to have an effect on the activity of PPARγ. Recent evidence supports a role for PPARγ in binding and being activated by a number of steroid derivatives including 20(OH)T3, 25(OH)T3, and T3. (Slominski et al., 2022) This overlap in ligand specificity combined with alterations in PPARγ controlled transcripts represents a unique signaling cascade leading to an integrated response of PPARγ to a myriad of ligands, outside of the canonical fatty acids.

4.2.6 Other Examples

There are additional LTPs outside of the FABP and START domain family that have been shown to also interact and regulate the activity of NRs. Acyl-CoA binding protein (ACBP) was determined to directly interact with HNF4α *in vitro* and in intact cells (Petrescu et al., 2003). ACBP induces a conformation change in HNF4α, altering the secondary structure composition as determined by circular dichroism (Petrescu et al., 2003). Furthermore, ACBP enhances the transcriptional activity of HNF4α (Petrescu et al., 2003). Oxysterol binding protein related protein 1S (ORP1S) translocates to the nucleus upon stimulation with specific sterols where it interacts with LXRα/β to enhance their transcriptional activity (Lee et al., 2012). α-Synuclein (α-Syn), the

protein implicated in Parkinson's disease, was recently identified to behave similarly to CRABPII, binding to retinoic acid, translocating to the nucleus to enhance the activity of RARs (Davidi et al., 2020). There are likely more LTPs that signal through NRs, yet these remain unexplored at this time. This regulation of nuclear receptor activity via ligand shuttling is not unique to LTPs, as there have been reports of enzymes involved in lipid metabolic processes directly interacting with and regulating the activity of nuclear receptors. An example of this is the ability for PexRAP to regulate the activity of PPARγ. (Lodhi et al., 2017; Lodhi et al., 2012)

4.3 Utility of LTPs as Drug Targets

Despite NRs utility as drug targets, many drugs targeting these receptors have detrimental tissue specific side effects. For instance, troglitazone, a PPARγ agonist, was withdrawn in 2000 due to hepatotoxicity (Scheen, 2001; Wagner and Wagner, 2020) Furthermore, some PPAR targeting drugs promote oncogenesis (Peters et al., 2012). Many NRs are ubiquitously expressed (Figure 4-3 A), like the PPARs, making it difficult to pharmacologically target these receptors in specific tissues, leading to unwanted side effects. However, many LTPs exhibit tissue specific expression (Figure 4-3B). FABPs display distinct tissue expression, with FABP1 and FABP2 being expressed in the liver and small intestines respectively, and FABP7 and FABP8 being expressed exclusively in the brain (Figure 4-3B). This raises the possibility to target PPARs in specific tissues through designing drugs to inhibit signaling through FABPs/STARDs. There is precedence for drugging FABPs, as a small molecule inhibitor of FABP4 protected genetically obese mice from hepatic steatosis, insulin insensitivity, and adipose tissue inflammation (Furuhashi et al., 2007). Similarly, STARD proteins could be leveraged as potential drug targets to modulate PPAR activity. Further work is required to investigate the detailed molecular underpinning of these interactions. For example while I've shown a role for STARD2 in regulating

PPARδ that appears to be ligand sensitive, the role of ligand has yet to be elucidated. Additional work is also need to define the interaction interface, role of PC in regulating PPARδ activity, and interrogate the other STARD-PPAR interactions. This underscores the importance of understanding LTP-NR interactions. Moving forward, more effort should be focused on identifying which LTPs regulate the activity of NRs, and how these interactions can be pharmacologically utilized to treat disease.

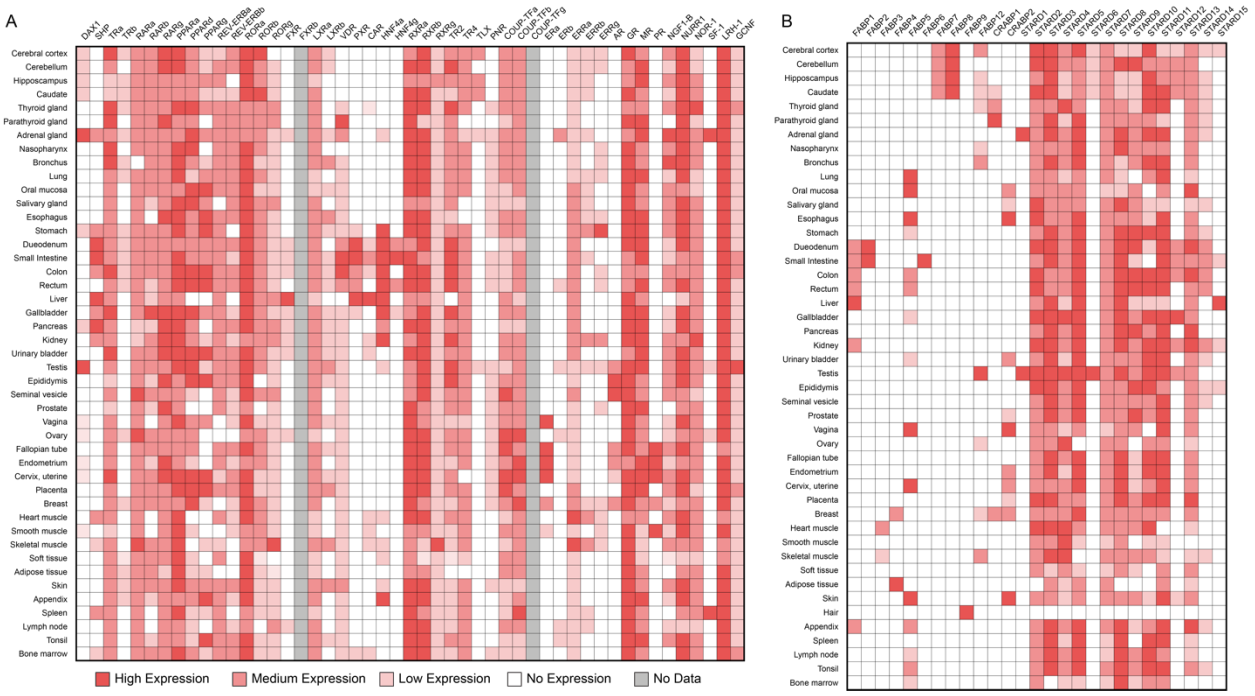

Figure 4- 3: Tissue expression pattern of NRs and LTPs in human tissues.

A.) Human NR and **B.)** LTP expression level in tissues. Most NRs are ubiquitously expressed, but a few NRs display tissue specificity. FABPs display distinct tissue specificity, while most START domains show no tissue specificity. The data was extracted from immunohistochemistry and RNA-seq data from the Human Protein Atlas (HPA; http://www.proteinatlas.org) (Uhlén et al., 2015). The HPA reports immunohistochemistry staining or RNA levels as high, medium, low, or not detected. NRs with no expression data are colored gray.

4.4 How does gut microbiome alter PPAR activity?

In addition to investigating the mechanism by which lipid transport proteins deliver ligands to nuclear receptors, I have also worked to elucidate a mechanism by which gut microbiome derived metabolites exert their effect on host metabolism. Initial work with collaborators from the Jones lab revealed a role for the novel metabolite, valerobetaine in regulating the activity of PPARs. While we posit this is a result of altered ligand abundance, it was not until recently that we have detailed interactions of carnitine analogues with host proteins, capable of explaining these phenomena. Here we identified the biosynthetic route of homocarnitine, a product of the interaction between VB and BBOX. We next characterized these putative interactors of VB and HC using SEA. Using these hits, we show that VB/HC can alter host lipid metabolism by decreasing cantante biosynthesis, and carnitine mediated lipid metabolism. Interestingly previous RNAseq studies identified an increase in PC-TP as a DEG associated with conventionalization under HFD. Increasing levels of PC-TP could further drive dysregulation of PPAR signaling, providing another mechanism by which VB could indirectly affect PPAR activity. Further work should focus on the role of other gut microbiome derived metabolites in modulating host nuclear receptors function, as well as investigate the role LTPs play in responding to metabolic adaptations elicited by such metabolites.

4.5 What roles do PPARs play in viral infections?

In the appendix, I have also investigated the manner by which SARs-CoV-2 effects host metabolism, and plasma protein composition. While not centric on PPAR regulation there is a well characterized role for members of this family in regulating inflammatory and metabolic processes known to be dysregulated in viral infections. Additionally exercise and diet have been shown to be important prophylactic treatments to attenuate the severity of SARs-CoV-2. Our

characterization of the proteome, metabolome and lipidome of adults and children known to be infected with COVID-19 support previous findings which show metabolic dysregulation. Our thorough characterization identifies elevated fibrinogen as a unique driver of COVID severity in adults while a heightened inflammatory state drives metabolic dysregulation in children with COVID-19. While not the focus of the work present in this dissertation, LTPs have also been shown to be hijacked by viruses, begging the question, could altered NR activity as a result of viral infection be driven, in part through dysregulation of their cognate LTP? (Avula et al., 2021)

4.6 Conclusion:

The work present here expands the knowledge and scope of how PPARs are regulated by host and pathological processes. Nuclear receptors have evolved to respond to ligands and adjust their transcription of genes to restore homeostasis. Dysregulation of these processes has been implicated in a number of disease states. One of the most important conclusions from these studies centers around an emerging paradigm by which FABPs and STARDs are capable of regulating transcription of PPARs. These studies open a new mechanism to target receptors known to play important roles in metabolic dysregulation driven by diet, gut dysbiosis, or viral infections. While PPARs have realized much of their potential as therapeutic targets, activation of these receptors in certain tissues leads to the development of cancer, stifling their potential. Discovery and characterization of LTP-PPAR interactions opens the exciting possibility for tissue specific modulation of these receptors, allowing for activation or repression, in a pointed manner mitigating potential side effects. Further work to investigate the role these LTPs play in regulating pathogenesis of metabolic disease driven by altered gut microbiome, or inflammation driven by viral infection would further support lipid transport proteins as viable drug targets.

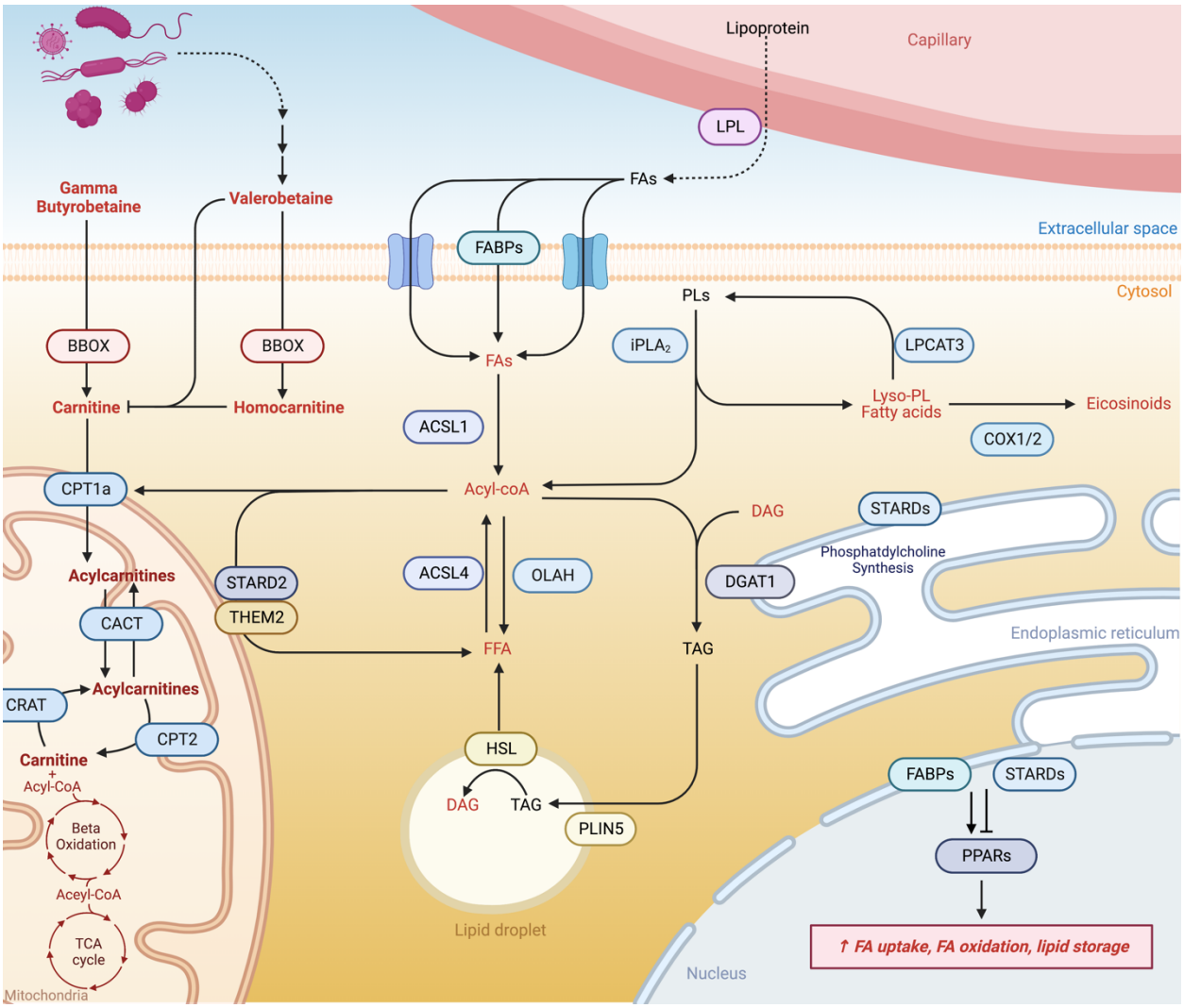

Figure 4- 4: Regulation of PPARs by host and pathogenic processes.

Taken together the aforementioned chapters detail signaling through PPARs controlled by lipid transport protein or gut microbiome derived metabolites. All of the proteins present in this figure are transcriptionally regulated by PPARs. Chapter 2 outlines the novel mechanism by which PC-TP regulates PPARδ transactivation of genes opposing the characterized role of FABP5. In Chapter 3, we show a role for a gut microbiome analyte delta-valerobetaine in regulating PPARδ. PPARδ transcriptionally controls a number of genes responsible for connecting these two regulatory arms in response to alterations in diet, all shown above. PPARs are known to regulate the expression of all proteins in the carnitine pathway. PPARδ specifically regulates the expression

of PLA2, an enzyme responsible for the generation of lyso-PC and free fatty acids(FFA) from PCs, as well as LPCAT3, which opposes this function. PPARs also modulates both OLAH and ACSL4, which regulate the pool of acyl-CoA species. Importantly PPARs have also been shown to regulate CPT1, CPT2, BBOX and proteins in the biosynthesis of PCs. PPARs regulation of the acyl-CoA pool in concert with the PC-TP-THEM2 complex leads to the generation of FFA which, in the context of over nutrition, are shunted into PL synthesis. Alterations in the levels of these metabolites can be relayed to PPARs in the nucleus, resulting in either activation or repression of FA uptake, oxidation and storage.

4.7 References:

Avula K, Singh B, Kumar PV and Syed GH (2021) Role of lipid transfer proteins (LTPs) in the viral life cycle. *Frontiers in microbiology* **12**.

Carrat GR, Haythorne E, Tomas A, Haataja L, Müller A, Arvan P, Piunti A, Cheng K, Huang M and Pullen TJ (2020) The type 2 diabetes gene product STARD10 is a phosphoinositide-binding protein that controls insulin secretory granule biogenesis. *Molecular metabolism* **40**: 101015.

Carrat GR, Hu M, Nguyen-Tu M-S, Chabosseau P, Gaulton KJ, van de Bunt M, Siddiq A, Falchi M, Thurner M and Canouil M (2017) Decreased STARD10 expression is associated with defective insulin secretion in humans and mice. *The American Journal of Human Genetics* **100**(2): 238-256.

Chakravarthy MV, Lodhi IJ, Yin L, Malapaka RR, Xu HE, Turk J and Semenkovich CF (2009) Identification of a physiologically relevant endogenous ligand for PPARalpha in liver. *Cell* **138**(3): 476-488.

Davidi D, Schechter M, Elhadi SA, Matatov A, Nathanson L and Sharon R (2020) α-Synuclein Translocates to the Nucleus to Activate Retinoic-Acid-Dependent Gene Transcription. *iScience* **23**(3): 100910.

Flores-Martin J, Rena V, Angeletti S, Panzetta-Dutari GM and Genti-Raimondi S (2013) The lipid transfer protein StarD7: structure, function, and regulation. *International journal of molecular sciences* **14**(3): 6170-6186.

Furuhashi M, Tuncman G, Gorgun CZ, Makowski L, Atsumi G, Vaillancourt E, Kono K, Babaev VR, Fazio S, Linton MF, Sulsky R, Robl JA, Parker RA and Hotamisligil GS (2007) Treatment of diabetes and atherosclerosis by inhibiting fatty-acid-binding protein aP2. *Nature* **447**(7147): 959-965.

Horibata Y and Sugimoto H (2010) StarD7 mediates the intracellular trafficking of phosphatidylcholine to mitochondria. *Journal of Biological Chemistry* **285**(10): 7358-7365.

Ito M, Yamanashi Y, Toyoda Y, Izumi-Nakaseko H, Oda S, Sugiyama A, Kuroda M, Suzuki H, Takada T and Adachi-Akahane S (2013) Disruption of Stard10 gene alters the PPARα-

mediated bile acid homeostasis. *Biochimica et Biophysica Acta (BBA)-Molecular and Cell Biology of Lipids* **1831**(2): 459-468.

Kang HW, Kanno K, Scapa EF and Cohen DE (2010) Regulatory role for phosphatidylcholine transfer protein/StarD2 in the metabolic response to peroxisome proliferator activated receptor alpha (PPARalpha). *Biochimica et biophysica acta* **1801**(4): 496-502.

Kohn J *Novel Allosteric Communication in Nuclear Receptor Activation*.

Lee S, Wang PY, Jeong Y, Mangelsdorf DJ, Anderson RG and Michaely P (2012) Sterol-dependent nuclear import of ORP1S promotes LXR regulated trans-activation of apoE. *Experimental cell research* **318**(16): 2128-2142.

Leman ES, Magheli A, Yong KMA, Netto G, Hinz S and Getzenberg RH (2009) Identification of nuclear structural protein alterations associated with seminomas. *Journal of cellular biochemistry* **108**(6): 1274-1279.

Lin S, Ikegami M, Moon C, Naren AP and Shannon JM (2015) Lysophosphatidylcholine acyltransferase 1 (LPCAT1) specifically interacts with phospholipid transfer protein StarD10 to facilitate surfactant phospholipid trafficking in alveolar type II cells. *Journal of Biological Chemistry* **290**(30): 18559-18574.

Lodhi IJ, Dean JM, He A, Park H, Tan M, Feng C, Song H, Hsu F-F and Semenkovich CF (2017) PexRAP inhibits PRDM16-mediated thermogenic gene expression. *Cell reports* **20**(12): 2766-2774.

Lodhi IJ, Yin L, Jensen-Urstad AP, Funai K, Coleman T, Baird JH, El Ramahi MK, Razani B, Song H and Fu-Hsu F (2012) Inhibiting adipose tissue lipogenesis reprograms thermogenesis and PPARγ activation to decrease diet-induced obesity. *Cell metabolism* **16**(2): 189-201.

Ning Y, Bai Q, Lu H, Li X, Pandak WM, Zhao F, Chen S, Ren S and Yin L (2009) Overexpression of mitochondrial cholesterol delivery protein, StAR, decreases intracellular lipids and inflammatory factors secretion in macrophages. *Atherosclerosis* **204**(1): 114-120.

Peters JM, Shah YM and Gonzalez FJ (2012) The role of peroxisome proliferator-activated receptors in carcinogenesis and chemoprevention. *Nature reviews Cancer* **12**(3): 181-195.

Petrescu AD, Payne HR, Boedecker A, Chao H, Hertz R, Bar-Tana J, Schroeder F and Kier AB (2003) Physical and functional interaction of Acyl-CoA-binding protein with hepatocyte nuclear factor-4 alpha. *The Journal of biological chemistry* **278**(51): 51813-51824.

Scheen AJ (2001) Thiazolidinediones and liver toxicity. *Diabetes & metabolism* **27**(3): 305-313.

Schrick K, Bruno M, Khosla A, Cox PN, Marlatt SA, Roque RA, Nguyen HC, He C, Snyder MP, Singh D and Yadav G (2014) Shared functions of plant and mammalian StAR-related lipid transfer (START) domains in modulating transcription factor activity. *BMC biology* **12**: 70.

Schrick K, Nguyen D, Karlowski WM and Mayer KF (2004) START lipid/sterol-binding domains are amplified in plants and are predominantly associated with homeodomain transcription factors. *Genome biology* **5**(6): R41.

Slominski AT, Kim TK, Slominski RM, Song Y, Janjetovic Z, Podgorska E, Reddy SB, Song Y, Raman C and Tang EK (2022) Metabolic activation of tachysterol3 to biologically active hydroxyderivatives that act on VDR, AhR, LXRs, and PPARγ receptors. *The FASEB Journal* **36**(8): e22451.

Uhlén M, Fagerberg L, Hallström BM, Lindskog C, Oksvold P, Mardinoglu A, Sivertsson Å, Kampf C, Sjöstedt E, Asplund A, Olsson I, Edlund K, Lundberg E, Navani S, Szigyarto CA, Odeberg J, Djureinovic D, Takanen JO, Hober S, Alm T, Edqvist PH, Berling H, Tegel

H, Mulder J, Rockberg J, Nilsson P, Schwenk JM, Hamsten M, von Feilitzen K, Forsberg M, Persson L, Johansson F, Zwahlen M, von Heijne G, Nielsen J and Pontén F (2015) Proteomics. Tissue-based map of the human proteome. *Science (New York, NY)* **347**(6220): 1260419.

Wagner N and Wagner K-D (2020) PPAR beta/delta and the hallmarks of cancer. *Cells* **9**(5): 1133.

Woerly G, Honda K, Loyens M, Papin J-P, Auwerx J, Staels B, Capron M and Dombrowicz D (2003) Peroxisome proliferator–activated receptors α and γ down-regulate allergic inflammation and eosinophil activation. *The Journal of experimental medicine* **198**(3): 411-421.

Yang L, Lewkowich I, Apsley K, Fritz JM, Wills-Karp M and Weaver TE (2015) Haploinsufficiency for Stard7 is associated with enhanced allergic responses in lung and skin. *The Journal of Immunology* **194**(12): 5635-5643.

Appendix I: Multiplatform Analyses Reveal Distinct Drivers of Systemic Pathogenesis in Adult Versus Pediatric COVID-19

Samuel Druzak[1]*, Elizabeth Iffrig[2&6]*, Blaine R. Roberts[1&5], Tiantian Zhang[2a], Kirby S. Fibben[6], Yumiko Sakurai[3&6], Hans P. Verkerke[4], Christina A. Rostad[3&12f], Ann Chahroudi[3&12f], Frank Schneider[4], Andrew Kam Ho Wong[4&7], Anne Roberts[1&5], Joshua D. Chandler[3b&12], Susan O. Kim[3b], Mario Mosunjac[4&7c], Marina Mosunjac[4], Rachel Geller[4&10], Igor Albizua[4], Sean R. Stowell[8], Connie Arthur[8], Evan J. Anderson[3,2&12], Anna Ivanova[2a], Jun Ahn[2a], Snow Liu[2a], Kristal Maner-Smith[2a], Thomas Bowen[2a], Mirko Paiardini[4&7c], Steve Bosinger[2,4,7cd&9], John D. Roback[4], Deanna Kulpa[4,7c,9e&11], Guido Silvestri[4&7c], Wilbur A. Lam[3,6&12g**], Eric A. Ortlund[1&2a**] and Cheryl L. Maier[4**]

Department of Biochemistry[1], Emory University School of Medicine, Atlanta, GA, USA:
Department of Medicine[2], Emory University School of Medicine, Atlanta, GA, USA:
Emory Integrated Metabolomics and Lipidomics Core[a]
Department of Pediatrics[3], Emory University School of Medicine, Atlanta, GA, USA:
Division of Pulmonology, Allergy & Immunology, Cystic Fibrosis, and Sleep Medicine[b]
Department of Pathology and Laboratory Medicine[4], Emory University School of Medicine, Atlanta, GA, USA:
Department of Neurology[5], Emory University School of Medicine, Atlanta, GA, USA;
Wallace H Coulter Department of Biomedical Engineering[6], Georgia Institute of Technology and Emory University, Atlanta, GA, USA;
Emory National Primate Research Center[7], Atlanta, Ga, USA;
Division of Microbiology and Immunology[c]
Emory Genomics Core Laboratory[d]
Department of Pathology [8], Brigham and Women's Hospital, Harvard Glycomics Center, Harvard Medical School, Boston, MA, USA;
Emory Vaccine Center[9], Atlanta, GA, USA;
Virology and molecular biomarkers Core[e]
DeKalb County Medical Examiner[10], Decatur, GA, USA;
Center for AIDS Research[11], Emory university, Atlanta, Ga, USA;
Children's Healthcare of Atlanta[12], Atlanta, GA, USA;
Center for Childhood Infections and Vaccines[f]
Aflac Cancer and Blood Disorders Center[g]

This chapter is currently in review at Cell.

G.S., W.L., E.A.O., and C.M. conceived, designed and, oversaw the study. E.I. developed video analysis workflow for cell membrane deformability and red cell aggregation assays and acquired experimental data for these experiments. Y.S. assisted with experimental and microfluidics device design as well as microscopy image collection. K.F manufactured microfluidic devices cultured with endothelial cells and completed glycocalyx degradation assays. A.I., J.A., S.L., K.M.S., B.R., T.B., Prepared samples and acquired MS data. T.Z. Integrated these analyses. S.A.D analyzed integrated data, generated figures for MS analysis, and wrote the corresponding results and discussion sections and any intellectual contributions therein.

AI.1 Summary:

The pathogenesis of multi-organ dysfunction associated with severe SARS-CoV-2 infection remains poorly understood. Endothelial damage has been identified as a driver of COVID-19 severity, yet the mechanisms underlying endotheliopathy remain elusive. A multiomics approach identified upregulated fluid shear stress-responsive pathways in critically ill COVID-19 adults as compared to non-COVID critically ill adults. Mechanistic microvasculature-on-chip studies revealed fibrinogen-mediated red blood cell aggregation directly damages the endothelial glycocalyx. Notably, this mechanism appears unique to COVID-19, with non-COVID sepsis causing microvascular damage related to increased red blood cell membrane rigidity. Multiomic analyses in pediatric patients with acute COVID-19 or the post-infectious multi-inflammatory syndrome in children (MIS-C) demonstrate little overlap in plasma cytokine and metabolite changes between adults with COVID-19 and children with COVID-19 or MIS-C. These findings link altered red blood cell biomechanics with endotheliopathy in adult patients with severe COVID-19 and highlight differences in the key mediators of pathogenesis between adults and children.

AI.2 Introduction

The spectrum of clinical disease resulting from SARS-CoV-2 infection is broad, ranging from mild to severe COVID-19 in symptomatic adults and including a post-infectious multisystem inflammatory syndrome in children (MIS-C). Large-scale epidemiologic studies demonstrate that up to 5% of symptomatic adults with COVID-19 develop critical illness, with affected patients experiencing acute respiratory distress syndrome (ARDS), organ failure and sometimes death (Wu and McGoogan, 2020). The rate of severe COVID-19 is much lower in children; nevertheless, 10-33% of those requiring hospitalization are critically ill (Delahoy et al., 2021; Kim et al., 2020; Siegel et al., 2021). While the primary clinical manifestations of COVID-19 reflect infected epithelium of the upper and lower respiratory tracts, multi-organ involvement is common in severely ill adult patients (Gupta et al., 2020; Wiersinga et al., 2020). In addition, children with post-infectious MIS-C experience systemic manifestations, which may occur after mild or even asymptomatic infection (Feldstein et al., 2020; Riphagen et al., 2020; Viner and Whittaker, 2020). Previous studies generating proteomic, metabolomic and transcriptomic data from patients with COVID-19 have uncovered alterations in numerous biological pathways associated with clinical severity (D'Alessandro et al., 2020; Danlos et al., 2021; Diorio et al., 2021; Shen et al., 2020; Su et al., 2020). Nevertheless, to our knowledge, pairing of multiomic datasets with mechanistic studies to uncover mediators of severe disease in both adult and pediatric patients has not been performed.

Increasing evidence suggests much of the organ dysfunction associated with severe COVID-19 results from widespread endothelial dysfunction and microvascular thrombosis (Libby and Luscher, 2020; Lowenstein and Solomon, 2020; Rapkiewicz et al., 2020). The etiology of microthrombi appears multifactorial, with descriptions of hypercoagulability resulting from

elevations in prothrombotic factors, like the hepatic acute phase protein fibrinogen or endothelial-derived factor VIII and von Willebrand factor, as well as blood hyperviscosity (Goshua et al., 2020; Maier et al., 2020; Ranucci et al., 2020). Furthermore, endothelial damage and vasculopathy appear to be exacerbated by formation of neutrophil extracellular traps (NETs), complement activation, and increases in inflammatory cytokines (Barnes et al., 2020; Holter et al., 2020; Libby and Luscher, 2020; Lowenstein and Solomon, 2020; Middleton et al., 2020; Teuwen et al., 2020). The extent of these features may be unique to SARS-CoV-2 infection, as one autopsy series demonstrated severe endothelial injury and nine-times more alveolar capillary microthrombi in patients expiring from COVID-19 compared to those expiring from H1N1 influenza (Ackermann et al., 2020). Although endothelial cells express ACE2, the receptor used by SARS-CoV-2 for cellular entry, evidence supporting the presence of virus particles in the microvasculature that would account for the degree of systemic endotheliopathy has been limited and remains controversial. Recent data instead suggests endothelial damage arises from indirect processes related to complement and immune-mediated pathways resulting in microvascular injury (Nicosia et al., 2021).

Blood rheology, the behavior of blood flow at the cellular level, is a major determinant of endothelial health and function, and biophysical changes in blood flow can cause pathologic endothelial damage and associated microvascular clotting. Red blood cell (RBC) aggregation and membrane stiffness are major determinants of blood flow, and others have correlated these parameters with mortality in critically ill patients prior to the COVID-19 pandemic (Donadello et al., 2015; Muranaka et al., 2006). In addition, intravital studies using sublingual darkfield microscopy in critically ill patients have shown altered microvascular perfusion patterns and an associated volume loss of the endothelial glycocalyx, the proteoglycan complex involved in

maintaining endothelial health (Rovas et al., 2021). However, the phenomenon remains understudied and has not been reported in patients with SARS-CoV-2 infection. Targeting the pro-inflammatory and pro-thrombotic factors in the plasma of critically ill COVID-19 patients has been identified as a potential therapeutic intervention (Truong et al., 2021), yet the contribution of altered plasma components in influencing the microvascular and endothelial biomechanical environment in COVID-19 remain unexplored.

Here, we undertook a combined multiomic and microfluidic-based approach to better understand the plasma and biophysical factors contributing to endothelial dysfunction and systemic disease in COVID-19. Through targeted and untargeted proteomic, lipidomic and metabolomic analyses, we identify complement and coagulation pathways as common elements in both adult and pediatric populations, and a unique pathway in adults related to fluid shear stress. Newly developed microfluidic analyses, modeling the hemodynamic environment of the microvasculature and incorporating human endothelial cells and blood components, suggest this pathway reflects changes in the biophysical properties of blood related to fibrinogen-induced RBC aggregation that directly damages the endothelial glycocalyx. Notably, this mechanism appears distinct from the microvascular damage related to increased RBC rigidity we observe in association with non-COVID sepsis. We propose that alterations in the biomechanical properties of blood are an important and previously unappreciated contributor to the widespread endotheliopathy and organ dysfunction of adults with severe COVID-19. In contrast, integrative cytokine and multiomic analyses demonstrate strikingly little overlap between adult and pediatric cohorts, underscoring the role of immune dysregulation in pediatric disease and the dichotomous nature of pathophysiology between these populations.

AI.3 Results

AI.3.1 Integrated multiomic analyses identify proteomic alterations in coagulation and fluid shear stress response pathways in adults with COVID-19

Given the systemic disease manifestations observed in COVID-19, we hypothesized that characterization of the plasma lipidome, metabolome and proteome from severely ill patients might inform our understanding of novel mechanisms driving disease pathogenesis. We were most interested in identifying disease-related pathways unique to COVID-19, as compared to non-COVID severe illness. To do so, plasma was obtained from critically ill PCR-confirmed COVID-19-positive patients (COVID+, n=15) and from critically ill PCR-confirmed COVID-19-negative patients (COVID-, n=10) for multiomic investigation (Figure AI-1 A). Notably, all patient samples in this adult cohort were obtained on a single day in April 2020, before the use of now standard therapies or the availability of vaccines. Patient demographics and relevant clinical characteristics are provided in the Supplemental materials (Table AI-1).

Table AI - 1: Patient Demographics for Adult Multiomic Studies, n=25.

	COVID Cohort, n=15	Sepsis Cohort, n=10
Age, median years (range)	70 (49 – 92)	65 (31 – 84)
Women, number (%)	7 (47%)	1 (10%)
Race, number (%)		
African American	12 (80%)	5 (50%)
White	3 (20%)	4 (40%)
Asian/Pacific Islander	0	1 (10%)
Body Mass Index, mean (SD)	33 (11)	29 (14)
Sample Time, mean number days post diagnosis (SD)	15 (12)	14 (13)
Illness Severity, median WHO COVID ordinal scale (range)	7 (5 – 8)	N/A
Non-COVID Underlying Diagnosis, number (%)		4 (40%)
Sepsis		5 (50%)
ARDS	N/A	1 (10%)
Cerebrovascular Accident		1 (10%)
Acute Leukemia		1 (10%)
Cardiogenic Shock		
Interventions, number (%)		
Renal-replacement therapy	7 (47%)	2 (20%)
Mechanical Ventilation	13 (87%)	5 (50%)
Vasopressor Support	9 (60%)	4 (40%)
Medications, number (%)		
Therapeutic Anticoagulation	11 (73%)	4 (40%)
Dexamethasone	1 (7%)	3 (30%)
Tocilizumab/Baricitinib/Remdesivir	0	0
Hydroxychloroquine	1 (7%)	0
Co-infections, number (%)		
Bacterial Pneumonia	1 (7%)	1 (10%)
Fungal Pneumonia	3 (20%)	2 (20%)
Urinary Tract Infection	1 (7%)	0
Clostridium difficile Colitis	1 (7%)	0
Co-morbidities		
Hypertension	11 (73%)	5 (50%)
Diabetes mellitus	9 (60%)	2 (20%)
Renal Disease	4 (27%)	3 (30%)

Obesity	6 (40%)	2 (20%)
Asthma or COPD	2 (13%)	4 (40%)
30 Day Disposition (%)		
Death/Hospice	5 (33%)	2 (20%)
Hospitalized/Transfer (inpatient rehab, long term acute care or other facility)	7 (47%)	1 (10%)
Home	3 (20%)	7 (70%)

Untargeted and targeted lipidomic and metabolomic analyses identified 88 significant, unique and named analytes. Significant alterations were detected in xanthine, acylcarnitines, polyunsaturated fatty acids (PUFA) and kynurenine (Figure AI-2), consistent with previous reports (D'Alessandro et al., 2020; Schwarz et al., 2020; Shen et al., 2020; Shi et al., 2021; Song et al., 2020; Thomas et al., 2020b). Despite differences between the cohorts, no analytes or pathways stood out for explaining the widespread endotheliopathy associated with severe COVID-19; therefore, we focused on changes detected in plasma proteomes. Label-free proteomics yielded over 100,000 peptide spectral matches, with approximately 8000 unique peptides identified that mapped to 625 unique proteins (Figure AI-1 A). Using a cut-off of a P adjusted value <0.1 and an abundance ratio of +/- 1.3, 109 differentially abundant proteins (DAPs) were detected in COVID+ versus COVID- patients, with balanced sampling indicating that identified DAPs were not an artifact of severe illness (Figure AI-1 B). Principal component analysis (PCA) of the identified DAPs resulted in clustering and partial separation of COVID+ and COVID- patients (Figure AI-1 C). Of the 109 identified DAPs, 97 were up-regulated and 12 were down-regulated in COVID+ patients compared to COVID- patients (Figure AI-1 D & G).

We next performed Kyoto Encyclopedia of Genes and Genomes (KEGG) pathway analysis inputting up-regulated DAPs from the COVID+ cohort. In line with previous reports (D'Alessandro et al., 2020; Shen et al., 2020), our analysis demonstrated enrichment in complement and coagulation cascades, neutrophil extracellular trap formation, and extracellular matrix protein (ECM) interactions (Figure 1E). KEGG analysis also detected alterations in pathways associated with many of the co-morbidities known as risk factors for increased COVID-19 severity, such as diabetes (AGE-RAGE signaling; albeit not significant) and hypertension (renin-angiotensin system). Pathway analysis uncovered differences related to fluid shear stress

response and perturbations in glycan homeostasis that have not been reported previously, but which support clinical observations of altered blood flow and RBC hemodynamics as unique aspects of COVID-19 pathogenesis (Figure 1E). Specific proteins associated with these pathways include various sheddases, enzymes involved in remodeling of the endothelial glycocalyx, and markers of cell stress. Analysis by organ system demonstrated that the most significant alterations were related to the liver, with both up- and down-regulated proteins in COVID+ patients mapping to the liver when compared to expression profiling from the human genome atlas (Figure 1F). This aligns with the induction of a strong hepatic acute phase response to SARS-CoV-2 infection, reflected by significant increases in the presence of all three fibrinogen chains (Figure 1H) and additionally supported by the most significant KEGG pathway being the complement and coagulation cascades.

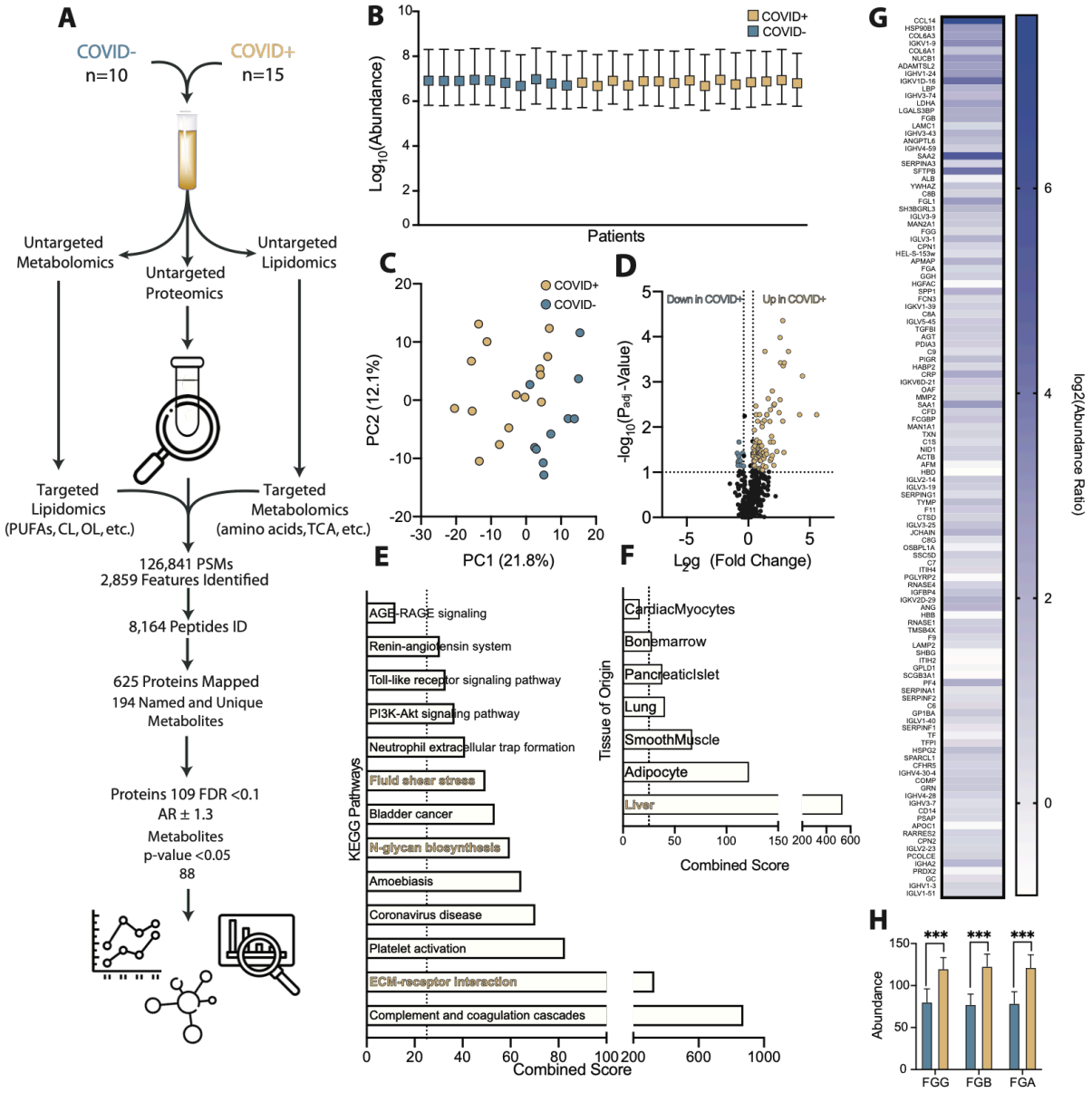

Figure AI - 1: Multiomic analysis of adults with severe COVID uncovers fluid shear stress. **A.)** Schematic overview of the approach and identified species in the adult cohorts of COVID+ and COVID- critically ill patients. **B.)** Relative abundance of detected peptides per patient sample. **C.)** Principal component analysis (PCA) plot of proteomics data demonstrating clustering and partial separation of plasma samples from COVID+ and COVID- adults**. D.)** Volcano plot showing relative distribution of identified proteins. **E.)** KEGG pathway analysis of differentially abundant proteins (DAPs) highly upregulated (Padj >0.1 AR>1.4) in COVID+ patients highlights novel

alterations in fluid shear stress response pathways (gold) and previously reported changes in ECM receptor interactions (also gold). **F.)** Comparison of DAPs to the human genome atlas showing relative origin of proteins identified highlights perturbations in liver, lung, and immune cell homeostasis. **G.)** Heat map of DAPs identified by proteomics analysis that are altered in COVID+ adults as compared to COVID- adults. **H.)** The abundance of all 3 chains of the hepatic acute phase protein fibrinogen is increased in COVID+ compared to COVID- adult patients, ***p-value <0.01.

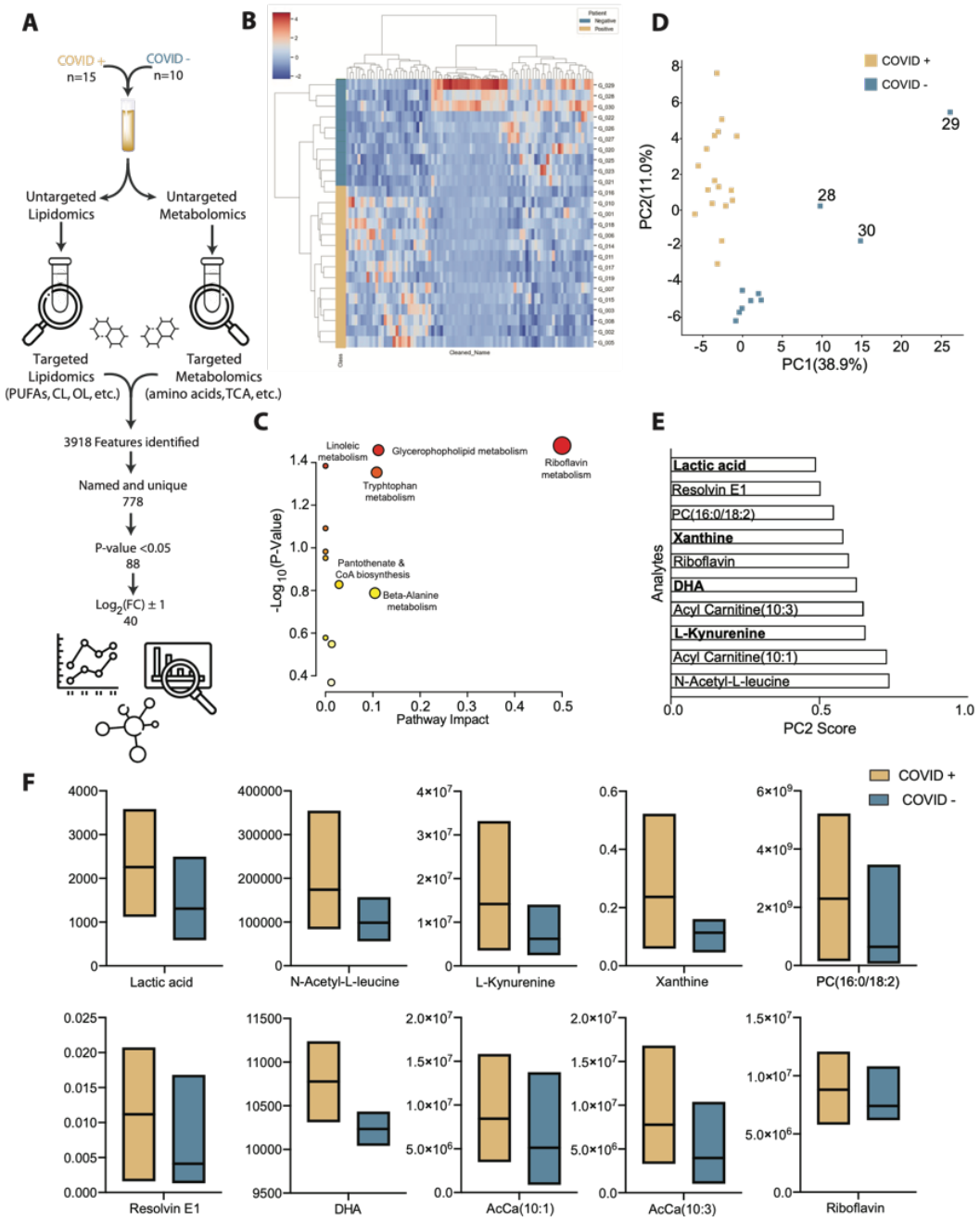

Figure AI - 2:Lipidomic and metabolomic analyses of adult cohort reveal alterations in Lactic acid, Xanthine, DHA and L-Kynurenine in COVID-19, consistent with findings from previous reports.

A.) Workflow showing the targeted and untargeted assays used to interrogate lipid and metabolite changes occurring in COVID-19 patients (COVID+) compared to non-COVID patients (COVID-). **B.)** Heatmap with unbiased hierarchal clustering using significant analytes from COVID+

versus COVID- adults. **C.)** Bubble plot of analytes mapped to KEGG pathways using metaboanalyst 5.0. **D.)** Principal component analysis (PCA) using statistically significant metabolites. **E.)** and **F.)** Top 10 analytes that define separation of principal component two with abundances as determined by mass spectrometry (MS) analysis.

AI.3.2 Fibrinogen mediates red blood cell aggregation under static and physiological flow conditions

We next performed a series of rheological studies to investigate the mechanism driving the significant difference in COVID+ versus COVID- adults related to fluid shear stress, a reflection of endothelial injury and dysfunction from altered blood flow. Clinical observations revealed increased RBC sedimentation in COVID-19 patients correlating strongly with levels of fibrinogen (Figure AI-3 A). We also noted increased RBC sedimentation and marked RBC aggregation under static conditions in blood from COVID-19 patients compared with that from healthy volunteers (Figure AI-3 B), consistent with findings reported previously (Nader et al., 2022; Russo et al., 2022). To investigate the consequences of this phenomenon under physiological flow conditions, we tested the influence of fibrinogen on RBC aggregation using advanced microfluidic devices. Washed RBCs isolated from a healthy blood group O volunteer were combined with increasing concentrations of purified fibrinogen in PBS ranging from 0-900 mg/dL, spanning both the normal range (approximately 200-400 mg/dL) and reported median level in critically ill adult COVID-19 patients (approximately 800 mg/dL) (Ranucci et al., 2020).

Suspensions of RBCs and fibrinogen were perfused through microfluidic devices with a hydraulic diameter of 17.5 μm, which approximates the peri-capillary vessel size and associated physiologic flow rate (Figure AI-3 C). Video microscopy was obtained for each condition for aggregation analysis (Figure AI-3 D). Differential cell velocity clusters (DCVCs) were used as a measure of RBC aggregation and defined as groups of RBCs traveling at the same relative velocity and in close physical proximity to each other. These DCVCs were quantified from velocity fields using a previously described method which employs a commercially available video tracking algorithm (Szafraniec et al., 2022) and additional custom software (see STAR methods as well as

Figure AI- 4 for detailed explanation of image processing workflow). These experiments revealed an increase in the number of DCVCs with increasing fibrinogen levels (Figure AI-3 E). Additionally, the highest fibrinogen condition showed the largest size and widest spread of DCVC size (Figure AI-3 F). DCVCs detected at a fibrinogen concentration of 900 mg/dL were significantly larger than those in any other concentration (198±100 pixels^2 vs 158±36 pixels^2 for 0 mg/dL, vs 141±23 pixels^2 for 300 mg/dL, and 150±32 pixels^2 for 600 mg/dL). These results confirm the persistence of fibrinogen-mediated RBC aggregation under physiological flow conditions and demonstrate that higher fibrinogen concentrations increase the absolute size and range of sizes of RBC aggregates.

AI.3.3 Fibrinogen-mediated red blood cell aggregation induces endothelial glycocalyx degradation

We next examined whether fibrinogen-dependent RBC aggregation results in pathologic damage to the endothelium using a humanized microfluidics device with branches of variable dimensions. Devices were cultured with human umbilical vein endothelial cells (HUVECs) for 72 hours and the endothelial glycocalyx layer visualized using a fluorescently tagged wheat germ agglutinin (Figure 2G). The endothelial glycocalyx was chosen as a target given its important role in regulating endothelial health and its responsiveness to perturbations in the shear stress environment (Uchimido et al., 2019). The fluorescence signal was visualized using a digital microscope and quantified in each isolated channel segment. The same fibrinogen concentrations used for cluster measurement analysis were again combined with healthy volunteer RBCs and perfused into microfluidic devices for 30 minutes. The devices were then re-imaged and a ratio of residual glycocalyx was calculated for each channel segment. The results of these experiments demonstrate a significant reduction in the glycocalyx in the condition with a fibrinogen

concentration of 900 mg/dL compared with 600 mg/dL at all channel sizes, and with 300 mg/dL at all but the largest channel size ($p<0.05$ for all indicated comparisons in the figure). These results indicate that fibrinogen-mediated RBC aggregation directly and pathologically affects the endothelium by promoting glycocalyx degradation.

To investigate if our observations regarding fibrinogen concentration in a tightly controlled in vitro experimental setup translate to clinical samples, we next evaluated the role of fibrinogen in plasma from COVID-19 patients. Plasma was collected from anticoagulated whole blood from four COVID+ patients with abnormally high fibrinogen levels (765 mg/dL to >1000 mg/dL, normal range 200-393 mg/dL). Aliquots were re-calcified and allowed to clot with the supernatant, thereby approximating sera and decreasing the fibrinogen concentration without loss of other non-clotting plasma-based factors (e.g. cytokines, etc). Each of the native samples (Plasma) and re-calcified plasma samples (Serum) were combined with healthy RBCs, perfused into microfluidic devices, and analyzed in the same manner as the fibrinogen concentration experiments. When stratified by channel size, there was no statistically significant change between the residual glycocalyx for plasma versus serum suspensions at any one channel size. However, when all channel sizes were pooled for each individual patient, a paired t-test revealed a significant difference between the two groups (mean difference in residual glycocalyx 0.13 ± 0.03, $p=0.0006$; Figure 2I). While the difference in residual glycocalyx between the plasma and serum for any one given patient was not large, this likely reflects variable amounts of residual fibrinogen present in recalcified samples. Nevertheless, these data further demonstrate a direct effect of fibrinogen-mediated RBC aggregation on endothelial cell dysfunction. Fibrinogen has been studied for its role in inducing RBC aggregation previously, yet the phenomenon has been assumed to be a byproduct of systemic inflammation rather than a contributor to acute pathology. These data show

a direct pathogenic effect of fibrinogen-mediated RBC aggregation on the endothelium and provide a potential therapeutic target, as suggested by clinical work proposing a survival benefit associated with reduction in systemic fibrinogen levels in COVID-19 patients (Truong et al., 2021).

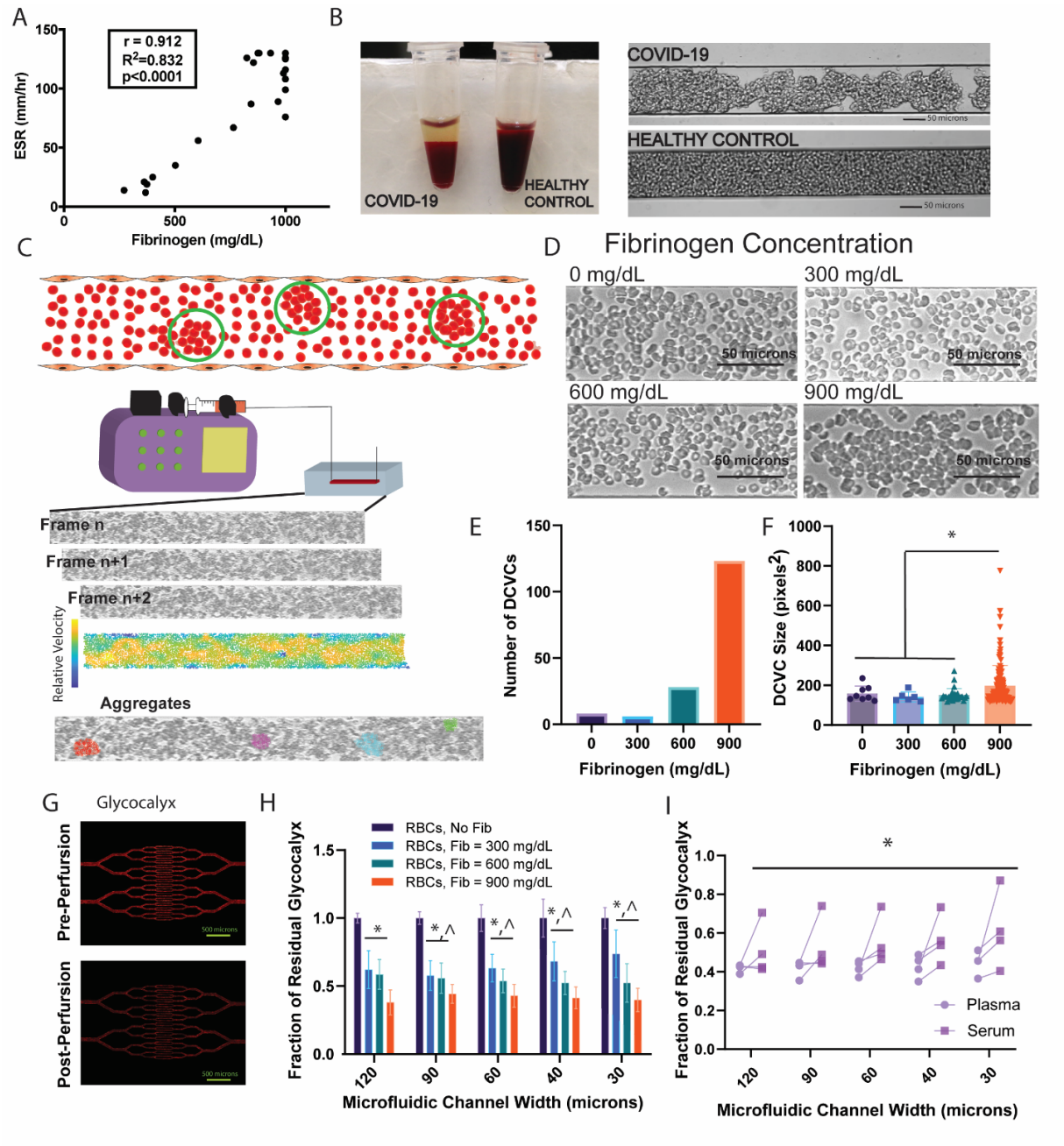

Figure AI - 3: Fibrinogen mediates RBC aggregation and biophysically induces endothelial cell damage.

A.) Strong positive correlation between erythrocyte sedimentation rate (ESR, normal <30mm/hr) and fibrinogen levels (normal range 200-393 mg/dL) in COVID-19 patient samples. **B.)** (Left) COVID-19 patient blood shows rapid sedimentation on the benchtop and (Right) aggregation in a microfluidics channel under static conditions compared with

healthy control. **C.)** (Top) Cartoon figure demonstrating the RBC aggregation detected using our velocity field calculations and the differential cell velocity cluster (DCVC) identification. (Bottom) Experimental setup of perfusion of RBC samples into the microfluidics device with a representative time series of still images obtained via video microscopy. Relative velocity map of a set of tracked points over time with identification of a group of points meeting the defined cluster criteria of our RBC DCVC calculations. **D.)** Still images from video microscopy at each of the four tested fibrinogen concentrations showing a qualitative increase in RBC aggregation with increasing fibrinogen. **E.)** Exponential increase in the number of detected DCVCs with increasing fibrinogen level as compared to minimal amount of aggregation seen at a fibrinogen concentration of 0mg/dL or at the physiologic level of 300mg/dL**. F.)** There is an increase in both the mean size and variance of DCVC size with increasing fibrinogen concentration. A size of 115 square pixels is approximately 15 RBCs. *indicates a significant difference in DCVC size, $p<0.05$. **G.)** Visualization of the endothelial glycocalyx in serially branching microvasculature -on-chip devices using fluorescently tagged wheat germ agglutin before (top) and after (bottom) perfusion of samples. **H.)** Average fraction of residual glycocalyx detected in the microfluidics devices from (G) at each of the tested fibrinogen levels. *indicates a significant reduction in residual glycocalyx with a fibrinogen level of 900mg/dL compared with 600mg/dL, ^ indicates a significant reduction compared with 300mg/dL. I). Measurement of glycocalyx degradation induced by paired plasma and serum (i.e. recalcified fibrinogen-decreased plasma) samples from COVID+ patients. Pooled results across all channel sizes show a significantly greater degree of glycocalyx degradation in plasma versus sera samples

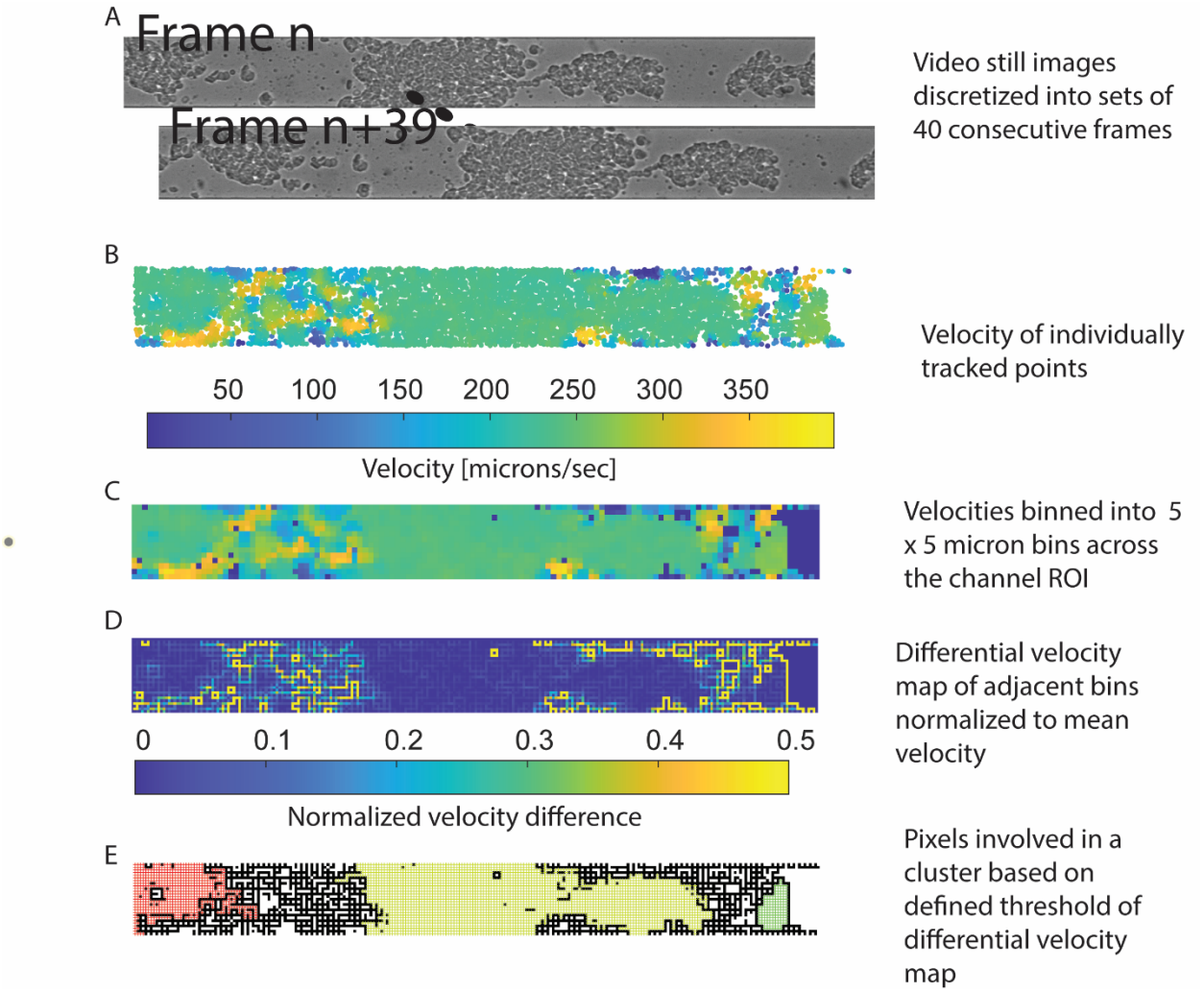

Figure AI - 4: Detailed Explanation of DCVC Quantification Workflow.

A.) Ten seconds of video microscopy were captured at a frame rate of 160 frames per second yielding 1600 frames per sample. This time resolved frame sample was discretized into 40 sets of 40 frames, corresponding to 0.25 seconds per set for cell feature tracking. **B.)** Individual cell features were detected in the first frame of each set and tracked over the subsequent 39 frames using a built-in Matlab (Mathworks) object which employs the Kanade-Lucas-Tomasi tracking algorithm. A cell feature was only included in the analysis if it was detected in all 39 frames. Instantaneous velocity was calculated from each frame step and then averaged over all frames within a set. **C.)** To account for the difference in the number of cell features tracked per unit area

the velocity field was binned into a matrix with bin size 5 μm x 5μm, slightly smaller than the larger diameter of a single RBC. **D.)** The absolute difference in velocity between neighboring points in the binned velocity map were calculated and normalized to the average velocity for the set of images**. E.)** A black white image is created in which a threshold is applied to differential velocity map for a Boolean inclusion process of neighboring bins with <5% difference in velocity. Groups of connected points are then identified using a connectivity map and included as a DCVC (red, yellow, green) if they were at least the area of 15 RBCs which corresponded to 115 pixels in the image set . The size of each DCVC is calculated and mapped to the binned velocity matrix in (C) to calculate the aggregate velocity.

AI.3.4 Plasma from patients with COVID-19 induces increased red blood cell aggregation

The significance of the pathologic involvement of the liver in combination with the unexpected shear stress response pathways in our proteomic analysis was of great interest, especially given our prior observation of increased blood viscosity related to hyperfibrinogenemia in the sickest COVID-19 patients (Maier et al., 2020). Building on observations from our in vitro experiments using purified fibrinogen, we next sought to evaluate how plasma from COVID-19 patients influences RBC aggregation compared with critically ill COVID-19-negative patients under biologically relevant conditions. We prospectively collected anticoagulated blood from patients meeting sepsis criteria as a result of SARS-CoV-2 infection (COVID+, n=6) or from another infectious source (non-COVID sepsis, n=6), as well as from healthy volunteers (Healthy, n=4). Patient cohorts were matched for illness severity by SOFA score, age, and number of comorbidities, and samples obtained within 72 hours of admission to a single ICU (Table AI-2). Plasma from each participant was combined with isolated RBCs and aggregation assessed as above. Qualitative evaluation showed increased RBC aggregation in the COVID+ patients as compared to non-COVID sepsis patients or healthy controls (Figure AI-5 A). When the number of clusters was calculated, plasma from both COVID+ and non-COVID sepsis patients induced a greater number of DCVCs than healthy volunteers (Figure AI-5 B, 125±58 & 101±57 vs 17±7 respectively, $p<0.05$). While there was no difference in the number of clusters between COVID+ and non-COVID sepsis, the size of the aggregates in the COVID+ cohort was significantly larger (Figure AI-5 C, 435±413 pixels vs 336±313 pixels, $p<0.0001$).

In addition to aggregate size, we compared the velocity distribution of the DCVCs among the 3 groups. The average velocity of the DCVC was similar between all 3 groups (Figure AI-5 D,

180 μm/s vs 173 μm/s vs 199 μm/s for COVID+, non-COVID sepsis, and healthy volunteers respectively); however, the variance of pooled aggregate velocities in the COVID+ group was larger than either non-COVID sepsis or healthy controls. To assess this on an individual level, we evaluated the interquartile range (IQR) of aggregate velocities for each participant in the 3 groups (Figure AI-5 E). The average IQR for the COVID+ cohort was larger than the IQR for the other two groups; however, the difference did not reach significance in comparing the COVID+ vs non-COVID sepsis groups (57±48 μm/sec vs 22±35 μm/sec, p=0.21). These findings show that while plasma from both patients with COVID-19 and patients with non-COVID sepsis result in an increase in RBC clustering, the clusters in patients with COVID-19 are larger and exhibit a wider variability in velocity. How larger aggregates in the microvasculature can lead to endothelial cell damage is an intuitive finding, as large RBC aggregates physically degrade endothelial glycocalyx in the microcirculation. However, the variability in velocity is an important new experimental finding. Extensive literature including work by our own group demonstrates increased endothelial cell activation and a pro-inflammatory response following exposure to time-variable shear rates as compared to laminar flow (Zhang et al., 2020); still, this is often in chronic vascular disease and has not been implicated in acute critical illness. The variation in velocity field values, even in a steady state system such as ours, highlights the influence that changes in plasma of patients with COVID-19 can have on rheologic properties in the microvasculature.

AI.3.5 Differences in RBC membrane deformability between critically ill patients with and without COVID-19

As RBCs enter the capillary bed, membrane deformation is essential to permit cells to pass singly and quickly through the small vessel to maintain consistent flow. Given the evidence of microvascular pathology in patients with COVID-19, we next investigated whether changes in

RBC biomechanics at this scale may contribute. To do so, RBCs were isolated from critically ill patients with COVID-19 (COVID+, n=9), critically ill patients with infectious sources other than SARS-CoV-2 (non-COVID sepsis, n=11) and healthy controls (Healthy, n=5), and washed of all plasma (Table AI-2). Cells were resuspended in PBS and perfused through microfluidic channels (Figure AI-5 F). Changes in the single cell RBC deformability indices were evaluated by tracking transit time via video microscopy capture of at least 250 cells per patient or control. Both COVID+ and non-COVID sepsis patients exhibited a lower deformability index compared with healthy volunteers, indicating more rigid/less deformable RBCs (0.40 ± 0.086 & 0.33 ± 0.02 vs 0.46 ± 0.088 respectively) (Figure AI-5 G). These results indicate that RBCs from patients with COVID-19 are stiffer than those from healthy adults; however, patients with sepsis from causes other than COVID-19 are even less deformable. Stiffened RBCs not only damage the capillary endothelium but also influence the rheologic properties of blood flow, particularly in the microvasculature, as stiffer particles marginate to the vessel wall and flexible cells (like healthy biconcave RBCs) move toward the center. There is precedent in other conditions showing that RBC populations with differential membrane stiffness cause inflammatory endothelial changes (Caruso et al., 2022). This distribution of RBC membrane stiffness changes the overall cross sectional velocity profile of the microvasculature and consequently the wall shear stress and mechanotransductive signaling at the endothelium. In combination with the aggregation studies, these results suggest that the rheologic disturbances in critical infectious illness differ in patients with SARS-CoV-2 as compared to patients with sepsis from other causes.

AI.3.5 COVID-19 plasma interacts with red blood cells to damage the endothelial glycocalyx in a vessel size-dependent manner

To evaluate if the differences in rheology observed between COVID+, non-COVID sepsis and healthy volunteers results in endothelial damage, we again employed our humanized microvascular microfluidics platform. The same experimental protocol using a microfluidic device cultured with HUVECs was used for COVID+ (n=11), non-COVID sepsis (n=5), and healthy controls (n=4) to measure this effect. Previous reports have demonstrated that circulating sheddases are upregulated and can increase the degradation of the endothelial glycocalyx (Becker et al., 2015). For this reason, we designed our assays using a time scale on which biomechanical effects on the glycocalyx could be assessed while limiting the impact of enzymatic degradation. Comparing the results using COVID+ plasma with that obtained from healthy controls (Figure AI-5 H), there was a significant increase in glycocalyx degradation in the smallest channel size (0.44 ± 0.09 vs 0.66 ± 0.16, $p<0.05$), but not between the COVID+ and non-COVID sepsis cohorts (0.44 ± 0.09 vs 0.43 ± 0.068). A repeated measures ANOVA analysis between each of the patient groups and the healthy controls produced a significant difference. These results suggest that changes in circulating plasma components and subsequent biophysical changes can result in endothelial damage in the microvascular system, most pronounced in the smallest caliber vessels, and is a feature of critical illness in both COVID and non-COVID sepsis.

AI.3.6 Indicators of endothelial damage are prominent in patients with COVID-19

Finally, well-established markers of endothelial activation or damage were compared among COVID+ (n=10), non-COVID sepsis (n=11), and healthy (n=5) cohorts (Table AI-2). COVID+ patients had higher levels of syndecan-1, a component of the endothelial glycocalyx, than either patients with non-COVID sepsis (Figure AI-5 I, 812±65 ng/mL vs 283±188 ng/mL,

p=0.0094) or healthy volunteers (812±65 ng/mL vs 65±10 ng/mL, p=0.03 and 283±188 vs 65±10 ng/mL ng/mL, p=0.02). Both COVID+ and non-COVID sepsis patients had higher levels of circulating vWF than healthy controls (Figure AI-5 J) 20,929 ± 9016 ng/mL vs 4792 ± 3513 ng/mL, p<0.001 and 16518 ± 10552 ng/mL vs 4792 ± 3513 ng/mL, p=0.01). Moreover, pathologist review of pulmonary microvascular integrity in patients who succumbed to COVID-19 highlighted RBC aggregates clogging the capillaries alongside evidence of endothelial injury (Figure AI-5 K). Taken together, these clinical findings corroborate microfluidics studies demonstrating the role of endothelial damage from altered blood rheology in COVID-19.

Table AI - 2: Patient Demographics for Adult Microfluidic Studies, n=29	COVID Cohort, n=13	Sepsis Cohort, n=16
Age, median years (range)	57 (24 – 84)	58 (19 – 81)
Women, number (%)	7 (54%)	4 (25%)
Race, number (%)		
African American	12 (92%)	12 (75%)
White	1 (8%)	4 (25%)
Asian/Pacific Islander	0 (0%)	0 (0%)
Body Mass Index, mean (SD)	33 (12)	28 (9)
Sample Time, mean number days post diagnosis (SD)	1.7 (0.7)	2.1 (0.7)
Illness Severity, median SOFA ordinal scale (range)	10 (3 – 19)	8.5 (5 – 15)
Interventions, number (%)		
Renal-replacement therapy	5 (38%)	3 (19%)
Mechanical Ventilation	10 (77%)	15 (94%)
Vasopressor Support	9 (69%)	14 (87%)
Medications, number (%)		
Therapeutic Anticoagulation	9 (69%)	3 (19%)
Dexamethasone	13 (100%)	0 (0%)
Tocilizumab/Baricitinib/Remdesivir	8 (62%)	0 (0%)
Infectious Source, number (%)		
Pneumonia	13 (100%)	8 (50%)
Bacteremia	0	5 (31%)
Urinary Tract Infection	0	2 (13%)
Skin and Soft Tissue Infection	0	1 (6%)
Co-morbidities, number (%)		
Hypertension	6 (46%)	8 (50%)
Diabetes mellitus	3 (23%)	5 (31%)
Renal Disease	2 (15%)	3 (19%)
Obesity	3 (23%)	5 (31%)
Asthma or COPD	3 (23%)	7 (43%)
30 Day Disposition, number (%)		
Death/Hospice	4 (31%)	8 (50%)
	5 (38%)	2 (13%)

Hospitalized/Transfer (inpatient rehab, long term acute care or other facility) Home	4 (31%)	6 (37%)

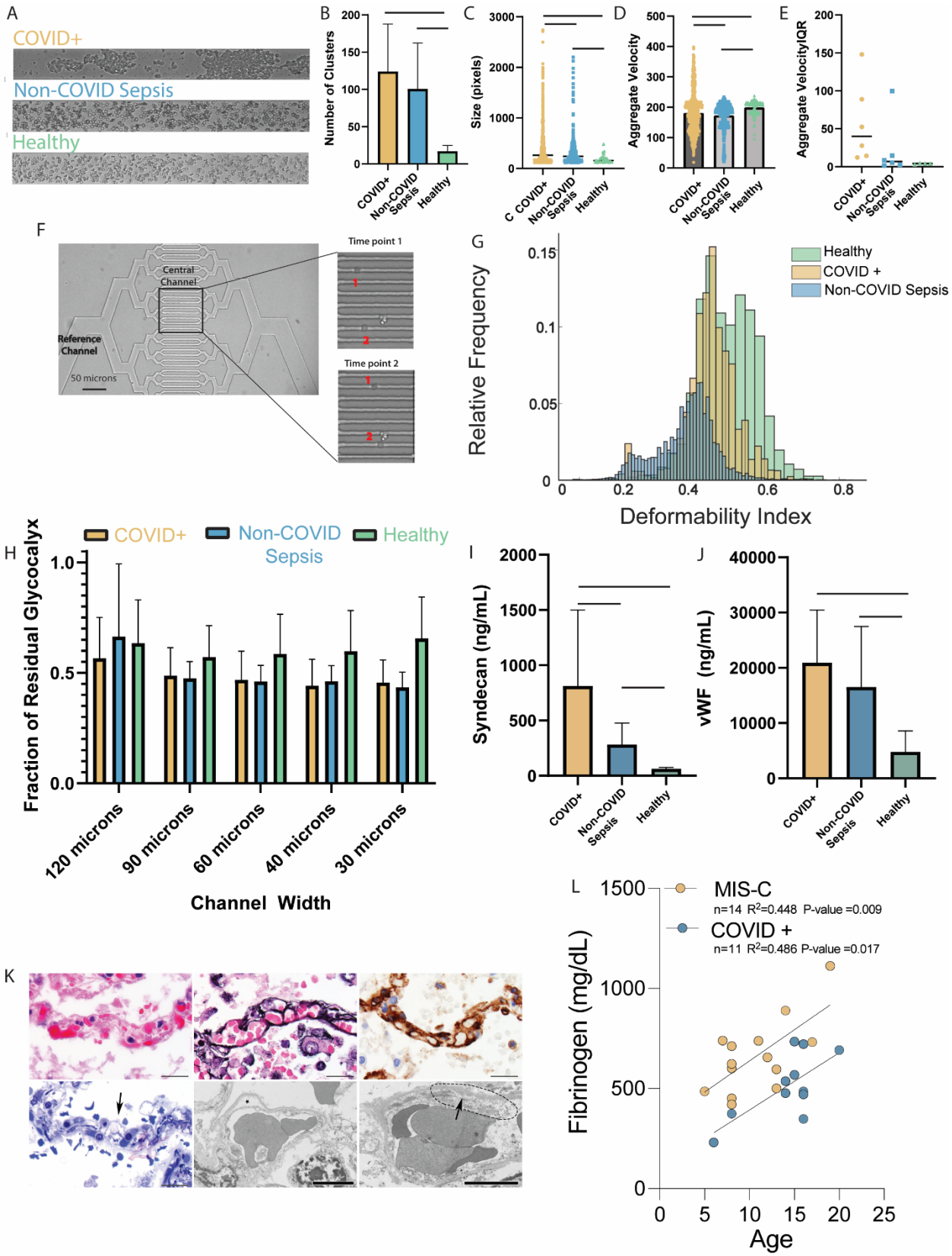
A
COVID+
Non-COVID Sepsis
Healthy
B
Number of Clusters
C
Size (pixels)
D
Aggregate Velocity
E
Aggregate VelocityIQR
COVID+
Non-COVID Sepsis
Healthy
F
Central Channel
Reference Channel
50 microns
Time point 1
Time point 2
G
Relative Frequency
Deformability Index
Healthy
COVID +
Non-COVID Sepsis
H
Fraction of Residual Glycocalyx
Channel Width
120 microns
90 microns
60 microns
40 microns
30 microns
I
Syndecan (ng/mL)
J
vWF (ng/mL)
K
L
Fibrinogen (mg/dL)
Age
MIS-C
n=14 R²=0.448 P-value =0.009
COVID +
n=11 R²=0.486 P-value =0.017

Figure AI - 5: Plasma from both COVID+ and non-COVID sepsis patients results in endothelial glycocalyx damage but from different mechanisms.

A.) Still frame from videomicroscopy showing the rheologic behavior of healthy RBCs under shear when recombined with plasma from a patient with COVID-19 (top), non-COVID sepsis (middle), or a healthy volunteer (bottom). **B.)** There was a greater number of DCVCs detected when RBCs were recombined with plasma from the COVID+ and non-COVID sepsis compared with healthy volunteers, solid bar indicate $p<0.05$ **C.)** The average size of DCVCs produced by plasma from each of the three groups was significantly different among all cohorts, with plasma from COVID+ patients inducing the largest DCVCs**. D.)** The average velocity of the DCVCs was similar among all three groups; however, there was a significant difference in the velocity variance when the measures for all individuals were pooled, solid bar indicates $p<0.05$ by f-test. **E.)** The interquartile range of DCVC velocity was calculated for each patient or volunteer sample, COVID+ patients tended to have a wider range of DCVC velocities on an individual level, but it did not reach significance when compared with the non-COVID sepsis or healthy controls. **F.)** (Top left) RBC deformability assay with magnified area of interest showing the transit of two RBCs across the central channels. **G.)** Normalized histogram of pooled single-cell RBC deformability indices from COVID+ patients and healthy volunteers demonstrating that RBCs from COVID+ patients are less deformable than healthy controls, but not as stiff as patients with non-COVID sepsis. **H.)** Plasma from COVID+ and non-COVID sepsis patients induces greater glycocalyx damage at the smallest channel size in our microfluidics platform**. I.)** COVID+ patients have higher circulating levels of syndecan-1, a marker of glycocalyx damage, than patients with non-COVID sepsis and healthy volunteers (solid bar indicates $p<0.05$). **J.)** Both COVID+ and non-COVID sepsis patients have increased levels of vWF compared with healthy controls, but there is not significant difference between the two patient populations (solid bar indicates $p<0.05$).

K.) Pulmonary capillaries in COVID-19 patients examined post-mortem. Vascular architecture is intact by routine light microscopy (top left), with clogging of capillaries by erythrocytes and scant fibrin. Jones (top middle) and CD34 (top right) stains highlight the integrity of the capillary basement membrane and endothelial lining. Semi-thin sections prepared for ultrastructural examination (bottom left) show capillary endothelial injury (arrow) characterized by endothelial cell swelling and disruption. Transmission electron microscopy (bottom middle, bottom right) shows endothelial cell dehiscence from underlying basement membrane (star) and loss of structural integrity (dotted line) with feathering of the basement membrane (arrow). **L.)** Strong correlation between maximum fibrinogen level during hospital admission and age in both COVID+ pediatric and MIS-C patients.

AI.3.7 Multiplatform analyses of plasma from pediatric COVID-19 or MIS-C patients suggests diverging pathophysiology from adult COVID-19

Clinical observations in patients and evidence obtained from murine studies suggest the severity of COVID-19 infection is largely determined by host response and age (Bajaj et al., 2020). To determine if our findings in adults were recapitulated in children, we attempted to perform similar rheological analyses using blood from pediatric patients. Unfortunately, attempts to obtain either fresh plasma prospectively or interpretable data from studies using biobanked pediatric plasma were unsuccessful, largely due to limitations in the microfluidic studies that necessitate large, freshly-collected citrated samples. Nevertheless, clinical data from our cohort of pediatric patients with severe disease demonstrated lower levels of maximum fibrinogen during admission in acute COVID (n = 11, median = 481mg/dL, interquartile range 422-630) and MIS-C (n = 14, median = 640mg/dL, interquartile 524-736) (Table AI-3), compared to published reports in adults (794 mg/dL, interquartile range 583-933 (Ranucci et al., 2020), as levels from much of our adult cohort were unavailable). Interestingly, fibrinogen levels in these pediatric patients demonstrated a positive correlation with age (Figure AI-5 L) (Table AI-2). Taken together with our fibrinogen-concentration studies, these data suggest fibrinogen-mediated RBC aggregation is less likely to occur in pediatric patients given the lower degree of hyperfibrinogenemia.

Table AI - 3: Patient Demographics for Pediatric Rheological Studies, n=25.

	COVID, n=11	MIS-C, n=14
Age, median years (range)	15 (6-20)	9.5 (5-19)
Girls, number (%)	7 (64%)	6 (43%)
Race/Ethnicity, number (%) African American/Non-Hispanic African American/Hispanic White/Non-Hispanic White/Hispanic Asian Declined/Non-Hispanic Declined/Hispanic	 4 (36%) 1 (9%) 3 (27%) 1 (9%) 2 (18%) 0 0	 10 (71%) 0 0 1 (7%) 0 1 (7%) 2 (14%)
Body Mass Index, mean (SD)	30 (14)	22 (8)
COVID or MIS-C Symptom Severity Severe, number (%)	 11 (100%)	 14 (100%)
Immunocompromised State, number (%) None Malignancy	 9 (82%) 2 (18%)	 13 (93%) 1 (7%)
Medications Anticoagulation Dexamethasone or other steroid Tocilizumab/Baricitinib/Remdesivir IVIG	 8 (73%) 8 (73%) 9 (82%) 2 (18%)	 11 (79%) 12 (86%) 2 (14%) 13 (93%)
Interventions Mechanical Ventilation Vasopressor Support ECMO	 1 (9%) 3 (27%) 0	 3 (21%) 12 (86%) 1 (7%)
Co-morbidities Obesity Asthma	 5 (45%) 4 (36%)	 1 (7%) 2 (14%)
Peak Fibrinogen, normal 200-393 mg/dL Mean (SD) Median (interquartile range)	 512 mg/dL (161) 485 mg/dL (422-630)	 662 mg/dL (189) 640 mg/dL (524-736)
Discharge Disposition (%)		

Death/Hospice	2 (18%)	1 (7%)
Home	9 (82%)	13 (93%)

We next turned back to multiomic analyses to gain insight into alternative mechanisms characterizing SARS-CoV-2 pathogenesis in children. Plasma samples were obtained from healthy children (n=7), children admitted with PCR-confirmed COVID-19 (COVID+, n=7), and children admitted with a diagnosis of MIS-C (n= 5) (Table AI-4). Label-free proteomics of plasma detected over 100,000 peptide spectrum matches covering 447 proteins, with 131 being statistically significant between all three groups (Figure AI-6 A). Balanced sampling indicated that identified DAPs were not an artifact (Figure AI-6 B). PCA analysis demonstrated that PC1 best differentiates healthy versus COVID+ pediatric patients, with greater separation between children with COVID-19 and those with MIS-C (Figure AI-6C). To assess unique drivers of COVID versus MIS-C, we performed pairwise comparisons between each of our three cohorts, finding that MIS-C has the most significant perturbations (Figure AI-6 D & G). Interestingly, our analysis showed minimal significant alterations between COVID+ children and MIS-C children, as they share ~80% of identified DAPs when compared to healthy controls. In general, shared DAPs are more significantly altered in MIS-C, suggesting that MIS-C results in exacerbation of the changes occurring upon acute COVID-19 infection in children.

Table AI - 4: Patient Demographics for Pediatric Multiomic Studies, n=19.

	COVID, n=7	**MIS-C, n=5**	**Healthy, n=7**
Age, median years (range)	15 (3-16)	8 (5-19)	9 (5-12)
Girls, number (%)	3 (43)	1 (20)	5 (71)
Race/Ethnicity, number (%)			
African American/Non-Hispanic	3 (43%)	4 (80%)	5 (71%)
White/Non-Hispanic	1 (14%)	0	2 (29%)
Declined/Hispanic	3 (43%)	1 (20%)	0
Body Mass Index, mean (SD)	26 (12)	24 (7)	Unknown
Sample Time, mean number days post diagnosis (SD)	4 (3)	6 (4)	N/A
COVID or MIS-C Severity, median WHO ordinal scale (range)	3 (2-5)	5 (4-7)	N/A
Immunocompromised State, number (%)			N/A
None	4 (57%)	4 (80%)	
Malignancy	3 (43%)	1 (20%)	
Medications			N/A
Anticoagulation	2 (29%)	3 (60%)	
Dexamethasone or other steroid	1 (14%)	3 (60%)	
	3 (43%)	2 (40%)	
Tocilizumab/Baricitinib/Remdesivir	2 (29%)	1 (20%)	
IVIG			
Interventions			N/A
Mechanical Ventilation	0	2 40%)	
Vasopressor Support	1 (14%)	4 (80%)	
ECMO	0	0	
Co-morbidities			N/A
Obesity	3 (43%)	0	
Asthma	2 (29%)	1 (20%)	
Immunosuppressive therapy	3 (43%)	1 (20%)	
Co-infections			N/A
Acute appendicitis	1 (14%)	0	
Discharge Disposition (%)			N/A
Death/Hospice	1 (14%)	1 (20%)	
Home	6 (86%)	4 (80%)	

Pathway analysis comparing DAPs in our pediatric cohort to the human genome atlas detected similar tissues of origin between pediatric COVID-19 or MIS-C that we observed in adult patients (Figure 4E). Specifically, KEGG pathway analysis combining the DAPs that were increased or decreased for each pair wise comparison uncovered common changes related to complement and coagulation cascades, inflammatory processes (such as IL-17A signaling, various infections, and even cancer) and autoimmune disease (Figure AI-6 F). This same analysis also uncovered changes unique to acute COVID+ children and MIS-C. Acute COVID+ children showed alterations in various infectious processes, including coronavirus infection, and metabolic processes associated with nucleotides and proteins. MIS-C showed similarity to African trypanosomiasis and alterations in metabolic processes associated with lipid metabolism (Figure AI-6 G). Interestingly, children with MIS-C but not children with acute COVID demonstrated some alterations in fluid shear stress response pathway proteins, though this did not reach our stringent cut-off for statistical significance. Considering our microfluidics data, this may reflect the higher fibrinogen levels in the MIS-C versus acute pediatric COVID cohort; however, other non-fibrinogen mediators may cause the alterations highlighting this pathway, given the fact that MIS-C is characterized by a highly inflammatory vasculitis. Proteomics supports this supposition, as no significant increase in the abundance of fibrinogen chains was detected in acute COVID+ or MIS-C children (Figure AI-6 I).

Notably, KEGG pathway analysis detected changes in our pediatric cohort not present in COVID+ adults, mainly related to various metabolic processes, as well as those distinguishing acute pediatric COVID from post-infectious MIS-C. To delineate these unique aspects of SARS-CoV-2 in children, we compared DAPs between the pediatric COVID+ and adult COVID+ cohorts. Only 28 DAPs were shared, with proteins involved in processes like the complement and

coagulation cascades, alterations in the extracellular matrix receptor interactions, and indicators of liver injury. Our analysis also detected proteins involved in pathways distinguishing pediatric COVID-19 and MIS-C (Figure AI-6 G). Proteins that increased as a function of disease severity included those associated with coagulation, inflammation, and immune cell function, whereas proteins that were decreased tended to be associated with glycoproteins, inhibitors of various proteolytic processes and lipoprotein metabolism.

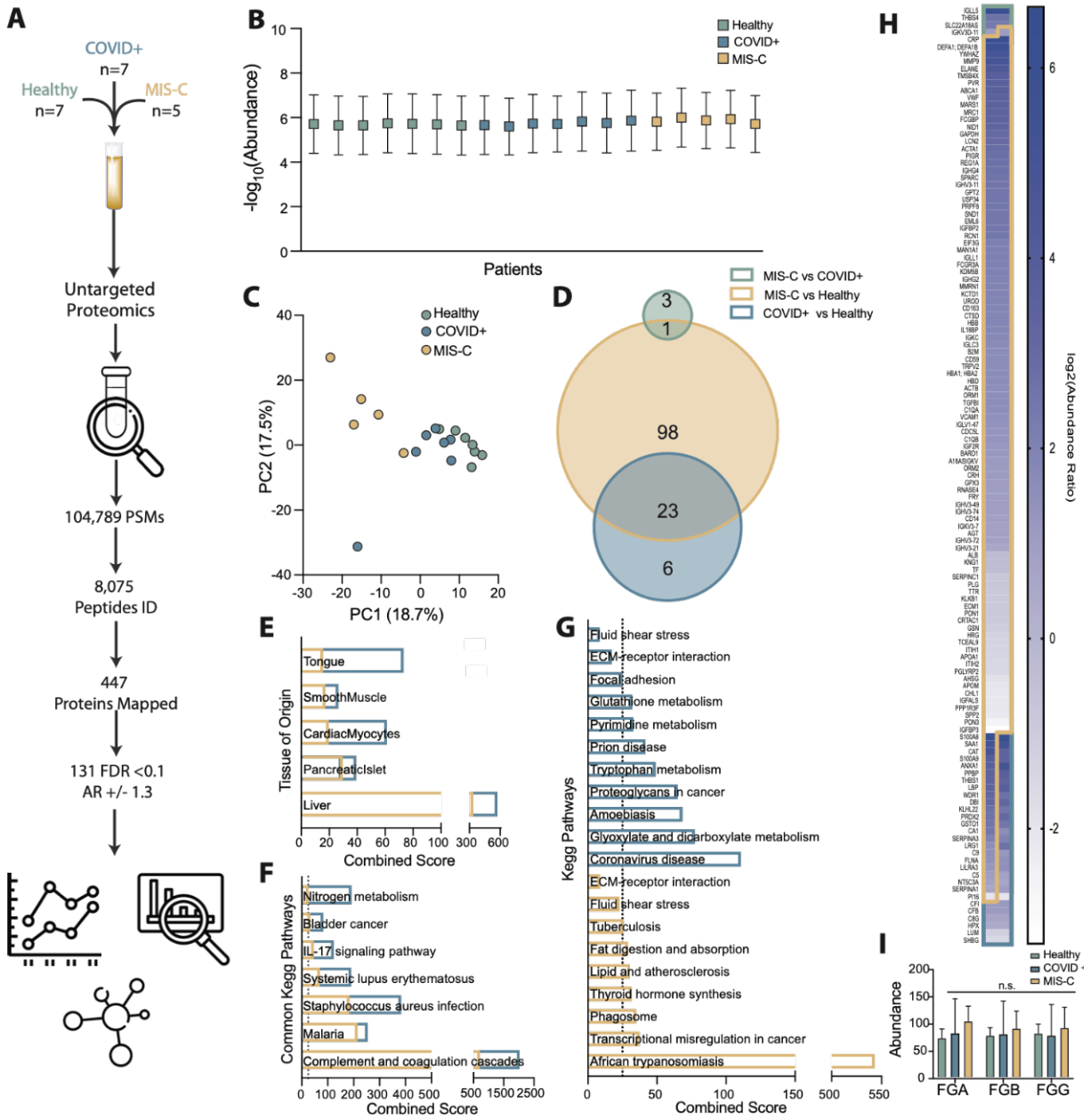

Figure AI - 6: Proteomic analysis of pediatric plasma from patients with acute COVID-19 or post-infectious MIS-C.

A.) Overview of untargeted plasma proteomics on sera from pediatric patients with COVID-19 (COVID+), MIS-C, or healthy controls. **B.)** Relative abundance of detected peptides per sample. **C.)** PCA plot of proteomics data for pediatric group. **D.)** Venn diagram showing the relative distribution of differentially abundant proteins (DAPs). **E.)** Comparison of DAPs to the human

genome atlas highlights perturbations in liver and lung; Gold reflects MIS-C compared to healthy controls while blue reflects COVID+ compared to healthy controls. **F.)** KEGG pathway analysis highlights alterations in pathways common between MIS-C and COVID+ cohorts. **G.)** KEGG pathway analysis of those significant in either MIS-C (Gold) or COVID+ (Blue) highlight perturbations unique to each group, neither of which achieve significance for the fluid shear stress or ECM-receptor interaction pathways identified in the adult cohort. **H.)** Heat map of identified DAPs altered upon SARS-CoV-2 infection in children. **I.)** The abundance of all 3 chains of the hepatic acute phase protein fibrinogen is increased in MIS-C, albeit not significantly.

Metabolites and lipids are cellular effectors which reflect host cell biological processes, and alterations from their normal levels can inform the pathophysiology underlying a particular disease state. This consideration, combined with alterations in metabolism as suggested by our proteomic analyses, led us to perform global high-resolution metabolomics and lipidomics on our pediatric cohorts. Analysis identified over 2000 features, with 206 being statistically significant between the groups (Figure AI-7 A). Unbiased hierarchal clustering using all identified analytes shows partial separation between each group, with COVID+ and MIS-C clustering together (Figure AI-7 B). Similar to our proteomic analysis, most of these differentially abundant analytes (DAAs) are driven by comparison between MIS-C and healthy controls, with less significant changes detected between other pairwise comparisons (Figure AI-7 C). In agreement with this analysis, we also observed separation in our PCA, with PC1 driving most differences between disease states (Figure AI-7 D). Unlike the adult cohort, variables most responsible for the separation were predominantly lipids, many of which contained polyunsaturated fatty acyl chains. While we cannot identify the precise location of the saturation on each fatty acyl chain, this analysis points to alterations in essential fatty acid homeostasis, which is in line with detected changes in nutrient uptake and changes in systemic inflammation associated with MIS-C (Figure AI-7 E). Looking at the most significantly altered metabolites when comparing healthy controls and either COVID+ children or MIS-C further supports this, as alterations in inflammatory mediators derived from either omega 3 or omega 6 fatty acids predominate (Figure AI-7 F). KEGG pathway analysis comparing each cohort within the pediatric data set shows expected areas of overlap as well as unique differences (Figure AI-7 G). Increases in metabolites such as lactic acid and inflammatory mediators (20-HETE and 9-HpODE) seemed to be diagnostic for MIS-C, whereas analytes such as DHA and aconitic acid were significantly decreased.

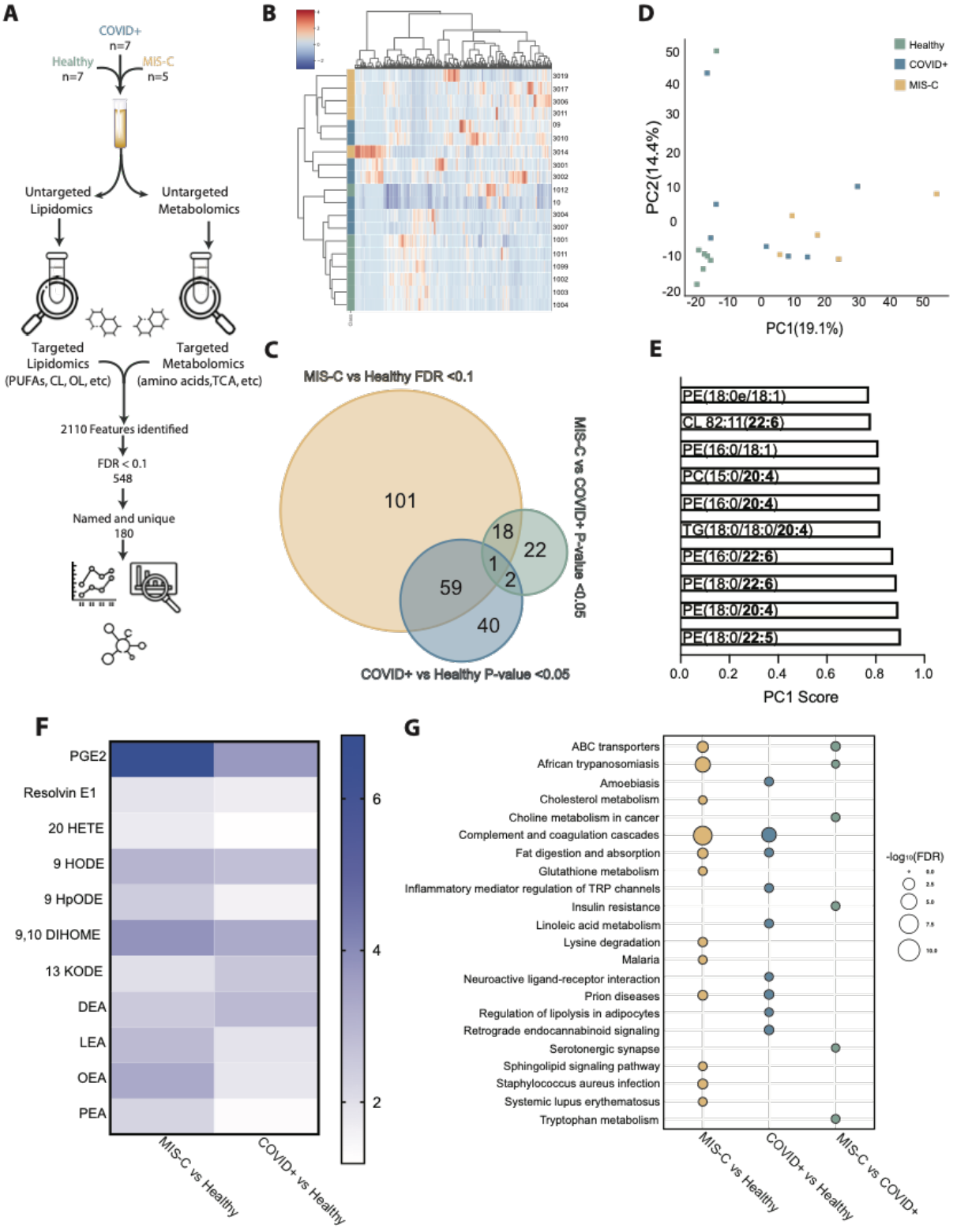
A
COVID+
n=7
Healthy
n=7
MIS-C
n=5
Untargeted
Lipidomics
Untargeted
Metabolomics
Targeted
Lipidomics
(PUFAs, CL, OL, etc)
Targeted
Metabolomics
(amino acids,TCA, etc)
2110 Features identified
FDR < 0.1
548
Named and unique
180
B
C
MIS-C vs Healthy FDR <0.1
MIS-C vs COVID+ P-value <0.05
COVID+ vs Healthy P-value <0.05
101
18
22
1
2
59
40
D
Healthy
COVID+
MIS-C
PC2(14.4%)
PC1(19.1%)
E
PE(18:0e/18:1)
CL 82:11(22:6)
PE(16:0/18:1)
PC(15:0/20:4)
PE(16:0/20:4)
TG(18:0/18:0/20:4)
PE(16:0/22:6)
PE(18:0/22:6)
PE(18:0/20:4)
PE(18:0/22:5)
PC1 Score
F
PGE2
Resolvin E1
20 HETE
9 HODE
9 HpODE
9,10 DIHOME
13 KODE
DEA
LEA
OEA
PEA
MIS-C vs Healthy
COVID+ vs Healthy
G
ABC transporters
African trypanosomiasis
Amoebiasis
Cholesterol metabolism
Choline metabolism in cancer
Complement and coagulation cascades
Fat digestion and absorption
Glutathione metabolism
Inflammatory mediator regulation of TRP channels
Insulin resistance
Linoleic acid metabolism
Lysine degradation
Malaria
Neuroactive ligand-receptor interaction
Prion diseases
Regulation of lipolysis in adipocytes
Retrograde endocannabinoid signaling
Serotonergic synapse
Sphingolipid signaling pathway
Staphylococcus aureus infection
Systemic lupus erythematosus
Tryptophan metabolism
MIS-C vs Healthy
COVID+ vs Healthy
MIS-C vs COVID+
-log10(FDR)

Figure AI - 7: Lipidomic and metabolomic analysis of pediatric cohorts reveals alterations in nutrient absorption and metabolism and increases in inflammatory mediators.

A.) Workflow showing targeted and untargeted assays used to interrogate lipid and metabolite changes associated with acute pediatric COVID+ and MIS-C. **B.)** Unbiased hierarchal clustering of significant analytes. **C.)** Overlap between each pairwise comparison with respective statistical criterion. **D.)** Principal component analysis (PCA) using statistically significant metabolites**. E.)** Top 10 analytes that define separation of principal component one. **F.)** Significant features present in both COVID+ and MIS-C (p-adjusted value <0.1) show changes in inflammatory mediators. **G.)** Bubble Plot of KEGG pathway analysis comparing groups highlights unique aspects of MIS-C using analytes with a p-value <0.05 and DAPs determined from proteomic analysis.

Finally, to gain additional insight into the underlying mechanisms driving the differential presentation of COVID-19 in adults versus children, we measured levels of COVID-19-associated cytokines and correlated these with our multiomic data. Interestingly both COVID+ children and children with MIS-C present with a different cytokine profile as compared to COVID+ adults (Figure AI-8 A). Our results demonstrate similar alterations as those previously reported (Consiglio et al., 2020). Given the well-defined functional roles of these cytokines in combination with the differentiating capability of our metabolomic data, we performed an integrated correlation analysis between lipid, metabolite, and cytokine levels. Adult and pediatric acute COVID cohorts demonstrated less correlation between cytokines and DAAs as compared to the MIS-C cohort (Figure AI-8 B). Adults tended to have strong correlations with IL-6, while COVID+ children seemed to have a strong correlation with IL-12p70. Notably, IL-6 is known to be associated with increases in fibrinogen, including in patients with COVID-19 (Ranucci et al., 2020). This differs drastically from MIS-C, where we saw an increased correlation between all cytokines and analytes, which may reflect an increased metabolic burden associated with immune cell activation.

Network analysis of the integrative correlation data demonstrated positive (red lines) and negative (blue lines) correlations in each cohort (Figure AI-8 C,D,E). Communities, shown by assorted colors, were determined by the number of connections between measured cytokines (depicted as squares) and DAAs (depicted as circles). This analysis shows less connectivity between cytokines and metabolites in the adult cohort (Figure AI-8 C), compared to acute COVID infection in children (Figure AI-8 D). Children with MIS-C demonstrated a greatly magnified effect (Figure AI-8 E), further supporting the notion that a heightened inflammatory state drives much of the metabolic differences observed in MIS-C. In general, our data suggests that IL-10 correlates strongly with IFN-γ during COVID infection, with each other assayed cytokine

displaying a more distinct set of correlated analytes. Network analysis also suggests a difference in the effect of elevated cytokines in adults as compared to pediatrics patients, as adults display distinct communities that correlate well to specific analytes. Finally, our analysis shows a muddling of these networks in various disease states, with 5 cytokine-analyte communities present in the adult COVID+ cohort, 3 present in the pediatric COVID+ cohort, the MIS-C cohort.

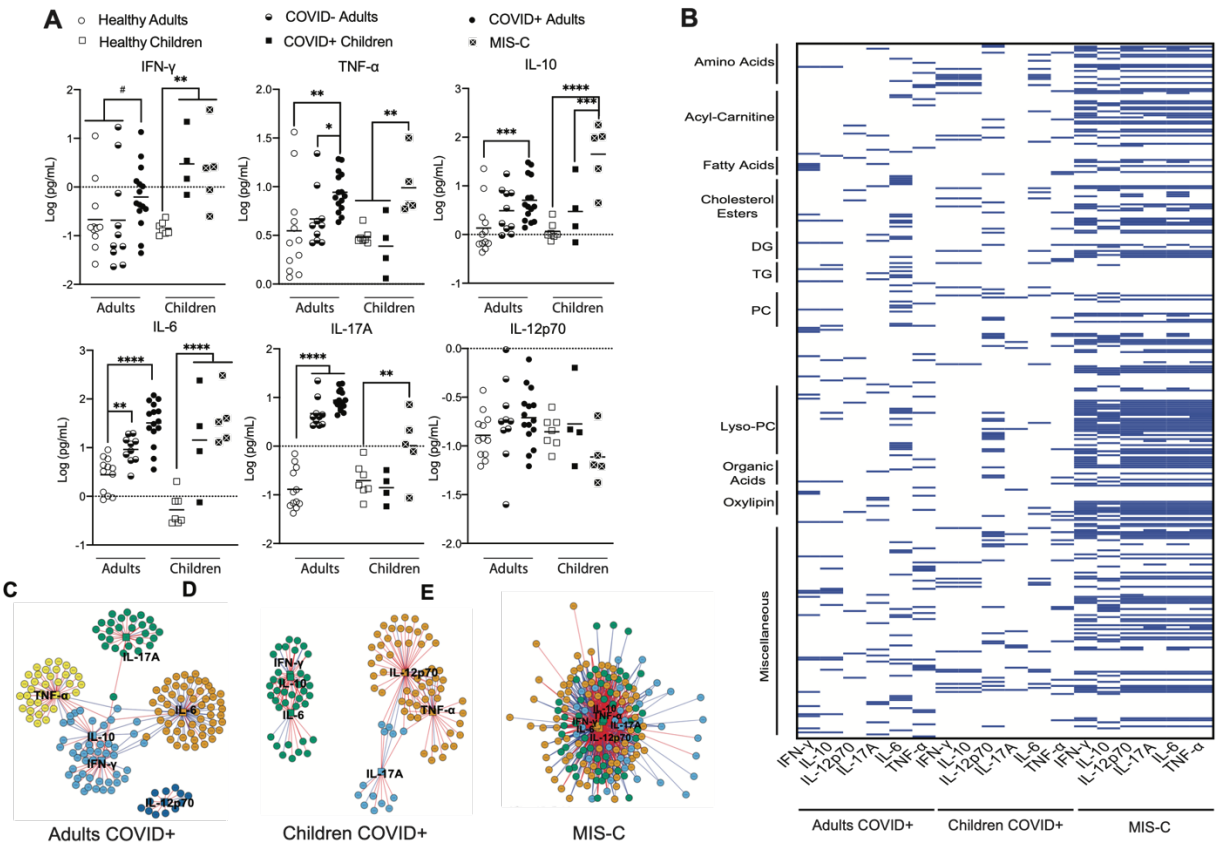

Figure AI - 8: Comparison of cytokine responses in COVID+ adults, COVID+ children or children with MIS-C.

A.) Plasma levels of cytokines present in various cohorts indicated. Both COVID+ children (n=4) and children with MIS-C (n=5) present with a different cytokine profile compared to healthy children (n=7) (p-value<*0.05, **0.01, **** 0.0001, ns not significant, one-way ANOVA with Sidak's multiple comparison test). COVID+ adults (n=15) have the highest increase in these cytokines followed by severely ill COVID– adults (n=10) and healthy controls (n=12). **B.)** Comparison of identified analytes by multiomic studies with measured cytokines further demonstrates distinct pathogenesis of COVID-19 in adults as compared to pediatric patients with COVID-19 or with MIS-C. **C-E.)** Network analysis of the metabolites that correlate with cytokines in COVID+ adults (Tables S12 &S13) (C), COVID+ children (D) or children with MIS-C (E)

Network plots were generated using a centrality cut-off determined by xmWAS (Uppal et al., 2018).

AI.4 Discussion

While the scientific and medical communities have made considerable strides in mitigating SARS-CoV-2 infection through vaccines and antiviral therapies, there remains a fundamental lack of knowledge in understanding the molecular mechanisms responsible for severe COVID-19. Both pediatric and adult COVID-19 patients demonstrate a wide spectrum of disease severity, and critically ill patients remain difficult to treat and even refractory to standard treatment - in large part because the pathophysiologic mechanisms underlying the development of severe COVID-19 have not been defined. In this study we used a comprehensive set of complementary technologies - coupling multiomic biochemical studies with sophisticated “microvasculature-on-chip" assays - to uncover an unappreciated mechanism of systemic pathogenesis in adult patients stemming from biophysically-induced microvascular damage. Importantly, this mechanism of COVID-19 pathogenesis in adults appears distinct from the immune dysregulation characterizing acute pediatric COVID-19 or post-infectious MIS-C (Figure AI-9).

Our proteomic analysis in adult patients confirms associations of COVID-19 with previously described changes in host response pathways, including the complement and coagulation cascades, NET formation, and ECM interactions (D’Alessandro et al., 2020; Shen et al., 2020). These data support laboratory findings exploring these pathways and highlight the convergence of COVID-19-induced pathophysiology on endothelial cell health and blood-endothelial interaction (Afzali et al., 2021; Montaldo et al., 2021; Perico et al., 2021; Skendros et al., 2020). Compared with previous reports, however, our proteomic analysis also uncovered unappreciated changes related to fluid shear stress responsive pathways, including alterations in VCAM1 (important in recruiting circulating inflammatory mediators to the endothelial surface), GSTO1 and TXN (cysteine-based redox regulatory and signaling proteins), MMP2 (related to

extracellular matrix homeostasis), and ACTB (beta actin, part of the intracellular mechanotransductive pathway). Perturbations in shear stress profiles have long been considered indicators of an unhealthy endothelium, as well as implicated in the development of chronic vascular diseases (Brooks et al., 2002; Chatzizisis et al., 2007; Davies, 2009; Davies et al., 2005). Thus, our findings provide mechanistic insight into why epidemiological studies demonstrate worse clinical outcomes in COVID-19 patients with certain risk factors, such as those with diabetes, hypertension, underlying vasculopathy or advanced age, all of which are associated with compromised endothelial function.

Microfluidic-based studies and novel image-capture algorithms allowed for the specific elucidation of COVID-19-associated changes in blood biomechanical properties at the microvascular scale (Lipowsky, 2005), including the influence of altered rheology from pathologically elevated fibrinogen on human endothelium. RBC properties contributing to microvascular changes in critical infective illness have been reported previously and represent an active and growing area of research (Bateman et al., 2017; Reggiori et al., 2009; Said et al., 2015). Our work now demonstrates that plasma from adult COVID-19 patients causes significant RBC aggregation under flow, more so than non-COVID sepsis, and that fibrinogen-mediated aggregation directly damages the endothelial glycocalyx. We posit that this cascade contributes to the impaired microvascular perfusion, thrombosis and endotheliopathy observed clinically and in post-mortem studies (Favaron et al., 2021; Kanoore Edul et al., 2021; Menter et al., 2020; Romanova et al., 2021). Importantly, the 30-minute time scale on which these sets of experiments were conducted suggests that the destruction of the protective glycocalyx layer is not a result of enzymatic degradation, but that direct alterations in the shear stress profiles contribute to endothelial pathology. Moreover, changes identified in the plasma proteome demonstrate

alterations in glycan homeostasis related to endothelial glycocalyx maintenance, which have not yet been reported but are in agreement with prior studies (Fernandez et al., 2022; Ogawa et al., 2021; Stahl et al., 2020). The importance of these findings is two-fold. First, the ability of RBC aggregation to directly damage the endothelial glycocalyx has not been reported previously and presents a novel paradigm for endotheliopathy in critical illness. Second, while patients with critical illness from either COVID-19 or non-COVID sepsis demonstrate microvascular injury, the underlying mechanisms are distinct and provide novel insight into the unique pathophysiology associated with SARS-CoV-2 infection.

Our metabolomic and lipidomic analyses of adult and pediatric COVID-19 plasma similarly agree with previously reported findings, including changes in our adult cohort related to xanthine, acylcarnitines, PUFAs, and lactic acid (Caterino et al., 2021; Dei Cas et al., 2021; Michaelis et al., 2021; Wu et al., 2021). These metabolites and lipid by-products have been implicated previously in inflammatory processes (Rutkowsky et al., 2014). Previous lipidomic studies of COVID-19 patients have also identified alterations in lipids associated with RBC membrane constituents, again consistent with our data (Thomas et al., 2020a). These findings suggest a role for changes in RBC membranes, including stiffness or deformability, which are directly supported by our rheological assays, although it is worth noting that the changes in RBC rigidity were significantly less in COVID-19 patients than in our non-COVID sepsis cohort. Finally, targeted combinatorial analyses revealed convergence of these pathways on the liver, (Wu et al., 2020) providing an important link between COVID-induced activation of the hepatic acute phase response, including fibrinogen production, and changes in blood rheology at the microvascular level.

Given the different clinical phenotype of SARS-CoV-2 infection in adults and children, as well as the spectrum of disease seen in both populations, we performed comparative analyses on plasma from children with COVID-19 or with MIS-C. The profiles of pediatric patients with COVID-19 or with MIS-C demonstrate increases in proteins involved in pro-inflammatory pathways, including complement and coagulation cascade alterations, similarly to what was seen in the adult COVID-19 population. Unique pathways identified in children, compared with adult COVID-19, include those related to parasitic infection and nutrient digestion and absorption. Additionally, and in contrast to adult patients, elevations in cytokine levels demonstrated strong correlation with disease severity in pediatric patients. This is consistent with cytokine profiling studies previously reported in pediatric patients and our current understanding of the role of immune dysregulation in driving systemic disease in children (Diorio et al., 2021; Porritt et al., 2021; Ravichandran et al., 2021; Wang et al., 2021a). Notably, the vascular shear stress response pathway was not significant in pediatric acute COVID or MIS-C, though it was near to achieving statistical significance in MIS-C. Finally, in comparing the multiomic profiles of children with COVID versus those with MIS-C, dramatic decreases in aconitic acid and IL-17A were seen in MIS-C. IL-17 has been shown to correlate with disease severity in other acute systemic vascular diseases, like Kawasaki Disease, and is implicated in several autoimmune conditions. Together, these data support the idea that a hyperinflammatory process contributes to the development of MIS-C in pediatric patients(Kuwabara et al., 2017; Panaro and Cattalini, 2021; Pierce et al., 2020; Wang et al., 2021b).

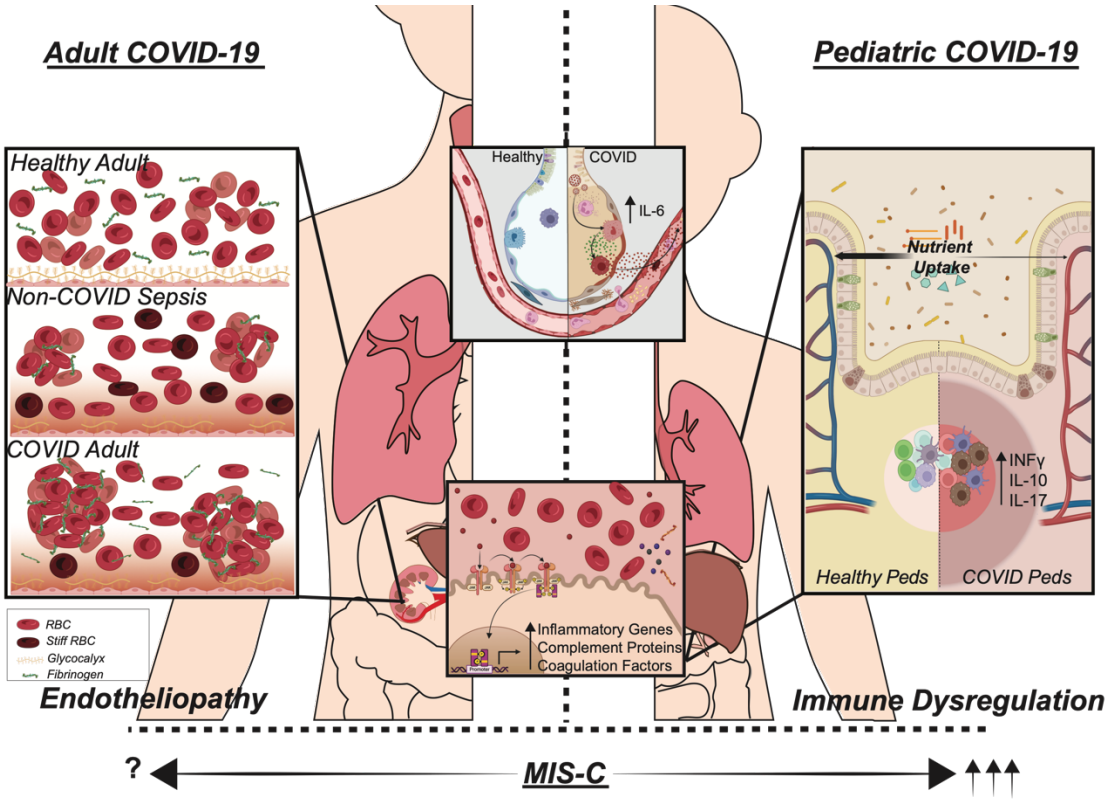

Figure AI - 9: SARS-CoV-2 infection induces distinct changes in adult versus pediatric patients.

Although SARS-CoV-2 is a respiratory virus, multiomic analyses demonstrate systemic changes related to inflammation and the hepatic acute phase response. In adults, the lung-liver axis alterations associated with COVID-19 lead to hypercoagulability and alterations in blood hemodynamics. Pathologically elevated fibrinogen causes RBC aggregation that damages the endothelial glycocalyx, resulting in endotheliopathy and associated microvascular thrombi formation. In contrast, analyses of samples from pediatric patients suggest that alterations in inflammatory signals cause immune dysregulation. MIS-C demonstrates greater immune dysregulation than acute pediatric COVID and results in a hyper-inflamed state, with an uncertain contribution of fibrinogen in mediating the vasculopathy observed clinically in MIS-C.

AI.5 Materials and methods

AI.5.1 PATIENT SAMPLES:

Specimen collection and all studies were performed in accordance with protocols approved by Emory's Institutional Review Board. Demographic information for all patients was obtained by electronic chart review as summarized in Supplemental Tables 1, 6, 7 and 8.

Adult plasma samples used in proteomic, lipidomic and metabolomic studies were obtained from residual clinical specimens available from patient testing at Emory University Hospital. Clinical samples were collected by venipuncture into EDTA-containing tubes, separated from cells within 4 hours of phlebotomy, used in clinical testing and then held at 4 °C for up to 24 hours. Residual specimens were then collected, aliquoted and frozen at –80°C until use in multiomic studies. Plasma for healthy controls was obtained from healthy adult volunteer donors ≥18 years old meeting AABB eligibility criteria for source plasma donation. For microfluidics studies, patients were identified within 48 hours of hospital admission and screened for a diagnosis of sepsis by Sepsis-III criteria as a result of PCR positive SARS-CoV-2 (Singer et al., 2016). Patients or their legal next of kin were contacted for consent according to the approved IRB protocol. Blood was collected in citrated vacutainer collection tube (BD) for same-day experimentation and plasma was isolated and frozen at -80 °C for later use.

Pediatric plasma samples used in proteomic, lipidomic, and metabolomic studies were collected from patients 0 to 21 years of age hospitalized at Children's Healthcare of Atlanta. Prospectively collected blood and/or residual samples were collected following informed consent and assent, as appropriate for age. Children were classified as having COVID-19 if they were hospitalized with a clinically compatible illness and positive SARS-CoV-2 testing by nasopharyngeal RT-PCR. Children were classified as having MIS-C if they met the CDC case

definition (Prevention, 2020): fever, laboratory evidence of inflammation, evidence of more than 2 organs affected, plus evidence of SARS-CoV-2 infection (current or recent nasopharyngeal RT-PCR–positive result for SARS-CoV-2 or positive SARS-CoV-2 serology) or exposure to an individual with confirmed or suspected COVID-19 within the preceding 4 weeks. Demographic, clinical, and outcome data were abstracted from the electronic medical record and entered into a Research Electronic Data Capture (REDCap) database hosted at Emory University (Harris et al., 2019; Harris et al., 2009). Controls were healthy outpatient children who participated in a healthy phlebotomy study.

AI.5.2 PROTEOMICS:

Preparation of plasma samples for proteomics.

All reagents were of HPLC grade or higher. Plasma samples were thawed on ice and gently mixed by agitating the side of the tube. The 10 µL of neat plasma was diluted 1:10 in 100 mM triethylammonium biocarbonate (TEAB, Sigma Aldrich). Protein concentration was then determined by performing a Bradford protein assay. 150 µg of total protein was transferred to a low binding centrifuge tube and diluted with sodium deoxycholate to a final concentration of 1% (w/v) and 5 mM tris(2-carboxyethyl)phosphine (TCEP, Thermofisher). The sample was then incubated at 60˚C for 30 minutes. After cooling for 5 min at room temperature, alkylation of the cysteines was initiated by the addition of iodoacetamide (SigmaAldrich) to a final concentration of 10 mM. This solution was incubated in the dark for 30 minutes at 37 ˚C. The alkylation reaction was quenched by the addition of DL-dithiothreitol (DTT, Sigma Aldrich) at a final concentration of 10 mM, followed by 30 minutes of incubation at 37˚C. From this reaction, 50 µg of total protein (~1/3 of the total) was removed and digested with TPCK treated trypsin (Sigma Aldrich) and Lys-

C protease (Pierce) at a protein to enzyme ratio of 1:10 for trypsin and 1:20 for LysC. The digestion was left to proceed overnight at 37 ˚C.

On the second day, samples were acidified with 10% TFA (Trifluoroacetic acid, ThermoFisher) to precipitate sodium deoxycholate and stop the proteolysis. Samples were incubated for 15 min at room temperature and then centrifuged at 18,000 x g for 10 minutes. The supernatant was then desalted using solid phase extraction HLB matrix (Oasis HLB µelution plate plate, 30µm) with 0.1% FA (Formic acid) for the first wash and 5% methanol 0.1% TFA for the second wash. Samples were eluted with 75%ACN (Acetonitrile)/0.1% FA, dried using a centrifugal vacuum evaporator (LabConco) and stored in the -20 °C.

AI.5.3 LC-MS Method.

Digested peptides were resuspended with 0.1% FA at a concentration of 400 ng µL-1 and 1 µg was injected directly on to an analytical Aurora C18 column (15 cm x 75 µm ID, 1.6 µm C18, Ionopticks, Australia) using an Easy-nLC 1200 UHPLC system (Thermo Fischer). The column temperature was maintained at 60˚C with an integrated column oven equipped with a spray adaptor and larger chamber to accommodate the fittings of the column (Sonation, Biberach, Germany, PROSO-V1). The LC gradient was generated using 0.1% formic acid in ddH2O, buffer A, and 80% acetonitrile 0.1% FA (SigmaAldrich), buffer B, linear gradient from 2-40% B over 60 minutes followed by an increase to 80% B in 2 minutes with a 4 min hold at 80% B before re-equilibration at 2% B prior to the next sample injection. The flow rate was 400 nL*min-1. The samples were analyzed on an Eclipse Tribrid Orbitrap mass spectrometer (Thermo Fisher) equipped with a FAIMS Pro source (Thermo Fisher). Spray voltage was set to 2-2.5 kV, FAIMS CV voltages of -50 and -70, RF funnel 40V, heated capillary 305 ˚C. The instrument was operated in data dependent mode with full profile MS spectra collected at 120k resolution (at 200m/z), 375-1500

m/z, AGC target of 250% with maximum injection time set to Auto. The data dependent acquisition used a monoisotopic peak determination filter set to peptides, intensity set to 5e3, charge states 2-6, dynamic exclusion of 60 seconds and a total cycle time of 0.6 seconds for each FAIMS CV voltage. The MS/MS fragmentation was collected with high energy collision induced dissociation (HCD) with the following settings; quadrupole isolation with 1.2 Da window, normalized collision energy set to 30%, detector set to ion trap with turbo scan rate and defined mass range of 200-1400, AGC 250% with a maximum injection time of 25 ms. Information stored as centroid data.

AI.5.4 Data analysis.

Proteomic data was analyzed using the commercially available software Proteome Discoverer v 2.4 (ThermoFisher). The LC-MS/MS files were recalibrated and MS/MS spectra were searched with Sequest using the following parameters; protein database homo sapiens (uniprot taxon ID9606 reviewed with 20,385 sequence entries), N-terminal modifications Met-loss, met-loss and acetylation, peptides fixed modifications carbamidomethylation of cys, dynamic modification included oxidation of Met, and pyroglutamate formation of N-terminal glu, Enzyme was set to trypsin with 2 miss cleavages, 10 ppm error on MS1 and 0.5 Da error on MS2. All spectra not matched were then re-processed using trypsin with semi tryptic cleavage and 2 missed cleavages. All data were passed through Percolator with FDR set at 1%. Label free quantitation was done using the standard workflow provided with default settings, except the retention time filter was reduced to 3 minutes, due to the high reproducibility of the retention time using the current LC setup. MS1 features were extracted using minor feature detection and. ANOVA statistical analysis was done using pairwise protein-based abundance with the ratio of COVID

positive/control samples. A Benjamini-Hochberg correction for FDR was applied and adjusted p-values <0.01 and an abundance ratio of at least ±1.3.

AI.5.5 Unified Metabolite and Lipidomic Data Analysis Methods.

Data from each metabolomics assay (Biocrates Quant500, Oxylipins, PUFA, Untargeted high-resolution lipidomics and Untargeted high-resolution metabolomics) were independently analyzed using the R package, xmsPANDA (https://github.com/kuppal2/xmsPANDA). Missing values were imputed using the k-nearest neighbors/half minimum feature method and data were normalized by z-score. Significant features (p-value < 0.05) were identified using Limma (linear models for microarray data). For adults, significant features were further filtered by covariate analysis including sex (pvalue_sex < 0.05) and gender (pvalue_gender < 0.05). KNN nearest neighbor method was used to impute values identified in some patients but not others. Significant metabolomics features from each platform were merged and duplicates were cleaned. Pathway analysis was performed using Metaboanalyst, also integrating our proteomics data sets.(Pang et al., 2021) Z-Normalization was used to compare different methods. This method is a metabolite-based normalization method to adjust the metabolite variances identified via our suit of metabolomics/lipidomic analyses. Metabolites are comparably scaled to unit variance based on the assumption that all metabolites are equally important. Z-score is calculate for each metabolite as $(x-\mu)/\sigma$, where x is the metabolite (unit: concentration or area), μ is the mean of the metabolite, and σ is the standard deviation of the metabolite.

AI.5.6 Cytokine and Metabolomics Data Driven Integration Methods.

Statically significant metabolomics data were pre-filtered to retain only features with non-zero values in >50% in all samples and >80% in each group. The R package xMWAS (https://github.com/kuppal2/xMWAS) was used to integrate cytokines and metabolomics data.

Multivariate statistical method partial least squares regression (PLS) was used where correlation threshold is 0.4 and P-value threshold is 0.05. The integration network was evaluated by eigenvector centrality (importance) and nodes' centrality > 0.4 were selected and their edges were used to plot the heatmap.

AI.5.7 LIPIDOMICS

For all lipidomics and metabolomics experiments, patient samples were de-identified prior to receipt. The subsequent analysis of lipids was blinded. All patient samples were processed in a cold room at 4 °C.

AI.5.7.1 Untargeted Lipidomics.

Quality Control and Internal Standards:

Pooled quality control samples were prepared by aliquoting 5 ml of each patient plasma into a single vial. This sample was spiked with 10 ml internal standard (Splash Lipidomix, Avanti Polar, Birmingham, AL) and extracted in the same manner as patient samples. This analytical grade standard contains odd-chain, deuterated lipids in lipid classes and ratios present in human plasma. Pooled QC samples were run after every 10 patient samples as well as at the beginning and end of the analytical run. Quality control samples were used to ensure the stability of the instrument during the course of analysis. The coefficient of variation for each identified lipid within the pooled QC was then calculated using a cutoff of <40%. The internal standard was used to optimize instrumental parameters, such as electrospray voltage, collision energy, and others; these parameters were held consistent over the course of analysis. Lipids in the internal standard were also used to monitor injection consistency from sample to sample.

Extraction:

Lipids were extracted from plasma using a high throughput, monophasic, methyl t-butyl ether (MtBE) based method. Using an automated pipetting and sample preparation system (Biotage Extrahera, Uppsala, Sweden), 50 µL of patient plasma was loaded into preconditioned wells containing 10µL methanol and 10 µL of internal standard, Splash Lipidomix (Avanti Polar, Birmingham, AL). To each well, 200 µL methanol containing 50 µg/mL BHT was then added and the sample was mixed by 3 up and down passes of the automated sample handling pipette. The samples were then centrifuged at 4000 rpm for 5 minutes to pellet precipitated protein. The supernatant was recovered and transferred to a separate deep well 96-well plate for extraction. To extract lipids from the supernatant, 250 µL MtBE:methanol (3:1 v/v) was added to all wells and mixed with 3 up and down passes of the automated sample handling pipette. The sample plate was then centrifuged at 1000xg for 3 minutes and the supernatant filtered through a 0.25mm polytetrafluoroethylene (PFTE) filter plate (Biotage, ISOLUTE® FILTER+, Uppsala, Sweden) The recovered extract was then dried under nitrogen gas and subsequently reconsitituted to 200ml in acetonitrile:isopropanol (1:1 v/v) methanol for LC/MS analysis.

Chromatography:

Ten microliters of extracted lipids were resolved on a Vanquish UHPLC (Thermo Scientific, Waltham, MA) using a Thermo Scientific Accucore C18 (4.6 x 100 mm, 2.6 µm) column on a 15 minute linear gradient, whereby Solvent A was 60:40 acetonitrile:water and Solvent B 90:10 isopropanol:acetonitrile. Both solvents in the mobile phase contained 0.1% formic acid and 10mM ammonium formate. The column temperature was set at 50 °C and a flow rate of 0.4 mL/min was constant throughout analysis. All chromatography parameters are shown in Table 1.

Time (min)	A: 60:40 ACN:H2O	B: 90:10 IPA:ACN
0	60	40
0.2	60	40
1.5	40	60
6	30	70
9	15	85
11	0	100
12.5	0	100
13	60	40
15	60	40

Mass Spectrometry:

Eluted lipids were analyzed by a Thermo IDX Fusion mass spectrometer operated in both the positive and negative ionization modes successively (Thermo Scientific, Waltham, MA). To complete the untargeted lipidomics analysis, a data dependent acquisition method was used. For this, a high-resolution MS scan was conducted on each sample at 120,000 FWHM resolution and ions above instrumental noise threshold were systematically fragmented for structural elucidation. All MS/MS spectra were conducted using 30,000 FWHM resolution. Instrumental parameters used during analysis were optimized using the pooled quality control sample and the analytical grade internal standard. Parameters were held constant over the course of the analysis. A table of all instrumental parameters is recorded in Table 2.

Parameter	**Setting**

Ion Source Type	H-ESI
Spray Voltage	Static
Positive Ion (V)	3500 V
Negative Ion (V)	3500 V
Sheath Gas (arb. units)	50
Aux Gas (arb. units)	10
Sweep Gas (arb. units)	1
Ion Transfer Tube Temp (°C)	300
Capillary Temp (°C)	275
S-Lens RF Level	40V
Data Acquisition Strategy	Full scan and data dependent acquisition
Full scan resolution (FWHM)	120,000
MS/MS resolution (FWHM)	30,000
HCD Fragmentation:	Normalized collision energy (NCE) of 25, 35, 45, 55 eV Stepped NCE of 10, 20, 50 eV

Lipid Identification:

Raw mass spectral data was uploaded into LipidSearch software ver 4.2 (Thermo, San Jose, CA) for lipid identification (Table S16). This software scans user data against an extensive database to identify lipids. Peaks were detected and quantified using the QEX product ion search

parameters, where 5.0 ppm was used as both parent and product mass tolerances. Other LipidSearch parameters, such as the selected database, retention time tolerance, precursor and product mass tolerances, intensity threshold, m-score threshold, ID quality filters, lipid class, and adducts, are provided in the supplement. For alignment, the pooled QC was designated as the control and its' fragment data used for identification of lipid species. The identified features were then aligned with the full scan data from each respective patient sample using a 0.1 minute retention time tolerance. XCMS software was used to process raw data files and identify features in the samples. Lipids were annotated with LipidSearch 4.2 software (Thermo). Only MS2 level confirmed lipid species grade A, B and, C were used and lipids with grade D or lower were removed. Grade "A" calls are lipids of which fatty acid chains and class were identified completely, grade "B" calls are lipids of which class and some fatty acid chains were identified ,grade "C" calls are lipids of which class or fatty acid was identified, while low confidence "D" identifications are only matched according to mass. Search parameters used for the LipidSearch software are provided in the supplementary (Table S17). All preliminary identifications made by the software were manually reviewed to ensure appropriate identification and quantitation.

AI.5.7.2 Polyunsaturated Fatty Acids.

Extraction:

Polyunsaturated Fatty Acids (PUFAs) were extracted according to an adapted Bligh and Dyer method. For this, 1.2 mL of methanol and 0.6 ml chloroform was added to 100 µL patient plasma of sample. Samples were vortexed for 30 minutes and subsequently centrifuged at 4000 rpm for 10 minutes at 4 °C. The supernatant was collected and 1 mL of 0.1 M Sodium Chloride and 1 mL of chloroform was added to each sample. Samples were then vortexed and centrifuged as above. The organic phase was retained and dried under a gentle stream of nitrogen gas. Dried

samples were reconstituted in 100 mL 1:1 chloroform/methanol and 10 µL of Splash Mix (Avanti Polar, Alabaster, AL) was added. This sample was transferred to a HPLC vial for LC/MS analysis.

Chromatography:

Extracted lipids were resolved using an Exion AC UPLC (Sciex, Framingham, MA), whereby 10 mL of extract was deposited on an Accucore C18 column (100 x 4.6 mm; Thermo Waltham, MA) and resolved on an 18-minute linear gradient. For the mobile phase, 60:40 acetonitrile:water was used as Solvent A and 90:10 isopropanol:acetonitrile as Solvent B, both containing 10 mM ammonium formate and 0.1% formic acid. The column temperature was set to 50 °C and a 0.5 mL/min flow rate was held consistent over the course of the run. Chromatography parameters are shown below.

Time (min)	60:40 ACN:Water	90:10 IPA: ACN
0	80	20
2.0	80	20
2.1	60	40
10.0	30	70
10.1	0	100
15.0	0	100
15.1	80	20
18.0	80	20

Mass Spectrometry:

Eluted lipids were analyzed by a Qtrap 5500(Sciex, Framingham, MA). For this, precursor ion scanning was conducted in the negative ion mode for m/z 277, m/z 279, m/z 301, m/z 303, and m/z 327, corresponding to the mass to charge ratio of linolenic (18:3), linoleic (18:2), eicosapentaenoic (20:5), arachidonic (20:4), and docosahexaenoic (22:6) fatty acyl anions. Using an independent data acquisition (IDA) method, all resulting ions from each precursor ion scan within the mass range of m/z 200-m/z 1000 with signal intensities greater than 500 cps were fragmented for structural elucidation in a top 4 manner. Instrumental parameters were optimized using the internal standard and held consistent during analysis. A table of mass spectrometry parameters is presented below.

	Negative polarity
Curtain gas	20 arb. units
Collision Gas	Low
IonSpray Voltage	-4500 V
Temperature	650C
Ion Source Gas 1	55 arb. units
Ion Source Gas 2	60 arb. units
Declustering Potential	-90 arb. units
Entrance Potential	-10eV
Collision Energy	-30eV
Collision Cell Exit Potential	-11eV

Identification and Quantification:

Lipids were identified using LipidView (Table S17) identification software (Sciex, Waltham, MA). This software scans fragment data against an extensive database. After upload of raw data, lipids are identified by matching MS/MS data. Preliminary identifications were made by default "confirmed and common" search parameters and verified by manual review of product ion data. Quantification of identified lipids was achieved by single point calibration, whereby the area of the analyte was divided by the area of the internal standard and multiplied by the concentration of the internal standard, 15:0-18:1D7 PC. Standard lipidomics nomenclature was maintained throughout (x:y), where x is the number of acyl carbons and y are the number of double bonds. Ether linked lipids are denoted as e; those with no qualifier are acyl linkages.

AI.5.7.3 Oxylipins and endocannabinoids (OXY).

Standards:

Oxylipins and endocannabinoids are quantified by an external calibration curve using analytical grade standards, all purchased from Cayman Chemical (Ann Arbor, MI). These are PGE2 Ethanolamide (PGE2-EA), Oleoyl Ethanolamide (OEA), Palmitoyl Ethanolamide (PEA), ARA-Ethanolamide (AEA), Docosahexaenoyl Ethanolamide (DHEA) , Linoleoyl Ethanolamide (LEA), Stearoyl Ethanolamide (ceramid), oxy-Arachidonoyl Ethanolamide (oxy-AEA), 2-Arachidonoyl Glycerol (2AG), Docosatetraenoyl Ethanolamide (DEA), alpha-linolenoyl ethanolamide(ALEA), 9Z-octadecenamide (oleamide), dihomo-gamma-linolenoyl ethanolamide, docosanoyl ethanolamide , (±)9,10-dihydroxy-12Z-octadecenoic acid (9,10 DIHOME), prostaglandin E2 (PGE E2), 20-hydroxy-5Z,8Z,11Z,14Z-eicosatetraenoic acid (20- HETE), (±)-9-hydroxy-5Z,7E,11Z,14Z-eicosatetraenoic acid (9-HETE), (±)14,15-dihydroxy-5Z,8Z,11Z-eicosatrienoic acid (14,15 DHET), (±)5-hydroxy-6E,8Z,11Z,14Z-eicosatetraenoic acid (5 HETE), 12R-hydroxy-5Z,8Z,10E,14Z-eicosatetraenoic acid (12 R-HETE), (±)11,12-dihydroxy-

5Z,8Z,14Z-eicosatrienoic acid (11,12-DHET), (±)8,9-dihydroxy-5Z,11Z,14Z-eicosatrienoic acid (8,9-DHET), (±)5,6-epoxy-8Z,11Z,14Z-eicosatrienoic acid (5,6 EET), (±)5,6-dihydroxy-8Z,11Z,14Z-eicosatrienoic acid (5,6-DHET), Thromboxane (TXB2), (±)12(13)epoxy-9Z-octadecenoic acid (12(13)-EPOME), (±)-13-hydroxy-9Z,11E-octadecadienoic acid (13 HODE), prostaglandin F2a (PGF2A), (±)14(15)-epoxy-5Z,8Z,11Z-eicosatrienoic acid (14(15)-EET), (±)15-hydroxy-5Z,8Z,11Z,13E-eicosatetraenoic acid (15-HETE), Leukotriene B4 (LTB4), (±)8,9-epoxy-5Z,11Z,14Z-eicosatrienoic acid (8(9)-EET), (±)11,(12)-epoxy-5Z,8Z,14Z-eicosatrienoic acid (11(12)-EET). Calibration curves were prepared of these standards over the linear range of 0.1-10nM and the equation of the slope used for quantification of the corresponding lipid in the patient's plasma.

Extraction:

Oxilipins were isolated from plasma samples using an automated C18 solid phase extraction manifold, the Biotage Extrahera (Biotage, Uppsala, Sweden). Samples were prepared by pipetting 100 µL of patient plasma to a 96 well plate. To the sample, 300 µL of 20:80 methanol:water, 55 mL 1% butylated hydroxytoluene (BHT), and 80 µL of glacial acetic acid was added to achieve pH 3.0. Samples were centrifuged at 4000 rpm for 10 minutes at 4 °C to pellet any precipitated solids. The supernatant was transferred to a C18 SPE plate (Isolute C18, Biotage, Uppsala, Sweden) that was preconditioned with 1mL ethyl acetate and 1 mL of 95:5 water:methanol. After depositing the sample on the SPE plate, the sample was rinsed with 800 µL water, followed by 800 µL hexane. The oxylipins were then eluted off the SPE column with 400 µL methyl formate. The recovered oxylipin fraction was then dried under nitrogen gas and subsequently reconstituted in 100 ml methanol to be analyzed by LC/MS.

Chromatography:

Extracted lipids were resolved using an Exion LC/QTrap 5500 LC/MS system (Sciex, Framingham, MA). To quantify the oxylipins in extract, 10 µL sample was injected onto an Accucore C18 column (100 x 4.6, Thermo, Waltham, MA) and resolved on a 16-minute gradient using water as Solvent A and acetonitrile as Solvent B, both containing 0.1% formic acid. The column was heated to 50 °C in a temperature controlled column chamber and 0.5 ml/min flow rate was used for analysis. The gradient used for analysis is listed below.

Time (min)	Percent A: 0.1% FA in water	Percent B: 0.1% FA in ACN
0	90	10
0.5	90	10
1	50	50
2	50	50
2.1	25	75
5	25	75
7	15	85
12	15	85
12.1	0	100
14	0	100
15	90	10
16	90	10

To detect endocannabinoids in the extract, a shortened chromatography gradient was programmed, utilizing the same analytical column and mobile phase referenced above. For

endocannabinoids, 1 µL of extract was injected into the column for analysis and resolved on a 13-minute linear gradient. Gradient parameters are recorded below.

Time (min)	Percent A: 0.1% FA in water	Percent B: 0.1% FA in ACN
0	90	10
0.5	90	10
1	50	50
2	50	50
2.1	15	85
5	15	85
7	15	85
12	15	85
12.1	90	10
13.0	90	10

Mass spectrometry:

Eluted oxylipins and endocannabinoids were analyzed by a QTrap5500 (Sciex, Framingham, MA) mass spectrometer. Instrumental parameters were optimized using external analytical grade standards and were held consistent over the course of analysis. Instrumental parameters are reported below. Oxylipins were analyzed in the negative ion mode and endocannabinoids were analyzed in the positive ion mode in successive analytical runs. Both classes of lipids were targeted using a multiple reaction monitored (MRM) based method. For this,

the mass of the target lipid and a characteristic fragment were targeted for detection. A table of transitions used for analysis is reported below.

	Negative polarity	Positive polarity
Curtain gas	20	20
Collision Gas	Low	Low
IonSpray Voltage	-4500	5000
Temperature	650	650
Ion Source Gas 1	60	55
Ion Source Gas 2	50	60
Declustering Potential	-200	90
Entrance Potential	-10	10
Collision Energy	-40	47
Collision Cell Exit Potential	-11	18

LIPID	Q1 MASS	Q3 MASS
9,10 DIHOME	313.2	201.0
PGE E2	351.2	315.1
20- HETE	319.2	289.2
9-HETE	319.2	167.2

14,15 DHET	337.2	207.0
5 HETE	319.2	115.1
12 R-HETE	319.2	179.1
11,12-DHET	337.2	167.1
8,9-DHET	337.2	127.2
5,6 EET	319.2	191.1
5,6-DHET	337.2	71.0
TXB2	369.2	169.1
12(13)-EPOME	295.2	195.1
13 HODE	295.2	195.1
PGF2A	353.2	193.3
14(15)-EET / 15-HETE	319.2	219.0
LTB4	335.2	195.1
8(9)-EET	319.2	69.2
11(12)-EET	319.2	167.1
PGE2 Ethanolamide (PGE2-EA)_271.3	396.5	271.3
Oleoyl Ethanolamide (OEA)	326.4	62.1
Palmitoyl Ethanolamide	300.4	62.1
ARA-Ethanolamide (AEA)	348.4	62.1
Docosahexaenoyl Ethanolamide (DHEA)	372.4	62.1

Linoleoyl Ethanolamide (LEA)	324.4	62.1
Stearoyl Ethanolamide (ceramid)	328.4	62.1
oxy-Arachidonoyl Ethanolamide (oxy-AEA)	364	76
2-Arachidonoyl Glycerol (2AG) trans1	379.4	135
Docosatetraenoyl Ethanolamide (DEA)	376.59	62.1
alpha-linolenoyl ethanolamide(ALEA)	322.4	62.1
oleamide	282.5	247.4
dihomo-gamma-linolenoyl ethanolamide	350.4	62.1
docosanoyl ethanolamide	384.5	62.1

Quantification:

To quantify oxylipins and endocannabinoids, the area under the curve of each identified lipid is calibrated against an external calibration curve. To create the curve, analytical grade standards in the linear range of 0.1 nM-10 nM are created for each standard. The lower limits of detection and upper limits of detection are determined, plotting concentration versus area under the curve. The slope of the linear regression equation is used for calibration of the corresponding analyte.

AI.5.8 METABOLOMICS

AI.5.8.1 Untargeted Metabolomics.

Extraction:

Metabolites were extracted from patient plasma using a 1:1 mixture of acetonitrile:methanol. Two-hundred µL 1:1 acetonitrile:methanol was added to 50 ml plasma. This solution was vortexed for 3 seconds and incubated on ice for 30 minutes. The sample was then centrifuged at 20000 x g for 10 minutes at 4 ˚C to pellet precipitated protein. The supernatant was then transferred to an amber autosampler vial for LC-MS/MS analysis.

Quality Control:

A pooled quality control sample was created by combining 5 µl of each sample extract into a separate vial. This sample was run in triplicate and the beginning and end of analysis, as well as intermittently over the course of analysis. This was done as an analytical control and to assess instrument suitability. Additionally, the NIST Standard Reference Material 1950 (metabolites in human plasma) was injected as a global reference material to assess performance between studies. Both the global QC and the Standard Reference Material 1950 were also used to generate MS/MS scans using data-dependent acquisition (see below).

Chromatography:

Untargeted metabolomics was performed using an ID-X Fusion (Thermo, San Jose, CA) tribrid mass spectrometer coupled to a Vanquish UHPLC (Thermo, San Jose, CA). Metabolites in the sample extracts were injected and resolved using a SeQuant ZIC-HILIC (3.5µm, 100A 150x2.1mm) column with a 23-minute linear gradient method (detailed below). For chromatography, water was used as Solvent A and acetonitrile as Solvent B; both contained 0.1% formic acid. For analysis, 1 ml extract was injected by the autosampler and introduced to the LC column. The column was maintained at 50 °C. HESI-II source parameters are listed below. A full

scan MS1 spectrum was obtained for each sample, including the pooled QC and procedural blanks, at 120,000 FWHM resolution within a scan range of *m/z* 67-1000. The mass spectrometer was operated in both positive and negative ionization modes (as separate injections). Additional MS/MS scans were acquired in separate runs with data-dependent acquisition to support identification of metabolites. The top 20 ion intensities per MS1 scan were selected for fragmentation, generating substructure information. This process was done iteratively across repeated injections of the QC materials, excluding prior selections to increase coverage.

Time (min)	Solvent A: 0.1% FA in Water	Solvent B: 0.1% FA in ACN	Flow Rate (ml/min)
-4.0	10	90	0.35
0	10	90	0.25
17.5	80	20	0.25
23.0	80	20	0.35
24.0	10	90	0.35

Sheath Gas	40 arb. units	Electrospray Voltage (Positive)	3000 V
Aux Gas	8 arb. units	Electrospray Voltage (Negative)	2750 V
Sweep Gas	1 arb. units	Capillary Temp.	275 ˚C
RF Level	50	Probe Temp.	320 ˚C

Metabolite Identification:

After collection, data were processed using Thermo Compound Discoverer software ver 3.2 (San Jose, CA) (Table S18). Metabolites from the IROA Mass Spectrometry Metabolite Library of Standards (MilliporeSigma) were analyzed to generate a compound library of accurate mass and retention time data for the method described above. Metabolites were subsequently identified by accurate mass and retention time (denoted as 'AMRT'), following data alignment and peak integration by the Compound Discoverer software ver 3.2. Additional annotations were made by comparing MS2 results to the mzCloud library (mzcloud.org) of reference MS2 spectra (denoted as 'MS2L'). Compounds detected were compared to a compound library of exact mass and retention time of 413 validated reference standards, i.e., Schymanski level 1 (Schymanski et al., 2014), and/or were annotated according to sufficient substructure information as determined from MS/MS scans, i.e., Schymanski level 2. If AMRT and MS2L designations for the same compound produced conflicting results, the reference standard data took precedence. Signal intensities were normalized by batch drift correction using the pooled QC sample and the maximum RSD after normalization was set at 30% (filtering those compounds with greater RSD), while compounds with a ratio of the max sample area to max blank area less than 5 were also filtered.

AI.5.8.2 Targeted Metabolomics

To validate the metabolic pathway enrichments identified in untargeted LC-MS data, a targeted MS/MS approach combining LC-MS/MS and flow injection analysis (FIA-MS/MS) using reference compounds (Biocrates Life Sciences) was employed. This allowed for metabolite identification and quantification at level 1 (matching accurate mass, retention time, and MS/MS relative to authentic standards).

AI.5.9 MICROFLUIDICS ASSAYS

All microfluidic devices were generated in house using a standard workflow employed by our group beginning with soft photolithography and a silicon wafer etched with custom device design(Mannino et al., 2018). For each of the three microfluidic device designs used in the described experiments, three dimensional channels were constructed by first casting the wafer with polydimethylsiloxane (PDMS, Dow Corning) and then cured overnight at 60 °C. Casts were then separated from the mold and cylindrical biopsy punches were used to create inlet and outlet sites. For the microfluidic assays involving endothelial cell culture, each device was bonded to a second thin sheet of PDMS and for the aggregation and deformability assays, devices were bonded to cover glass slips (VWR) using a plasma bonder (PlasmaTech) and kept at 60 °C for at least 24 hours before use.

AI.5.9.1 Shear and Conduit Size Dependent RBC Aggregation.

RBC aggregation under flow was assessed using a novel device consisting of two 500µm bypass channels surrounding the central straight conduits. There devices contains duplicate copies of four channel widths 20µm, 30µm, 45µm and 70µm each with a height of 10µm. Resistance is equal among all channels to permit equal distribution of flow. Only the 70µm channel was used for aggregation analysis in these experiments. Each device was first coated with 1% bovine serum albumin (BSA, Sigma) in phosphate buffered saline (PBS) for one hour at room temperature to limit potential interaction between the blood sample and the device material. For all tested conditions and patient samples, solutions were perfused into the devices using a flow controlled syringe pump (Harvard Apparatus) to a target shear rate of $100s^{-1}$ based on a solution to laminar flow in a microfluidic rectangular cross sectional tube. RBC aggregation was quantified as the number of differential cell velocity clusters (DCVCs) using video microscopy coupled with a custom post processing workflow. A Grasshopper 3 high speed camera (FLIR) was used to obtain

10 seconds of video frame data at a frame rate of 160 frames per second, with a FOV of 1200x1920 pixels and image resolution of 2.57 pixels/µm. Each of these video of 1600 frames was discretized into 40 sets of 40 consecutive frames for the tracking function, spanning 0.25 seconds. This time frame was chosen because the average particle velocity would be approximately 200µm/s at this flow rate and 0.25 seconds would yield average displacement of 50µm which is slightly greater than the expected length of an endothelial cell in the direction of flow. For the first frame of each set, cell features were identified using an algorithm to identify corner points or edges (Shi and Tomasi, 1994) which detects ares of an image with sharp gradients in image intensity.The Kanade-Lucas-Tomasi feature tracking algorithm was then used in Matlab (Mathworks) to follow the pathline for each of these cell features across the next 39 frames in the set using forward and backward validity checks set to maximum fidelity (Kalal et al., 2010). This would ensure that any noise within the image would not contribute to the profile of tracked points. This method for tracking velocity in microfluidics devices using red cell features has been previously published and was adapted for purposes in this study (Szafraniec et al., 2022). Supplemental Figure 2 shows the described workflow. A velocity field for each frame was generated from this tracking algorithm and instantaneous velocity for each tracked point was averaged over all frames within the set. The cumulative average velocity field was then discretized into 5µm x 5µm bins to create a standardized velocity matrix. The difference in velocity between neighboring bins was calculated and normalized to the average velocity of that frame set. A threshold was applied to this differential velocity field map to identify all adjacent bins that had velocities which were different by less that 5% of the mean velocity to create a logical image of similar (map value =1) or dissimilar (map value =0). A connectivity map was then generated in which all contiguous areas meeting the defined threshold were identified (SFig 2E). All areas that were at least 115 pixels^2 large in this

differential velocity map, corresponding to an area roughly the size of 15 RBCs, were considered a DCVC and the total number of DCVCs over the length of the video was quantified. The size of each DCVC was then calculated in image coordinates and the position of these clusters in the differential velocity map was mapped to the original velocity field to calculate the DCVC's velocity. This definition was chosen to identify groups of tracked cells that moved together as a cluster under flow mediated either by interactions between RBC membranes or by differential changes in the biophysical properties of the blood from changes in the plasma viscosity or circulating proteins. The results were compared between patients with COVID and volunteers for both channel sizes and each target shear rate using an unpaired t-test between the two population and repeated measures ANOVA within each population for the two channel sizes.

For the variable fibrinogen dose aggregation experiments, purified fibrinogen (Enzyme Research Laboratory) was diluted in PBS to concentrations of 900mg/dL, 600 mg/dL and 300 mg/dL. A negative control without fibrinogen was also tested. These dilutions were combined with RBCs isolated from healthy control volunteer. Blood was collected into a blood collection tube containing citrated anticoagulant. The platelet rich plasma was removed from the red cells by the first centrifugation step and then the RBCs were washed of all residual plasma twice by the addition of PBS at twice the volume and repeated centrifugation steps. For the patient and healthy plasma aggregation experiments, plasma was collected, processed and stored as described in the 'Patient Sample' section of the methods.

AI.5.9.2 RBC Deformability.

To evaluate changes in RBC membrane properties, a previously described RBC deformability assay (Figure 3D, top left) was used (Rosenbluth et al., 2008). This assay allows visualization and measurement of the velocity of individual RBCs moving through a channel

measuring 5 μm x 6 μm, the scale of the capillary, as a surrogate for membrane deformability. RBCs were isolated from each patient or volunteer on the day of collection as described above. The RBCs were then resuspended in PBS at 0.5% by volume and perfused at a steady flow rate of 1 μL/min using a flow controlled syringe pump. Two minutes of video microscopy at a frame rate of 40 frames per second with image resolution of 2.57 pixels/μm was obtained to capture deformability data for at least 250 cells for each patient or volunteer. To determine a deformability index individual RBC velocity was calculated using at least three video frames of the cell's movement across the channel and then normalized to a mean reference value calculated by measuring the velocity of the cells through a larger channel in the device representing unobstructed flow (Figure 3D, top left). The deformability indices for each patient or volunteer were pooled within the respective populations and the results were compared between patients with COVID+, non-COVID sepsis and healthy controls. The average number of cells evaluated across all subjects from the three cohorts was 735 ± 505.

AI.5.9.3 Glycocalyx Degradation in Endothelialized Microfluidic Devices.

To investigate the interaction between RBC aggregation and endothelial activation, a microfluidics platform was constructed with serial branches ranging in width from 120 μm to 30 μm with a constant height of 30 um (Figure 2G) mimicking the approximate size and geometry of the pericapillary vasculature. Human umbilical vein endothelial cells (HUVECs, passage 4-7, Lonza) were cultured in this device using a well-established protocol (Myers et al., 2012; Tsai et al., 2012). Devices were first with fibronectin 50 μg/mL (Sigma) for 1 hr at 37°C and then washed with endothelial cell growth basal media (EBM) supplemented with EGM-2 Endothelial SingleQuots (Lonza). HUVECs grown to confluence in T25 flasks were washed twice with PBS, then detached from the flask by the addition of trypsin-EDTA and neutralized with EGM-2 media.

Cells were pelleted by centrifugation, excess media was aspirated and cells were resuspended in 65-85μL of EGM-2 with 8% dextran (500kDa, Sigma) weight by volume to increase fluid viscosity and promote settling of cells. This cell resuspending was injected into the device inlet using negative pressure applied at the outlet of the device. Cells were allowed to adhere, and the inlets and outlets were cleaned of excessive cells. Cells were then cultured under steady flow using a flow-controlled syringe pump to target shear stress of 5 dyn/cm^2 and reached confluence by 72 hours for use in the experiments.

For the variable fibrinogen dose experiments, fibrinogen was diluted to its final concentration in EGM-2 with the volumes of the lower fibrinogen levels normalized using PBS so that all conditions had identical volumes of cell culture media.

For the experiments comparing the influence of plasma and serum from COVID patients, plasma was collected in citrated blood collection tubes and serum was created by the addition of calcium to a final concentration of 10mM. Clot formation was allowed to occur and separated by high rotational centrifugation. The resultant supernatant was then used as serum.

For the patient and volunteer sample experiments, plasma was isolated from blood in citrated collection tubes from eleven patients with COVID, five patients with sepsis from infectious causes other than SARS-Cov-2, and five healthy volunteers.

In each of these experiments, RBCs obtained from a healthy volunteer and isolated as above were combined with the fibrinogen dilutions, plasma, or serum to 25% by volume. The experiments involving plasma required samples to be re-calcified to 4 mM Ca to maintain endothelial cell homeostasis. In the case of serum and the fibrinogen dilution the calcium concentration was adequate either through the addition of cell culture media or the additional calcium supplementation.

Devices cultured with confluent endothelial cells were perfused with Alex Flour 647 wheat germ agglutinin (Invitrogen) 10µg/mL in EGM-2 for 1 hour and then washed with EGM-2 for 30 minutes. The devices were then imaged on a digital microscope (Keyence, BZ-X series) using high sensitivity resolution and an exposure time 1/15 seconds using a Cy-5 filter (Keyence). Tile scans of both the fluorescent and bright field images were obtained. The fluorescent signal was quantified in each channel size after an adaptive background subtraction was applied. The combined fibrinogen dilution/plasma/serum and RBCs were then perfused into the device at a steady rate using a flow controlled syringe pump for 30 minutes. The imaging process was repeated using identical acquisition parameters. The pre and post perfusion images were co-registered and the fractional residual glycocalyx was calculated as ratio of fluorescent signal in each channel segment and stratified by channel size. The residual glycocalyx ratio was compared across all channel sizes between the experiments using a paired repeated measures ANOVA test.

AI.5.10 Plasma ELISAs.

Plasma samples were processed and handled according to the manufacturer's instructions for each of the assays: syndecan-1 (abcam), vWF (abcam). All samples and standards were run in duplicate for each marker of endothelial dysfunction

AI .6 References

Abdelmegeed MA, Yoo S-H, Henderson LE, Gonzalez FJ, Woodcroft KJ and Song B-J (2011) PPARα expression protects male mice from high fat–induced nonalcoholic fatty liver. *The Journal of nutrition* **141**(4): 603-610.

Ackermann M, Verleden SE, Kuehnel M, Haverich A, Welte T, Laenger F, Vanstapel A, Werlein C, Stark H, Tzankov A, Li WW, Li VW, Mentzer SJ and Jonigk D (2020) Pulmonary Vascular Endothelialitis, Thrombosis, and Angiogenesis in Covid-19. *N Engl J Med* **383**(2): 120-128.

Adams PD, Afonine PV, Bunkóczi G, Chen VB, Davis IW, Echols N, Headd JJ, Hung L-W, Kapral GJ and Grosse-Kunstleve RW (2010) PHENIX: a comprehensive Python-based system for macromolecular structure solution. *Acta Crystallographica Section D: Biological Crystallography* **66**(2): 213-221.

Adida A and Spener F (2006) Adipocyte-type fatty acid-binding protein as inter-compartmental shuttle for peroxisome proliferator activated receptor γ agonists in cultured cell. *Biochimica et Biophysica Acta (BBA)-Molecular and Cell Biology of Lipids* **1761**(2): 172-181.

Afzali B, Noris M, Lambrecht BN and Kemper C (2021) The state of complement in COVID-19. *Nat Rev Immunol*.

Alves-Bezerra M, Li Y, Acuña M, Ivanova AA, Corey KE, Ortlund EA and Cohen DE (2019) Thioesterase superfamily member 2 promotes hepatic VLDL secretion by channeling fatty acids into triglyceride biosynthesis. *Hepatology* **70**(2): 496-510.

Amber-Vitos O, Kucherenko N, Nachliel E, Gutman M and Tsfadia Y (2015) The Interaction of FABP with Kapalpha. *PLoS One* **10**(8): e0132138.

Arikawa E, Quellhorst G, Han Y, Pan H and Yang J (2010) RT2 Profiler PCR Arrays: Pathway-focused gene expression profiling with qRT-PCR. *SA Biosciences Technical Article* **11**.

Armstrong EH, Goswami D, Griffin PR, Noy N and Ortlund EA (2014a) Structural basis for ligand regulation of the fatty acid-binding protein 5, peroxisome proliferator-activated receptor beta/delta (FABP5-PPARbeta/delta) signaling pathway. *The Journal of biological chemistry* **289**(21): 14941-14954.

Armstrong EH, Goswami D, Griffin PR, Noy N and Ortlund EA (2014b) Structural basis for ligand regulation of the fatty acid-binding protein 5, peroxisome proliferator-activated receptor β/δ (FABP5-PPARβ/δ) signaling pathway. *Journal of Biological Chemistry* **289**(21): 14941-14954.

Ayers SD, Nedrow KL, Gillilan RE and Noy N (2007) Continuous nucleocytoplasmic shuttling underlies transcriptional activation of PPARgamma by FABP4. *Biochemistry* **46**(23): 6744-6752.

Bäckhed F, Manchester JK, Semenkovich CF and Gordon JI (2007) Mechanisms underlying the resistance to diet-induced obesity in germ-free mice. *Proc Natl Acad Sci U S A* **104**(3): 979-984.

Bajaj V, Gadi N, Spihlman AP, Wu SC, Choi CH and Moulton VR (2020) Aging, Immunity, and COVID-19: How Age Influences the Host Immune Response to Coronavirus Infections? *Front Physiol* **11**(1793).

Barish GD, Atkins AR, Downes M, Olson P, Chong L-W, Nelson M, Zou Y, Hwang H, Kang H and Curtiss L (2008) PPARδ regulates multiple proinflammatory pathways to suppress atherosclerosis. *Proceedings of the National Academy of Sciences* **105**(11): 4271-4276.

Barnes BJ, Adrover JM, Baxter-Stoltzfus A, Borczuk A, Cools-Lartigue J, Crawford JM, Dassler-Plenker J, Guerci P, Huynh C, Knight JS, Loda M, Looney MR, McAllister F, Rayes R,

Renaud S, Rousseau S, Salvatore S, Schwartz RE, Spicer JD, Yost CC, Weber A, Zuo Y and Egeblad M (2020) Targeting potential drivers of COVID-19: Neutrophil extracellular traps. *J Exp Med* **217**(6).

Bassaganya-Riera J, Reynolds K, Martino-Catt S, Cui Y, Hennighausen L, Gonzalez F, Rohrer J, Benninghoff AU and Hontecillas R (2004) Activation of PPAR γ and δ by conjugated linoleic acid mediates protection from experimental inflammatory bowel disease. *Gastroenterology* **127**(3): 777-791.

Bateman RM, Sharpe MD, Singer M and Ellis CG (2017) The Effect of Sepsis on the Erythrocyte. *Int J Mol Sci* **18**(9).

Becker BF, Jacob M, Leipert S, Salmon AH and Chappell D (2015) Degradation of the endothelial glycocalyx in clinical settings: searching for the sheddases. *Br J Clin Pharmacol* **80**(3): 389-402.

Bibbò S, Ianiro G, Dore MP, Simonelli C, Newton EE and Cammarota G (2018) Gut microbiota as a driver of inflammation in nonalcoholic fatty liver disease. *Mediators of inflammation* **2018**.

Bitsch F, Aichholz R, Kallen J, Geisse S, Fournier B and Schlaeppi JM (2003) Identification of natural ligands of retinoic acid receptor-related orphan receptor alpha ligand-binding domain expressed in Sf9 cells--a mass spectrometry approach. *Analytical biochemistry* **323**(1): 139-149.

Blind RD (2014) Disentangling biological signaling networks by dynamic coupling of signaling lipids to modifying enzymes. *Advances in biological regulation* **54**: 25-38.

Bose HS, Sugawara T, Strauss JF, 3rd and Miller WL (1996) The pathophysiology and genetics of congenital lipoid adrenal hyperplasia. *The New England journal of medicine* **335**(25): 1870-1878.

Bremer J (1983) Carnitine - Metabolism and Functions. *Physiological Reviews* **63**(4): 1420-1480.

Brooks AR, Lelkes PI and Rubanyi GM (2002) Gene expression profiling of human aortic endothelial cells exposed to disturbed flow and steady laminar flow. *Physiol Genomics* **9**(1): 27-41.

Budhu A, Gillilan R and Noy N (2001) Localization of the RAR interaction domain of cellular retinoic acid binding protein-II. *Journal of molecular biology* **305**(4): 939-949.

Budhu AS and Noy N (2002) Direct channeling of retinoic acid between cellular retinoic acid-binding protein II and retinoic acid receptor sensitizes mammary carcinoma cells to retinoic acid-induced growth arrest. *Molecular and cellular biology* **22**(8): 2632-2641.

Candelli M, Franza L, Pignataro G, Ojetti V, Covino M, Piccioni A, Gasbarrini A and Franceschi F (2021) Interaction between lipopolysaccharide and gut microbiota in inflammatory bowel diseases. *International journal of molecular sciences* **22**(12): 6242.

Carbonetti G, Wilpshaar T, Kroonen J, Studholme K, Converso C, d'Oelsnitz S and Kaczocha M (2019) FABP5 coordinates lipid signaling that promotes prostate cancer metastasis. *Scientific reports* **9**(1): 18944.

Carboni E, Carta AR and Carboni E (2020) Can pioglitazone be potentially useful therapeutically in treating patients with COVID-19? *Medical hypotheses* **140**: 109776.

Carrat GR, Haythorne E, Tomas A, Haataja L, Müller A, Arvan P, Piunti A, Cheng K, Huang M and Pullen TJ (2020) The type 2 diabetes gene product STARD10 is a phosphoinositide-binding protein that controls insulin secretory granule biogenesis. *Molecular metabolism* **40**: 101015.

Carrat GR, Hu M, Nguyen-Tu M-S, Chabosseau P, Gaulton KJ, van de Bunt M, Siddiq A, Falchi M, Thurner M and Canouil M (2017) Decreased STARD10 expression is associated with defective insulin secretion in humans and mice. *The American Journal of Human Genetics* **100**(2): 238-256.

Caruso C, Fay ME, Cheng X, Liu AY, Park SI, Sulchek TA, Graham MD and Lam WA (2022) Pathologic Mechanobiological Interactions between Red Blood Cells and Endothelial Cells Directly Induce Vasculopathy in Iron Deficiency Anemia. *iScience*.

Caterino M, Costanzo M, Fedele R, Cevenini A, Gelzo M, Di Minno A, Andolfo I, Capasso M, Russo R, Annunziata A, Calabrese C, Fiorentino G, D'Abbraccio M, Dell'Isola C, Fusco FM, Parrella R, Fabbrocini G, Gentile I, Castaldo G and Ruoppolo M (2021) The Serum Metabolome of Moderate and Severe COVID-19 Patients Reflects Possible Liver Alterations Involving Carbon and Nitrogen Metabolism. *Int J Mol Sci* **22**(17).

Chakravarthy MV, Lodhi IJ, Yin L, Malapaka RR, Xu HE, Turk J and Semenkovich CF (2009a) Identification of a physiologically relevant endogenous ligand for PPARalpha in liver. *Cell* **138**(3): 476-488.

Chakravarthy MV, Lodhi IJ, Yin L, Malapaka RR, Xu HE, Turk J and Semenkovich CF (2009b) Identification of a physiologically relevant endogenous ligand for PPARα in liver. *Cell* **138**(3): 476-488.

Chatzizisis YS, Coskun AU, Jonas M, Edelman ER, Feldman CL and Stone PH (2007) Role of endothelial shear stress in the natural history of coronary atherosclerosis and vascular remodeling: molecular, cellular, and vascular behavior. *J Am Coll Cardiol* **49**(25): 2379-2393.

Chiapparino A, Maeda K, Turei D, Saez-Rodriguez J and Gavin AC (2016) The orchestra of lipid-transfer proteins at the crossroads between metabolism and signaling. *Progress in lipid research* **61**: 30-39.

Ciavarella C, Motta I, Valente S and Pasquinelli G (2020) Pharmacological (or synthetic) and nutritional agonists of PPAR-γ as candidates for cytokine storm modulation in COVID-19 disease. *Molecules* **25**(9): 2076.

Consiglio CR, Cotugno N, Sardh F, Pou C, Amodio D, Rodriguez L, Tan Z, Zicari S, Ruggiero A, Pascucci GR, Santilli V, Campbell T, Bryceson Y, Eriksson D, Wang J, Marchesi A, Lakshmikanth T, Campana A, Villani A, Rossi P, Team CS, Landegren N, Palma P and Brodin P (2020) The Immunology of Multisystem Inflammatory Syndrome in Children with COVID-19. *Cell* **183**(4): 968-981 e967.

Cox RA and Hoppel CL (1973) Biosynthesis of carnitine and 4-N-trimethylaminobutyrate from 6-N-trimethyl-lysine. *The Biochemical journal* **136**(4): 1083-1090.

D'Alessandro A, Thomas T, Dzieciatkowska M, Hill RC, Francis RO, Hudson KE, Zimring JC, Hod EA, Spitalnik SL and Hansen KC (2020) Serum Proteomics in COVID-19 Patients: Altered Coagulation and Complement Status as a Function of IL-6 Level. *J Proteome Res* **19**(11): 4417-4427.

D'Alessandro A, Thomas T, Dzieciatkowska M, Hill RC, Francis RO, Hudson KE, Zimring JC, Hod EA, Spitalnik SL, Hansen KC and (2020) Serum Proteomics in COVID-19 Patients: Altered Coagulation and Complement Status as a Function of IL-6 Level. *American Chemical Society* **19**(11): 4417-4427.

Dalan R, Bornstein SR, El-Armouche A, Rodionov RN, Markov A, Wielockx B, Beuschlein F and Boehm BO (2020) The ACE-2 in COVID-19: foe or friend? *Hormone and Metabolic Research* **52**(05): 257-263.

Danlos FX, Grajeda-Iglesias C, Durand S, Sauvat A, Roumier M, Cantin D, Colomba E, Rohmer J, Pommeret F, Baciarello G, Willekens C, Vasse M, Griscelli F, Fahrner JE, Goubet AG, Dubuisson A, Derosa L, Nirmalathasan N, Bredel D, Mouraud S, Pradon C, Stoclin A, Rozenberg F, Duchemin J, Jourdi G, Ellouze S, Levavasseur F, Albiges L, Soria JC, Barlesi F, Solary E, Andre F, Pene F, Ackerman F, Mouthon L, Zitvogel L, Marabelle A, Michot JM, Fontenay M and Kroemer G (2021) Metabolomic analyses of COVID-19 patients unravel stage-dependent and prognostic biomarkers. *Cell Death Dis* **12**(3): 258.

Davidi D, Schechter M, Elhadi SA, Matatov A, Nathanson L and Sharon R (2020) α-Synuclein Translocates to the Nucleus to Activate Retinoic-Acid-Dependent Gene Transcription. *iScience* **23**(3): 100910.

Davies PF (2009) Hemodynamic shear stress and the endothelium in cardiovascular pathophysiology. *Nat Clin Pract Cardiovasc Med* **6**(1): 16-26.

Davies PF, Spaan JA and Krams R (2005) Shear stress biology of the endothelium. *Ann Biomed Eng* **33**(12): 1714-1718.

Davies SS, Pontsler AV, Marathe GK, Harrison KA, Murphy RC, Hinshaw JC, Prestwich GD, Hilaire AS, Prescott SM and Zimmerman GA (2001) Oxidized alkyl phospholipids are specific, high affinity peroxisome proliferator-activated receptor γ ligands and agonists. *Journal of Biological Chemistry* **276**(19): 16015-16023.

Dawson MI and Xia Z (2012) The retinoid X receptors and their ligands. *Biochimica et biophysica acta* **1821**(1): 21-56.

Dawson MI, Xia Z, Liu G, Ye M, Fontana JA, Farhana L, Patel BB, Arumugarajah S, Bhuiyan M, Zhang XK, Han YH, Stallcup WB, Fukushi J, Mustelin T, Tautz L, Su Y, Harris DL, Waleh N, Hobbs PD, Jong L, Chao WR, Schiff LJ and Sani BP (2007) An adamantyl-substituted retinoid-derived molecule that inhibits cancer cell growth and angiogenesis by inducing apoptosis and binds to small heterodimer partner nuclear receptor: effects of modifying its carboxylate group on apoptosis, proliferation, and protein-tyrosine phosphatase activity. *Journal of medicinal chemistry* **50**(11): 2622-2639.

De Gerónimo E, Hagan RM, Wilton DC and Córsico B (2010) Natural ligand binding and transfer from liver fatty acid binding protein (LFABP) to membranes. *Biochimica et Biophysica Acta (BBA)-Molecular and Cell Biology of Lipids* **1801**(9): 1082-1089.

de Lera Á R, Krezel W and Rühl R (2016) An Endogenous Mammalian Retinoid X Receptor Ligand, At Last! *ChemMedChem* **11**(10): 1027-1037.

Dei Cas M, Ottolenghi S, Morano C, Rinaldo R, Roda G, Chiumello D, Centanni S, Samaja M and Paroni R (2021) Link between serum lipid signature and prognostic factors in COVID-19 patients. *Science Reports* **11**.

Delahoy MJ, Ujamaa D, Whitaker M, O'Halloran A, Anglin O, Burns E, Cummings C, Holstein R, Kambhampati AK, Milucky J, Patel K, Pham H, Taylor CA, Chai SJ, Reingold A, Alden NB, Kawasaki B, Meek J, Yousey-Hindes K, Anderson EJ, Openo KP, Teno K, Weigel A, Kim S, Leegwater L, Bye E, Como-Sabetti K, Ropp S, Rudin D, Muse A, Spina N, Bennett NM, Popham K, Billing LM, Shiltz E, Sutton M, Thomas A, Schaffner W, Talbot HK, Crossland MT, McCaffrey K, Hall AJ, Fry AM, McMorrow M, Reed C, Garg S, Havers FP, Team C-NS and Team C-NS (2021) Hospitalizations Associated with COVID-19 Among Children and Adolescents - COVID-NET, 14 States, March 1, 2020-August 14, 2021. *MMWR Morb Mortal Wkly Rep* **70**(36): 1255-1260.

Delva L, Bastie JN, Rochette-Egly C, Kraïba R, Balitrand N, Despouy G, Chambon P and Chomienne C (1999) Physical and functional interactions between cellular retinoic acid

binding protein II and the retinoic acid-dependent nuclear complex. *Molecular and cellular biology* **19**(10): 7158-7167.

Devaraj S, Hemarajata P and Versalovic J (2013) The human gut microbiome and body metabolism: implications for obesity and diabetes. *Clinical chemistry* **59**(4): 617-628.

Ding J, Zhao L, Wang L, Zhao W, Zhai Z, Leng L, Wang Y, He C, Zhang Y and Zhang H (2016) Divergent selection-induced obesity alters the composition and functional pathways of chicken gut microbiota. *Genetics Selection Evolution* **48**(1): 1-9.

Diorio C, Shraim R, Vella LA, Giles JR, Baxter AE, Oldridge DA, Canna SW, Henrickson SE, McNerney KO, Balamuth F, Burudpakdee C, Lee J, Leng T, Farrel A, Lambert MP, Sullivan KE, Wherry EJ, Teachey DT, Bassiri H and Behrens EM (2021) Proteomic profiling of MIS-C patients indicates heterogeneity relating to interferon gamma dysregulation and vascular endothelial dysfunction. *Nat Commun* **12**(1): 7222.

Donadello K, Piagnerelli M, Reggiori G, Gottin L, Scolletta S, Occhipinti G, Zouaoui Boudjeltia K and Vincent JL (2015) Reduced red blood cell deformability over time is associated with a poor outcome in septic patients. *Microvasc Res* **101**: 8-14.

Dong D, Ruuska SE, Levinthal DJ and Noy N (1999) Distinct roles for cellular retinoic acid-binding proteins I and II in regulating signaling by retinoic acid. *The Journal of biological chemistry* **274**(34): 23695-23698.

Duffy J MA, Wang M (2017) Lipid Metabolism, Lipid Signalling and Longevity. 307-329.

Ehrlich A, Uhl S, Ioannidis K, Hofree M, tenOever BR and Nahmias Y (2020) The SARS-CoV-2 transcriptional metabolic signature in lung epithelium. *Available at SSRN 3650499*.

Emsley P, Lohkamp B, Scott WG and Cowtan K (2010) Features and development of Coot. *Acta Crystallographica Section D: Biological Crystallography* **66**(4): 486-501.

Fan W, Waizenegger W, Lin CS, Sorrentino V, He M-X, Wall CE, Li H, Liddle C, Ruth TY and Atkins AR (2017) PPARδ promotes running endurance by preserving glucose. *Cell metabolism* **25**(5): 1186-1193. e1184.

Fan Y, Wang Y, Tang Z, Zhang H, Qin X, Zhu Y, Guan Y, Wang X, Staels B and Chien S (2008) Suppression of pro-inflammatory adhesion molecules by PPAR-δ in human vascular endothelial cells. *Arteriosclerosis, thrombosis, and vascular biology* **28**(2): 315-321.

Farhana L, Dawson MI, Leid M, Wang L, Moore DD, Liu G, Xia Z and Fontana JA (2007) Adamantyl-substituted retinoid-related molecules bind small heterodimer partner and modulate the Sin3A repressor. *Cancer research* **67**(1): 318-325.

Favaron E, Ince C, Hilty MP, Ergin B, van der Zee P, Uz Z, Wendel Garcia PD, Hofmaenner DA, Acevedo CT, van Boven WJ, Akin S, Gommers D and Endeman H (2021) Capillary Leukocytes, Microaggregates, and the Response to Hypoxemia in the Microcirculation of Coronavirus Disease 2019 Patients. *Crit Care Med* **49**(4): 661-670.

Fei N and Zhao L (2013) An opportunistic pathogen isolated from the gut of an obese human causes obesity in germfree mice. *The ISME journal* **7**(4): 880-884.

Feldstein LR, Rose EB, Horwitz SM, Collins JP, Newhams MM, Son MBF, Newburger JW, Kleinman LC, Heidemann SM, Martin AA, Singh AR, Li S, Tarquinio KM, Jaggi P, Oster ME, Zackai SP, Gillen J, Ratner AJ, Walsh RF, Fitzgerald JC, Keenaghan MA, Alharash H, Doymaz S, Clouser KN, Giuliano JS, Jr., Gupta A, Parker RM, Maddux AB, Havalad V, Ramsingh S, Bukulmez H, Bradford TT, Smith LS, Tenforde MW, Carroll CL, Riggs BJ, Gertz SJ, Daube A, Lansell A, Coronado Munoz A, Hobbs CV, Marohn KL, Halasa NB, Patel MM, Randolph AG, Overcoming C-I and Team CC-R (2020) Multisystem Inflammatory Syndrome in U.S. Children and Adolescents. *N Engl J Med* **383**(4): 334-346.

Fernandez S, Moreno-Castano AB, Palomo M, Martinez-Sanchez J, Torramade-Moix S, Tellez A, Ventosa H, Segui F, Escolar G, Carreras E, Nicolas JM, Richardson E, Garcia-Bernal D, Carlo-Stella C, Moraleda JM, Richardson PG, Diaz-Ricart M and Castro P (2022) Distinctive Biomarker Features in the Endotheliopathy of COVID-19 and Septic Syndromes. *Shock* **57**(1): 95-105.

Flores-Martin J, Rena V, Angeletti S, Panzetta-Dutari GM and Genti-Raimondi S (2013) The lipid transfer protein StarD7: structure, function, and regulation. *International journal of molecular sciences* **14**(3): 6170-6186.

Folick A, Oakley HD, Yu Y, Armstrong EH, Kumari M, Sanor L, Moore DD, Ortlund EA, Zechner R and Wang MC (2015) Aging. Lysosomal signaling molecules regulate longevity in Caenorhabditis elegans. *Science (New York, NY)* **347**(6217): 83-86.

Fothergill E, Guo J, Howard L, Kerns JC, Knuth ND, Brychta R, Chen KY, Skarulis MC, Walter M and Walter PJ (2016) Persistent metabolic adaptation 6 years after "The Biggest Loser" competition. *Obesity* **24**(8): 1612-1619.

Friedman S Fau - Fraenkel G and Fraenkel G Reversible enzymatic acetylation of carnitine. (0003-9861 (Print)).

Fritz I The effect of muscle extracts on the oxidation of palmitic acid by liver slices and homogenates. (0001-6772 (Print)).

Fritz IB (1959) Action of carnitine on long chain fatty acid oxidation by liver. *Am J Physiol* **197**(2): 297-304.

Fu J, Gaetani S, Oveisi F, Lo Verme J, Serrano A, Rodríguez De Fonseca F, Rosengarth A, Luecke H, Di Giacomo B, Tarzia G and Piomelli D (2003) Oleylethanolamide regulates feeding and body weight through activation of the nuclear receptor PPAR-alpha. *Nature* **425**(6953): 90-93.

Furuhashi M and Hotamisligil GS (2008) Fatty acid-binding proteins: role in metabolic diseases and potential as drug targets. *Nature reviews Drug discovery* **7**(6): 489-503.

Furuhashi M, Tuncman G, Gorgun CZ, Makowski L, Atsumi G, Vaillancourt E, Kono K, Babaev VR, Fazio S, Linton MF, Sulsky R, Robl JA, Parker RA and Hotamisligil GS (2007) Treatment of diabetes and atherosclerosis by inhibiting fatty-acid-binding protein aP2. *Nature* **447**(7147): 959-965.

Gagnière J, Raisch J, Veziant J, Barnich N, Bonnet R, Buc E, Bringer M-A, Pezet D and Bonnet M (2016) Gut microbiota imbalance and colorectal cancer. *World journal of gastroenterology* **22**(2): 501.

Garg S, Kim L, Whitaker M, O'Halloran A, Cummings C, Holstein R, Prill M, Chai SJ, Kirley PD and Alden NB (2020) Hospitalization rates and characteristics of patients hospitalized with laboratory-confirmed coronavirus disease 2019—COVID-NET, 14 States, March 1–30, 2020. *Morbidity and mortality weekly report* **69**(15): 458.

Garin-Shkolnik T, Rudich A, Hotamisligil GS and Rubinstein M (2014) FABP4 attenuates PPARγ and adipogenesis and is inversely correlated with PPARγ in adipose tissues. *Diabetes* **63**(3): 900-911.

Giguère V (1999) Orphan nuclear receptors: from gene to function. *Endocrine reviews* **20**(5): 689-725.

Giguère V, Yang N, Segui P and Evans RM (1988) Identification of a new class of steroid hormone receptors. *Nature* **331**(6151): 91-94.

Gillilan RE, Ayers SD and Noy N (2007) Structural basis for activation of fatty acid-binding protein 4. *Journal of molecular biology* **372**(5): 1246-1260.

Go Y-M, Liu K, Jarrell Z, Bellissimo M and Jones D (2020) Association of Microbiome Metabolite Valerobetaine with Aging. *Current Developments in Nutrition* **4**(Supplement_2): 26-26.

Goshua G, Pine AB, Meizlish ML, Chang CH, Zhang H, Bahel P, Baluha A, Bar N, Bona RD, Burns AJ, Dela Cruz CS, Dumont A, Halene S, Hwa J, Koff J, Menninger H, Neparidze N, Price C, Siner JM, Tormey C, Rinder HM, Chun HJ and Lee AI (2020) Endotheliopathy in COVID-19-associated coagulopathy: evidence from a single-centre, cross-sectional study. *Lancet Haematol* **7**(8): e575-e582.

Gou Q, Jiang Y, Zhang R, Xu Y, Xu H, Zhang W, Shi J and Hou Y (2020) PPARδ is a regulator of autophagy by its phosphorylation. *Oncogene* **39**(25): 4844-4853.

Gronemeyer H and Moras D (1995) Nuclear receptors. How to finger DNA. *Nature* **375**(6528): 190-191.

Group RC (2021) Dexamethasone in hospitalized patients with Covid-19. *New England Journal of Medicine* **384**(8): 693-704.

Grygiel-Górniak B (2014) Peroxisome proliferator-activated receptors and their ligands: nutritional and clinical implications--a review. *Nutrition journal* **13**: 17.

Gupta A, Madhavan MV, Sehgal K, Nair N, Mahajan S, Sehrawat TS, Bikdeli B, Ahluwalia N, Ausiello JC, Wan EY, Freedberg DE, Kirtane AJ, Parikh SA, Maurer MS, Nordvig AS, Accili D, Bathon JM, Mohan S, Bauer KA, Leon MB, Krumholz HM, Uriel N, Mehra MR, Elkind MSV, Stone GW, Schwartz A, Ho DD, Bilezikian JP and Landry DW (2020) Extrapulmonary manifestations of COVID-19. *Nat Med* **26**(7): 1017-1032.

Hanada K (2018) Lipid transfer proteins rectify inter-organelle flux and accurately deliver lipids at membrane contact sites. *Journal of lipid research* **59**(8): 1341-1366.

Harris PA, Taylor R, Minor BL, Elliott V, Fernandez M, O'Neal L, McLeod L, Delacqua G, Delacqua F, Kirby J, Duda SN and Consortium RE (2019) The REDCap consortium: Building an international community of software platform partners. *J Biomed Inform* **95**: 103208.

Harris PA, Taylor R, Thielke R, Payne J, Gonzalez N and Conde JG (2009) Research electronic data capture (REDCap)--a metadata-driven methodology and workflow process for providing translational research informatics support. *J Biomed Inform* **42**(2): 377-381.

Hatty C, Neumann A, Neumann A, Bartoschik T, Rieger J, Gupta AJ, Cherepanov P and Fuchter MJ Application of Temperature Related Intensity Change (TRIC) in biophysical drug discovery projects with Dianthus. *Target* **2**: 3.

He W, Barak Y, Hevener A, Olson P, Liao D, Le J, Nelson M, Ong E, Olefsky JM and Evans RM (2003) Adipose-specific peroxisome proliferator-activated receptor gamma knockout causes insulin resistance in fat and liver but not in muscle. *Proceedings of the National Academy of Sciences of the United States of America* **100**(26): 15712-15717.

Heffernan KS, Ranadive SM and Jae SY (2020) Exercise as medicine for COVID-19: On PPAR with emerging pharmacotherapy. *Medical hypotheses* **143**: 110197.

Helledie T, Antonius M, Sorensen RV, Hertzel AV, Bernlohr DA, Kølvraa S, Kristiansen K and Mandrup S (2000) Lipid-binding proteins modulate ligand-dependent trans-activation by peroxisome proliferator-activated receptors and localize to the nucleus as well as the cytoplasm. *Journal of lipid research* **41**(11): 1740-1751.

Helmkamp GM, Jr., Harvey MS, Wirtz KW and Van Deenen LL (1974) Phospholipid exchange between membranes. Purification of bovine brain proteins that preferentially catalyze the transfer of phosphatidylinositol. *The Journal of biological chemistry* **249**(20): 6382-6389.

Hertzel AV, Smith LA, Berg AH, Cline GW, Shulman GI, Scherer PE and Bernlohr DA (2006) Lipid metabolism and adipokine levels in fatty acid-binding protein null and transgenic mice. *American journal of physiology Endocrinology and metabolism* **290**(5): E814-823.

Holter JC, Pischke SE, de Boer E, Lind A, Jenum S, Holten AR, Tonby K, Barratt-Due A, Sokolova M, Schjalm C, Chaban V, Kolderup A, Tran T, Tollefsrud Gjolberg T, Skeie LG, Hesstvedt L, Ormasen V, Fevang B, Austad C, Muller KE, Fladeby C, Holberg-Petersen M, Halvorsen B, Muller F, Aukrust P, Dudman S, Ueland T, Andersen JT, Lund-Johansen F, Heggelund L, Dyrhol-Riise AM and Mollnes TE (2020) Systemic complement activation is associated with respiratory failure in COVID-19 hospitalized patients. *Proc Natl Acad Sci U S A* **117**(40): 25018-25025.

Horibata Y and Sugimoto H (2010) StarD7 mediates the intracellular trafficking of phosphatidylcholine to mitochondria. *Journal of Biological Chemistry* **285**(10): 7358-7365.

Hostetler HA, Balanarasimha M, Huang H, Kelzer MS, Kaliappan A, Kier AB and Schroeder F (2010) Glucose regulates fatty acid binding protein interaction with lipids and peroxisome proliferator-activated receptor α. *Journal of lipid research* **51**(11): 3103-3116.

Hostetler HA, McIntosh AL, Atshaves BP, Storey SM, Payne HR, Kier AB and Schroeder F (2009) L-FABP directly interacts with PPARalpha in cultured primary hepatocytes. *Journal of lipid research* **50**(8): 1663-1675.

Hotamisligil GS and Bernlohr DA (2015a) Metabolic functions of FABPs--mechanisms and therapeutic implications. *Nature reviews Endocrinology* **11**(10): 592-605.

Hotamisligil GS and Bernlohr DA (2015b) Metabolic functions of FABPs—mechanisms and therapeutic implications. *Nature Reviews Endocrinology* **11**(10): 592-605.

Hotamisligil GS, Johnson RS, Distel RJ, Ellis R, Papaioannou VE and Spiegelman BM (1996) Uncoupling of obesity from insulin resistance through a targeted mutation in aP2, the adipocyte fatty acid binding protein. *Science (New York, NY)* **274**(5291): 1377-1379.

Huang H, Starodub O, McIntosh A, Atshaves BP, Woldegiorgis G, Kier AB and Schroeder F (2004) Liver fatty acid-binding protein colocalizes with peroxisome proliferator activated receptor α and enhances ligand distribution to nuclei of living cells. *Biochemistry* **43**(9): 2484-2500.

Hughes ML, Liu B, Halls ML, Wagstaff KM, Patil R, Velkov T, Jans DA, Bunnett NW, Scanlon MJ and Porter CJ (2015) Fatty Acid-binding Proteins 1 and 2 Differentially Modulate the Activation of Peroxisome Proliferator-activated Receptor alpha in a Ligand-selective Manner. *The Journal of biological chemistry* **290**(22): 13895-13906.

Hulme H, Meikle LM, Strittmatter N, van der Hooft JJ, Swales J, Bragg RA, Villar VH, Ormsby MJ, Barnes S and Brown SL (2020) Microbiome-derived carnitine mimics as previously unknown mediators of gut-brain axis communication. *Science advances* **6**(11): eaax6328.

Huynh FK, Green MF, Koves TR and Hirschey MD (2014) Measurement of fatty acid oxidation rates in animal tissues and cell lines, in *Methods in enzymology* pp 391-405, Elsevier.

IJpenberg A, Tan NS, Gelman L, Kersten S, Seydoux J, Xu J, Metzger D, Canaple L, Chambon P and Wahli W (2004) In vivo activation of PPAR target genes by RXR homodimers. *The EMBO journal* **23**(10): 2083-2091.

Ito M, Yamanashi Y, Toyoda Y, Izumi-Nakaseko H, Oda S, Sugiyama A, Kuroda M, Suzuki H, Takada T and Adachi-Akahane S (2013) Disruption of Stard10 gene alters the PPARα-mediated bile acid homeostasis. *Biochimica et Biophysica Acta (BBA)-Molecular and Cell Biology of Lipids* **1831**(2): 459-468.

Joost H-G (2011) The genetic basis of obesity and type 2 diabetes: lessons from the New Zealand obese mouse, a polygenic model of the metabolic syndrome. *Sensory and Metabolic Control of Energy Balance*: 1-11.

Joosten RP, Salzemann J, Bloch V, Stockinger H, Berglund A-C, Blanchet C, Bongcam-Rudloff E, Combet C, Da Costa AL and Deleage G (2009) PDB_REDO: automated re-refinement of X-ray structure models in the PDB. *Journal of applied crystallography* **42**(3): 376-384.

Kaczocha M, Vivieca S, Sun J, Glaser ST and Deutsch DG (2012) Fatty acid-binding proteins transport N-acylethanolamines to nuclear receptors and are targets of endocannabinoid transport inhibitors. *The Journal of biological chemistry* **287**(5): 3415-3424.

Kalal Z, Mikolajczyk K and Matas J (2010) Forward-Backward Error: Automatic Detection of Tracking Failures, in *20th International Conference on Pattern Recognition* pp 2756-2759.

Kanehisa M and Goto S (2000) KEGG: kyoto encyclopedia of genes and genomes. *Nucleic acids research* **28**(1): 27-30.

Kang HW, Kanno K, Scapa EF and Cohen DE (2010a) Regulatory role for phosphatidylcholine transfer protein/StarD2 in the metabolic response to peroxisome proliferator activated receptor alpha (PPARalpha). *Biochimica et biophysica acta* **1801**(4): 496-502.

Kang HW, Niepel MW, Han S, Kawano Y and Cohen DE (2012) Thioesterase superfamily member 2/acyl-CoA thioesterase 13 (Them2/Acot13) regulates hepatic lipid and glucose metabolism. *The FASEB Journal* **26**(5): 2209-2221.

Kang HW, Ribich S, Kim BW, Hagen SJ, Bianco AC and Cohen DE (2009) Mice lacking Pctp/StarD2 exhibit increased adaptive thermogenesis and enlarged mitochondria in brown adipose tissue [S]. *Journal of lipid research* **50**(11): 2212-2221.

Kang HW, Wei J and Cohen DE (2010b) PC-TP/StARD2: Of membranes and metabolism. *Trends in Endocrinology & Metabolism* **21**(7): 449-456.

Kang HW, Wei J and Cohen DE (2010c) Regulation of lipid and glucose metabolism by phosphatidylcholine transfer protein. *Trends in endocrinology and metabolism: TEM* **21**(7): 449.

Kanno K, Wu MK, Agate DS, Fanelli BJ, Wagle N, Scapa EF, Ukomadu C and Cohen DE (2007) Interacting proteins dictate function of the minimal START domain phosphatidylcholine transfer protein/StarD2. *Journal of Biological Chemistry* **282**(42): 30728-30736.

Kanoore Edul VS, Caminos Eguillor JF, Ferrara G, Estenssoro E, Siles DSP, Cesio CE and Dubin A (2021) Microcirculation alterations in severe COVID-19 pneumonia. *J Crit Care* **61**: 73-75.

Kasurinen J, Van Paridon PA, Wirtz KW and Somerharju P (1990) Affinity of phosphatidylcholine molecular species for the bovine phosphatidylcholine and phosphatidylinositol transfer proteins. Properties of the sn-1 and sn-2 acyl binding sites. *Biochemistry* **29**(37): 8548-8554.

Kaur J (2014) A comprehensive review on metabolic syndrome. *Cardiology research and practice* **2014**.

Kawano Y, Ersoy BA, Li Y, Nishiumi S, Yoshida M and Cohen DE (2014) Thioesterase superfamily member 2 (Them2) and phosphatidylcholine transfer protein (PC-TP) interact to promote fatty acid oxidation and control glucose utilization. *Molecular and cellular biology* **34**(13): 2396-2408.

Keiser MJ, Roth BL, Armbruster BN, Ernsberger P, Irwin JJ and Shoichet BK (2007) Relating protein pharmacology by ligand chemistry. *Nature biotechnology* **25**(2): 197-206.

Kersten S, Seydoux J, Peters JM, Gonzalez FJ, Desvergne B and Wahli W (1999) Peroxisome proliferator–activated receptor α mediates the adaptive response to fasting. *The Journal of clinical investigation* **103**(11): 1489-1498.

Kim L, Whitaker M, O'Halloran A, Kambhampati A, Chai SJ, Reingold A, Armistead I, Kawasaki B, Meek J, Yousey-Hindes K, Anderson EJ, Openo KP, Weigel A, Ryan P, Monroe ML, Fox K, Kim S, Lynfield R, Bye E, Shrum Davis S, Smelser C, Barney G, Spina NL, Bennett NM, Felsen CB, Billing LM, Shiltz J, Sutton M, West N, Talbot HK, Schaffner W, Risk I, Price A, Brammer L, Fry AM, Hall AJ, Langley GE, Garg S and Team C-NS (2020) Hospitalization Rates and Characteristics of Children Aged <18 Years Hospitalized with Laboratory-Confirmed COVID-19 - COVID-NET, 14 States, March 1-July 25, 2020. *MMWR Morb Mortal Wkly Rep* **69**(32): 1081-1088.

Klingler C, Zhao X, Adhikary T, Li J, Xu G, Häring H-U, Schleicher E, Lehmann R and Weigert C (2016) Lysophosphatidylcholines activate PPARδ and protect human skeletal muscle cells from lipotoxicity. *Biochimica et Biophysica Acta (BBA)-Molecular and Cell Biology of Lipids* **1861**(12): 1980-1992.

Kohn J *Novel Allosteric Communication in Nuclear Receptor Activation*.

Krisko TI, LeClair KB and Cohen DE (2017) Genetic ablation of phosphatidylcholine transfer protein/StarD2 in ob/ob mice improves glucose tolerance without increasing energy expenditure. *Metabolism* **68**: 145-149.

Krisko TI, Nicholls HT, Bare CJ, Holman CD, Putzel GG, Jansen RS, Sun N, Rhee KY, Banks AS and Cohen DE (2020) Dissociation of adaptive thermogenesis from glucose homeostasis in microbiome-deficient mice. *Cell metabolism* **31**(3): 592-604. e599.

Kuleshov MV, Jones MR, Rouillard AD, Fernandez NF, Duan Q, Wang Z, Koplev S, Jenkins SL, Jagodnik KM and Lachmann A (2016) Enrichr: a comprehensive gene set enrichment analysis web server 2016 update. *Nucleic acids research* **44**(W1): W90-W97.

Kuwabara T, Ishikawa F, Kondo M and Kakiuchi T (2017) The Role of IL-17 and Related Cytokines in Inflammatory Autoimmune Diseases. *Mediators Inflamm* **2017**: 3908061.

Lachmann A, Xu H, Krishnan J, Berger SI, Mazloom AR and Ma'ayan A (2010) ChEA: transcription factor regulation inferred from integrating genome-wide ChIP-X experiments. *Bioinformatics* **26**(19): 2438-2444.

Lamas Bervejillo M, Bonanata J, Franchini GR, Richeri A, Marqués JM, Freeman BA, Schopfer FJ, Coitiño EL, Córsico B, Rubbo H and Ferreira AM (2020) A FABP4-PPARγ signaling axis regulates human monocyte responses to electrophilic fatty acid nitroalkenes. *Redox biology* **29**: 101376.

Lawrence JW, Kroll DJ and Eacho PI (2000) Ligand-dependent interaction of hepatic fatty acid-binding protein with the nucleus. *Journal of lipid research* **41**(9): 1390-1401.

Lee S, Wang PY, Jeong Y, Mangelsdorf DJ, Anderson RG and Michaely P (2012) Sterol-dependent nuclear import of ORP1S promotes LXR regulated trans-activation of apoE. *Experimental cell research* **318**(16): 2128-2142.

Lei Y, Zhang J, Schiavon CR, He M, Chen L, Shen H, Zhang Y, Yin Q, Cho Y and Andrade L (2021) SARS-CoV-2 spike protein impairs endothelial function via downregulation of ACE 2. *Circulation research* **128**(9): 1323-1326.

Leman ES, Magheli A, Yong KMA, Netto G, Hinz S and Getzenberg RH (2009) Identification of nuclear structural protein alterations associated with seminomas. *Journal of cellular biochemistry* **108**(6): 1274-1279.

Leung IK, Krojer TJ, Kochan GT, Henry L, von Delft F, Claridge TD, Oppermann U, McDonough MA and Schofield CJ (2010) Structural and mechanistic studies on γ-butyrobetaine hydroxylase. *Chemistry & biology* **17**(12): 1316-1324.

Levi L, Lobo G, Doud MK, von Lintig J, Seachrist D, Tochtrop GP and Noy N (2013) Genetic ablation of the fatty acid-binding protein FABP5 suppresses HER2-induced mammary tumorigenesis. *Cancer research* **73**(15): 4770-4780.

Levi L, Wang Z, Doud MK, Hazen SL and Noy N (2015) Saturated fatty acids regulate retinoic acid signalling and suppress tumorigenesis by targeting fatty acid-binding protein 5. *Nature communications* **6**: 8794.

Levin AA, Sturzenbecker LJ, Kazmer S, Bosakowski T, Huselton C, Allenby G, Speck J, Kratzeisen C, Rosenberger M, Lovey A and et al. (1992) 9-cis retinoic acid stereoisomer binds and activates the nuclear receptor RXR alpha. *Nature* **355**(6358): 359-361.

Libby P and Luscher T (2020) COVID-19 is, in the end, an endothelial disease. *Eur Heart J* **41**(32): 3038-3044.

Lin S, Ikegami M, Moon C, Naren AP and Shannon JM (2015) Lysophosphatidylcholine acyltransferase 1 (LPCAT1) specifically interacts with phospholipid transfer protein StarD10 to facilitate surfactant phospholipid trafficking in alveolar type II cells. *Journal of Biological Chemistry* **290**(30): 18559-18574.

Lipowsky HH (2005) Microvascular rheology and hemodynamics. *Microcirculation* **12**(1): 5-15.

Liu KH, Owens JA, Saeedi B, Cohen CE, Bellissimo MP, Naudin C, Darby T, Druzak S, Maner-Smith K and Orr M (2021) Microbial metabolite delta-valerobetaine is a diet-dependent obesogen. *Nature Metabolism* **3**(12): 1694-1705.

Liu S, Brown JD, Stanya KJ, Homan E, Leidl M, Inouye K, Bhargava P, Gangl MR, Dai L and Hatano B (2013) A diurnal serum lipid integrates hepatic lipogenesis and peripheral fatty acid use. *Nature* **502**(7472): 550-554.

Liu S, Downes M and Evans RM (2015) Metabolic Regulation by Nuclear Receptors, in *Innovative Medicine: Basic Research and Development* (Nakao K, Minato N and Uemoto S eds) pp 25-37, Springer

Copyright 2015, The Author(s). Tokyo.

Lodhi IJ, Dean JM, He A, Park H, Tan M, Feng C, Song H, Hsu F-F and Semenkovich CF (2017) PexRAP inhibits PRDM16-mediated thermogenic gene expression. *Cell reports* **20**(12): 2766-2774.

Lodhi IJ, Yin L, Jensen-Urstad AP, Funai K, Coleman T, Baird JH, El Ramahi MK, Razani B, Song H and Fu-Hsu F (2012) Inhibiting adipose tissue lipogenesis reprograms thermogenesis and PPARγ activation to decrease diet-induced obesity. *Cell metabolism* **16**(2): 189-201.

Lowenstein CJ and Solomon SD (2020) Severe COVID-19 Is a Microvascular Disease. *Circulation* **142**(17): 1609-1611.

MacLeod KN and Baxter JD (1975) DNA binding of thyroid hormone receptors. *Biochemical and biophysical research communications* **62**(3): 577-583.

Maier CL, Truong AD, Auld SC, Polly DM, Tanksley CL and Duncan A (2020) COVID-19-associated hyperviscosity: a link between inflammation and thrombophilia? *Lancet* **395**(10239): 1758-1759.

Makishima M, Okamoto AY, Repa JJ, Tu H, Learned RM, Luk A, Hull MV, Lustig KD, Mangelsdorf DJ and Shan B (1999) Identification of a nuclear receptor for bile acids. *Science (New York, NY)* **284**(5418): 1362-1365.

Makowski L, Brittingham KC, Reynolds JM, Suttles J and Hotamisligil GS (2005) The fatty acid-binding protein, aP2, coordinates macrophage cholesterol trafficking and inflammatory activity. Macrophage expression of aP2 impacts peroxisome proliferator-activated receptor gamma and IkappaB kinase activities. *The Journal of biological chemistry* **280**(13): 12888-12895.

Mannino RG, Qiu Y and Lam WA (2018) Endothelial cell culture in microfluidic devices for investigating microvascular processes. *Biomicrofluidics* **12**(4).

McIntosh AL, Atshaves BP, Hostetler HA, Huang H, Davis J, Lyuksyutova OI, Landrock D, Kier AB and Schroeder F (2009) Liver type fatty acid binding protein (L-FABP) gene ablation reduces nuclear ligand distribution and peroxisome proliferator-activated receptor-alpha activity in cultured primary hepatocytes. *Archives of biochemistry and biophysics* **485**(2): 160-173.

Menter T, Haslbauer JD, Nienhold R, Savic S, Hopfer H, Deigendesch N, Frank S, Turek D, Willi N, Pargger H, Bassetti S, Leuppi JD, Cathomas G, Tolnay M, Mertz KD and Tzankov A (2020) Postmortem examination of COVID-19 patients reveals diffuse alveolar damage with severe capillary congestion and variegated findings in lungs and other organs suggesting vascular dysfunction. *Histopathology* **77**(2): 198-209.

Michaelis S, Zelzer S, Schnedl WJ, Baranyi A, Meinitzer A and Enko D (2021) Assessment of tryptophan and kynurenine as prognostic markers in patients with SARS-CoV-2. *Clin Chim Acta* **525**: 29-33.

Middleton EA, He XY, Denorme F, Campbell RA, Ng D, Salvatore SP, Mostyka M, Baxter-Stoltzfus A, Borczuk AC, Loda M, Cody MJ, Manne BK, Portier I, Harris ES, Petrey AC, Beswick EJ, Caulin AF, Iovino A, Abegglen LM, Weyrich AS, Rondina MT, Egeblad M, Schiffman JD and Yost CC (2020) Neutrophil extracellular traps contribute to immunothrombosis in COVID-19 acute respiratory distress syndrome. *Blood* **136**(10): 1169-1179.

Mo X, Qi Q, Ivanov AA, Niu Q, Luo Y, Havel J, Goetze R, Bell S, Moreno CS and Cooper LA (2017) AKT1, LKB1, and YAP1 revealed as MYC interactors with NanoLuc-based protein-fragment complementation assay. *Molecular pharmacology* **91**(4): 339-347.

Mo X-L and Fu H (2016) BRET: NanoLuc-based bioluminescence resonance energy transfer platform to monitor protein-protein interactions in live cells, in *High Throughput Screening* pp 263-271, Springer.

Montagner A, Polizzi A, Fouché E, Ducheix S, Lippi Y, Lasserre F, Barquissau V, Régnier M, Lukowicz C and Benhamed F (2016) Liver PPARα is crucial for whole-body fatty acid homeostasis and is protective against NAFLD. *Gut* **65**(7): 1202-1214.

Montaldo C, Messina F, Abbate I, Antonioli M, Bordoni V, Aiello A, Ciccosanti F, Colavita F, Farroni C, Najafi Fard S, Giombini E, Goletti D, Matusali G, Rozera G, Rueca M, Sacchi A, Piacentini M, Agrati C, Fimia GM, Capobianchi MR, Lauria FN and Ippolito G (2021) Multi-omics approach to COVID-19: a domain-based literature review. *J Transl Med* **19**(1): 501.

Morgan E, Kannan-Thulasiraman P and Noy N (2010) Involvement of Fatty Acid Binding Protein 5 and PPARβ/δ in Prostate Cancer Cell Growth. *PPAR research* **2010**.

Morillas M, López-Viñas E, Valencia A, Serra D, Gómez-Puertas P, Hegardt FG and Asins G (2004) Structural model of carnitine palmitoyltransferase I based on the carnitine acetyltransferase crystal. *Biochemical Journal* **379**(3): 777-784.

Mossad O, Nent E, Woltemate S, Folschweiller S, Buescher JM, Schnepf D, Erny D, Staeheli P, Bartos M and Szalay A (2021) Microbiota-dependent increase in δ-valerobetaine alters neuronal function and is responsible for age-related cognitive decline. *Nature Aging* **1**(12): 1127-1136.

Muranaka Y, Kunimoto F, Takita J, Sumino H, Nara M, Kuwano H and Murakami M (2006) Impaired blood rheology in critically ill patients in an intensive care unit. *J Int Med Res* **34**(4): 419-427.

Myers DR, Sakurai Y, Tran R, Ahn B, Hardy ET, Mannino R, Kita A, Tsai M and Lam WA (2012) Endothelialized microfluidics for studying microvascular interactions in hematologic diseases. *J Vis Exp*(64).

Nader E, Nougier C, Boisson C, Poutrel S, Catella J, Martin F, Charvet J, Girard S, Havard-Guibert S, Martin M, Rezigue H, Desmurs-Clavel H, Renoux C, Joly P, Guillot N, Bertrand Y, Hot A, Dargaud Y and Connes P (2022) Increased blood viscosity and red blood cell aggregation in patients with COVID-19. *Am J Hematol* **97**(3): 283-292.

Neels JG and Grimaldi PA (2014) Physiological functions of peroxisome proliferator-activated receptor β. *Physiological reviews* **94**(3): 795-858.

Nicholls HT, Hornick JL and Cohen DE (2017) Phosphatidylcholine transfer protein/StarD2 promotes microvesicular steatosis and liver injury in murine experimental steatohepatitis. *American Journal of Physiology-Gastrointestinal and Liver Physiology* **313**(1): G50-G61.

Nicosia RF, Ligresti G, Caporarello N, Akilesh S and Ribatti D (2021) COVID-19 Vasculopathy: Mounting Evidence for an Indirect Mechanism of Endothelial Injury. *Am J Pathol* **191**(8): 1374-1384.

Ning Y, Bai Q, Lu H, Li X, Pandak WM, Zhao F, Chen S, Ren S and Yin L (2009) Overexpression of mitochondrial cholesterol delivery protein, StAR, decreases intracellular lipids and inflammatory factors secretion in macrophages. *Atherosclerosis* **204**(1): 114-120.

Ogawa F, Oi Y, Nakajima K, Matsumura R, Nakagawa T, Miyagawa T, Sakai K, Saji R, Taniguchi H, Takahashi K, Abe T, Iwashita M, Nishii M and Takeuchi I (2021) Temporal change in Syndecan-1 as a therapeutic target and a biomarker for the severity classification of COVID-19. *Thromb J* **19**(1): 55.

Otwinowski Z and Minor W (1997) [20] Processing of X-ray diffraction data collected in oscillation mode, in *Methods in enzymology* pp 307-326, Elsevier.

Pan H-J, Agate DS, King BL, Wu MK, Roderick SL, Leiter EH and Cohen DE (2006) A polymorphism in New Zealand inbred mouse strains that inactivates phosphatidylcholine transfer protein. *FEBS letters* **580**(25): 5953-5958.

Panaro S and Cattalini M (2021) The Spectrum of Manifestations of Severe Acute Respiratory Syndrome-Coronavirus 2 (SARS-CoV2) Infection in Children: What We Can Learn From Multisystem Inflammatory Syndrome in Children (MIS-C). *Front Med (Lausanne)* **8**.

Pang Z, Chong J, Zhou G, de Lima Morais DA, Chang L, Barrette M, Gauthier C, Jacques PE, Li S and Xia J (2021) MetaboAnalyst 5.0: narrowing the gap between raw spectra and functional insights. *Nucleic Acids Res* **49**(W1): W388-W396.

Patil R, Mohanty B, Liu B, Chandrashekaran IR, Headey SJ, Williams ML, Clements CS, Ilyichova O, Doak BC, Genissel P, Weaver RJ, Vuillard L, Halls ML, Porter CJH and Scanlon MJ (2019) A ligand-induced structural change in fatty acid-binding protein 1 is associated with potentiation of peroxisome proliferator-activated receptor alpha agonists. *The Journal of biological chemistry* **294**(10): 3720-3734.

Pawlak M, Lefebvre P and Staels B (2012) General molecular biology and architecture of nuclear receptors. *Current topics in medicinal chemistry* **12**(6): 486-504.

Perico L, Benigni A, Casiraghi F, Ng LFP, Renia L and Remuzzi G (2021) Immunity, endothelial injury and complement-induced coagulopathy in COVID-19. *Nat Rev Nephrol* **17**(1): 46-64.

Peters JM, Shah YM and Gonzalez FJ (2012) The role of peroxisome proliferator-activated receptors in carcinogenesis and chemoprevention. *Nature reviews Cancer* **12**(3): 181-195.

Petrescu AD, Huang H, Martin GG, McIntosh AL, Storey SM, Landrock D, Kier AB and Schroeder F (2013a) Impact of L-FABP and glucose on polyunsaturated fatty acid induction of PPARα-regulated β-oxidative enzymes. *American journal of physiology Gastrointestinal and liver physiology* **304**(3): G241-256.

Petrescu AD, McIntosh AL, Storey SM, Huang H, Martin GG, Landrock D, Kier AB and Schroeder F (2013b) High glucose potentiates L-FABP mediated fibrate induction of PPARα in mouse hepatocytes. *Biochimica et biophysica acta* **1831**(8): 1412-1425.

Petrescu AD, Payne HR, Boedecker A, Chao H, Hertz R, Bar-Tana J, Schroeder F and Kier AB (2003) Physical and functional interaction of Acyl-CoA-binding protein with hepatocyte nuclear factor-4 alpha. *The Journal of biological chemistry* **278**(51): 51813-51824.

Pierce CA, Preston-Hurlburt P, Dai Y, Aschner CB, Cheshenko N, Galen B, Garforth SJ, Herrera NG, Jangra RK, Morano NC, Orner E, Sy S, Chandran K, Dziura J, Almo SC, Ring A, Keller MJ, Herold KC and Herold BC (2020) Immune responses to SARS-CoV-2 infection in hospitalized pediatric and adult patients. *Sci Transl Med* **12**(564).

Porritt RA, Binek A, Paschold L, Rivas MN, McArdle A, Yonker LM, Alter G, Chandnani HK, Lopez M, Fasano A, Van Eyk JE, Binder M and Arditi M (2021) The autoimmune signature of hyperinflammatory multisystem inflammatory syndrome in children. *J Clin Invest* **131**(20).

Prevention CfDCa (2020) Multisystem Inflammatory Syndrome in Children (MIS-C) Associated with Coronavirus Disease 2019 (COVID-19), in *CDC Health Alert Network*, CDC Health Alert Network.

Qiu X, Mistry A, Ammirati MJ, Chrunyk BA, Clark RW, Cong Y, Culp JS, Danley DE, Freeman TB, Geoghegan KF, Griffor MC, Hawrylik SJ, Hayward CM, Hensley P, Hoth LR, Karam GA, Lira ME, Lloyd DB, McGrath KM, Stutzman-Engwall KJ, Subashi AK, Subashi TA, Thompson JF, Wang IK, Zhao H and Seddon AP (2007) Crystal structure of cholesteryl ester transfer protein reveals a long tunnel and four bound lipid molecules. *Nature structural & molecular biology* **14**(2): 106-113.

Raghuram S, Stayrook KR, Huang P, Rogers PM, Nosie AK, McClure DB, Burris LL, Khorasanizadeh S, Burris TP and Rastinejad F (2007) Identification of heme as the ligand for the orphan nuclear receptors REV-ERBalpha and REV-ERBbeta. *Nature structural & molecular biology* **14**(12): 1207-1213.

Ranucci M, Ballotta A, Di Dedda U, Baryshnikova E, Dei Poli M, Resta M, Falco M, Albano G and Menicanti L (2020) The procoagulant pattern of patients with COVID-19 acute respiratory distress syndrome. *J Thromb Haemost* **18**(7): 1747-1751.

Rapkiewicz AV, Mai X, Carsons SE, Pittaluga S, Kleiner DE, Berger JS, Thomas S, Adler NM, Charytan DM, Gasmi B, Hochman JS and Reynolds HR (2020) Megakaryocytes and platelet-fibrin thrombi characterize multi-organ thrombosis at autopsy in COVID-19: A case series. *EClinicalMedicine* **24**.

Ravichandran S, Tang J, Grubbs G, Lee Y, Pourhashemi S, Hussaini L, Lapp SA, Jerris RC, Singh V, Chahroudi A, Anderson EJ, Rostad CA and Khurana S (2021) SARS-CoV-2 immune repertoire in MIS-C and pediatric COVID-19. *Nat Immunol* **22**(11): 1452-1464.

Reggiori G, Occhipinti G, De Gasperi A, Vincent JL and Piagnerelli M (2009) Early alterations of red blood cell rheology in critically ill patients. *Crit Care Med* **37**(12): 3041-3046.

Riphagen S, Gomez X, Gonzalez-Martinez C, Wilkinson N and Theocharis P (2020) Hyperinflammatory shock in children during COVID-19 pandemic. *Lancet* **395**(10237): 1607-1608.

Roderick SL, Chan WW, Agate DS, Olsen LR, Vetting MW, Rajashankar K and Cohen DE (2002) Structure of human phosphatidylcholine transfer protein in complex with its ligand. *Nature structural biology* **9**(7): 507-511.

Romanova ES, Vasilyev VV, Startseva G, Karev V, Rybakova MG and Platonov PG (2021) Cause of death based on systematic post-mortem studies in patients with positive SARS-CoV-2 tissue PCR during the COVID-19 pandemic. *J Intern Med* **290**(3): 655-665.

Rosenbluth MJ, Lam WA and Fletcher DA (2008) Analyzing cell mechanics in hematologic diseases with microfluidic biophysical flow cytometry. *Lab Chip* **8**(7): 1062-1070.

Rovas A, Osiaevi I, Buscher K, Sackarnd J, Tepasse PR, Fobker M, Kuhn J, Braune S, Gobel U, Tholking G, Groschel A, Pavenstadt H, Vink H and Kumpers P (2021) Microvascular dysfunction in COVID-19: the MYSTIC study. *Angiogenesis* **24**(1): 145-157.

Russo A, Tellone E, Barreca D, Ficarra S and Lagana G (2022) Implication of COVID-19 on Erythrocytes Functionality: Red Blood Cell Biochemical Implications and Morpho-Functional Aspects. *Int J Mol Sci* **23**(4).

Rutkowsky JM, Knotts TA, Ono-Moore KD, McCoin CS, Huang S, Schneider D, Singh S, Adams SH and Hwang DH (2014) Acylcarnitines activate proinflammatory signaling pathways. *Am J Physiol Endocrinol Metab* **306**(12): E1378-1387.

Said A, Rogers S and Doctor A (2015) Red cell physiology and signaling relevant to the critical care setting. *Curr Opin Pediatr* **27**(3): 267-276.

Sanderson LM, Degenhardt T, Koppen A, Kalkhoven E, Desvergne B, Müller M and Kersten S (2009) Peroxisome proliferator-activated receptor β/δ (PPARβ/δ) but not PPARα serves as a plasma free fatty acid sensor in liver. *Molecular and cellular biology* **29**(23): 6257-6267.

Scapa EF, Pocai A, Wu MK, Gutierrez-Juarez R, Glenz L, Kanno K, Li H, Biddinger S, Jelicks LA and Rossetti L (2008) Regulation of energy substrate utilization and hepatic insulin sensitivity by phosphatidylcholine transfer protein/StarD2. *The FASEB Journal* **22**(7): 2579-2590.

Scheen AJ (2001) Thiazolidinediones and liver toxicity. *Diabetes & metabolism* **27**(3): 305-313.

Schrick K, Bruno M, Khosla A, Cox PN, Marlatt SA, Roque RA, Nguyen HC, He C, Snyder MP, Singh D and Yadav G (2014) Shared functions of plant and mammalian StAR-related lipid transfer (START) domains in modulating transcription factor activity. *BMC biology* **12**: 70.

Schrick K, Nguyen D, Karlowski WM and Mayer KF (2004) START lipid/sterol-binding domains are amplified in plants and are predominantly associated with homeodomain transcription factors. *Genome biology* **5**(6): R41.

Schug TT, Berry DC, Shaw NS, Travis SN and Noy N (2007a) Opposing effects of retinoic acid on cell growth result from alternate activation of two different nuclear receptors. *Cell* **129**(4): 723-733.

Schug TT, Berry DC, Shaw NS, Travis SN and Noy N (2007b) Opposing effects of retinoic acid on cell growth result from alternate activation of two different nuclear receptors. *Cell* **129**(4): 723-733.

Schug TT, Berry DC, Toshkov IA, Cheng L, Nikitin AY and Noy N (2008) Overcoming retinoic acid-resistance of mammary carcinomas by diverting retinoic acid from PPARbeta/delta to RAR. *Proceedings of the National Academy of Sciences of the United States of America* **105**(21): 7546-7551.

Schwarz B, Sharma L, Roberts L, Peng X, Bermejo S, Leighton I, Massana AC, Farhadian S, Ko AI, Yale IT, Cruz CSD and Bosio CM (2020) Severe SARS-CoV-2 infection in humans is defined by a shift in the serum lipidome resulting in dysregulation of eicosanoid immune mediators. *medRxiv*.

Schymanski EL, Jeon J, Gulde R, Fenner K, Ruff M, Singer HP and Hollender J (2014) Identifying small molecules via high resolution mass spectrometry: communicating confidence. *Environ Sci Technol* **48**(4): 2097-2098.

Sessler RJ and Noy N (2005) A ligand-activated nuclear localization signal in cellular retinoic acid binding protein-II. *Molecular cell* **18**(3): 343-353.

Sever R and Glass CK (2013) Signaling by nuclear receptors. *Cold Spring Harbor perspectives in biology* **5**(3): a016709.

Sharma A and Sharma A (2011) Fatty acid induced remodeling within the human liver fatty acid-binding protein. *The Journal of biological chemistry* **286**(36): 31924-31928.

Shen B, Yi X, Sun Y, Bi X, Du J, Zhang C, Quan S, Zhang F, Sun R, Qian L, Ge W, Liu W, Liang S, Chen H, Zhang Y, Li J, Xu J, He Z, Chen B, Wang J, Yan H, Zheng Y, Wang D, Zhu J, Kong Z, Kang Z, Liang X, Ding X, Ruan G, Xiang N, Cai X, Gao H, Li L, Li S, Xiao Q, Lu T, Zhu Y, Liu H, Chen H and Guo T (2020) Proteomic and Metabolomic Characterization of COVID-19 Patient Sera. *Cell* **182**(1): 59-72 e15.

Shi D, Yan R, Lv L, Jiang H, Lu Y, Sheng J, Xie J, Wu W, Xia J, Xu K, Gu S, Chen Y, Huang C, Guo J, Du Y and Li L (2021) The serum metabolome of COVID-19 patients is distinctive and predictive. *Metabolism* **118**: 154739.

Shi J and Tomasi C (1994) Good Features to Track, in *IEEE Conference on Computer Vision and Pattern Recognition* pp 593-600.

Siegel DA, Reses HE, Cool AJ, Shapiro CN, Hsu J, Boehmer TK, Cornwell CR, Gray EB, Henley SJ, Lochner K, Suthar AB, Lyons BC, Mattocks L, Hartnett K, Adjemian J, van Santen KL, Sheppard M, Soetebier KA, Logan P, Martin M, Idubor O, Natarajan P, Sircar K, Oyegun E, Dalton J, Perrine CG, Peacock G, Schweitzer B, Morris SB and Raizes E (2021) Trends in COVID-19 Cases, Emergency Department Visits, and Hospital Admissions Among Children and Adolescents Aged 0–17 Years — United States, August 2020–August 2021. *MMWR Morb Mortal Wkly Rep* **70**: 1249-1254.

Singer M, Deutschman CS, Seymour CW, Shankar-Hari M, Annane D, Bauer M, Bellomo R, Bernard GR, Chiche JD, Coopersmith CM, Hotchkiss RS, Levy MM, Marshall JC, Martin GS, Opal SM, Rubenfeld GD, van der Poll T, Vincent JL and Angus DC (2016) The Third International Consensus Definitions for Sepsis and Septic Shock (Sepsis-3). *JAMA* **315**(8): 801-810.

Skendros P, Mitsios A, Chrysanthopoulou A, Mastellos DC, Metallidis S, Rafailidis P, Ntinopoulou M, Sertaridou E, Tsironidou V, Tsigalou C, Tektonidou M, Konstantinidis T, Papagoras C, Mitroulis I, Germanidis G, Lambris JD and Ritis K (2020) Complement and

tissue factor-enriched neutrophil extracellular traps are key drivers in COVID-19 immunothrombosis. *J Clin Invest* **130**(11): 6151-6157.

Slominski AT, Kim TK, Slominski RM, Song Y, Janjetovic Z, Podgorska E, Reddy SB, Song Y, Raman C and Tang EK (2022) Metabolic activation of tachysterol3 to biologically active hydroxyderivatives that act on VDR, AhR, LXRs, and PPARγ receptors. *The FASEB Journal* **36**(8): e22451.

Soliman S, Faris ME, Ratemi Z and Halwani R (2020) Switching host metabolism as an approach to dampen SARS-CoV-2 infection. *Annals of Nutrition and Metabolism* **76**(5): 297-303.

Sommars MA, Ramachandran K, Senagolage MD, Futtner CR, Germain DM, Allred AL, Omura Y, Bederman IR and Barish GD (2019) Dynamic repression by BCL6 controls the genome-wide liver response to fasting and steatosis. *Elife* **8**: e43922.

Song JW, Lam SM, Fan X, Cao WJ, Wang SY, Tian H, Chua GH, Zhang C, Meng FP, Xu Z, Fu JL, Huang L, Xia P, Yang T, Zhang S, Li B, Jiang TJ, Wang R, Wang Z, Shi M, Zhang JY, Wang FS and Shui G (2020) Omics-Driven Systems Interrogation of Metabolic Dysregulation in COVID-19 Pathogenesis. *Cell Metab* **32**(2): 188-202 e185.

Soprano DR, Qin P and Soprano KJ (2004) Retinoic acid receptors and cancers. *Annual review of nutrition* **24**: 201-221.

Spiegelman BM (1998) PPAR-gamma: adipogenic regulator and thiazolidinedione receptor. *Diabetes* **47**(4): 507-514.

Stahl K, Gronski PA, Kiyan Y, Seeliger B, Bertram A, Pape T, Welte T, Hoeper MM, Haller H and David S (2020) Injury to the Endothelial Glycocalyx in Critically Ill Patients with COVID-19. *Am J Respir Crit Care Med* **202**(8): 1178-1181.

Stehlin-Gaon C, Willmann D, Zeyer D, Sanglier S, Van Dorsselaer A, Renaud JP, Moras D and Schüle R (2003) All-trans retinoic acid is a ligand for the orphan nuclear receptor ROR beta. *Nature structural biology* **10**(10): 820-825.

Su Y, Chen D, Yuan D, Lausted C, Choi J, Dai CL, Voillet V, Duvvuri VR, Scherler K, Troisch P, Baloni P, Qin G, Smith B, Kornilov SA, Rostomily C, Xu A, Li J, Dong S, Rothchild A, Zhou J, Murray K, Edmark R, Hong S, Heath JE, Earls J, Zhang R, Xie J, Li S, Roper R, Jones L, Zhou Y, Rowen L, Liu R, Mackay S, O'Mahony DS, Dale CR, Wallick JA, Algren HA, Zager MA, Unit IS-SCB, Wei W, Price ND, Huang S, Subramanian N, Wang K, Magis AT, Hadlock JJ, Hood L, Aderem A, Bluestone JA, Lanier LL, Greenberg PD, Gottardo R, Davis MM, Goldman JD and Heath JR (2020) Multi-Omics Resolves a Sharp Disease-State Shift between Mild and Moderate COVID-19. *Cell* **183**(6): 1479-1495 e1420.

Szafraniec HM, Valdez JM, Iffrig E, Lam WA, Higgins JM, Pearce P and Wood DK (2022) Feature tracking microfluidic analysis reveals differential roles of viscosity and friction in sickle cell blood. *Lab Chip* **22**(8): 1565-1575.

Takase S, Ong DE and Chytil F (1986) Transfer of retinoic acid from its complex with cellular retinoic acid-binding protein to the nucleus. *Archives of biochemistry and biophysics* **247**(2): 328-334.

Tamori Y, Masugi J, Nishino N and Kasuga M (2002) Role of peroxisome proliferator-activated receptor-gamma in maintenance of the characteristics of mature 3T3-L1 adipocytes. *Diabetes* **51**(7): 2045-2055.

Tan NS, Shaw NS, Vinckenbosch N, Liu P, Yasmin R, Desvergne B, Wahli W and Noy N (2002) Selective cooperation between fatty acid binding proteins and peroxisome proliferator-

activated receptors in regulating transcription. *Molecular and cellular biology* **22**(14): 5114-5127.

Tars K, Leitans J, Kazaks A, Zelencova D, Liepinsh E, Kuka J, Makrecka M, Lola D, Andrianovs V and Gustina D (2014) Targeting carnitine biosynthesis: discovery of new inhibitors against γ-butyrobetaine hydroxylase. *Journal of medicinal chemistry* **57**(6): 2213-2236.

Teuwen LA, Geldhof V, Pasut A and Carmeliet P (2020) COVID-19: the vasculature unleashed. *Nat Rev Immunol* **20**(7): 389-391.

Thomas T, Stefanoni D, Dzieciatkowska M, Issaian A, Nemkov T, Hill RC, Francis RO, Hudson KE, Buehler PW, Zimring JC, Hod EA, Hansen KC, Spitalnik SL and D'Alessandro A (2020a) Evidence of Structural Protein Damage and Membrane Lipid Remodeling in Red Blood Cells from COVID-19 Patients. *J Proteome Res* **19**(11): 4455-4469.

Thomas T, Stefanoni D, Reisz JA, Nemkov T, Bertolone L, Francis RO, Hudson KE, Zimring JC, Hansen KC, Hod EA, Spitalnik SL and D'Alessandro A (2020b) COVID-19 infection alters kynurenine and fatty acid metabolism, correlating with IL-6 levels and renal status. *JCI Insight* **5**(14).

Thorsell AG, Lee WH, Persson C, Siponen MI, Nilsson M, Busam RD, Kotenyova T, Schuler H and Lehtio L (2011) Comparative structural analysis of lipid binding START domains. *PLoS One* **6**(6): e19521.

Tillman MC, Imai N, Li Y, Khadka M, Okafor CD, Juneja P, Adhiyaman A, Hagen SJ, Cohen DE and Ortlund EA (2020) Allosteric regulation of thioesterase superfamily member 1 by lipid sensor domain binding fatty acids and lysophosphatidylcholine. *Proceedings of the National Academy of Sciences* **117**(36): 22080-22089.

Tillman MC, Khadka M, Duffy J, Wang MC and Ortlund EA (2019) Structural characterization of life-extending Caenorhabditis elegans Lipid Binding Protein 8. *Scientific reports* **9**(1): 9966.

Tomas J, Mulet C, Saffarian A, Cavin J-B, Ducroc R, Regnault B, Kun Tan C, Duszka K, Burcelin R and Wahli W (2016) High-fat diet modifies the PPAR-γ pathway leading to disruption of microbial and physiological ecosystem in murine small intestine. *Proceedings of the National Academy of Sciences* **113**(40): E5934-E5943.

Truong AD, Auld SC, Barker NA, Friend S, Wynn AT, Cobb J, Sniecinski RM, Tanksley CL, Polly DM, Gaddh M, Connor M, Nakahara H, Sullivan HC, Kempton C, Guarner J, Duncan A, Josephson CD, Roback JD, Stowell SR and Maier CL (2021) Therapeutic plasma exchange for COVID-19-associated hyperviscosity. *Transfusion* **61**(4): 1029-1034.

Tsai M, Kita A, Leach J, Rounsevell R, Huang JN, Moake J, Ware RE, Fletcher DA and Lam WA (2012) In vitro modeling of the microvascular occlusion and thrombosis that occur in hematologic diseases using microfluidic technology. *J Clin Invest* **122**(1): 408-418.

Tsukahara T, Tsukahara R, Fujiwara Y, Yue J, Cheng Y, Guo H, Bolen A, Zhang C, Balazs L, Re F, Du G, Frohman MA, Baker DL, Parrill AL, Uchiyama A, Kobayashi T, Murakami-Murofushi K and Tigyi G (2010) Phospholipase D2-dependent inhibition of the nuclear hormone receptor PPARgamma by cyclic phosphatidic acid. *Molecular cell* **39**(3): 421-432.

Turnbaugh PJ, Ley RE, Mahowald MA, Magrini V, Mardis ER and Gordon JI (2006) An obesity-associated gut microbiome with increased capacity for energy harvest. *Nature* **444**(7122): 1027-1031.

Uchimido R, Schmidt EP and Shapiro NI (2019) The glycocalyx: a novel diagnostic and therapeutic target in sepsis. *Crit Care* **23**(1): 16.

Uhlén M, Fagerberg L, Hallström BM, Lindskog C, Oksvold P, Mardinoglu A, Sivertsson Å, Kampf C, Sjöstedt E, Asplund A, Olsson I, Edlund K, Lundberg E, Navani S, Szigyarto CA, Odeberg J, Djureinovic D, Takanen JO, Hober S, Alm T, Edqvist PH, Berling H, Tegel H, Mulder J, Rockberg J, Nilsson P, Schwenk JM, Hamsten M, von Feilitzen K, Forsberg M, Persson L, Johansson F, Zwahlen M, von Heijne G, Nielsen J and Pontén F (2015) Proteomics. Tissue-based map of the human proteome. *Science (New York, NY)* **347**(6220): 1260419.

Uppal K, Ma C, Go YM, Jones DP and Wren J (2018) xMWAS: a data-driven integration and differential network analysis tool. *Bioinformatics* **34**(4): 701-702.

Uysal KT, Scheja L, Wiesbrock SM, Bonner-Weir S and Hotamisligil GS (2000) Improved glucose and lipid metabolism in genetically obese mice lacking aP2. *Endocrinology* **141**(9): 3388-3396.

Vanier MT (2015) Complex lipid trafficking in Niemann-Pick disease type C. *Journal of inherited metabolic disease* **38**(1): 187-199.

Velkov T (2013) Interactions between Human Liver Fatty Acid Binding Protein and Peroxisome Proliferator Activated Receptor Selective Drugs. *PPAR research* **2013**: 938401.

Viner RM and Whittaker E (2020) Kawasaki-like disease: emerging complication during the COVID-19 pandemic. *Lancet* **395**(10239): 1741-1743.

Wagner N and Wagner K-D (2020) PPAR beta/delta and the hallmarks of cancer. *Cells* **9**(5): 1133.

Wang C, Li X, Ning W, Gong S, Yang F, Fang C, Gong Y, Wu D, Huang M, Gou Y, Fu S, Ren Y, Yang R, Qiu Y, Xue Y, Xu Y and Zhou X (2021a) Multi-omic profiling of plasma reveals molecular alterations in children with COVID-19. *Theranostics* **11**(16): 8008-8026.

Wang D, Wang H, Guo Y, Ning W, Katkuri S, Wahli W, Desvergne B, Dey SK and DuBois RN (2006) Crosstalk between peroxisome proliferator-activated receptor delta and VEGF stimulates cancer progression. *Proceedings of the National Academy of Sciences of the United States of America* **103**(50): 19069-19074.

Wang H, Chen J, Hollister K, Sowers LC and Forman BM (1999) Endogenous bile acids are ligands for the nuclear receptor FXR/BAR. *Molecular cell* **3**(5): 543-553.

Wang L, Li G, Yuan C, Yang Y, Ling G, Zheng J, Zhou Y, Zhang T, Lin W and Lin Z (2021b) Progress in the Diagnosis and Treatment of COVID-19 in Children: A Review. *Int J Gen Med* **14**: 8097-8108.

Wang Y, Kumar N, Crumbley C, Griffin PR and Burris TP (2010) A second class of nuclear receptors for oxysterols: Regulation of RORalpha and RORgamma activity by 24S-hydroxycholesterol (cerebrosterol). *Biochimica et biophysica acta* **1801**(8): 917-923.

Ward ZJ, Bleich SN, Cradock AL, Barrett JL, Giles CM, Flax C, Long MW and Gortmaker SL (2019) Projected US state-level prevalence of adult obesity and severe obesity. *New England Journal of Medicine* **381**(25): 2440-2450.

Weikum ER, Liu X and Ortlund EA (2018) The nuclear receptor superfamily: A structural perspective. *Protein science : a publication of the Protein Society* **27**(11): 1876-1892.

Wieckowski MR, Giorgi C, Lebiedzinska M, Duszynski J and Pinton P (2009) Isolation of mitochondria-associated membranes and mitochondria from animal tissues and cells. *Nature protocols* **4**(11): 1582-1590.

Wiersinga WJ, Rhodes A, Cheng AC, Peacock SJ and Prescott HC (2020) Pathophysiology, Transmission, Diagnosis, and Treatment of Coronavirus Disease 2019 (COVID-19): A Review. *JAMA* **324**(8): 782-793.

Wikoff WR, Anfora AT, Liu J, Schultz PG, Lesley SA, Peters EC and Siuzdak G (2009) Metabolomics analysis reveals large effects of gut microflora on mammalian blood metabolites. *Proceedings of the national academy of sciences* **106**(10): 3698-3703.

Wirtz KW and Zilversmit DB (1968) Exchange of phospholipids between liver mitochondria and microsomes in vitro. *The Journal of biological chemistry* **243**(13): 3596-3602.

Woerly G, Honda K, Loyens M, Papin J-P, Auwerx J, Staels B, Capron M and Dombrowicz D (2003) Peroxisome proliferator–activated receptors α and γ down-regulate allergic inflammation and eosinophil activation. *The Journal of experimental medicine* **198**(3): 411-421.

Wolfrum C, Borrmann CM, Borchers T and Spener F (2001a) Fatty acids and hypolipidemic drugs regulate peroxisome proliferator-activated receptors alpha - and gamma-mediated gene expression via liver fatty acid binding protein: a signaling path to the nucleus. *Proceedings of the National Academy of Sciences of the United States of America* **98**(5): 2323-2328.

Wolfrum C, Borrmann CM, Börchers T and Spener F (2001b) Fatty acids and hypolipidemic drugs regulate peroxisome proliferator-activated receptors α-and γ-mediated gene expression via liver fatty acid binding protein: a signaling path to the nucleus. *Proceedings of the National Academy of Sciences* **98**(5): 2323-2328.

Wolfrum C, Ellinghaus P, Fobker M, Seedorf U, Assmann G, Börchers T and Spener F (1999) Phytanic acid is ligand and transcriptional activator of murine liver fatty acid binding protein. *Journal of lipid research* **40**(4): 708-714.

Wong LH, Copic A and Levine TP (2017) Advances on the Transfer of Lipids by Lipid Transfer Proteins. *Trends in biochemical sciences* **42**(7): 516-530.

Wu C-C, Baiga TJ, Downes M, La Clair JJ, Atkins AR, Richard SB, Fan W, Stockley-Noel TA, Bowman ME and Noel JP (2017) Structural basis for specific ligation of the peroxisome proliferator-activated receptor δ. *Proceedings of the National Academy of Sciences* **114**(13): E2563-E2570.

Wu D, Shu T, Yang X, Song JX, Zhang M, Yao C, Liu W, Huang M, Yu Y, Yang Q, Zhu T, Xu J, Mu J, Wang Y, Wang H, Tang T, Ren Y, Wu Y, Lin SH, Qiu Y, Zhang DY, Shang Y and Zhou X (2020) Plasma metabolomic and lipidomic alterations associated with COVID-19. *Natl Sci Rev* **7**(7): 1157-1168.

Wu P, Chen D, Ding W, Wu P, Hou H, Bai Y, Zhou Y, Li K, Xiang S, Liu P, Ju J, Guo E, Liu J, Yang B, Fan J, He L, Sun Z, Feng L, Wang J, Wu T, Wang H, Cheng J, Xing H, Meng Y, Li Y, Zhang Y, Luo H, Xie G, Lan X, Tao Y, Li J, Yuan H, Huang K, Sun W, Qian X, Li Z, Huang M, Ding P, Wang H, Qiu J, Wang F, Wang S, Zhu J, Ding X, Chai C, Liang L, Wang X, Luo L, Sun Y, Yang Y, Zhuang Z, Li T, Tian L, Zhang S, Zhu L, Chang A, Chen L, Wu Y, Ma X, Chen F, Ren Y, Xu X, Liu S, Wang J, Yang H, Wang L, Sun C, Ma D, Jin X and Chen G (2021) The trans-omics landscape of COVID-19. *Nat Commun* **12**(1).

Wu Z and McGoogan JM (2020) Characteristics of and Important Lessons From the Coronavirus Disease 2019 (COVID-19) Outbreak in China: Summary of a Report of 72314 Cases From the Chinese Center for Disease Control and Prevention. *JAMA* **323**(13): 1239-1242.

Yang L, Lewkowich I, Apsley K, Fritz JM, Wills-Karp M and Weaver TE (2015) Haploinsufficiency for Stard7 is associated with enhanced allergic responses in lung and skin. *The Journal of Immunology* **194**(12): 5635-5643.

Yoo SH, Abdelmegeed MA and Song B-J (2013) Activation of PPARα by Wy-14643 ameliorates systemic lipopolysaccharide-induced acute lung injury. *Biochemical and biophysical research communications* **436**(3): 366-371.

Yu S, Levi L, Casadesus G, Kunos G and Noy N (2014) Fatty acid-binding protein 5 (FABP5) regulates cognitive function both by decreasing anandamide levels and by activating the nuclear receptor peroxisome proliferator-activated receptor β/δ (PPARβ/δ) in the brain. *The Journal of biological chemistry* **289**(18): 12748-12758.

Zhang X, Caruso C, Lam WA and Graham MD (2020) Flow-induced segregation and dynamics of red blood cells in sickle cell disease. *Phys Rev Fluids* **5**(5).

Zhao L, Wang G, Siegel P, He C, Wang H, Zhao W, Zhai Z, Tian F, Zhao J and Zhang H (2013) Quantitative genetic background of the host influences gut microbiomes in chickens. *Scientific reports* **3**(1): 1-6.

Zoete V, Grosdidier A and Michielin O (2007) Peroxisome proliferator-activated receptor structures: ligand specificity, molecular switch and interactions with regulators. *Biochimica et Biophysica Acta (BBA)-Molecular and Cell Biology of Lipids* **1771**(8): 915-925.

Zomer AW, van Der Burg B, Jansen GA, Wanders RJ, Poll-The BT and van Der Saag PT (2000) Pristanic acid and phytanic acid: naturally occurring ligands for the nuclear receptor peroxisome proliferator-activated receptor alpha. *Journal of lipid research* **41**(11): 1801-1807.